

Sheffield Hallam University

An investigation into frictional surface interactions and their effect on brake judder.

EGGLESTON, David.

Available from the Sheffield Hallam University Research Archive (SHURA) at:

<http://shura.shu.ac.uk/19601/>

A Sheffield Hallam University thesis

This thesis is protected by copyright which belongs to the author.

The content must not be changed in any way or sold commercially in any format or medium without the formal permission of the author.

When referring to this work, full bibliographic details including the author, title, awarding institution and date of the thesis must be given.

Please visit <http://shura.shu.ac.uk/19601/> and <http://shura.shu.ac.uk/information.html> for further details about copyright and re-use permissions.

SHEFFIELD S1 1WB.

101 667 481 3



REFERENCE

ProQuest Number: 10694482

All rights reserved

INFORMATION TO ALL USERS

The quality of this reproduction is dependent upon the quality of the copy submitted.

In the unlikely event that the author did not send a complete manuscript and there are missing pages, these will be noted. Also, if material had to be removed, a note will indicate the deletion.



ProQuest 10694482

Published by ProQuest LLC (2017). Copyright of the Dissertation is held by the Author.

All rights reserved.

This work is protected against unauthorized copying under Title 17, United States Code
Microform Edition © ProQuest LLC.

ProQuest LLC.
789 East Eisenhower Parkway
P.O. Box 1346
Ann Arbor, MI 48106 – 1346

**An Investigation into
Frictional Surface Interactions and
their effect on Brake Judder**

David Eggleston

A thesis submitted in partial fulfilment of the requirements of
Sheffield Hallam University for the degree of Doctor of Philosophy

Collaborating Organisation: B.B.A. Friction Ltd.

August 2000



Abstract

The chemical nature of the *Transfer Film* (T.F.) or *Third-Body Layer* (T.B.L.) formed at the friction interface of an automotive friction brake during off-brake motoring has been studied using *Energy Dispersive X-ray* (E.D.X.) analysis and *Scanning Electron Microscopy* (S.E.M.). Although these third-body layers are deposited on both mating surfaces of the friction couple, special attention has been paid to those formed on the disc brake rotor surface.

Concurrently, detailed investigations have been undertaken examining the temperature-dependent, physico-chemical interactions of friction material constituents with each other, atmospheric oxygen and countermember materials using *X-Ray Diffraction* (X.R.D.).

Evidence is presented relating the tribological performance of the friction pair to both the transfer film thermochemistry and the friction material composition. Among those characteristics describing the tribological performance of the friction couple, particular attention has been applied to the generation of *Disc Thickness Variations* (D.T.V.) induced by *Off-Brake* or *Non-Braking Wear* (O.B.W. or N.B.W.).

The critical role of solid lubricants and abrasive friction modifiers and their effectiveness over a range of contact pressures / temperatures has received particular attention. Information obtained using various surface analytical techniques combined with detailed dimensional assessments of the affected triboelements has been used to show the considerable significance of abrasive particle size in determining the overall tribological behaviour of the friction pair, especially with respect to the wear regime and extent encountered at the surface of the countermember during O.B.W.

Wear mechanisms are described for the generation of off-brake wear, these varying with friction material formulation. Dynamic and temperature-dependent influences on the level of in-service disc brake rotor runout are named as causes for particular forms of disc thickness variation generated by aggressive friction materials.

Keywords: Third-body layer; Transfer film; Tribochemistry; Automotive Friction Braking; Cold Judder; Disc Thickness Variation; Disc Brake; Friction Material.

Candidate's Statement

The author declares that no part of this work, other than those specifically referenced as either supporting or providing a foundation for subsequent investigations, has been submitted in support of another degree or qualification to either Sheffield Hallam University or to any other educational establishment. The author further declares that he has not been a registered research degree candidate or enrolled student for another award of either Sheffield Hallam University or other academic or professional institution during the course of the programme of research.

Acknowledgements

The author would like to express his sincere gratitude to Dr. Allan Wirth for his unstinting support, assistance, seemingly inexhaustible patience and his friendship throughout the duration of the investigation.

Thanks are due also to the staff of Sheffield Hallam University and the Materials Research Institute who provided a supportive working environment.

I would similarly like to thank the staff of the Research Department of B.B.A. Friction Ltd. at Cleckheaton, especially Mr. Bob Whitaker, who was an invaluable source of knowledge and experience.

Finally, I would like to thank my current employers (European Automotive Components) and in particular Dr. J.G. Krosnar for the numerous, and generous, periods of extended leave afforded to me in order that I might be able to complete this thesis.

Contents

1.0. Introduction	1
2.0. Literature Survey	2
2.1. Automotive Friction Brakes & Braking	2
2.1.1. Elements of Automotive Friction Braking	3
2.2. Brake Refinement Problems	4
2.3. Brake Judder Phenomena	6
2.3.1. Thermal Judder	8
2.3.1.1. Thermo-Mechanical Distortion of Disc Brake Rotors	10
2.3.1.2. Permanent Geometric & Microstructural Inconsistencies	11
2.3.1.3. Approaches to the Solution of Thermal Judder	13
2.3.2. Cold Judder	14
2.3.2.1. Axial Side-Face Runout & Disc Thickness Variation	16
2.3.2.2. Off-Brake Wear & Disc Thickness Variation	19
2.3.2.3. Judder Transmission & the Vibratory Environment	20
2.3.2.4. Corrective Mechanisms for Cold Judder	23
3.0. Automotive Friction Materials	28
3.1. Constitution of N.A.O. Friction Materials	29
3.1.1. Binding Agents	30
3.1.2. Fibre-Reinforcement	30
3.1.3. Metallic Friction Modifiers	33
3.1.4. Solid Lubricants	34
3.1.5. Abrasive Friction Modifiers	34
3.1.6. Organic Fillers	35
3.1.7. Inorganic Fillers	36
3.2. Wear of Automotive Friction Materials	38
3.2.1. Wear Mechanisms of Resin-Bonded Friction Materials	39
3.3. Generation of Third-Body Layers	42
4.0. Experimental Procedure	47
4.1. Characterisation of Disc Brake Rotor Material	47
4.1.1. Constitutional Characterisation	48
4.1.1.1. Chemical Composition	49
4.1.1.2. Microstructural Characterisation of the Graphite Structure	50
4.1.1.3. Microstructural Characterisation of the Material Matrix	50
4.1.2. Mechanical Uniformity of Vertically Cast Rotors	51
4.1.3. Geometric Characterisation	52
4.2. Characterisation of N.A.O. Friction Materials	53

4.2.1.	Abrasive Constituent Characterisation	54
4.2.2.	Distribution of Friction Material Constituents	55
4.3.	Physico-Chemical Interactions of Friction Material Constituents	56
4.4.	Disc Thickness Variation Evaluation rig Testing	59
4.5.	A.S.E.M. applied to Third-Body Layers and Friction Material Constituents	62
5.0.	Results & Discussion	68
5.1.	Characterisation of Disc Brake Rotor Material	68
5.1.1.	Constitutional Characterisation	69
5.1.1.1.	Chemical Composition	70
5.1.1.2.	Microstructural Characterisation of the Graphite Structure	76
5.1.1.3.	Microstructural Characterisation of the Material Matrix	78
5.1.2.	Mechanical Uniformity of Vertically Cast Rotors	79
5.1.3.	Geometric Characterisation	81
5.2.	Characterisation of N.A.O. Friction Materials	81
5.2.1.	Abrasive Constituent Characterisation	82
5.2.2.	Abrasive Constituent Distribution & Dispersion	83
5.3.	Thermochemistry of Friction Material Constituents	86
5.4.	Kinetics of Friction Material Constituents	108
5.5.	Disc Thickness Variation Evaluation rig Testing	115
5.5.1.	Tribological Characteristics of Burnished Rotors	117
5.5.2.	Tribomechanical Interactions and D.T.V. Generation	118
5.5.3.	Tribochemical Interactions and D.T.V. Generation	125
5.5.4.	Supplementary Observations and D.T.V. Generation	131
5.5.5.	Influence of Abrasive Friction Modifier Additions	133
6.0.	Conclusions	137
6.1.	Suggestions for Future Research	139
7.0.	References	141
8.0.	Bibliography	157
9.0.	Figures	163
10.0.	Plates	225
11.0.	Appendices	257
11.1.	Chemical Changes occurring at the Braking Interface	257
11.2.	Chemical Analysis of Cast Iron using Universal Vacuum Air Quantometry	263
11.3.	Chemical Analysis using Glow Discharge Optical Emission Spectroscopy	264
11.4.	Chemical Analysis of Cast Irons using X-Ray Fluorescence Spectroscopy	266
11.5.	Typical <i>Carballoy</i> Rotor Analysis	270
11.6.	Analytical Scanning Electron Microscopy	271
11.7.	Thermodynamics of Friction Material Constituents	273

11.8.	X-Ray Diffraction	279
11.9.	Full-scale Inertial Dynamometer Testing	281
11.10.	Calculation of Abrasive Particulate Loading	284
11.11.	X-ray Photoelectron Spectroscopy	287

1.0. Introduction

For a great many years, the brake linings of motor vehicles were composed of up to 50 % asbestos. With the realisation of the serious health hazards associated with blue asbestos, it, and its derivatives have steadily been removed from use in this market. However, although the hazard to health has now been reduced, the frictional (and thus braking) properties of individual replacement materials have proved inferior to asbestos and have resulted in the development of much more complex braking material formulations. This has affected braking stability and has accentuated several braking problems.

This project examines one particular aspect of the problems associated with the operation of vehicle disc brakes; that of *cold judder*. The phenomenon of cold judder manifests itself as a low frequency vibration of the steering system and indeed of the whole vehicle and is the result of a non-uniform brake disc (friction ring) thickness causing a cyclic variation in the brake torque output. Brake *Disc Thickness Variation* (D.T.V.) is thought to be the result of cyclic, intermittent contact with the brake pads under normal off-brake driving. This cyclic contact, although very light, acts over long periods of time causing non-uniform wear of the disc surface and hence a variation in disc thickness.

This study characterises the frictional surface interactions occurring within automotive braking friction couples by consideration of the friction material composition, the rotor metallurgy, the transfer films generated between the two surfaces and the physico-chemical interactions occurring during friction, factors now known or suspected to affect D.T.V. These findings are then used to elucidate the mechanisms contributing to the *in situ* generation of D.T.V. which will, in future, enable the development of friction materials that produce a minimum of D.T.V.

2.0. Literature Survey

2.1. Automotive Friction Brakes & Braking

In 1687, Sir Isaac Newton (1642 - 1727) formulated his laws of motion, the first of which, the principal of inertia, originally conceived by Galileo Galilei (1564 - 1642) in 1604, states:

A body continues in a state of rest or uniform motion in a straight line unless it is acted upon by an external force.

In the case of an automotive vehicle travelling at speed, such 'external' forces may include wind resistance or the effect of gravity on inclined road surfaces but also mechanical losses and residual drag factors acting within the vehicle as a result of friction, transmission of power from the engine unit to the wheels, steering and braking. It is the latter of these forces with which this study has been principally concerned.

During motoring, the action of braking is instigated by the vehicle driver by progressive depression of the brake pedal. Depressing the brake pedal displaces a proportional quantity of incompressible hydraulic fluid from a master cylinder (incorporating a fluid reservoir) and along narrow-bore brake lines to the brakes. Generally, at some stage between the master cylinder and the friction brake actuation mechanism, some amplification of the hydraulic pressure is induced by a servo-assist mechanism consisting a large cylinder and flexible diaphragm operating off the partial vacuum existing in the engine induction manifold. Pedal travel controls this reinforcing action by valve systems and mechanical linkages. At the brake assembly itself, the pressure at the hydraulic fluid line is fed to an appropriate number of pistons, which force the friction material lining against the spinning rotor.

The arrangement of the brakes lines, or brake circuitry, may vary greatly from model to model but will usually be split, i.e. dual-circuit, such that catastrophic failure of the brake system is avoided if a single brake hose fractures, becomes corroded or is punctured.

In many passenger car disc brake assemblies (plate 1), the rotor takes the form of an annular disc that rotates with the wheel and stub-axle. The friction material stators are housed such that they sandwich the rotor within the caliper housing, which sits straddling the disc. The caliper is connected rigidly to the stub-axle carrier and may be designed in such a way that pressure is transferred to the pads in one of two ways. The fixed or stationary caliper contains piston cylinders on both inboard and outboard sides of the disc. The floating caliper provides piston pressure from the inboard side only and as the inboard pad contacts the disc, the caliper housing slides on a pin or pins in the inboard direction to bring the outboard pad into contact with the rotor.

Disc brake rotor designs fall into two major categories, these being solid annular discs (sometimes said to be preferred in the European market), and ventilated annular discs consisting two brake plates separated by vanes or pillars through which airflow facilitates enhanced convective cooling (generally preferred by the US home market or on the front axles of any larger or higher performance vehicle). Cast iron remains the material of choice for rotor construction (1 – 9) although many other materials and their variants find widespread specialist application (10 – 23).

Similarly, friction material formulations may vary markedly according to their prospective operating regime (22 – 25). A more thorough appreciation of the major breakthroughs and developments in automotive braking systems can be gained by a review of references 1, 25 – 33.

2.1.1. Elements of Automotive Friction Braking

As the science has become more refined, an increasing number of factors have been incorporated into brake design. Driving style, national driving patterns, environment, tyre and road surface conditions must all be thoroughly examined when developing modern braking systems.

The numerous factors affecting braking and their interrelationships can be demonstrated by means of an interaction diagram, shown in figure 1. Of those factors listed, two fundamentally important subject areas are those of the frictional surface interactions between stator and rotor (the focus of the author's

programme of research) and of the heat generation and dissipation within the system (25, 34 – 53), an appreciation of the latter being essential to the nature of the former.

2.2. Brake Refinement Problems

Over the past century, the collection of functional or tribometric parameters describing the tribological performance of automotive braking friction couples has grown significantly. Basic factors such as friction (static and dynamic coefficients of friction), friction stability (fade and recovery response) and wear (rotor and stator material loss), although essential, have been seen to inadequately define the demands of an increasingly discerning customer and ultimately, international legislation.

In response to this scenario, the areas now receiving the greatest attention by automotive brake researchers and development engineers are those of ride comfort optimisation and brake refinement.

Brake refinement is, of course, still concerned with those crucial factors with which researchers were always concerned but once all safety critical considerations have been addressed, factors such as brake ‘feel’ or in-brake characteristics must also be incorporated into the customer satisfaction equation.

The majority of current brake refinement issues fall into the category of *Noise, Vibration and Harshness* (N.V.H.) (54). Further categorisation difficulties exist but generally, noise is classified as those phenomena exciting high frequency vibrations from 1 – 15 kHz (i.e. up to the limit of human pitch acuity), whereas judder, *hum* or low frequency vibration phenomena are defined by the range 1 – 500 Hz. Another important basis for categorisation, and one that is frequently overlooked, involves the fact that low frequency judder phenomena exert a deleterious effect on braking efficiency and are therefore not simply brake refinement issues, but safety-critical concerns.

The nature of the automotive components industry means that manufacturers provide *Original Equipment* (OE) products to automobile manufacturers (who subsequently interface with their customers through non-technical sales outlets and dealerships). However, despite the difficulty with which OE manufacturers obtain accurate, final-user feedback on their products, problems eventually materialise.

Table 1 prioritises the brake-related concerns of automobile and automotive components manufacturers affecting the industry.

It is often claimed that the majority of judder phenomena encountered by the average road-user are not brake dependent. It has been estimated that only about 10 % of all judder complaints are excited at the brake assembly (55 – 56), despite the speculative assertions and appreciable consternation of the customer. Other sources, which may give very similar subjective response, may originate at the suspension assembly, at the wheel as a result of tyre force variations (exciting vibrations in the range 1 Hz – 1 kHz) or wheel imbalance, or simply at the road surface itself. In fact, wheel imbalance forces are frequently introduced to otherwise equilibrium systems in order to simulate the brake judder phenomenon (57 – 58).

Table 1:

UK automotive friction braking research priorities as identified at the 1st Automotive Brakes Workshop, Weetwood Conference Centre at the University of Leeds in April, 1993.

Brake refinement research (prioritised):	Subdivision / phenomenon:	Priority within area:
Judder phenomena	Cold judder	1
	Thermal judder	2
Functional characteristics	Brake 'feel'	1
	In-stop characteristics	2
Noise	Squeal	1
	Squelch	2
	Graunch and creep groan (exclusive to automatic transmission vehicles)	3
	Squeak	4
	Wire-brush	5

2.3. Brake Judder Phenomena

Brake judder is a low frequency vibration, excited at the brakes, which may be transmitted to the passengers, but especially to the driver of a vehicle during automotive friction braking.

The critical feature of any type of judder phenomenon originating at the brake system is a cyclic fluctuation in the brake torque output, formally referred to as *Brake Torque Variation* (B.T.V.). The magnitude of the brake torque fluctuations encountered during judder may grow to as much as 50 % of the total torque output in extreme cases (59) although values of 5 – 15 % are more usual (60 – 61). The frequency range of the detected vibrations tends to be of the order of 10 – 500 Hz and varies continually, throughout an individual brake application since the vibration frequency is a function of wheel rotational speed, and hence a function of the vehicle's forward velocity.

The inherently low frequency of judder vibrations means that they are typically felt (1 – 100 Hz) as much as they are heard (100 – 500 Hz). The manifested characteristics that might be perceived by the vehicle's occupants are a low frequency torsional oscillation of the steering system about the column axis, a vibration radiated axially from cockpit panelling (windscreen, facia, doors, roof, floor-plan, etc.) and a vibration of the drivers seat rail / track, combined with a pulsing of the brake pedal.

These manifestations are primarily the result of cyclic, non-uniform contact between the friction material pad and the cast iron disc brake rotor during braking. This non-uniform contact induces a wheel-order, axial displacement of the friction material which translates as a rhythmic variation in the brake torque output. Such phenomena may be classified as mechanically forced, or exerted vibrations, as opposed to resonant, or self-excited vibrations, which tend to promote those phenomena termed noise.

Judder phenomena are most frequently experienced during high output braking such as when braking from high speed, the frequency of the vibration decreasing linearly with the vehicle's forward velocity. However, the observed amplitude of the vibration is not linear throughout a deceleration. The perceived vibration intensity may, in fact, vary markedly during a brake application due to the resonance of the individual components or mechanical systems transmitting the vibration. Such anomalies in the vibration intensity may persist only over a very narrow band of frequencies and are vehicle dependent.

Continued research into judder phenomena in automotive friction braking systems has identified that both the causes and the effects of judder can vary. Perhaps not surprisingly, the absence of a single, simple instability mechanism means that discrete distinctions, however convoluted, must be made. Different manufacturers use different terminology to define subtle differences in the physical effects of judder some of which include; judder (violent or noisy vibration), shudder, shake, shimmy (abnormal vibration or shaking, especially of the front wheels) and nibble (tangential vibration at the steering wheel rim). Although the effects may not always appear consistent, two major categories of judder excitation have been isolated:

- 1. THERMAL JUDDER (2.3.1.)**
- 2. COLD JUDDER (2.3.2.)**

The classification of judder phenomena according to the relative role of heat in causing variations in the braking torque is quite legitimate and indeed preferable when considering the causation of such problems (such as is the case during the author's programme of research). However, it is worthy to mention that when considering the effects of such phenomena, vibration modellers find it more useful to differentiate between these effects in terms of the vibrational orders induced, i.e. *Low Order* (L.O.) judder (traditionally analogous with cold judder) and *High Order* (H.O.) judder (associated with thermal judder) (62 – 65).

2.3.1. Thermal Judder

Thermal or hot judder, like cold judder, occurs as a result of non-uniform contact cycles between the friction material pad and the disc brake rotor. However, unlike cold judder, thermal judder occurs principally as an effect of localised *Thermo-Elastic Instabilities* (T.E.I.) active in the surface of the cast iron disc brake rotor, the initiating non-uniform contact producing non-uniform heat generation during braking.

These localised T.E.I. act at the friction ring surface generating intermittent hot bands around the rubbing path, which may in turn lead to the development of so-called heat, or focal hot spots. These hot spots are appreciably larger than would be expected from standard asperity interactions (table 2), are significantly narrower than the rubbing width of the contacting lining and exhibit a hyperunity aspect ratio in the rubbing direction. In addition, they tend to form at approximately equidistant intervals around the friction ring.

Table 2:

Comparative characteristics of the four principal varieties of hot spot as defined by Anderson and Knapp (66).

<i>Hot spot type:</i>	<i>Radial diameter, ϕ (mm):</i>	<i>Temperature ($^{\circ}\text{C}$):</i>	<i>Lifespan (s):</i>
Asperity	< 1	1,000 – 1,200	< 1×10^{-3}
Focal	5 – 20	750 – 1,200	0.5 – 20
Distortional	20 – 100	100 – 700	> 10
Regional	50 – 100	10 – 100	> 10

According to empirical observations, these hot spots generate judder frequencies of between 6 and 20 cycles per wheel revolution (67) ($\cong 10 - 500$ Hz). In separate observations of a vehicle braking from 170 – 60 km.h⁻¹, dominant vibration orders appeared between 7 and 13 cycles per wheel revolution (68), corresponding to vibration frequencies $\cong 60 - 300$ Hz.

Early work examining the frictional surface interactions associated with T.E.I. demonstrated how multiple asperity contacts can effectively conglomerate to produce discrete, concentrated areas of contact and postulated that the mechanism of agglomeration might be dependent on the presence of surface irregularities (69 – 70; cited in 71), i.e. an imperfect original contact geometry. Later work showed that surface irregularities were not prime-requisites to initiate a non-uniform contact regime and that the heat generated within smooth, sliding friction couples could readily develop uneven pressure distributions and contact areas (72; cited in 71).

It has been established both through observation and by the application of uncoupled thermo-elastic *Finite Element Modelling* (F.E.M.) of friction pairs that thermal judder is most likely to occur under conditions of relatively low contact pressures when total brake output is high. Further experimental work has demonstrated that, during braking, the heat generation and hence the pressure distribution in the radial plane is far from regular during contact and indeed, in small sections, partially discontinuous. Although the resultant hot bands appear to remain static during an individual brake application, their position may vary noticeably from one brake application to the next (59, 67). Further work applying fully coupled thermo-elastic F.E.M. (71) of friction pairs incorporating interfacial elements and wear simulation suggests that when considering long brake applications (> 5 seconds), such as one might expect on an extended mountain descent, hot bands do not necessarily remain radially static but will gradually shift with increasing wear of the original hot spot. In both the model described, and during experimental validation, it was noted that a narrow hot band can form very shortly after the onset of braking. The pad geometry dictates that the first hot banding generally occurs between the mean rubbing radius and the outer rubbing radius (68, 71), presumably at least partially as a result of the higher rubbing velocity encountered at increasing rubbing radii. Furthermore, the rubbing radius where the first hot band is generally observed to develop coincides with the position in the friction material geometry where the apparent tribocontact (ratio of pad area to rubbing area) is at its maximum. Thereafter, upon wear of the thermally expanded hot band, the local pressure redistributes but the increased heat generation associated with increasing rubbing radius ensures that hot banding continues to shift outwards until further wear induces it to retreat.

2.3.1.1. Thermo-Mechanical Distortion of Disc Brake Rotors

Further localisation of the friction contact may occur in response to increasing thermal deformation of the disc as a consequence of the continued, non-equilibrium thermal expansion of the constrained rotor. Some of the most frequently observed disc brake rotor geometries encountered as a result of excessive thermo-mechanical distortion are displayed in figure 2. Hot spots formed via this process are generally termed *distortional* and are large and diffuse.

Thermal deformation may, in the first instance, impart a corrugated, warped, rippled or wave-like longitudinal cross-section to the friction ring (primary thermal buckling), contributing to the continued real contact concentration. This effect is usually encountered at the onset of thermo-mechanical distortion where the linear thermal expansion of the friction ring section surpasses that at the nave of the disc (the linkage between the friction ring and top-hat section), i.e. a thermal non-equilibrium condition. The wavelength or rotational order of the corrugation may depend on a great many factors, especially the thermal gradient established between the friction ring and nave section.

In the second instance, thermal deformation may also lead to *disc coning*, a lateral deflection phenomenon whereby the friction ring section of the rotor component becomes fluted, the outer circumference of the friction ring displacing toward the top-hat section of the rotor component by up to 200 μm (73) and beyond. Since, in the majority of light- to medium-weight vehicles, the disc brake rotor is bolted at the wheel rim with the top-hat section outboard and the caliper housing straddles the rotor such that the piston-side pad is inboard and the finger-side pad is outboard, disc coning can be seen to effect the thermal judder contribution from each side of the friction ring disproportionately in favour of the finger, or outboard side. This has been confirmed using F.E.M. (59), the pattern of surface temperature variation in the radial direction of the friction ring being seen to be the same for both sides of the friction ring but the overall temperature profile being elevated at the outboard side in response to disc coning. In comparison with primary thermal buckling, disc coning is still a thermal non-equilibrium condition but varies in that the significant temperature gradient occurs between the nave and the constrained plateau of the top-hat section. Of course, in practice, multiple effects may well

superimpose leading to extremely complex dynamic geometries. The true answer as to whether the inboard or outboard pads are most affected by such phenomena is therefore much harder to predict.

Lateral / axial, *Side-face RunOut* (S.R.O.) of the disc brake rotor has also been shown to make some contribution to the phenomenon of hot spotting and thus to thermal judder (59). Perhaps not surprisingly, the greater the measured initial, bolted-up, rotor runout, the greater its contribution to hot spotting, although unacceptable hot spotting could still be induced by rotor runouts within the vehicle manufacturer's maintenance tolerances (2.3.2.).

2.3.1.2. Permanent Geometric & Microstructural Inconsistencies

Once the transient effects of thermal judder have been encountered, there are several mechanisms by which the problem can become permanent, necessitating rotor resurfacing or replacement if ride comfort is to be restored.

The occurrence of focal hot spots places an extremely high thermal load on the rotor material and may eventually lead to phase modifications and transformations within the cast iron should the environment become sufficiently severe. The formation of surface-retained carbides (74) may present a major problem, but is unusual.

Under appropriate circumstances of heating ($> 738^{\circ}\text{C}$) and subsequent cooling (to below $\approx 300^{\circ}\text{C}$ at a rate of $> 500^{\circ}\text{C}\cdot\text{s}^{-1}$), focal hot spots can be converted permanently to patches of martensite (650 – 800 H_V), termed *critical focal hot spots* or *bluespots* (due to their coloration). The transformation to martensite is dependent upon the carbon content of the matrix (and to a lesser extent, on the concentration of other alloying additions) and is associated with a 4 % volume increase in the area affected, which perpetuates to ambient temperatures, thus permanently affecting the surface geometry and tribometric characteristics of the friction pair. Figure 3 shows the variation in microhardness upon axially traversing the cross-section of a real bluespot. It is similar in profile, although not identical, to the microhardness variations resulting at the rubbing surface, albeit over a much reduced distance. On a

microscopic level, the martensitic transformation is a shearing mechanism prone to the introduction of severe local strain fields that may promote surface cracking upon cooling, and crack interconnection during subsequent thermal cycling.

As a result of the high thermal stresses involved, permanent deformations of the rotor geometry may also persist beyond the braking applications where judder phenomena are experienced. In particular, a butterfly geometry, shown in figure 2, has been noted (59), which becomes more pronounced on subsequent cycles of brake application. Although not commented upon in any great detail in the literature, this permanent, heat-induced distortion is suggested to come about as a result of relaxing strain domains within the discs which are introduced during manufacture (76 – 77). Such problems are especially true in the case of solid discs, which occasionally demand additional turning operations (three rather than two) to negate the effects. Other factors affecting these distortions might include casting variables – melt filtering, mould cooling, gating arrangements or location of the central air-gap; the extent to which castings have been *weathered* prior to subsequent processing; or rotor heat treatment parameters – pre- or post-machining or the position of the rotor in the furnace (73).

Another effect that is frequently overlooked is the effect of material loss at the rubbing surface. Wear rates of both the stator and rotor become considerably accelerated at the operating temperatures encountered during hot spotting and the uneven pressure distribution and non-uniform contact regime can serve to aggravate the situation dramatically. Brake D.T.V. (2.3.2.1. – 2.3.2.2.) can result and may provide a source for recurrent thermal judder, or for cold judder (2.3.2.). Indeed, it has been demonstrated that judder can introduce a low amplitude, periodic geometric waviness, to a previously non-wavy disc, that corresponds to the original judder frequency encountered (68).

The thermal judder phenomenon, if allowed to persist unchecked, may also lead to radial or craze-cracking (heat checking) as a result of the high generated compressive hoop stresses and / or plastic flow of the rotor surface. It has also been suggested that the oxidation of surface-impinging graphite flakes (which occurs readily at temperatures in excess of 700°C in the presence of air) may well serve to exacerbate cracking problems by providing a surfeit of natural stress raisers (24).

2.3.1.3. Approaches to the Solution of Thermal Judder

Approaches to the thermal judder denouement have, to date, focused on the elimination of both the hot banding phenomenon and the development of focal hot spots, i.e. improving the uniformity of heat generation at the friction ring. Empirically, several apparently beneficial solutions present themselves:

- Improving the thermal conductivity of the rotor material.
- Improving the specific heat capacity of the rotor material.
- Reducing the thermal expansivity of the rotor material.
- Optimising the compressibility of the friction material to reduce dilation.
- Increasing the sacrificial wear behaviour of the friction material.
- Minimising the thermal expansivity of the friction material.
- Reducing the length of friction material contact arc.
- Mounting of the rotor inboard to reduce disc coning.
- Physical redesign of the rotor to eliminate disc coning.
- Minimising the inherent radial flatness of the rotor.
- Minimising the axial side-face runout of the rotor.

When physical redesign of a ventilated disc brake rotor was attempted by Inoue (59) by attaching the bottom brake-plate of the friction ring (conventionally the top brake-plate) to the nave of the disc, disc coning was observed to be reversed, coning occurring in the opposite direction by a reduced amount (100 μm (73)). Such *back-vented* discs now represent a considerable proportion of disc constructions (although they do suffer from restricted air-cooling when compared with *through-vented* discs). In solid disc brake rotors where a choice of nave-to-brake-plate connections is not available, potential coning effects must be combated by the introduction of a critically designed groove at the inner diameter of the friction ring, this groove being known as the *undercut* (53).

The positive contribution of each of the above-listed modifications to the ultimate solution of hot spot generation, and consequently thermal judder, can be assessed quantitatively using constantly improving F.E.M. that will no doubt serve to optimise the design and comfort characteristics of automotive brake systems well into the future.

2.3.2. Cold Judder

The problem of cold judder (termed *brake roughness* in the US) in automotive braking friction couples is a relatively recent phenomenon when viewed in terms of the overall development of friction materials for automotive retardation. Indeed, incidences of cold judder as a brake refinement problem suggest that it was only in the early 1980s that the imbroglio came to light, occurrences originating in continental Europe followed shortly afterwards by cases cited in the UK and US.

The effects of cold judder may resemble those of thermal judder although the frequencies encountered tend to be confined to the 1 – 50 Hz range. This indicates that the excitation mechanism for cold judder operates at a lower order vibration of the wheel rotation, generally first or second. This is supported by what has come to be accepted as the classical definition of cold judder causation.

Cold judder occurs primarily as a result of a non-uniform circumferential rotor (friction ring) thickness, which causes a cyclic variation in the brake torque output during braking (78 – 79). These microscopic variations in the cross-sectional thickness of the disc brake rotor, axiomatically referred to as *Disc Thickness Variations* (D.T.V. or R.T.V. (*Rotor Thickness Variation*)) may arise during rotor manufacture as a product of the machining process (typical manufactured D.T.V. < 7 µm), or, as laboratory and field trial testing have demonstrated, may be generated throughout their lifetime in-service (79). Three manufactured non-conforming geometries possessing either inherent D.T.V. or the capacity for D.T.V. generation are illustrated in figure 4.

The principal cause of circumferential D.T.V. generation in-service is thought to be the cyclic, intermittent abrasive contact between the brake pad and disc under normal, off-brake driving. This heterogeneous contact regime occurs due to inadequate pad retraction after braking and is largely related to the magnitude of *swash*, or lateral / axial, side-face rotor runout inherent in the geometry of the system, figure 5. *Side-face RunOut* (S.R.O.) is the dynamic side-to-side axial displacement, or wobble, of the disc brake rotor. Although strict guidelines are provided by automobile manufacturers as to a vehicle's acceptable limits of axial S.R.O. (typically < 70 µm), it is historically suggested that some S.R.O. contributes positively to brake pad *knock-back* after braking, which reduces subsequent parasitic

drag at the brakes. Brake discs themselves are generally manufactured to maximum runout tolerances of 20 – 50 μm .

This cyclic contact, although very light ($\approx 0 - 100$ N per pad), acts over long periods of time causing unintentional, non-uniform wear of the disc surface (a process frequently referred to as *Off-Brake Wear* (O.B.W.), *Non-Braking Wear* (N.B.W.) and also, perhaps misleadingly, as *cold erosion*) and hence D.T.V. Figure 6 shows the anticipated pattern of O.B.W. in response to S.R.O.-induced contact. In actual fact, wear is likely over much more of the rotor surface but will always be most pronounced at the diametrically opposed, maximum contact pressure areas shown. Furthermore, O.B.W. of this kind is typically observed to increase parabolically rather than linearly towards to outer circumference of the friction ring due to the higher effective rubbing radii and normal pressure. The extent of O.B.W. on each side of the friction ring section is rarely equal meaning that first order vibrations of wheel rotation are more frequent than second order vibrations. As yet, no pattern has emerged indicating which side of the friction ring is most likely to be affected by O.B.W. of this kind (55 – 56).

The root cause of the cold judder phenomenon is frequently associated with variations in driving pattern trends, e.g. increased motorway driving. According to road and traffic report statistics (1985), up to 80 % of new car registrations made at that time were fleet or company purchases (80 – 82), a situation that has always suggested support for this precept. Other suspected contributory factors include; organic improvements in vehicle design and performance requirements, in particular, weight reduction, and the rejection of asbestos as an acceptable friction material constituent, coupled with the often unpredictable tribological response of its replacements. Furthermore, the increasing adoption of softer, and correspondingly less wear resistant, high carbon (3.5 – 4.0 %) rotor materials may also contribute further to the propensity of a brake system to generate O.B.W.

2.3.2.1. Axial Side-Face Runout & Disc Thickness Variation

The ease with which D.T.V. may be generated in-service is clearly linked to the original extent of the axial S.R.O. inherent in the system. However, as further D.T.V. develops the maximum axial S.R.O. (*peak-to-peak* or *Total Indicated Runout* (T.I.R.); figure 5) must be reduced by O.B.W., figure 7. It is also noted that the rate at which D.T.V. is generated falls as the maximum axial S.R.O. is reduced. If this situation is allowed to persist, D.T.V. will eventually reach an equilibrium point and start to fall and static S.R.O. may eventually vanish, result; a truing of the perceived rotor geometry. However, this is unfortunately a considerable oversimplification of the situation.

Thermal, thermo-mechanical and solely mechanical influences can significantly affect both the static and dynamic rotor geometry relative to the friction material stator aspect in disc brake systems. The magnitude of both inboard and outboard axial S.R.O. and of the *instantaneous* D.T.V. are dependent on a great many factors. These factors, although complex, can be satisfactorily grouped into three major areas:

- Static influences.
- Dynamic influences.
- Temperature-dependence.

Factors affecting the static S.R.O. are, in addition to those contributory factors mentioned previously, the manufacturing tolerances of the disc brake rotor, the hub to which the rotor is connected, the physical effects of bolt-up distortion, the condition of hub bearings, hub bearing clearance, etc. The situation described demonstrates how it is possible that such a great variability for judder propensity can arise from vehicle to vehicle (78). Mechanical influences may be static, such as distortions introduced during rotor attachment to the hub (dependent upon stud tightening torque, bolt-up connection sequence, location face flatnesses / form and geometric uniformity of the wheel), although such influences are transferred to the dynamic environment. Static D.T.V. also differs once mounted within the brake

assembly since vectorial combination of the inner and outer S.R.O. imparts a virtual contribution to D.T.V. as a function of axial inclination, shown in figure 8.

In the dynamic condition, S.R.O. and general disc movement can be influenced by rotor imbalance forces as a result of imperfect rotation geometry about a common axis, and a combination of rim or hub flexure inducing effects including; bump forces, drive forces, rolling resistance forces, braking forces and handling effects. (It should also be noted that the effects of rotor imbalance generally increase throughout the life of a vehicle as they are exacerbated by the wear extent of axle / hub bearings.) The planes and directions in which these forces act relative to the wheel, tyre and brake assembly are shown in figure 9. The effects of vehicle cornering can momentarily increase S.R.O. by as much as 150 μm , which although not acting over sufficiently long periods to directly affect overall O.B.W., could realign the caliper slide to an extent where D.T.V. generation is affected during subsequent motoring.

Studies examining the purely dynamic response of inboard and outboard S.R.O. and apparent D.T.V. with velocity have been conducted on vehicle-based trials (76). With increasing forward, unbraked velocity (70 – 140 km.h^{-1}) the inner and outer friction ring surfaces remain essentially parallel but the inner and outer S.R.O. phase shifts synchronously by 20°. At the same time, D.T.V. phase shifts by 20° in the opposite rotation. During brake applications at various speeds throughout the range described, and at approximately constant brake surface temperature, apparent D.T.V. has been observed to rise steadily by an average of 4 % per 10 km.h^{-1} increase. The D.T.V. phase shift varies by about 3° per 10 km.h^{-1} increase but in the opposite direction to unbraked motoring. More importantly, apparent D.T.V. is noted to have almost doubled during braking when compared with the unbraked condition but inner and outer S.R.O. have both fallen significantly. These phenomena are attributed to a combined sweep and wobble, rigid-body movement of the rotor in response to forces acting at the wheel, hub and rotor.

Some of the thermo-mechanical influences, such as disc distortion, act dynamically and have been illustrated previously (in section 2.3.1.1. and figure 2). However, many other thermal influences on S.R.O. and D.T.V. have been identified.

Certain types of ventilated disc brake rotors have been demonstrated to exhibit variable dynamic S.R.O. with rotor temperature. A study conducted by Sterne (73) applied precimeter laser sensors to the measurement of dynamic inboard and outboard S.R.O. on dynamometer-mounted disc brakes. It was

shown that although the S.R.O. of many rotors remained essentially invariable between operating temperatures of 0 – 400°C, the magnitude of S.R.O. for some rotors varied dramatically, by as much as 400 %, over certain rotor-dependent temperature ranges. For all discs it was noted that inboard S.R.O. surpassed outboard S.R.O., an observation contrary to the thermal effects of disc coning, discussed previously (2.3.1.1.). It was postulated that such distortion might be attributed to the fact that the inboard surface of the friction ring is not generally constrained by direct connection to the nave of the disc (a supposition supported by *back-venting* technology). Sterne also applied an L16 orthogonal array (Taguchi methodology) to isolate those parameters contributing to S.R.O. thermal instability at specific temperatures. The analysis suggested tentatively that heat treatment of the disc brake rotors post-machining was likely to give greatest improvement in thermal S.R.O. stability.

Dynamometer testing of disc brake rotors previously identified as exciting cold judder on vehicle-based, commercial brake assemblies has gone further in demonstrating the effect of temperature on *in situ* dynamic D.T.V. (61). During a single brake application, D.T.V. was observed to increase by 30 % as a result of thermal expansion and the constantly monitored variation between inboard and outboard S.R.O. It was also noted that a corresponding increase in B.T.V. amplitude occurs synchronously with this increase, i.e. B.T.V. amplitude at the brake is not purely linear throughout the brake application. Further investigation examining the influence of elevated *Initial Brake pad Temperatures* (I.B.T.) at the onset of braking demonstrated that not only does D.T.V. continue to increase but it does so to about the same extent; 34 %. The corresponding rise in B.T.V. intensity was again noted. The overall increase in B.T.V. in both examples was estimated to be of the order of 20 % over the entire brake application.

No definitive criteria exist that describe the amount of circumferential D.T.V. necessary to excite judder. Instead, the minimum quantity of D.T.V. necessary to initiate unacceptable judder is qualitatively labelled as the vehicle's judder sensitivity (figure 7). According to various published data, the figure can be quite low, e.g. 10 µm (82), 15 µm (74) (detectable at 15 µm (54)), 20 µm (73), 25 µm (81), etc.

2.3.2.2. Off-Brake Wear & Disc Thickness Variation

Other than by those mechanisms described in section 2.3.1., cyclic B.T.V. and thereby wheel-order judder phenomena may be excited in-service via a number of friction instability mechanisms that include non-uniform friction material deposition or physico-chemical interactions of the rotor with both its countersurface and its environment (such as non-uniform corrosion effects, axiomatically referred to as *lot rot*) and by O.B.W., or discontinuous on-brake wear behaviour, leading to the generation of circumferential D.T.V.

O.B.W.-induced D.T.V. has been studied by Kearns (81) who examined the role of the elastic recovery and sliding criteria of the distorted hydraulic piston seal. It was noted that for brake loads in excess of 88 N, piston seal sliding occurred. This result indicated that work examining the effect of off-brake forces needed to incorporate elastic pad retraction up to 88 N (for the system / piston seal employed) acting at any single row of caliper pistons (in a floating caliper or opposed piston system), i.e. per pad. Beyond 88 N (plus a small factor representing the friction material elastic-compressive behaviour), sufficient knock-back occurs to readjust the position of the seal to within a low contact force regime ($\approx 0 - 100$ N). However, the forces necessary to recentralise floating calipers by rotor impact on the finger-side, i.e. a function of the caliper slider pins, may vary beyond 100 N. Overall piston seal behaviour was seen to be Hookean, exhibiting a stiffness of 35 kg.mm^{-1} , i.e. 340 kN.m^{-1} . Kearns used a laboratory-based brake test rig to generate $20 \mu\text{m}$ D.T.V. on a single side of a disc brake rotor during a simulated running period of over 2,000 km at motorway speeds. Although two friction material formulations were examined during the testing, both gave very similar D.T.V. response although their microscopic tribological response was described as widely varying.

Aoki *et al* (83) considered several features of floating caliper systems in an attempt to reduce parasitic drag at the friction brake interface. Firstly they observed that the dragging torque at the outboard pad was 2 – 3 N.m greater than that experienced at the inboard pad, which was virtually nil. This indicated that the piston seal fulfilled its roll-back function but was let down by the caliper slider pin, thus penalising the outboard pad. Increasing pad compressibility was also seen to contribute to the dragging torque by a similar order in response to reduced clearance upon brake release.

An important feature of low contact forces acting in brake friction couples was identified by Jeacock (80). Jeacock demonstrated that at low braking forces, an apparent variation in the dynamic friction coefficient could arise; figure 10. It was suggested that such a phenomenon might arise if the asperity contacts of the friction material at low loads were not representative of the friction material as a whole. Friction materials are highly complex, multi-component composites (3.1.) that frequently show apparently inexplicable tribometric performance. It is conceivable that a low friction constituent is responsible for the effect. Solid lubricants are unlikely to protrude and even less likely to cause subsequent O.B.W. but hard ceramic particles, elastically displaced into the matrix during standard braking applications might well protrude at much lower loads causing relatively high wear at low friction. At exceptional rotational velocities, the phenomenon eventually disappeared.

Although such suppositions are yet to be confirmed in open forum, the critical influence of ceramic friction modifiers (3.1.5.) contained within friction material formulations has received some noteworthy attention. Shibata *et al* (84) suggested a relationship between the properties of abrasive friction modifiers (a product of the ceramic's hardness and its volume fraction within the stator material) and the material's propensity for D.T.V. generation, shown in figure 11. Although factors such as abrasive particle size, distribution and morphology are apparently omitted from the analysis, it is clear that large quantities of abrasive friction modifiers are to be avoided if O.B.W. is to be kept to a minimum.

2.3.2.3. Judder Transmission & the Vibratory Environment

Cold judder is a high amplitude vibration experienced during medium- to heavy-duty automotive friction braking. The vibratory environment is quite complex and the judder amplitude varies as the natural resonant frequencies, eigenfrequencies or *Frequency Response Functions* (F.R.F.) of structural components and sub-assemblies are excited. Most frequently observed is a low frequency vibration of the suspension assembly (10 – 20 Hz) in the fore-aft direction (a yaw motion), which is generally attributed to the dynamic behaviour of modern suspension compliance bushings under braking. This amplification

of the judder phenomenon further serves to magnify subjective effects as perceived by the driver since the frequency range is coincident with the self-exciting range of the steering column (also 10 – 20 Hz) (54, 61).

Further eigenfrequencies may be isolated as acting within the unsprung vehicle systems. Braking through 100 km.h⁻¹ (often also in the 10 – 20 Hz range) may result in the excitation of the stub-axle carrier and steering knuckle leading to an increase in virtual D.T.V. When braking from extremely high speeds (> 160 km.h⁻¹), judder characteristics may be accompanied by a low pitch, droning noise (100 – 500 Hz) which rises to an aural peak at 100 – 200 Hz as the natural frequency range of the front axle is excited (74).

One of the main difficulties associated with the simulation of a universally acceptable cold judder excitation model has been the way in which different vehicles react to both the causes, principally axial S.R.O. and subsequent D.T.V., and their effects, i.e. perceived judder and vibrations. Even vehicles of the same make, model or similar front suspensions (77) tend to show marked variability illustrating not only complex variations in the exact nature of excitation but also variation in the ways in which disturbances are transmitted. Similarly, different manufacturer's vehicles or models may not exhibit cold judder even though the generation of significant D.T.V. may have been identified, thus indicating that although the excitation mechanism may be operating, the resultant vibrations are not being transferred to the driver's point of contact. It is therefore fair to assume that components and couplings in the transfer path of these vibrations can be engineered to alleviate, or at least to minimise the perceived judder effect.

Several studies have been undertaken to examine the role of the vehicle component transfer path on the vibrations generated during cold judder. These generally start by identifying the contact points of the driver and passengers, referring to these as global transmission-functions (57, 77) or quality characteristics (60), and relating these to transfer critical or potentially transfer critical components within the vibration path, referring to these as local transmission-functions (57, 77) or control factors (60).

Figure 12 shows a schematic representation of the principal elements of the potential vibration path in a light passenger vehicle. Several features have been omitted such as the powertrain, the upper suspension

arm (present on heavier vehicles), front-end anti-roll bar (finding increasing use in newer models) and the position of the suspension strut system is merely indicated. (The wheels have been axially displaced so as not to clutter the schematic.)

Variations in assembly and chassis design have a considerable influence on any vehicle's judder sensitivity. This is particularly true for variations in the commercial brake assembly itself. Stationary or fixed calipers are bolted directly and rigidly to the steering knuckle. Thus, the vibration transfer from brake assembly to the contact points of the vehicle's occupants varies slightly, but tangibly from systems incorporating floating or sliding calipers (82).

It has long been appreciated that the propensity of automotive components to transmit elasto-kinematic vibrations are adversely affected by increasing the flexibility of the bushings connecting those components (85). Bosworth (60) applied Taguchi methodology using a L18 orthogonal array and a linear NASTRAN computerised vehicle model in an attempt to examine the influence of various vehicle component properties on vibration transfer from the brake system. By examining the effect of adjusting local transmission component properties, he was able to assess their quantitative effects on pre-determined quality characteristics; torsional, vertical (radial) and fore-aft (axial) vibration of the steering wheel and vertical and fore-aft vibration of the driver's seat rail. Optimum benefit was attained by increasing the stiffness of prime components in the vibration promoting planes; steering system tie-rod rubber bush stiffness in the fore-aft and radial directions, steering rack housing stiffness in the lateral direction, lower suspension arm bush stiffness in the fore-aft direction and the vertical stiffness of the anti-roll bar. The vibration transmission diagram for this system is shown in figure 13.

Comparative studies in vehicle-based trials examining commercially compatible sub-systems (57, 77) produced a similar vibration transmission diagram even though the elasto-kinematic behaviour of components was measured physically, figure 14. B.T.V. originating at the brake assembly was simulated by forced imbalance at the wheels, which generates disturbances transferred via the wheel knuckle, through the steering system tie-rods to the steering column, as would be the case from the brakes.

2.3.2.4. Corrective Mechanisms for Cold Judder

The search for a solution to the problem of cold judder has involved several approaches, each distinctly different in both their focus and scope. In isolation, it is unlikely that any individual corrective mechanism will yield sufficient improvement to eliminate the problem completely, an opinion shared by the majority of authors in this field. It is therefore apparent that a more holistic or systems approach is required, addressing, but also simultaneously compromising, each of the following to optimum benefit:

- Vehicle desensitisation to vibration transfer.
- Minimisation of axial side-face rotor runout.
- Physically increased axial clearance between stator and rotor.
- Increased piston-seal retraction within the brake caliper.
- Friction material solutions.

It has been suggested that vehicles and individual automotive components can be designed so as to desensitise a vehicle's propensity to experience cold judder (54). Careful scientific restructuring and redesign of suspension systems so as to minimise the effects of vibration excitation, amplification and transfer is a mechanical engineering approach that has attracted significant attention. Component's eigenvalues should not be coincident and should, where possible, be engineered to fall outside of the permissible range of first order brake excitations. Reductions in the level of pedal pulsation might be achieved through optimised hydraulic damping or brake circuit factors. Improved vibrational damping has also been considered.

Considerable efforts have been made to eliminate both axial S.R.O. and inherent, manufactured D.T.V. Based on conventional tenets, this approach has generally involved the tightening of manufacturing and assembly tolerances of the wheel, rotor, hub, stub-axle carrier bearings, etc. The extremes to which this potential solution has been pursued demonstrate the industry's conviction to eliminate judder phenomena. Some manufacturers have taken to machining disc brake rotors to final tolerances *in situ*, i.e. subsequent to their installation on the vehicle. However, this precision in the OE product is not

transferred when replacement discs are installed. Other manufacturers have reinvestigated the manufacture of integrated rotor and hub castings (86) and have applied this to production models, thus eliminating the stacked tolerance losses incurred through the fastening of these components. It should be noted that the integral hub concept is far from new although is more frequently applied to rear-axle brake units. In replacing disc brake rotors on vehicles that have shown a propensity for brake judder, some manufacturers have lately instigated almost draconian tolerances to give bolted-up, axial S.R.O. tolerances of no greater than 40 μm .

Attempts to alleviate the cold judder phenomenon have also concentrated on the removal of the excitation source, i.e. D.T.V. Rationally, it seemed appropriate to examine the possibility of increasing the pad / disc axial clearance, thus avoiding the intermittent contact of the stator and rotor responsible for the generation of D.T.V. The first approach to be examined was that of physically increasing the clearance but was eventually deemed unsuitable because of the associated increase in brake pedal travel required for brake actuation. Simplistically, this brake 'feel' characteristic appears to be valued higher than the elimination of D.T.V. generation since it would not be difficult to connect the piston seal to the piston cylinder. However, the current design compensates for continued lining wear whilst maintaining a constant pedal travel for a given brake duty. The axial clearance between pad and rotor could be increased by the modification of existing master cylinders with rapid-refill reservoirs although this does increase both the weight and the cost of the unit (83). Alternatively, increased axial clearance might also be achieved via the introduction of commercial, electronically-controlled *brake-by-wire* sub-systems or *drive-by-wire* systems (87) incorporating *Anti-lock Braking Systems* (ABS) and *Anti-Slip traction Control* (ASC, or ASR). By their very nature, stationary calipers providing one, two or more pistons to each of the friction material pads provide better pad retraction than floating calipers due to the fact that greater piston seal roll-back forces effect greater axial clearance. However, the additional benefits of floating calipers must be assumed to outweigh those of stationary calipers since no return exodus toward the fixed caliper has transpired.

Other approaches to increasing the axial clearance between pad and disc have also investigated. By increasing the distance by which the caliper piston seal (figure 15) may effectively roll-back after application of the brakes it was imagined that the off-brake operating clearance could be improved to

adequate levels. To this end, caliper manufacturers have incorporated such features as a piston seal roll-back chamfer in order to minimise shear stresses acting at the seal (88). Figure 16 shows a modified piston cylinder featuring an additional O-ring that is distorted during braking but relaxes upon brake release. The residual pressure remaining between the O-ring and the piston seal is suggested to be sufficient to enhance piston seal retraction (89). The designers of fist-type, floating calipers have also adopted sealed, lubricated, monopin sliders located inboard of the thermally-loaded rotor and torque input side of the brake in an attempt to minimise parasitic brake drag.

In order to minimise off-brake contact and, simultaneously, off-brake residual drag while avoiding unacceptable axial clearances, several solutions have been proposed (83). Many problems arise as a result of non-uniform friction material wear. Floating calipers may lead to a concave wear geometry on the inboard pad coupled with a convex wear geometry on the outboard pad. Friction material wear may also occur in a tapered geometry in response to caliper inclination (longitudinal taper in the direction of rotation) or in response to higher temperatures with increasing rubbing radius (radial taper). All of these imperfect geometries lead to situations where axial clearance at some point on the pad is restored after braking, but, other areas of the pad remain in contact with the rotor. Solutions include:

- More rigid backing plates.
- Rearrangement of spigot holes away from the piston.
- More rigid anchor plate.
- More rigid caliper mounting.
- Friction material with wear rate insensitive to rubbing radii.
- Consolidation of rotor braking surfaces.

The latter of these encompasses both minimising the original surface roughness of the virgin rotor's friction surfaces and supplementary surface treatments so as to develop surface characteristics that closely resemble those of a bedded surface. The intention of such surface preparations, which may involve various forms of cross-hatch grinding, honing (e.g. Mitsubishi) or roller-burnishing (e.g. Rover),

is to minimise the abundance of macroscopic peaks that exaggerate the D.T.V. perceived by the pads during the early stages of O.B.W. (see plate 2).

Friction material formulation solutions have led to the establishment of two principal schools of thought. The first is to produce friction materials exhibiting a sufficiently mild rotor wear response such that D.T.V. generation will be alleviated. This is termed the passive approach and has tended to become associated with Japanese friction material manufacturers. Unfortunately, the disadvantages associated with this solution are that manufactured or pre-existing D.T.V. will likely persist throughout the lifetime of the brake, this being combined with difficulties in attaining sufficiently high dynamic friction coefficients. Several associated shortcomings have been attributed to this formulation methodology, the majority of which focus on the material's reduced capability in effecting rotor clean-up in the event of rotor surface irregularity, i.e. friction instability-derived B.T.V. effects (2.3.2.2.).

The second approach is to produce friction materials exhibiting sufficiently severe rotor wear response that any D.T.V. is removed by an *in situ* machining, planing or truing of the disc geometry during normal braking. This is termed the aggressive approach and has tended to become associated with German friction material manufacturers. This also helps in the removal of physico-chemical inconsistencies at the brake interfaces such as uneven transfer film deposition or corrosion products. The down-side to this approach is obviously the tangible reduction in rotor life but also that the heavily abrasive action of these materials mean that hot, electrostatically-charged, metallic wear debris being ejected from the friction pair is deposited unattractively on neighbouring ventilated wheel rims. Indeed, the nature of this coarse debris results in the effect being partially permanent on plastic hub caps or plastic-encapsulated, alloy wheel rims. This has become especially significant in areas of the US market where hot and dry weather patterns mean that wheels are infrequently rinsed.

The wear response to both the passive and aggressive friction material formulations described, with respect to increasing operating temperature during a drag test to failure, is shown in figure 17.

With a greater understanding of microscopic tribological interactions such as physico-chemical phenomena and their influence on wear behaviour, a third and potentially more elegant friction material solution has emerged in recent years. Studies investigating the effect of low contact forces, such as those associated with O.B.W. and consequently, with D.T.V. generation, have noted widely varying rotor wear

response to different varieties of friction material (90 – 91). Transfer films (discussed later in section 3.3.) rich in barium sulphate and carbonaceous char have been observed to manifest notable wear resistance in comparison with the greater wear response of films also containing copper-derived compounds and lubricating metallic sulphides. Since the friction material provides the reservoir from which such transfer films are ultimately derived, it seems fair to assume that an answer based on transfer film engineering precepts may well be at hand. The study in point also suggested that low contact force (or rubbing speed, or temperature-dependent) wear regime thresholds exist in certain friction materials which may also prove significant. It is this avenue of investigation that has received previous attention (92 – 97) and is the one upon which the author's programme of research has been based (98 – 100).

Whatever solution might reveal itself as an adequate combatant to D.T.V. generation, it is essential to recall that cold judder did not become a brake refinement issue until asbestos fibres were removed from friction materials.

3.0. Automotive Friction Materials

Automotive friction materials are traction devices used in clutches and brake systems. Convention dictates that, although all of the various friction components contained within clutch and brake assemblies could be referred to as *friction materials*, the label is traditionally reserved for the expendable or consumable triboelement. Other sub-differentiations are possible both in terms of formulation and properties, where, for example, many similarities exist between commercial brake linings and clutch plates. The opposing triboelement to the friction material, which is generally a cast and turned metallic, i.e. drum or disc rotors in brakes or the pressure plate and flywheel in clutches, are parochially referred to as the countermember or countersurface.

Here we are particularly concerned with those automotive friction materials manufactured for use in disc braking systems on road-going, passenger vehicles, especially the *Non-Asbestos Organic* (N.A.O.) formulations, an example of which is pictured in plate 3. The development and formulation of such friction materials is a balance of functional, physico-chemical and abstract properties, constantly fraught with paradox. However, the following friction material properties are generally desirable:

- High static and dynamic coefficient of friction under all permissible environmental circumstances.
- Stable and predictable dynamic friction coefficient within the requisite range of operating conditions, e.g. -40°C – $1,200^{\circ}\text{C}$ (flash-surface rather than bulk temperature).
- Minimum wear characteristics combined with frictional properties that inhibit countersurface wear, i.e. kind to the rotating countermember.
- Adequate shear strength to resist rupture or catastrophic failure.
- Adequate corrosion resistance to retain the preferred property spectrum in the presence of water, salt, sand and mud, etc.
- Sufficiently thermally insulating to avoid brake fluid overheating and vapour-lock.
- Conformance to the countersurface to enable uniform heat generation.

- Zero N.V.H. and judder generation or excitation characteristics.
- Optimised costs of raw materials, processing and manufacturing technologies.

3.1. Constitution of N.A.O. Friction Materials

N.A.O. friction materials (a.k.a. asbestos-free, resin-bonded or moulded friction materials) are multi-component composites, the compositions of which having become increasingly complex since the abandonment of asbestos fibres. Formulations, some proprietary, and their resultant properties may vary dramatically according to the required operating conditions.

Table 3 lists many friction material constituents in current use, these being grouped according to their nominal or primary function. These groupings are then individually expounded, making particular reference to those constituents involved in the current study.

Table 3:

Major constituents of modern friction materials. Expanded from reference 84.

<i>Constituent type:</i>	<i>Varieties:</i>	<i>Nominal function:</i>
Resin	Phenolic, epoxy, silicone, rubber, etc.	Binder
Fibre	Glass, aramid, potassium titanate, carbon, ceramic, copper, brass, steel, stainless steel, rock-wool, etc.	Friction material reinforcement
Metal powder	Cu, Cu-Zn, Cu-Sn, Zn, Fe, Al, etc.	Increase friction coefficient
Solid lubricant	Graphite, MoS ₂ , Sb ₂ S ₃ , Sn ₂ S ₃ , PbS, ZnS, mica, etc.	Prevents micro-stick to rotor
Abrasive	Al ₂ O ₃ , SiO ₂ , MgO, Fe ₃ O ₄ , Cr ₂ O ₃ , SiC, ZrSiO ₄ , kyanite (Al ₂ SiO ₅), etc.	Friction level modifier, cleaning surface of rotor
Organic filler	C.N.S.L. dust, rubber crumb, etc.	Reduce low temperature wear
Inorganic filler	Vermiculite, BaSO ₄ , CaCO ₃ , Ca(OH) ₂ , MgO, etc.	Reduce high temperature wear

3.1.1. Binding Agents

The binding agent, or resin system, forms the major organic portion of all modern N.A.O. friction material formulations, usually representing anywhere between 25 – 40 % of the component by volume, equivalent to 5 – 15 % by mass. The component is critical to the performance of organic, resin-bonded friction materials since, more than any other constituent, it dictates the mechanical properties of the pad and in particular, the thermal load capacity prior to failure.

Friction material formulation currently represents about 1 % of the World-wide consumption of phenolic resins (**101**), such thermosetting phenolics being by far the most common binding agents used. A great many varieties of phenolics exist, some of which are shown in figure 18. Novolak resins modified with inorganic additions (Si, P, B, Ti, etc.) infer superior thermal resistance at the expense of strength and wear characteristics. Novolak resins modified with organic additions show the reverse property characteristics and are therefore prone to fading.

The polymerisation of phenolic resin is generally catalysed using strong acids or alkalis although weak, or Lewis acids such as zinc acetate are also frequently used. Contemporary experimental resins based on the polyimide, bismaleimide or diallylphthalate systems have also been developed in the pursuit of superior thermal properties.

3.1.2. Fibre-Reinforcement

As their generic title suggests, fibre-reinforcements exert a much greater influence over the mechanical properties of a friction material (elastic modulus, compressibility and strength; flexural, compressive and especially shear) than they do over tribometric properties. In order to impart these physical properties, a minimum concentration of dispersed fibres is necessary such that fibre-overlapping is possible, after which the pad properties are influenced by the following fibre characteristics (**102**):

- Fibre orientation.
- Fibre aspect ratio – influences matrix-fibre load transfer.
- Fibre / binder adhesion – influences matrix-fibre energy transfer.
- Fibre strength.
- Fibre morphology / size – to minimise stress concentrations.

Fibre-reinforcements used in friction material formulation may be segregated into four main categories; glass, synthetic (aramid (notably Kevlar™), potassium titanate, carbon, ceramic, etc.), metallic (copper, brass, steel and stainless steel wire, iron wool, etc.) and natural, or mineral (e.g. chrysotile asbestos (although obviously not in N.A.O. formulations) and rock-wool).

Carbon fibres enhance the high temperature stability of the friction coefficient, aramid fibres improve strength and wear resistance, glass and ceramic fibres reduce the thermal conductivity of the composite while providing high temperature strength and a friction coefficient supplement, in a similar way as metallic friction modifiers (as do, of course, metallic fibres). Since fibre properties are so diverse, they are often used in selected combinations, although the interrelated mechanical and thermochemical processes that promote the tribological synergy of given combinations is only superficially understood.

Table 4:

Comparative tribological characteristics of common fibre-reinforcements used in friction material formulation. Duplicated from reference 84.

① = Excellent ② = Good ③ = Fair ④ = Poor

Characteristic:	Glass	Aramid	Potassium titanate	Carbon	Ceramic	Copper / brass	Steel	Asbestos	Rock-wool
Friction coefficient	②	②	②	③	②	②	②	②	②
Thermal stability	③	③	②	①	②	②	②	②	②
Wear rate	②	②	②	②	②	②	①	③	③
Material strength	②	②	③	②	③	②	①	②	④
Noise	③	②	③	②	③	②	③	③	③
Rotor attack	③	②	③	②	④	②	③	②	③
Thermal conductivity	②	②	②	④	①	④	④	②	②
Ease of processing	③	③	②	③	③	②	②	②	③
Economy	②	③	③	④	③	③	②	①	①

3.1.3. Metallic Friction Modifiers

Metallic friction modifiers may be added to friction materials to perform a multitude of functions. Metallic powder additions of copper (m.p. $\approx 1,083^{\circ}\text{C}$) or brass (Cu : 0 – 50 % Zn), i.e. metals or alloys softer than the countersurface material, are frequently made to increase the dynamic coefficient of friction and as such, tend to be used more widely in heavier-duty linings. Simultaneously, their inherently poor chip-forming characteristics ensure that loosened wear debris can be reincorporated into the mating surfaces, effectively recycling otherwise lost material. This characteristic is described as *scavenging* behaviour. Similarly, because of their generally high plasticity, especially that of copper, their deposition on the countersurface enlarges the area of real contact between the rotor and stator facilitating more uniform temperature generation while simultaneously breaking up undesirable surface films by resisting the subsequent deposition of decomposition products from the friction material.

They are also particularly corrosion resistant but more importantly, they reduce the temperature gradient at the friction material surface and reduce high velocity and high load (and thus high temperature) wear (103).

The use of lower melting point metals such as aluminium (m.p. $\approx 660^{\circ}\text{C}$) and zinc (m.p. $\approx 420^{\circ}\text{C}$, b.p. $\approx 908^{\circ}\text{C}$) is generally confined to rear-axle, drum linings where the operating regime is considerably milder. However, this is not always the case and indeed, the inclusion of zinc within disc brake pads contributes significantly to the recovery of friction performance following fade.

As with ceramic friction modifiers, the effect of particle size and particle size combinations of metallic friction modifier additions has been observed to have a significant effect on friction material properties, especially wear. The blending of both small ($< 100\ \mu\text{m}$) and large particles ($> 200\ \mu\text{m}$) is thought to increase the charging density, which prevents the premature loss of smaller particulates (84).

Depending on the overall formulation of the friction material, metallics may present certain difficulties with respect to noise phenomena, their inherent adhesive compatibility with the rotor providing opportunities for slip-stick interaction.

3.1.4. Solid Lubricants

A wide variety of solid lubricants can be found in commercial N.A.O. friction material formulations. Generally, these might include graphite, molybdenum disulphide (MoS_2), antimony trisulphide (Sb_2S_3), and to a lesser extent, the sulphides of lead, tin and zinc. Less expensive, carbonaceous additions such as carbon black or petroleum coke flour may also be included.

Solid lubricants are a distinct class of friction modifier that aid in the formation of the *Third-Body Layer* (T.B.L. – 3.3.) acting at the friction interface, and in particular, on the surface of the cast iron countermember. They provide friction stability over given ranges of interfacial temperature, reduce the wear of the friction material component from which they derive and enable the optimisation / minimisation of slip-stick interactions. In relation to the temperature ranges over which individual lubricants remain effective, high energy pads usually contain a combination that selectively maintains their effects throughout the permissible operating regime.

A disadvantage with the addition of solid lubricants to brake linings is their deleterious effect on the load-bearing capacity of the composite, an effect that is partially compensated for by the proportion of fibre-reinforcement added to the material.

3.1.5. Abrasive Friction Modifiers

Abrasive particulates may be added to a friction material formulation in order to attain an increased level of dynamic friction. In order that such materials are capable of generating an increase in the friction level when coupled with grey cast iron, they must usually exhibit a Moh's hardness of 5 – 6+ and so those exhibiting 6 – 7+ are usually selected.

Abrasive particulates also serve to *clean-up* the disc, their abrading action ensuring homogeneity (both in nature and in thickness) of the crucial T.B.L. Also notable is the considerable influence that abrasive

additions exert over the wear rate of both triboelements, which may be either beneficial or deleterious, demonstrating the importance of their careful control.

Although abrasive friction modifiers exhibit many common properties, e.g. they are all virtually insoluble, mildly basic, exhibit high hardness to elevated temperature and general refractoriness, such additions are critical, being extremely sensitive to chemical nature, refractoriness, hardness, toughness, size (104), morphology, distribution and volume fraction (84, 2.3.2.2.).

It should be noted that rather than in the conventional sense of the word, *abrasive* friction modifiers may be considered any constituent that abrades the counter member, i.e. Fe_3O_4 would not generally be considered an abrasive particulate, but in the context of friction material constituents it does exert an abrasive response on the rotor.

Commonly used abrasives include alumina (Al_2O_3 – both fused and calcined), silica (SiO_2 – quartz, tridymite or cristobalite, sand and silicon IV oxide), magnesia (MgO – periclase mineral), magnetite (Fe_3O_4), chromia (Cr_2O_3 – green chromic oxide, chromium sesquioxide or chromium III oxide), silicon carbide (SiC – carborundum) and zirconium silicate (ZrSiO_4 or $\text{ZrO}_2 \cdot \text{SiO}_2$ – zircon sand), etc. Although fused alumina might appear to clearly define an abrasive type, many sub-distinctions are usually possible, e.g. fused Al_2O_3 may be regular brown bauxite (microcrystalline and semi-friable) or white, pink and ruby bauxite grades; SiC can be of a light green, dark green or black variety. Despite repeated references to mineral grades, abrasive friction modifiers must usually be of a highly pure form.

3.1.6. Organic Fillers

Organic fillers typically include cashew dust (partially or completely polymerised Cashew Nut Shell Liquid / oil (C.N.S.L.), a.k.a. cured cardanol-based resin) and particles of rubber crumb. Such additions generally provide low temperature wear resistance although specialised organic fillers may also be added to deter the condensation and concentration of metallic, inorganic friction material constituents at the friction surface.

3.1.7. Inorganic Fillers

The inorganic filler portion of a friction material, which represents the major inorganic constituent of N.A.O. brake linings, is generally a combination of relatively inexpensive, comminuted minerals, the most important of which being described as follows.

Barytes, baryte or barite is a mineral form of BaSO_4 . The addition of a barytes filler to N.A.O. formulations is intended to reduce high temperature wear and increase product density, the material itself being relatively soft (and thus exhibiting low abrasive characteristics) and extremely chemically inert.

Other commonly prescribed mineral fillers include china clay (calcium carbonate; CaCO_3 , ground limestone or *whiting*) or finely divided silicas, which again offer thermal stability at low cost. The blend of inorganic fillers incorporated into a friction material formulation may also include pH conditioners like calcium hydroxide, such additions being intended to keep the overall pH of the lining alkaline so as to prevent corrosive adhesion to the rotor.

Vermiculite is a mica-type compound that can be categorised not only as an inorganic filler, but also as a mild solid lubricant (since its structure is essentially plate-like) and even as a fibrous reinforcing agent. Exfoliated vermiculite is a thermally stable and essentially inert mineral filler that finds application in automotive friction materials as an asbestos replacement. Mineralogically, vermiculite refers to a specific material of exclusive chemical composition although in a more commercial context the definition of vermiculite is frequently broadened to include any member of a family of secondary monoclinic, hydrated ferro-magnesium alumino-silicates that find industrial application in an expanded, or exfoliated form. (Typical chemical analyses of the main sources of mined vermiculite are shown in table 5.) The expansion of the crude vermiculite is attained by rapid exposure to high temperatures, swelling the original particle size by 15 to 30 times via the generation of interlamellar steam. Once comminuted, the final product for use in brake linings tends to resemble finely granulated cork. In its exfoliated form, vermiculite exhibits a high resistance to cracking (high capacity to absorb local stresses), provides exceptional thermal and acoustic insulation, is corrosion and combustion-resistant and is also light weight (table 6).

Table 5:

Typical chemical analyses (by mass percent) of the World's major sources of commercial vermiculite.

Adapted from reference 105.

Compound:	Libby, Montana, USA:	Enoree, South Carolina, USA:	Palabora, Northern Transvaal, South Africa:	Typical analysis of processed vermiculite:
SiO ₂	38.64	38.66	39.37	38 - 46
MgO	22.68	20.04	23.37	16 - 24
Al ₂ O ₃	14.94	17.36	12.08	11 - 16
Fe ₂ O ₃	9.29	8.45	5.45 (total Fe)	8 - 13
FeO	---	---	---	---
K ₂ O	7.84	5.24	2.46	4 - 6
CaO	1.23	0.75	1.46	1 - 3
Cr ₂ O ₃	0.29	0.50	0.00	0.05 - 0.2
Mn ₃ O ₄	0.11	0.12	---	---
MnO	---	---	0.30	0.1 - 0.2
P ₂ O ₅	Trace	trace	0.15	---
S	Trace	trace	0.18	---
Cl	0.28	0.52	0.02	---
H ₂ O	5.29	8.71	14.24 (L.O.I.)	---
Na ₂ O	---	---	0.80	0.1 - 0.3
TiO ₂	---	---	1.25	1.3
BaO	---	---	0.03	---
Li ₂ O	---	---	0.03	---
ZrO ₂	---	---	0.00	---
NiO	---	---	0.00	---
CoO	---	---	0.00	---
CuO	---	---	0.00	---
SrO	---	---	0.00	---
V ₂ O ₃	---	---	0.00	---
Other:	---	---	---	0.0 - 0.5

Table 6:

The properties of exfoliated vermiculite. Duplicated from reference 105.

Property characteristic:	Property value:
Sintering temperature (°C)	≈ 1,260
Melting point (°C)	≈ 1,315
Specific heat capacity (J.kg ⁻¹ .°C ⁻¹)	840
Specific gravity (g.cm ⁻³)	2.6
Thermal conductivity (W.m ⁻² .°C ⁻¹)	0.062 – 0.065
Loose bulk density (of exfoliated form) (kg.m ⁻³)	56 – 192
Loose bulk density (of crude, unexfoliated form) (kg.m ⁻³)	640 – 960

The consistency or bulk uniformity of mineral products is frequently extremely poor, this being true of many friction material constituents, which necessitates strict quality controls and acceptance sampling criteria, typically involving detailed analysis and blending of incoming raw materials.

3.2. Wear of Automotive Friction Materials

Although the generation of D.T.V. by O.B.W., and hence cold judder, is governed in some respects by the wear behaviour of the metallic countermember, the wear of the mating friction material contributes significantly to the critical transfer films formed at both surfaces of the friction interface.

Wear may be defined as the physical disturbance or damage to a solid surface which is generally associated with a progressive loss of material. Traditionally, the friction material element of the friction braking couple has been considered the consumable portion, relative to the rotor element. This remains the case since, in the majority of cases, an individual rotor will rarely require replacement solely due to consistent but uniform wear during the first 100,000 miles of a vehicle's lifetime. (The permissible wear extent of a rotor, expressed in terms of a minimum disc thickness, usually accounts for only 0.9 – 1.8

mm of material from either side of the friction ring.) However, continuous efforts to improve the lifespan of friction materials mean that many modern brake pads are quite capable of 40,000 miles of trouble-free use in the hands of a temperate motorist.

Research aiming to further reduce the wear rate and improve the life of friction materials continues although the qualification and theoretical assessment of these vital characteristics remains complex (106 – 112).

3.2.1. Wear Mechanisms of Resin-Bonded Friction Materials

Organic friction materials in tribological contact with a metallic countersurface, be they asbestos-based or asbestos-free, may be subject to material loss by any of the following *wear modes* (110 – 112):

- Abrasion
- Adhesion
- Ablation
- Fatigue
- Macroshear

The distinctions made between such broad classifications are essentially notional and, strictly speaking, artificial, but do serve to enable the rationalisation of tribological data. The major distinction between abrasion and adhesion was popularised by Bowden and Tabor (113 – 114) although further subdistinctions are frequently made. *Wear mechanisms* can be used to describe these sub-distinctions of individual modes and to discriminate qualitatively between varying tribological environments. An example for abrasive wear might be that abrasion occurs by ploughing, scoring and polishing wear mechanisms and similarly, may occur by two-body or three-body abrasion. Such classifications further serve to illustrate the complexity of the overall *wear regime*.

The term *wear regime* describes the combination of mechanisms acting concurrently at any moment in time. It may also take into account the contribution of each mechanism to the total material loss occurring during a given time period.

Abrasive wear results from the interaction of hard particles or protruberances with a solid surface. According to Moh's scale of hardness, one material must exhibit a hardness 10 % greater than that of its contacting countersurface in order to effect discernible abrasion. However, for more linear hardness scales, such as Vickers, Rockwell or Brinell, contact mechanics can be used to show the value to be more like 20 %. The types of abrasive contact that are encountered during friction braking are described as closed two-body, i.e. two opposed surfaces in contact, and closed three-body, i.e. the action of trapped interfacial debris between two opposed surfaces. The abrasive wear component of the friction material acting at the rotor countersurface will be seen to be of critical importance to the author's programme of research in later chapters, any abrasive wear components affecting the friction material being essentially ignored. However, since an oxidised ferrous surface exhibits a higher Moh's hardness than > 95 volume % constitution of a typical N.A.O. friction material, it is not difficult to see why it is the pad that is considered the sacrificial triboelement.

Adhesive or *adhesive-tearing* wear arises from the generation, rupture and detachment of adhesively-bonded contact junctions made between solid surfaces in relative motion (115). Adhesion is known to be the greatest contributor to sliding resistance since it operates over an extremely narrow interfacial zone, $\approx 0.1 \mu\text{m}$ (116), which corresponds to the region exhibiting high rates of energy dissipation. Thus, adhesion is an essential prime-requisite for successful friction braking although, strictly speaking, adhesion is not the direct cause of wear but results as a consequence of contact (117). Adhesion is generally recognised as the principal mechanism by which matter may be transferred from one tribosurface to another and vice-versa, although such transfer may result from mechanical interlocking adhesion as well as by adhesive bonding.

The rate at which friction material constituents may adhere to a cast iron counterface is extremely difficult to predict although it is fair to assume that the extent of transfer is not equal between constituents since the strength of any adhesive bond is obviously material dependent. Self-mating metal contact, such as that which might be experienced between the rotor substrate and steel wool protruding from the friction material provides an extremely strong bond comparable to that of the bulk material and frequently leads to severe wear regimes. Contact between disparate metals may also be significant because of interatomic diffusion but depends upon the two metal's alloying compatibility. Ionic or

covalently bonded materials, such as ceramics, are unlikely to form strongly adhesive bonds with metals but may bond to each other if lattice parameters and orientations coincide.

Ablative, or thermal wear occurs upon thermal decomposition of the friction material resin. Unlike the other mechanisms taking place at the friction interface, ablative wear takes place at a predictable rate, increasing exponentially with interfacial temperature (figure 19). The onset of ablative wear may be defined precisely from the results of *Thermo-Gravimetric Analysis* (T.G.A.), whereby the thermal degradation of the resin initiates at about 232°C (according to historical data) and continues until the material is virtually completely decomposed at around 700°C. Modern N.A.O. friction materials incorporating modified binder systems exhibit fade-free performance at operating temperatures of up to 350°C, this figure providing a more contemporary footing upon which to base the onset of significant ablative wear.

Fatigue wear is the process by which material may become fractured and detached from its original surface via a fatigue mechanism in response to cyclic stress variations. Such cyclic stress variations are manifold in the friction brake system where thermo-mechanical cycling and thermal shock situations abound. The natural upshot of such effects is the loss of material by the interconnection of surface fatigue cracks. It is important to note that if similar fatigue effects were observed to affect the rotor, this would not be considered the onset of a wear mechanism, rather as the onset of potential catastrophic failure via thermal rupture necessitating immediate replacement of the offending component.

Macroshear, as its name suggests, involves the removal of relatively large quantities of matter from the friction material surface. Macroshear wear tends to be most pronounced at the interface periphery but may also occur due the high temperature delineation of the pad surface such as that experienced during the final stages of *metallization* when foliate ferrous accretions, which have transferred to the friction material surface, become dislodged. Ultimately, macroshear wear is simply a descriptive mechanism of large-scale delineative adhesive wear.

In general, the overall tribological performance and wear response of automotive friction couples are heavily influenced by the physico-chemical behaviour of friction material constituents. As a foundation for those thermochemical investigations featured later, appendix 11.1. describes some of the earlier work examining the reactions of early, asbestos-based friction material formulations. The numerous physico-

chemical interactions occurring at the frictional interface, and the generation of a *Friction Heat Affected Layer* (F.H.A.L.), char layers or glazes, are nowadays collectively studied under the heading of T.B.L.

3.3. Generation of Third-Body Layers

During dry sliding friction, a host of complex interrelated triboprocesses may take place, the overall effects of which lead to a surface and near-surface structure that differs significantly in both its nature and tribological properties from those of the bulk of the two triboelements. These layers, which dominate the behaviour of the friction pair under boundary lubricating conditions, occur on *both* surfaces of the interface and are termed *Third-Body*, or three body, *Layers* (T.B.L., also *glaze*, friction film, transfer film (T.F.) / layer, etc.).

The nature of these T.B.L.s are governed by such triboprocesses as elastic and plastic deformation, phase transformations and microstructural changes, work hardening, contact zone cohesive failure, diffusion processes, chemical changes and oxidative mechanisms, electrolytic processes, decomposition, degassing, softening, crystallisation and recrystallisation and comminution (127). Although their nature is obviously extremely complex given the diverse array of active processes, an explanation of the generation of these layers can be somewhat simplified.

Prior to material transfer due to adhesive sliding contact, all materials are typically covered in up to 10 nm of adsorbed gases and hydrocarbons. In addition, metals and non-oxide ceramics may be partially oxidised, ceramic oxides may be hydrolysed, as may polymeric surfaces which also contain 'bloomed' plasticisers and mould release agents. When such surfaces first come into dry sliding contact, such as in an automotive friction brake on a new car, an initial period elapses where the two opposing surfaces, but essentially the metallic surface, undergoes *bedding-in*, a process whereby the surface roughness profile of the virgin, as-machined surface is reduced to an eroded state that supports relatively uniform contact between the two triboelements (plate 2). During this initial period, the dynamic coefficient of friction peaks, wear loss at both surfaces is high and other tribometric parameters are erratic and unpredictable.

Designers therefore seek to minimise the duration of this running-in phase, a requirement that is partially accommodated by the inclusion of solid lubricants within the brake lining. Once surface compatibility is arrived at, material begins to transfer from one surface to the other, normally until a stable and constant mean thickness of layer is attained, after which, the friction couple behaves much more predictably since a state of interfacial equilibrium has been induced (figure 20).

The T.B.L. created at an automotive friction brake interface must be considered to include all those components that are present within the velocity accommodating zone. This will usually include layers of transferred and back-transferred friction material constituents, their decomposition products, coherent and delineated oxide films and thin films of adsorbed gases. At times, the layer may also 'contain' liquid or gaseous phases as they are released either by volatilisation or by thermodynamic interaction (appendix 11.1.). Perhaps the greatest complication in the definitive characterisation of these layers is that they are constantly in a state of transient regenerative flux, being continually generated, destroyed and recreated. For this reason they are commonly referred to as 'superficial' in nature.

One of the greatest influences on the nature of the T.B.L. is that of material transfer. Material transfer in metals, which is analogous with a significant proportion of the tribological interactions occurring during automotive braking, originates by a micromechanism known as prow formation (115). The prow formation process involves adhesion points, in regions of real contact, which resist interfacial slip, plastic deformation and work hardening, leading to junction growth and finally, crack propagation which elicits the partial or complete detachment of adhered particles. Material flow during this process can be extremely complex but perhaps the most important factor to note is that the tangential shear resistance acting at enlarging junctions operates against the relative motion of one or both of the triboelements. Figure 21 illustrates graphically how transfer films develop from continued adhesive asperity interactions and subsequent cohesive failure.

A particularly exaggerated mechanism of material transfer, encountered in particular by the friction material surface, is that of *metallization*. Metallization may occur as fragments or delineated sheets of countersurface material become embedded or adhere to the lining rubbing surface (130; cited in 127). The mechanism is generally detrimental to the triboproperties of the friction pair having been identified as being responsible for brake torque reduction and raising contact temperatures.

Other than by direct metallization, it is frequently noted that the friction interface at the friction material triboelement contains a greater proportion of metallics and metallic reaction products than does the bulk matrix material (84, 118, appendix 11.1., etc.), this transition occurring over a narrow region. This increases the propensity for metal-to-metal contact, which increases the propensity for slip-stick behaviour and thus noise and is therefore to be avoided.

A correlation between the softness of a friction material constituent and the uniformity of its resultant T.B.L. under tribological action is perhaps not surprising with graphite, MoS₂, Cu powder and Sb₂S₃ all being observed to promote continuous T.F.s. Additionally, these relatively stable films tend to readily incorporate other friction material constituents, or decomposition product thereof, up to and including semi-hard materials such as vermiculite, CuO, Sb₂O₃ and barytes. MoS₂, in addition to its natural propensity to bond at ferrous surfaces, shows excellent lattice parameter coincidence with Fe which further accounts for the ease with which a uniform, continuous T.F. is formed in its presence. The alloying compatibility of Cu with Fe permits significant interatomic diffusion that persists upon oxidation of the metals. The ready interaction of Sb₂S₃ with the countersurface is assured since at relatively low temperature, the lubricious sulphide loses microhardness and is energetically displaced by the thermodynamically-favourable FeS that continues to lubricate the friction pair. Thermoplastic materials are covalently bonded such that their chains may cross-bond but their bonding to cast iron is likely to be Van der Waals. Thermosetting materials, a category that encompasses the vast majority of organic constituents of N.A.O. friction materials, do not transfer in the undecomposed state. Otherwise, the presence of significant quantities of a tenacious oxide film on the iron provides a suitable bonding substrate for the majority of friction material constituents.

Practical efforts to examine the nature, and the change in nature, of the T.B.L. *in situ* have been imaginative, such as using a transparent quartz rotor, if not wholly successful. Attempts to recreate the physico-chemical environment active at the interface have involved real-time surface analysis of laser-simulated interactions. During the author's programme of research, unsuccessful efforts were made to examine crystal structures and chemical bonding of the various T.B.L. components in thin film sections using *Transmission Electron Microscopy* (T.E.M.).

Early investigations into the influences and properties of T.B.L.s induced during friction braking were prompted by attempts to formulate definitive wear and friction relationships which, given certain conditions of say nominal pressure per unit pad area, relative velocity, time, mechanical properties of the friction elements, coefficient of reciprocal covering (128), etc. would enable the automotive designer to predict the friction and wear response of a given friction couple over a wide range of conditions. Some equations materialised but most of these only enabled quantification of empirical observations and rarely proved capable of predicting tribological response.

Much of the early work undertaken investigated the scale and effects of T.F. coverage, with respect to both film continuity and apparent thickness, on the behaviour of the friction couple. Liu *et al* (106) observed T.F.s to vary in thickness between 1 and 7 μm , the thickness and continuity of the film appearing to increase with the severity of the running conditions. Furthermore, films produced by rear drum linings were generally significantly thicker than those produced by front disc brake linings. (Although essentially speculative, Liu also suggested that it was plausible to describe the behaviour of automotive friction braking T.B.L.s as visco-elastic, given the wear behaviour of automotive braking friction pairs over time.) Continued investigations by numerous researchers suggest that the T.F.s deposited on the friction ring surface of disc brake rotors are generally less than 1 μm in average thickness and are typically much less.

More recent studies of the T.B.L. have correlated the triboperformance of friction pairs to the complex physico-chemical interactions occurring at the friction interface (90 – 100, 131), some of which have focused particular attention on the nature and influence of the T.B.L. formed under the conditions of low interfacial contact pressures associated with O.B.W. and D.T.V. generation. Since 1990, Wirth *et al* (92 – 100) have dedicated considerable attention to automotive friction braking T.B.L.s generated using both the *Friction Assessment Screening Test* (F.A.S.T.). (132 – 138) and dynamometer testing (139 – 140). In general their approach has been to expose simple, parametrically-varying friction materials to uncomplicated test schedules and have then, in combination with the performance characteristics data generated, closely examined the T.B.L.s generated to simulate or elucidate those micro-mechanisms acting during automotive braking.

Much remains only partially understood about the generation, nature and effects of T.B.L.s created between automotive friction couples, especially with regard to the specific influences of individual friction material constituents, a situation which cannot be improved by the ever increasing complexity of friction material formulations.

4.0. Experimental Procedure

The candidate's programme of research was conducted between 01.12.92 and 30.11.95 in conjunction with parallel studies being conducted at both Sheffield Hallam University and B.B.A. Friction Ltd. (formerly Mintex Don Ltd.), Cleckheaton. The experimental methodology applied during the programme of research has been based on chemical, metallurgical and tribological analyses and has set out, in broad terms, to:

- Characterise raw materials and the microstructures of both triboelements.
- Develop a library of physico-chemical interactions using A.S.E.M., X.R.D. and X.P.S.
- Characterise T.F.s generated at the rotor surface.
- Relate the tribochemical and tribomechanical interactions of friction brakes to tribological behaviour.
- Assess the influence of both T.F. characteristics and abrasive interaction on D.T.V. generation.

4.1. Characterisation of Disc Brake Rotor Material

A single heat of iron was employed to produce 200 vertically cast, solid, grey cast iron disc brake rotors, a number intended to supply the needs of the entire programme to completion. The characterisation and control of both raw materials and finished components is an essential preparatory stage in any programme of research. In the past, several authors have chosen to substantiate this statement with respect to the brake rotor material:

The friction and wear characteristics of automotive friction materials are strongly dependent on the composition and microstructure of the rotor surface (6).

Cast iron rotors in brake systems are not as envisioned, passive, relatively unchanging parts of the friction couple (as compared with the friction material). Instead, they are metallurgically quite active. For this reason, they must be well characterised during tests of friction materials (6).

The friction, wear, noise, fade, judder, crazing and speed sensitivity of a brake assembly all depend as much on the grey cast iron used for the brake disc or drum as on the formulation of the friction material (141).

The role of the rotor as friction partner with the brake linings within the total brake system ... has been ... shown to be of major significance (3).

Various analytical techniques were employed to assess compositional variability throughout the cast. In addition to what might be considered a standard metallurgical characterisation of the disc brake rotor material, described next in section 4.1.1., subsequent sections; 4.1.2. and 4.1.3., examine both fundamental production issues and the effect of temperature on the dimensional stability of the finished component. In each case, particular attention is paid to those factors potentially exerting an influence over the characterisation and interpretation of rotor O.B.W. resulting in D.T.V.

4.1.1. Constitutional Characterisation

The object of this part of the investigation was to examine the microstructural and compositional uniformity of solid, disc brake rotor castings intended for use in the project (142). From the available literature, several microstructural and compositional factors were identified as having a potential influence on the metallurgical activity and tribological response of pearlitic, grey cast irons used in automotive friction couples:

4.0. Experimental Procedure

- | | |
|--|---|
| ➤ Chemical composition (4.1.1.1.) | ➤ Mean pearlitic grain size (4.1.1.3.) |
| ➤ Flake graphite distribution (4.1.1.2.) | ➤ Mean pearlitic domain size (4.1.1.3.) |
| ➤ Flake graphite aspect ratio (4.1.1.2.) | ➤ Mean pearlite spacing (4.1.1.3.) |
| ➤ Flake graphite size (4.1.1.2.) | ➤ Pearlite consistency (4.1.1.3.) |
| ➤ Eutectic colony size (4.1.1.2.) | ➤ Ferrite content (4.1.1.3.) |

A sample of 10 discs were prepared in order to assess the microstructural, constitutional and compositional uniformity of the cast as a whole such that continued experimental reproducibility of results and effective comparative testing might be assured. The compositional and microstructural uniformity of the 10 unmachined, solid, grey cast iron disc brake rotors was assessed as outlined in sections 4.1.1.1. – 4.1.1.3.. The friction ring section of the components was used at all stages of the investigation, this zone being selected as the microstructure and composition of the material to be exposed to braking / non-braking friction.

4.1.1.1. Chemical Composition

Chemical analyses to determine the compositional uniformity of the discs were performed using a variety of techniques; *Universal Vacuum Air Quantometry* (U.V.A.Q. (or Uni.VAC.) – appendix 11.2.), *Glow Discharge Optical Emission Spectroscopy* (G.D.O.E.S. – appendix 11.3.) and *X-Ray Fluorescence* (X.R.F. – appendix 11.4.). The material grade used to produce the pilot heat was perhaps that most commonly applied (equating to a BS EN 1561 (143) (formerly BS 1452 (144)) : EN-GJL-200 grade (*cf.* GG 20)), a typical analysis of which is shown in appendix 11.5..

4.1.1.2. **Microstructural Characterisation of the Graphite Structure**

Assessment of the graphite characteristics of the rotor material included the qualitative determination of form (morphology, e.g. flake), type (distribution and orientation) and size (nominal comparative) by *Optical Light Microscopy* (O.L.M.) and visual examination of scanning electron micrographs. Quantification of graphite flake aspect ratio was accomplished using a computerised digital contrast filtering and analysis facility called *SeeScan* Quantitative Metallography (Quanti.Met.).

The eutectic colony size was evaluated from backscattered electron micrographs produced at a standard, minimum magnification. Regions were selected such that a non-interpolated cell count over a unit area of 1 cm² might be arrived at.

4.1.1.3. **Microstructural Characterisation of the Material Matrix**

Mean pearlitic grain sizes (mean grain diameters) were attained by low-magnification, O.L.M. examination of samples polished and etched for eutectoid cell enhancement and for the discernment of ferritic grain boundaries in a predominantly pearlitic matrix.

The *Mean Linear Intercept* (M.L.I.) method of grain size determination was employed, the resultant mean grain diameters equating to (*mean D*) in the associated calculations. The same approach was used to assess the pearlitic domain, or sub-grain, size of the material even though the shape of a pearlitic colony equates more to a flat-ended sphere than to a tetrakaidecahedron.

Minimum pearlitic lamellae-spacings were determined using intermediate resolution, scanning electron microscopic surveys taken of all the disc samples. The minimum spacings occasioned were taken to most closely represent normal orientation. Given the difficulty in assessing this particular pearlite characteristic within the microscope itself, dark-field, secondary electron micrographs were developed at noted magnifications to enable retrospective measurement of the spacings. Minimum spacings were taken as a mean across 15 cementite lamellae.

The consistency of the pearlite structure was evaluated at three equidistant regions on each outboard friction ring surface using O.L.M. and quoted in terms of the proportion of pearlite lamellae resolvable at magnifications of x100 and x200. The apparent free ferrite content (as a percentage of total cross-sectional area) observed within the microstructure was assessed by visual estimate at an O.L.M. magnification of x100.

4.1.2. Mechanical Uniformity of Vertically Cast Rotors

In order to achieve a uniform filling of the disc brake mould and subsequently, as close as possible a uniform cooling rate throughout the casting, some industrial-scale manufacturers produce disc brake rotors that are cast horizontally employing an axial gating arrangement. This aspect of the virgin component characterisation was undertaken to examine the structural variation, and consequently the structural anomalies, if any, present in a vertically cast, solid disc brake rotor produced on a DISAmatic 2013 moulding line by Precision Disc Castings Ltd., Poole.

The mechanical property that most readily illustrates the microstructural uniformity of a cast iron component is that of hardness. A horizontal casting system generally produces only minor hardness variations across the disc, these being due to gating arrangements, the outside diameter of the disc, and chilling effects at the external surfaces (3).

A vertically cast, solid brake rotor was sectioned across its diameter and again at a diameter perpendicular to the first and a slice of the disc removed at each diameter for sampling of the surface hardness (145). Sections were prepared for Vickers hardness (as opposed to Brinell) testing using traditional metallurgical methods. At this stage of the investigation, the rotors were supplied in their as-cast, unmachined state. The removal of a surface layer of approximately 1 mm in depth was considered sufficient to provide an adequate surface for testing (based on quality control and inspection criteria applied by the manufacturers) while simultaneously providing a worse-case scenario with respect to

structural inhomogeneities. (The finish-machined surface of the friction ring would normally be arrived at after the removal of 1.50 – 2.20 mm of surface material.)

Tensile strength (expressed in N.mm^{-2}), another important physical characteristic of the rotor material and typically described as the principal material design criteria (as defined by BS EN 1561 : 1997 (143)), was not assessed during this investigation but was certified by the manufacturer as conforming to specification.

4.1.3. Geometric Characterisation

Given the propensity of grey cast iron rotors to distort in-service upon severe thermal loading as a result of stress-relief (2.3.1.2.), potential recrystallisation and general deflection phenomena, and the potential detriment that this might infer upon subsequent D.T.V. test results, a brief investigation of the potential for this effect was initiated.

The friction ring of a rotor was measured around its circumference (relative to a datum set to the hub location face) using a pre-programmed *Co-ordinate Measuring Machine* (C.M.M.). By duplicating this procedure subsequent to heat-treatment, stress-relief and cooling, a brief, non-statistical assessment of the permanent effect of uniform heating on D.T.V. and strain-field buckling could be made.

The majority of impure metals exhibit a recrystallisation temperature within the range 0.3 – 0.5 m.p. (K), where m.p. is the metal's melting point, although the temperature is not entirely time-independent.

A soak temperature of 580°C (853 K, *cf.* m.p. \approx 1,153°C (1,426 K)) was selected so as to:

- Allow adequate stress relief and dissipation of local strain accumulated during solidification, cooling, mould knock-out and machining, without commencing a low-temperature (ferritising) anneal ($> 595^\circ\text{C}$).
- Promote minimal rotor surface oxidation, which might corrupt stylus contact during co-ordinate measuring.

- Represent bulk rotor temperatures that would be unlikely to be exceeded during either subsequent burnishing procedures or O.B.W. schedules.
- Minimise the potential contribution of internal phase transformations to overall distortion.

A significant period heat-treatment duration was required (> 1 hr / 10 mm of section thickness) since a short time at less than 595°C generally exerts only an insignificant influence on the structure of cast iron. A duration of 5 hours was arbitrarily selected to permit a thorough soak based on component section thickness and material properties.

4.2. Characterisation of N.A.O. Friction Materials

Although not obviously contributing to non-uniform wear of the countermember in a single plane at any particular point in time, the structural uniformity of the mating friction material stator is important when considering the countersurface wear response during extended test procedures such as O.B.W. schedules.

Twelve compression moulded disc brake pads were formulated using conventional dry processing techniques in order to assess the micro- and macro-structural homogeneity of linings produced using the B.B.A. pilot plant. Given the assumed influence of abrasive friction modifiers on O.B.W. and hence, the D.T.V. generation-potential of the friction material, it was decided to assess the basic uniformity of pilot-plant manufactured pads in terms of abrasive particulate distribution, the adventitious dispersion of other constituents being considered of secondary importance.

The twelve pads were designated pads AB 1 – 12 (AB indicating ABrasives) and were formulated according to a three-dimensional array enabling assessments of particle distribution relative to the nature of the abrasive, the particle size distribution and the resinous binder system utilised. Prior to the assessment of abrasive particulate distribution within model friction materials AB 1 – 12, several

abrasive constituent characteristics were investigated (including particle size, particle size distribution and seating within the friction material matrix).

Table 7:

3-D array of constitutional characteristics for the assessment of friction material compositional uniformity.

Friction material:	Resin system:	Abrasive:	Abrasive size descriptor:
AB 1	24 / 988 ❶	fused alumina (Al ₂ O ₃)	200
AB 2	24 / 988 ❶	fused alumina (Al ₂ O ₃)	500
AB 3	24 / 988 ❶	fused alumina (Al ₂ O ₃)	800
AB 4	24 / 988 ❶	Zircosil (ZrSiO ₄)	100
AB 5	24 / 988 ❶	Zircosil (ZrSiO ₄)	200
AB 6	24 / 988 ❶	zircon sand (ZrSiO ₄)	
AB 7	24 / 989 ❷	fused alumina (Al ₂ O ₃)	200
AB 8	24 / 989 ❷	fused alumina (Al ₂ O ₃)	500
AB 9	24 / 989 ❷	fused alumina (Al ₂ O ₃)	800
AB 10	24 / 989 ❷	Zircosil (ZrSiO ₄)	100
AB 11	24 / 989 ❷	Zircosil (ZrSiO ₄)	200
AB 12	24 / 989 ❷	zircon sand (ZrSiO ₄)	

❶ = 24 / 988 = straight phenolic resin system

❷ = 24 / 989 = phenolic resin system incorporating modified nitrile rubber

4.2.1. Abrasive Constituent Characterisation

Samples of various abrasive particulates were supplied for visual inspection using O.L.M. and *Analytical Scanning Electron Microscopy* ((A.S.E.M.) - appendix 11.6.). For the O.L.M. studies, aluminium stubs were thinly coated with a surface adhesive and then pressed into a pile of abrasive, after which, the

excess powder was brushed off. The relatively flat, thin, abrasive-coated surface thus presented enables reasonable scope for the inspection of multiple particles within the same frame, otherwise difficult given the extremely poor depth resolution using light microscopy. For further examination of the particles within the A.S.E.M. environment, these same samples were gold sputtered (4.5).

The particle size distributions of several commercial abrasive particulates were externally assessed using local laboratory facilities. Friction material samples were also prepared to observe the manner and orientation in which abrasive particles were seated within the surface of the pads.

4.2.2. Distribution of Friction Material Constituents

Microstructural assessments were made of friction material constituent distribution and dispersion, especially with respect to those of the abrasive particulates. Each of the friction materials were supplied in their unused, as-ground state. Sections were cut from the centre of each pad and polished (burnished) using standard metallographic techniques. Observations made were both quantitative (in terms of the actual apparent content of a given constituent over a given area) and qualitative (in terms of general dispersion of a given constituent).

The distribution of friction material constituents was investigated using O.L.M. and A.S.E.M. (utilising secondary, back-scattered and combined electron emissions), the latter facilitating energy dispersive X-ray analysis enabling the generation of detailed elemental digital distribution maps (*digimaps*) of the surfaces prepared. Given the shortcomings of the elemental analysis technique, conventional filler materials were selected according to the ease with which the chosen abrasive particulates could be distinctly isolated (4.5). Calcium carbonate was employed, offering perfect differentiation of both fused alumina and zirconium silicate, and expanded vermiculite rejected entirely due to its complex, multi-elemental composition. Consistent additions of shredded iron wool and spheroidal copper powder were added for authenticity, their inclusion further enabling cross-referenceable comparisons of particulate dispersion. Graphite was also included.

4.3. Physico-Chemical Interactions of Friction Material Constituents

Within the literature describing the characteristics and factors influencing triboperformance, the nature of the T.B.L. formed is frequently emphasised (3.3.), this forming a critical element of the programme of research. It has already been established that the properties of a friction couple operating under boundary lubrication are dominated by the physico-chemical interactions acting at the interface and so it was decided to characterise these chemical reactions over the range of operating temperatures.

The number of permissible combinations (as opposed to permutations) of a multi-elemental system is given by:

$${}^nCr = \frac{n!}{(n-r)! \cdot r!} \quad \text{①}$$

where nCr = no. of permissible combinations of elements.

n = no. of elements to be considered reactive, i.e. possessing potential for combination.

r = no. of different elements forming a given combination, e.g. $X + Y = 2$, $X + Y + Z = 3$, etc.

Thus for a multi-component friction material containing 20 different elements reacting with the same elements, in air and in contact with a typical countersurface, i.e. $n \approx 20$; when $r = 2$, ${}^nCr = 190$, when $(r = 2) + (r = 3)$, ${}^nCr = 1,330$, and when we add this to $(r = 4) + (r = 5)$, ${}^nCr = 21,679$. It is easy to see that the number of combinations necessary to consider the formation of chemical complexes (3 – 5+ components) is impractical to simulate experimentally. It was therefore necessary to determine the most likely theoretical thermodynamic environment (appendix 11.7., figures 22 and 23) and to compare this with simplified experimental combinations.

Various powdered friction material constituents were combined in equal mass proportions (table 8). Commercial grade raw materials were used to enable the detection any significant impurity interaction.

4.0. *Experimental Procedure*

All powder samples were pre-formed into small annular pellets ($\varnothing = 12$ mm, $t = 1 - 1.5$ mm) and cold isostatically pressed at 1.8 MN.m^{-2} to provide adequate mechanical properties for handling prior to heat-treatment. Pellets were then placed in alumina crucibles and heat-treated individually in a pre-heated muffle furnace for 24 hours. After treatment, the samples were immediately transferred to a laboratory desiccator for temporary storage. The pellets were then analysed to show their resultant chemical natures using *X-Ray Diffraction* ((X.R.D.) – appendix 11.8.).

Table 8:

Friction material constituents, alone and in selected combinations, the thermochemical behaviour of which was examined experimentally by isothermal holding in air for 24 hours. All samples were treated from 0 – 800 °C in steps of 200 °C. Samples from MNS 13 onwards were also heat-treated on a cast iron substrate from 0 – 1,000 °C in steps of 100 °C.

Designation:	Formulation (elemental constitution):
MNS 1 ❶	Graphite (C)
MNS 2 ❶	Black iron oxide (Fe ₃ O ₄)
MNS 3 ❶	Red iron oxide (Fe ₂ O ₃)
MNS 4 ❶	Antimony trisulphide (Sb ₂ S ₃)
MNS 5 ❶	Red iron oxide (Fe ₂ O ₃) + molybdenum disulphide (MoS ₂)
MNS 6 ❶	Black iron oxide (Fe ₃ O ₄) + graphite (C)
MNS 7 ❶	Black iron oxide (Fe ₃ O ₄) + copper powder (Cu)
MNS 8 ❶	Barytes (BaSO ₄) + graphite (C)
MNS 9 ❶	Molybdenum disulphide (MoS ₂)
MNS 10 ❶	Barytes (BaSO ₄)
MNS 11 ❶	Black iron oxide (Fe ₃ O ₄) + antimony trisulphide (Sb ₂ S ₃)
MNS 12 ❶	Barytes (BaSO ₄) + copper powder (Cu) + graphite (C)
MNS 13 ❶	Barytes (BaSO ₄) + copper powder (Cu) + antimony trisulphide (Sb ₂ S ₃)
MFM 1 ❷	Barytes (BaSO ₄) + copper powder (Cu) + graphite (C) + black iron oxide (Fe ₃ O ₄) + vermiculite
MFM 2 ❷	Copper powder (Cu) + graphite (C) + molybdenum disulphide (MoS ₂) + black iron oxide (Fe ₃ O ₄)
MFM 3 ❷	Barytes (BaSO ₄) + copper powder (Cu) + graphite (C) + molybdenum disulphide (MoS ₂) + black iron oxide (Fe ₃ O ₄)
DM 24 / 3264 ❸	Black iron oxide (Fe ₃ O ₄) + china clay (CaCO ₃) + steel fibre (Fe) + brass (Cu:Zn) / copper (Cu) + antimony trisulphide (Sb ₂ S ₃) + (binders + abrasives + carbons) (Si, O, Zr, Cr, Al, S, C)
DM 24 / 3353 ❸	Steel fibre (Fe) + brass (Cu:Zn) / copper (Cu) + antimony trisulphide (Sb ₂ S ₃) + vermiculite + magnesium oxide (MgO) + zinc sulphide (ZnS) + (binders + abrasives + carbons) (Si, O, Zr, Cr, Al, S, C)

❶ = *MNS* = Mintex Nominal Standard

❷ = *MFM* = Model Friction Material

❸ = *DM* = Dry Mix = unpolymerised commercial grade friction material

4.4. Disc Thickness Variation Evaluation rig Testing

The testing of friction materials to examine, characterise and screen their tribological response has always been central to automotive friction braking system research, development and manufacture. The D.T.V. evaluation test rig, which formed a principal component of the collaborative DTI *LINK* initiative, was conceived and constructed by engineers at B.B.A. Friction Ltd., Cleckheaton, as a peripheral add-on to a standard single-end, full-scale inertial dynamometer (appendix 11.9.) to induce O.B.W. under controlled conditions so as to enable an assessment of the influence of given frictional surface interactions on the D.T.V. generation process. The principal objectives of the D.T.V. evaluation rig were that it be capable of providing the following:

- Repeatable and reproducible test conditions.
- Accurate simulation of conditions approximating to normal on- and off-brake running over extended periods.
- Automated operation enabling unsupervised testing during day or night.
- The capacity for testing of various schedules to simulate a variety of usage patterns.
- Precision control of the off-brake contact and loading regime.
- Capacity for monitoring of both on- and off-brake contact and their effects; i.e. D.T.V. generation and rotor surface clean-up.
- Capacity for variable monitoring rates and sampling intervals.
- Data analysis, condensing and formatting capabilities for readily comparable test results.

The peripheral assembly corresponds to a large prototype caliper incorporating dual actuation mechanisms; one, hydraulically controlled to simulate the on-brake pressures required ($0 - 30 \text{ MN.}(\text{pad area})^{-1}$) and the second, stepper motor actuated (and load-cell monitored) to simulate off-brake pressures ($0 - 100 \text{ N.}(\text{pad area})^{-1}$). The complex logistics of providing a dual actuation mechanism means that the low pressure actuation sub-system was located inside the load transfer apparatus required for the normal brake application pressures. Piston seal roll-back was simulated using *Belleville* washers. A schema of

the D.T.V. rig is shown in figure 24 and an outline of its operation for both off-brake and on-brake testing is illustrated in figure 25. The test schedule development programme was based around the generation of control files establishing parametric variables from the following running modes:

- Constant torque mode.
- Constant pressure mode.
- Off-brake running mode.

Thirteen test schedules were undertaken as part of the programme of research, these tests involving the examination of two different commercial friction materials; designated S (a supposedly aggressive material demonstrating high on- and off-brake wear) and N (a milder formulation demonstrating low on-brake wear and indeterminate O.B.W. performance), and an experimental material designated Exp. A (which received considerably less attention). Table 9 shows the general formulations (analysed) of the four outlined friction materials and table 10 shows the programme of test schedules to which these specimens were subjected.

Table 9:

Guideline formulations of friction material designations; N, S and Exp. A.

Material:	Fibre reinforcement:	Abrasive:	Solid lubricant:	Mineral filler:	Other:
N	Stainless steel fibre	SiC (Ø 10 µm)	Sb ₂ S ₃ , MoS ₂	BaSO ₄ , vermiculite	Trace Ca ❶, bronze (Cu-Sn)
S	Steel wool	ZrSiO ₄ (Ø 50 – 75 µm)	MoS ₂	BaSO ₄ (> N), vermiculite	Trace Ca ❶, copper
Exp. A	Steel fibre, cyanamid	Al ₂ O ₃ (Ø 50 – 75 µm)	Graphite flakes	BaSO ₄ , CaCO ₃	Cu chips, phenolic resin

❶ = detected trace Ca in response to either release agent compound or CaF₂ from BaSO₄

Table 10:

Preliminary D.T.V. evaluation test rig schedules.

<i>Test:</i>	<i>Formulation designation:</i>	<i>Schedule:</i>	<i>Original S.R.O. (μm):</i>	<i>Applied load ($\text{N}\cdot\text{pad}^{-1}$):</i>	<i>L.I.P. ③:</i>
2	N	Manual ①	120	40	24.0
3	S	Manual ①	100	40	52.0
4	Exp. A	Manual ①	100	40	82.5
5	Exp. A	D.T.V. ①	125	40	76.5
6	N	Bedding ②	120		
7	S	Bedding ②	170		
9	N	D.T.V. ②	120	40	80.0
10	N	D.T.V. ②	90	40	80.0
11	S	D.T.V. ②	120	40	80.0
12	N	D.T.V. ②	110	40	80.0
13	S	D.T.V. ②	110	40	80.0

① = No bedding schedule, used in the as-machined and degreased condition.

② = Bedded by applying 100 stops from 25 m.s⁻¹.

③ *L.I.P.* = Duration of running at Low Interfacial Pressure (in hours).

The pre-treatment bedding schedule (②) involved consecutive braking applications at a constant line pressure of 30 bar (300 N.mm⁻²), each successive brake application commencing as the bulk temperature of the test rotor (measured using a simple rubbing thermocouple) fell to between 120 and 90°C. Prior to the commencement of each of the test, the test rotors were measured by C.M.M. to check their dimensional conformity against nominal manufacturing tolerances for axial S.R.O. relative to the locating face, circumferential D.T.V. and radial braking surface flatness.

Discs were mounted on the rig and the point of maximum inherent runout identified, quantified and its location noted. This point of maximum runout was then tuned to achieve the desired natural runout using tapered shims and the runout reassessed iteratively.

Upon completion of the test schedule, the discs were carefully prepared for surface analysis. Standard precautions involved minimum handling, zero handling of the friction ring surface and lubricant-free, i.e. clean / dry, sectioning. Sections were removed from the discs at the points of maximum and minimum contact for each side of the friction ring, these regions being *approximately* diametrically opposed and coincident for either side of the rotor. Samples were then investigated using A.S.E.M. The suitability of various A.S.E.M. imaging conditions were evaluated and optimum analysis conditions established. An accelerating voltage of 10 kV was applied over an area magnified to x150, equating to an sample area of 0.5 mm². The effect of these conditions on the electron interaction volume are described in detail next. These conventions were then applied to subsequent analyses.

4.5. A.S.E.M. applied to Third-Body Layers and Friction Material Constituents

When applying A.S.E.M. to surface analytical investigations, it is important to have some appreciation of the interaction volume affected by the incident beam. Quantification of such an area is attained via a Monte Carlo electron trajectory simulation, a computerised model that calculates the effects of elastic and inelastic electron scattering based on various material properties. Important examples of such models for an oxidised cast iron surface (nominally representing the rotor material) over a range of useful accelerating voltages are shown in figure 26. Table 11 quantifies both the depth and spatial resolutions over the same range of accelerating voltages with respect to electron interaction volumes. Unfortunately, analogous data for the surfaces of brake linings cannot be simulated so readily due to the inherent inhomogeneity and variability in the material properties of their constituents.

As with resinography, sample preparation is crucially important in A.S.E.M. investigations. In contrast to electronically-conducting, essentially metallic specimens, both ceramic particulate (4.2.1.) and organic friction materials samples (4.2.2.) need to be sputter-coated to build up an extremely thin ($\approx 2 - 3$ atomic layers) conductive film. Sputtering simply involves the electric arc ionisation of the sputtering material in the direction of the sample, in vacuo. Sputtering materials are generally either graphite, which finds application where X-ray information must be retrieved, or gold, which offers slightly superior spatial resolution but at the expense of several additional characteristic X-ray peaks.

Table 11:

The depth and spatial resolution of electron interaction within the A.S.E.M. as determined by Monte Carlo electron trajectory simulation of an electron beam impinging on an oxidised iron substrate. The simulated surface consists of a 1 μm layer of red iron oxide (Fe_2O_3) on an otherwise pure iron specimen.

<i>Accelerating voltage (kV):</i>	<i>Depth resolution (μm):</i>	<i>Spatial resolution (μm):</i>
5	0.2	0.2
10	0.6	0.7
15	1.2	1.4
20	1.7	2.3
25	2.3	3.0

Additionally, such samples need to be adhered to their mounts using an electrically conductive paste (silver dag; principal elemental constituents including silver, chlorine and sodium). This initially volatile, solvent-based suspension dries to provide a circuit, which is essential in A.S.E.M. to facilitate the discharge of the incident probe current during analysis. Best results are obtained when the dag is administered from the incident surface in a continuous path to the intrinsically conducting metallic stub upon which the sample is mounted.

The identification or distribution mapping of materials using A.S.E.M. is based on the collection of X-ray peaks that are characteristic of the element involved but show no chemical data other than can be

gleaned from the atomic number contrast afforded by backscattered electron imaging, the relative intensities of multiple characteristic X-ray peaks under given excitation conditions, or the physical coincidence of elemental data.

Table 12 lists the positions on the X-ray spectrum of those major characteristic X-ray peaks finding application in the study of automotive, N.A.O. friction materials and the T.B.L.s generated by their functional interactions.

Table 12:

Principal X-ray peaks of common friction material elemental constituents in increasing order of characteristic X-ray energy (i.e. their relative position on the X-ray spectrum).

<i>Elemental constituent:</i>	<i>Atomic no., Z:</i>	<i>X-ray peaks isolated:</i>	<i>X-ray energy (keV):</i>	<i>Wavelength, λ (nm):</i>	<i>K edge, E (keV):</i>	<i>K edge, λ (nm):</i>
Carbon	6	$K\alpha_1$	0.277	4.47	0.284	4.368
Oxygen	8	$K\alpha_1$	0.525	2.362	0.532	2.332
Iron	26	$L\alpha_1$	0.705	1.759	L_3 0.707	L_3 1.753
Zinc	30	$L\alpha_1$	1.012	1.225	L_3 1.022	L_3 1.231
Magnesium	12	$K\alpha_1$	1.254	0.989	1.303	0.9512
Aluminium	13	$K\alpha_1$	1.487	0.8339	1.560	0.7948
Silicon	14	$K\alpha_1$	1.740	0.7125	1.84	0.6738
Zirconium	40	$L\alpha_1$	2.042	0.6071	L_3 2.223	L_3 0.5579
Molybdenum	42	$L\alpha_1$	2.293	0.5407	L_3 2.523	L_3 0.4913
Sulphur	16	$K\alpha_1$	2.308	0.5372	2.470	0.5019
Lead	82	$M\alpha_1$	2.346	0.5286	M_5 2.502	M_5 0.496
Potassium	19	$K\alpha_1$	3.314	0.3741	3.608	0.3437
Tin	50	$L\alpha_1$	3.414	0.3600	L_3 3.929	L_3 0.3156
Antimony	51	$L\alpha_1$	3.605	0.3439	L_3 4.123	L_3 0.3000
Calcium	20	$K\alpha_1$	3.692	0.3358	4.038	0.3070
Barium	56	$L\alpha_1$	4.466	0.2776	L_3 5.247	L_3 0.2363
Chromium	24	$K\alpha_1$	5.415	0.2290	5.989	0.2070
Iron	26	$K\alpha_1$	6.404	0.1936	7.111	0.1743
Copper	29	$K\alpha_1$	8.048	0.1541	8.980	0.1381

'Useful', or statistically significant peaks were rarely collected above that of copper $K\alpha$ when applying an accelerating voltage no greater than 25 kV. Of particular difficulty when utilising solely energy dispersive X-ray techniques is the coalescence of coincident peaks (alluded to earlier in selecting the formulations for pad materials AB 1 – 12). Within the context of friction material and T.F. analyses, this is most readily seen at the overlapping peaks of Mo $L\alpha$ and S $K\alpha$, which are impossible to differentiate using conventional E.D.X. However, throughout this study MoS₂ was rarely included in a formulation that did not enable qualitative differentiation by, say, the presence of additional metallic sulphides or barytes.

Although all friction material micrographs were collected using an electron beam accelerating voltage of 10 kV, such a low accelerating voltage was rarely sufficient to excite the necessary characteristic X-rays of certain elements, e.g. Zr. Indeed, even at an accelerating voltage of 25 kV, the primary characteristic X-ray peak isolated for Zr analyses (and hence zirconium silicate) is the $L\alpha$ as opposed to the more usual $K\alpha$ since the high energy $K\alpha_1$ peak occurring at 15.775 keV ($\lambda = 7.859$ nm, K edge; $E = 17.999$, $\lambda = 6.888$) is still beyond detectable limits (detection limit of a characteristic X-ray at Z keV $\approx 1/3 \times Z$ kV (accelerating voltage)).

The majority of these analyses were conducted employing an accelerating voltage of 25 kV so as to permit the monitoring of higher energy peaks. However, the quantitative X-ray analysis and mapping of low-energy (< 0.7 keV) $K\alpha$ lines such as that of O ($K\alpha_1 = 0.525$ keV) or C ($K\alpha_1 = 0.277$ keV) are difficult because the mass absorption coefficients for low-energy X-rays are very large. Mapping of such elements is thus best catered for by the use of either a low electron-beam energy (e.g. 10 kV), which limits beam penetration leading to the production of X-rays nearer to the specimen surface, or an increased take-off angle, which would shorten the path length for absorption within the specimen. The more inappropriate the applied accelerating voltage to a particular characteristic X-ray peak, the greater the likelihood there is for the corresponding elemental digimap to be indistinct or 'fuzzy'.

With respect to the examination of automotive friction brake triboelements, X-ray digimapping can prove extremely useful. For example, oxygen distributions tend to show an approximately uniform dispersion with voids, such as is illustrated in plate 4. Subtle variations in the strength of the signal are detectable according to the proportion of O within the interaction volume facilitated by the species, and

the distinct voids correspond to metallics and particles of graphite at low magnification and also to topographically *shadowed* regions at higher magnifications. The distributions of Si, Mg, Al, K and Fe are frequently closely associated due to the vermiculite contained in a material. Graphite flakes (of up to 1 mm in diameter) are naturally identified as particles exhibiting high C concentrations that are notably devoid of O. These particles appear as a proportion of the darkest features of backscattered electron images. The remainder of the very dark / black patches evident in backscattered electron images are friction dusts that can be identified as those regions appearing dark in B.E.I. while exhibiting a relatively high C concentration but average O concentration in the digimap.

The distribution of the phenolic resin binder is not so readily differentiated. However, more specialised treatments exist such as the preferential staining of selected organic artefacts by increasing the emissivity or electron scatter of a particular polymeric functional group; bisphenol A-based epoxies may be stained using ruthenium tetroxide, and rubber (unsaturated hydrocarbon) inclusions may be distinguished using osmium tetroxide, ruthenium tetroxide or ebonite.

Of the various friction materials examined during the research (excluding pads AB 1 – 12), barytes was observed to be distributed throughout the matrix in discrete lumps, these appearing almost white in B.E.I. Metallic friction modifiers such as Cu powder, brass or bronze chips, Al or Zn granules, steel wool, stainless steel fibres, etc. are usually very easily distinguished by the majority of suitable techniques. Their strong, discrete X-ray signals make them readily distinguishable from their oxides such as might form a vermiculite- or glass fibre-contribution.

The elemental X-ray analysis of friction materials can be more difficult. Complications should be minimised by learning as much as possible about the constituent grades of materials being introduced (e.g. the inherent multi-component nature of vermiculite (table 5) or the fact that commercially mined barytes is frequently contaminated with a trace proportions of highly-lubricious calcium fluoride (CaF_2)), chemical treatments or manufacturing processes (e.g. mould release agents or the fact that about 2.0 mass % of zinc oxide (ZnO_2) may be added to accelerate curing of the rubber bonding agent).

Investigations into the T.B.L. generated on cast irons after coupling with N.A.O. friction materials were assisted considerably by the application of A.S.E.M. techniques. A.S.E.M. enables significant thickness-dependent information to be retrieved simply by appropriate control of the electron beam accelerating

voltage. Upon examining several cast iron surfaces using a relatively high accelerating voltage, the relative peak heights of the Fe $K\alpha$ to the much lower energy, and hence escape-restricted $L\alpha$, contributes much to the appreciation of the relative thickness of the T.B.L.s deposited on the rotor surface. Of course, higher $L\alpha : K\alpha$ peak ratios, which might be thought to indicate a relatively thin T.B.L., might also suggest the presence of a significantly thicker but high-iron film. It therefore becomes necessary to take account of surface-impinging graphite flake visibility, increased visibility in A.S.E.M. indicating their increasing proximity to the surface. In order to assist in, and better quantify this second physical phenomenon in terms of the level of 'abrasion' to which grey cast iron surfaces have been exposed, samples of rotor material were prepared using standard metallographic techniques to provide comparable visual standards polished down to increasingly fine levels of surface finish (plate 5) and these surfaces assessed using A.S.E.M. to show the variation in C $K\alpha$ emission with surface roughness (figure 27).

5.0. Results & Discussion

5.1. Characterisation of Disc Brake Rotor Material

To a considerable extent, in-process manufacturing controls maintain the melt composition via a combination of intermittent spectrographic analyses of chilled 'lollipop' samples (table 13) and continuous monitoring of the melt's *Carbon Equivalent Liquidus* value (C.E.L.). The interpretation of such data with respect to appraising the overall melt homogeneity must, however, consider the process in greater depth. According to conventional manufacturing practices at the foundry in question, upon attainment of satisfactory lollipop analyses, the five-tonne melt is conveyed to the intermediate one-tonne transfer ladle for transport to a ten-tonne autopour unit, which provides further opportunities for melt homogenisation and late-stream inoculation immediately prior to laser-controlled, sand casting.

Table 13:

Chemical analyses of heat samples collected during pouring from the auto-pour furnace.

<i>Element (mass %):</i>	<i>Beginning:</i>	<i>Middle:</i>	<i>End:</i>
Carbon (C)	3.37	3.29	3.37
Silicon (Si)	2.14	2.15	2.18
Manganese (Mn)	0.66	0.67	0.67
Phosphorus (P)	0.04	0.04	0.04
Sulphur (S)	0.08	0.07	0.07
Chromium (Cr)	0.16	0.11	0.11
Nickel (Ni)	0.05	0.05	0.05
Molybdenum (Mo)	0.017	0.020	0.021
Copper (Cu)	0.26	0.26	0.27
Aluminium (Al)	0.001	0.001	0.001
Titanium (Ti)	0.025	0.018	0.016
Lead (Pb)	0.003	0.003	0.003

Towards the end of a pour, it is not uncommon to experience a decrease in the P composition, an increase in Al and Cu concentration, and a consistent but small increase in the Si content of the melt (148), observations that are tentatively corroborated by the minor melt variation evident from table 13. However, these observations are perhaps a little misleading given that the level of the melt within the auto-pour unit is constantly being replenished by further charges from the transfer ladle. It is also evident from subsequent analyses (table 15) that such controvertible inhomogeneities do not persist to the solidified castings.

In considering the actual levels of the various alloying constituents relative to those values determined later (5.1.1.1., table 15), the 'in-pour' concentrations of C, Si, Mn, Mo and Cu all appear highly consistent with those of the solidified product (to within $\pm \sigma$ mass %), although P and S appear a little high ($> \pm 3\sigma$ mass %) in the finished casting analyses. Cr and Ni are found to be generally slightly higher in the as-cast product but only to a level within the analytical precision of the techniques employed.

5.1.1. Constitutional Characterisation

Information yielded additional to the predefined objectives of the investigation included an assessment of the application-specific effectiveness of various chemical etchants with respect to the examination of pearlitic, grey cast iron microstructural artefacts. Thus, in each case, the etchant found to give best results for the examination of specific microstructural features is quoted in table 14.

Table 14:

Preferred chemical etchants for the microstructural characterisation of pearlitic, grey cast irons.

<i>Microstructural characteristic:</i>	<i>Etchant:</i>
Exposed flake graphite	aggressive HCl / HF deep etch
Flake graphite distribution	polished but unetched
Flake graphite aspect ratio	polished but unetched
Flake graphite size	polished but unetched
Eutectic colony size	polished but unetched
Pearlitic grain size	Modified Fry's reagent
Pearlitic domain size	Modified Fry's reagent
Pearlite spacing	4 % Picral
Ferrite content	6 % Nital

5.1.1.1. Chemical Composition

Several factors affected the selection process as to which analytical technique could most accurately represent the true elemental content of a specific constituent, these varying from straightforward restrictions on equipment availability to the statistical repeatability of specific elemental analyses.

Each set of analyses was undertaken four times, the first analyses being used to establish optimum analysis parameters prior to being discarded. Ultimately, all U.V.A.Q. analyses on the graphitised samples were dismissed since repeated analyses failed to show Gaussian distribution for the major constituents of the material, these non-normal distributions exerting similarly misleading influences on the other analyses undertaken.

With the exception of the all-important C content, G.D.O.E.S. analysis results proved extremely consistent, all concentrations exhibiting a standard deviation well below 5 % of that of the mean. However, this technique in particular was limited by the poor availability of elemental standards for comparative analysis. X.R.F. analysis proved extremely effective but required very close control of the

sample's surface preparation. The difference between the relative X-ray penetration of the flake graphite and the ferrous matrix required that a perfectly representative, effectively undeformed surface be presented. Coarse finishing was found capable of compressing and removing surface-impinging graphite leading to the partial or complete surface covering of the flake by plastically deformed, pearlite matrix. This effect commonly caused would-be, surface-impinging graphite flakes to become effectively buried, appearing sub-surface in cross-section to a depth of up to 2 μm or more, depending on the severity of the finishing operation. Adversely, overpolishing on a finely napped cloth was generally found to overexpose the periphery of surface-impinging flakes thereby generating an analysis funnel whereby a disproportionate signal could be received from the graphitic component. Further observations of these phenomena were detailed in a separate project report (142).

Table 15:

Compositional analyses of the 10 grey cast iron, disc brake rotor samples provided. (A typical analysis of the grade, as quoted by the manufacturer in appendix 11.5., also appears).

<i>Element:</i>	<i>Selected mean (mass %):</i>	<i>Standard deviation, σ:</i>	<i>Standard deviation (%):</i>	<i>Analysis technique:</i>	<i>Typical analysis (mass %):</i>
C	3.42	+/- 0.28	+/- 8.2%	X.R.F.	3.49
Si	2.17	+/- 0.02	+/- 0.7%	X.R.F.	2.14
Mn	0.664	+/- 0.006	+/- 1.0%	G.D.O.E.S.	0.66
P	0.061	+/- 0.001	+/- 2.4%	X.R.F.	0.04
S	0.102	+/- 0.003	+/- 3.0%	X.R.F.	0.08
Cr	0.16	+/- 0.005	+/- 3.1%	X.R.F.	0.16
Mo	0.02	+/- 0	+/- 0%	X.R.F.	0.017
Ni	0.060	+/- 0.003	+/- 4.2%	G.D.O.E.S.	0.05
Cu	0.26	+/- 0.0	+/- 0%	X.R.F.	0.26
Ti	0.016	+/- 0.001	+/- 6.3	X.R.F.	0.025
Pb	N/A	N/A	N/A	----	0.003
Mg	0.002	+/- 0	+/- 0%	G.D.O.E.S.	not quoted
V	0.01	+/- 0	+/- 0%	X.R.F.	not quoted

Ultimately, the X.R.F. analyses upon which much of table 15 is based were undertaken on a relatively finely polished surface from the braking axis of the friction ring of the disc. All of these results exhibited a standard deviation of < 10 % including a carbon content of 3.42 %.

Compositional analyses of those elements for which appropriate calibration standards were available, can be seen to be both consistent and correlate closely with suggested values. A further factor corroborating the accuracy of these results is the close correlation in the C.E.L. and C.E. values. The in-process sampling (table 13) shows a hypoeutectic composition where C.E. = 4.04 – 4.09. Table 15 also shows a clearly hypoeutectic cast iron with a mid-range C.E. = 3.99, a very minor deviation (1 – 2 %) that is certainly within the confidence limits of the analytical procedures applied.

Other than to define the consistency of the components to be used for experimentation, this exercise also enabled the product's anticipated tribological response to be partially assessed. Table 16 characterises the effects of various important alloying additions made, many of which exert a significant influence over the material's triboproperties.

Many alloying additions are made to increase the mechanical strength of the matrix material. Prima facie, mechanical strength is not a major influence on the successful performance of the rotor but benefits made in strength can be simultaneously sacrificed for even higher carbon contents and the benefits that this instils; improved thermal fatigue cracking resistance, thermal shock / cycling resistance, vibrational damping capacity and, in particular, thermal conductivity. Increasing the thermal conductivity of the rotor material has been observed to reduce the wear of the friction material stator (2, 8) although the rate by which this improvement in pad life occurs varies with lining material.

The addition of strengthening alloying additions such as Cr (0.2 – 0.4 %, *cf.* 0.16 %), Mo (0.3 – 0.6 %, *cf.* 0.02 %), Cu (0.35 – 1.15 %, *cf.* 0.26 %), Ni (0.1 – 0.3 %, *cf.* 0.060 %) and V (0.15 – 0.7 %, *cf.* 0.01 %) must be carefully controlled since almost all of these constituents increase the iron's chilling potential. Such additions are frequently made in combination, e.g. Cr + Cu, Cr + Mo, etc. Figures 28 and 29 illustrate the relative effectiveness of various alloying additions in increasing the strength and hardness of grey cast irons (149).

Table 16:

The effect of alloying additions on the tribological performance of a grey cast iron disc brake rotor.

Duplicated from Chapman and Hatch (141).

<i>Elemental Addition:</i>	<i>Graphitiser</i>	<i>Carbide stabiliser</i>	<i>Deoxidant</i>	<i>Hard particles</i>	<i>Ferrite promoter</i>	<i>Effect on performance</i>
Titanium	•		•	•	•	<i>Reduced</i>
Chromium		•				<i>None</i>
Zirconium	•		•		•	<i>None</i>
Vanadium		•		•		<i>Reduced</i>
Tungsten		•				<i>None</i>
Molybdenum		•				<i>None</i>
Aluminium	•		•		•	<i>None</i>
Niobium		•		•		<i>Reduced</i>
Nitrogen						<i>None</i>
Sulphur		•				<i>None</i>

'Reduced' performance refers to reduced dynamic coefficient of friction, reduced rotor wear and reduced friction material wear.

Cr, Ni and V have, in the past, been used to increase the elastic modulus of the cast iron but the precipitation of hard carbides (highly abrasive, wear resistant and thermally insulating) may frequently lead to promote hot spotting and thermal judder (2.3.1.). However, in general, the effects of adding such alloying elements are to increase the base material's resistance to both thermal cracking and distortion. In this respect, Mo additions are particularly effective, simultaneously negating the inherent propensity for the development of hard particles within the microstructure. However, given the potentially deleterious influences with respect to judder phenomena and their causes, none of these additions were made to the batch utilised during this investigation.

Although not at levels adequate to promote notable strength improvements, Cu supplements also benefit the cast iron by improving its resistance to corrosion.

Mn (0.5 – 0.9 %, *cf.* 0.664 %) is generally added to steels to combine with excess S (0.12 max., *cf.* 0.102 %) to form small, uniformly distributed, dove grey inclusions of manganese sulphide (MnS) and performs the same function within the steel-like matrix of grey cast iron. The reaction of Mn with S occurs in preference to those of Fe with S that would otherwise lead to grain boundary segregation and a consequential weakening of the matrix material. In grey cast irons, although both Mn and S would usually exert a carbide stabilising effect when added in isolation, the early formation of MnS neutralises these effects and serves the additional need to provide nucleation sites for eutectic cell formation in the absence of heterogeneous inoculant nucleants. Additionally, MnS inclusions improve the free machining properties of the material and also, in tribological operation, the dry sliding wear performance of the counter member in the same way as metallic sulphides present within the friction material. However, unlike those solid lubricants contained in the friction material (3.1.4.), MnS remains essentially unchanged throughout the range of temperatures attained during braking, melting at about the same temperature as low carbon steel at 1,530°C.

P (0.06 – 0.75 %, *cf.* 0.061 %) may be added to improve the material's abrasive wear resistance by promoting the formation of phosphide eutectic. Phosphide eutectic is a hard, interdendritic phase that exists in two principal forms; pseudobinary and ternary, the constitution, hardness and component hardnesses of which are given below.

Table 17:

The nature and hardness of phosphide eutectics and their components.

<i>Phase derivative:</i>	<i>Constitution:</i>	<i>Vickers hardness (H_V):</i>
Pseudobinary phosphide eutectic	Ferrite (α-Fe) + iron phosphide (Fe ₃ P)	420 – 600
Ternary phosphide eutectic	Ferrite + cementite (Fe ₃ C) + iron phosphide (Fe ₃ P)	780 – 800
Ferrite	Carbon (C) in interstitial solid solution with iron (Fe)	100 – 200
Cementite	Iron carbide (Fe ₃ C)	800 – 1015

Pseudobinary phosphide eutectic is an equilibrium phase that forms as austenite and iron phosphide from the molten state during casting. The associated austenite converts to ferrite and pearlite upon subsequent cooling. If the chilling tendency of the original melt is increased, e.g. by the presence of certain alloying additions (typically greater than 0.1 mass % Cr (*cf.* 0.16 %) or V (*cf.* 0.01 %)), a ternary phosphide eutectic forms, which is generally the case. Upon cooling from the liquidus, the austenite and cementite phase combination is encountered in preference to austenite alone. The associated austenite converts to ferrite upon subsequent cooling and the cementite is retained. Islands of ternary phosphide eutectic tend to situate in the vicinity of cell boundaries, frequently being associated with trace element compounds present in the matrix material, especially carbide stabilising agents. The presence of phosphide eutectics is generally encouraged in grey cast irons to promote sliding wear resistance although in-service conversion to the ternary form, which was avoided in the control batch, will significantly effect friction stability and is likely to increase lining wear.

In a similar, but more pronounced way to that of P additions, the introduction of Ti (0.025 – 0.035 %, *cf.* 0.016 %) to the base material leads to the formation of hard, wear resistant phase constituents. Essentially, the mechanism by which such constituents reduce wear is by restricting, or, by inducing a decline in, rotor surface delineation (3.3., *cf.* friction material delineation (3.2.1.)). Chapman *et al* (141, 150) were the first to identify the significance of Ti additions. In their work, they described how the formation of minute (\varnothing 2 – 6 μm), randomly dispersed, hard, titanium carbonitride particles dominated the friction and wear behaviour of a grey cast iron disc (also noted later in reference 151). Ti may be added to cast irons for several reasons, these being to promote undercooling and degassing while simultaneously increasing the amount of free ferrite observed in the matrix. Figure 30, which is consistent for some but not all friction linings, shows that, for a given concentration of titanium carbonitride particles, expressed analogously in terms of mass percent concentration, a critical transformation point exists between high friction, high rotor wear and high stator wear and low friction, low rotor wear and low stator wear. The exact position of this critical transformation point may vary with friction partner and indeed, some linings show a more sigmoidal curve. Subsequent research (152) examining the ‘titanium’ effect demonstrated that friction materials could be formulated such that, due to the controlled thermochemical interactions of their ingredients, such effects could be negated. Figure

31 shows the extremely varied performance of five different friction materials in response to the titanium effect prior to the isolation and control of the appropriate 'tolerant' formulations. Despite such work, Ti is still alluded to as being the alloying addition exerting the single greatest individual influence on friction behaviour of pearlitic, grey cast irons (153). V and niobium alloying additions also form hard carbides upon alloying that have similar effects on tribological performance, V, in particular, proving equivalent both in its effect and the quantity addition to achieve that effect.

Besides the compositional artefacts already described, the fundamental functionality of rotors is ultimately defined more by the characteristics of the graphite structure (5.1.1.2.) and the pearlitic matrix (5.1.1.3.).

5.1.1.2. Microstructural Characterisation of the Graphite Structure

Graphite type, form, size and distribution (143, 154 – 155) can have a radical effect on the wear behaviour of grey cast irons (156), independent of associated mechanical properties. This comes as no surprise when considering the volumetric portion of the material occupied by the phase. The quantity of free graphite (specific gravity, $\rho = 2.25 \text{ g.cm}^{-3}$) present in the principally pearlitic matrix can be demonstrated to be of the order of 2.50 mass % (3.42 mass % (nominal C content) - 0.80 mass % (cementitic C in pearlite) - 0.12 mass % (in solid solution and in combination as carbides and carbonitrides). Given the specific density of iron as 7.86 g.cm^{-3} , the corresponding free graphite content in the cast iron approximates to about 8 volume percent. Plate 6 shows deep etched graphite flakes.

Free graphite imparts excellent machining and sliding wear properties. Graphite cavities provide for short chip removal while the graphite itself, a ubiquitous solid lubricant, confers outstanding wear resistance in dry sliding conditions. Grey cast irons containing very fine, undercooled graphite flakes, as opposed to large, well developed graphite flakes, give generally lower friction and wear in a dry sliding environment. It is therefore easier to ensure friction stability in the final friction pair by the promotion of smaller graphitic structures, the magnitude of these islands being intrinsically linked to the size of the

eutectic cells in which they solidify. The eutectic cell size of a grey cast iron is normally expressed in terms of the number of eutectic cells per unit area or *cell count*. In terms of mechanical properties, a high cell count is preferred and may be attained by increasing the cooling rate upon solidification (and hence the accompanied undercooling that increases the attendant risk of carbide formation) or by inoculation of the melt. A typically quoted specification for this characteristic in automotive disc brake rotors is that the number of eutectic colonies observed in the microstructure should exceed 400 in any given square centimetre (*cf.* 512 cells.cm⁻²)

Table 18:

Microstructural and constitutional analyses of 10 grey cast iron, disc brake rotors.

<i>Microstructural / constitutional analysis:</i>	<i>Mean (or mode):</i>	<i>Standard deviation:</i>	<i>σ (%):</i>	<i>Spec.:</i>
Graphite morphology	VII (lamellar (flake or plate) graphite (F.G.))	0	0	VII
Graphite distribution (and type)	A (uniform distribution, random orientation)	+ B, D, C	N / A	Mainly A
Flake graphite distribution (flakes / mm ²)	440	+/- 53	+/- 13	Not quoted
Flake graphite – mean aspect ratio	2.83	+/- 0.13	+/- 4.5	Not quoted
Flake graphite size (dimensionless)	4 – 5	0	0	3 – 5
Eutectic cell size (cell count.cm ⁻²)	512	+/- 36	+/- 7.0	> 400
Mean grain size, M.L.I. (mm)	1.30	+/- 0.19	+/- 14.6	Not quoted
Mean domain size, M.L.I. (μm)	14.6	+/- 0.9	+/- 6.0	Not quoted
Pearlite interlamellar spacing (nm)	194	+/- 30	+/- 15	Not quoted
Pearlite unresolvable @ x 100 (%)	100 %	0	0	not quoted
Pearlite unresolvable @ x 200 (%)	75 %	+/- 25 %	N / A	not quoted
Ferrite content (%)	1.4	+/- 1.4	+/- 100	< 5 %

The preferred lamellar or flake morphology of graphite tends to be regarded as the characteristic form of graphite although the true form is actually a spherical morphology. Lamellar graphite is however

promoted purely by the presence of impurities, (the restoration of spherical, fibrous graphite crystals being attained by small Mg additions before casting).

The nature of graphite dictates that the form developed during solidification remains essentially unchanged and that subsequent modification by the heating or cooling cycles encountered as a result of friction braking parameters and environmental considerations is negligible. Table 18 identifies the predominant graphite island morphology to be consistently lamellar (flake or plate, F.G.), known as graphite shape VII. Table 18 also shows the predominant lamellar graphite distribution to be uniform, exhibiting generally random orientation, known as type A. Other types are apparent although only in the near-surface ('skin') region (< 1.5 mm deep) where casting conditions are most unstable.

5.1.1.3. Microstructural Characterisation of the Matrix Material

A fine pearlitic matrix offers excellent sliding wear triboproperties while simultaneously providing adequate strength characteristics to meet the specified design criteria. Plate 7 shows electron micrographs of the finest pearlite structures evident in the microstructures of samples 1 – 10. Table 18 gives an indication of the efforts made to accurately characterise a pearlitic matrix in terms of all popular measures in contemporary use; statistics concerning pearlite interlamellar spacing, mean pearlite (or eutectoid) grain size, sub-grain size and the percentage of unresolvable lamellae at standard magnifications.

With respect to non-pearlitic matrix components, even in the worst case assessment, all of the free ferrite concentrations were observed to comply with the upper limit of 5 %. Although contributing to improvements in the thermal conductivity of the friction rotor, the presence of free ferrite is detrimental to both the tribological behaviour, mechanical properties and machinability of the component. For the majority of applications therefore, the free ferrite content is to be kept to a minimum. Thus, although nil free ferrite would be ideal for a rotor material specified as requiring a predominantly pearlitic matrix, specifications typically vary from a permissible maximum of 3 – 15 %. The presence of ferrite in a

pearlite-specified matrix results from an inadequate cooling rate from the eutectoid point although ferrite formation is generally most pronounced at the geometric extremities of this type of casting. However, the practical influence of up to 10 % free ferrite content on the basic mechanical properties of a principally pearlitic material are, at most, minimal. What is of importance is that an overall ferrite content of 30 % or greater (2) can contribute to unacceptable levels of manufactured D.T.V.

Summarising, the results of the various microstructural and constitutional analyses undertaken were deemed to satisfactorily characterise the disc brake rotor material and to demonstrate both acceptable values and uniformity from one component to another. All determined values conformed to typically quoted material specifications while simultaneously minimising the potential influence of those characteristics known to affect either manufactured or in-service D.T.V.

5.1.2. Mechanical Uniformity of Vertically Cast Rotors

The surface hardness variation across two, perpendicular, diametric sections of a rotor are shown in figure 32. Although generally uniform and structurally homogeneous, several basic observations and qualifications can be noted:

- At the 12 comparable zones of the four major elements examined, all maximum hardness deviations observed were less than 20 % (maximum to minimum) and 75 % of these were less than 8 %.
- Considering the maximum hardness deviations from the mean hardnesses at each of the 12 comparable zones, all of these were seen to be less than 10 % and 75 % of these were less than 5 %.
- Generally, the friction ring is hardest at its O.D., gradually softening towards its I.D. as would be expected from chilling effect variations in a casting of this type.

- The lower surface of the top-hat increases in hardness upon traversing radially inward from the thermally sheltered region to the location bore where, accordingly, any chilling effect would be expected to be most pronounced.
- The upper surface of the top-hat section is significantly harder at its extreme external and internal diameters than it is along a radius central to these extremities.
- In this case, a ferrostatic head of pressure is observed not to have been sufficiently active during vertical casting to cause a variation in the directional properties of the resultant casting.

Over the applicable range of hardness values encountered in grey cast iron, disc brake rotor manufacture, the Vickers number (H_V) is consistently five points higher than the Brinell number (HB) (157) although such simplified comparisons are rarely meaningful. HB is a measure that finds purposeful application in industry-wide quality control activities where it is desirable to average, or dilute the volumetric effects of free graphite (5.1.1.2.). Typical tolerances quoted for HB consistency over the friction ring of a brake disc state no variation > 20 Brinell hardness points, this typically being monitored at three points, 120° apart. As has been shown, components that readily comply with such a specification during manufacture (showing only 7 HB points variation) show a difference of 35 H_V points over the entire rotor surface when considered in detail. However, since such variations are evidently non-anisotropic and fall well within the hardness ranges of the modal phases present it can be deduced that vertical casting can produce brake disc rotors of a suitable structural homogeneity to be considered to have negligible orientation-related property variations or anomalies induced through the casting process.

5.1.3. Geometric Characterisation

Figure 33 shows the C.M.M. dimensional profile of both the upper and lower surfaces of the friction ring. The two profiles show very good dimensional correlation illustrating that the rotor has not changed in shape on cooling. The mean increase in rotor friction ring thickness after heat-treatment was 5.0 μm (\cong 2.5 μm per surface), which is not significantly greater than might be expected from the additional thicknesses of oxide films at 580°C (*cf.* figure 34) (158 – 159) although some linear relaxation of the matrix material might also have occurred.

Given the linear nature of any stress-relief transpiring, it was decided that no further destressing or weathering of the components was necessary, the potentially stressing processing steps involved in the casting process being unlikely to be linear in nature. (The rotor showed an as-machined axial S.R.O. of 20 μm which was typical of those discs utilised throughout the research programme. The D.T.V. was measured at just less than 10 μm , this point originating from an anomalous high-spot located at 60° on the outboard brake-face.) Based on these findings, it was assumed that the dimensional variability in the rotors on test on the D.T.V. evaluation rig, due to thermo-mechanically induced changes under equilibrium conditions of isothermal holding and cooling, were negligible and were therefore to be ignored. It would not be possible to apply such assumptions with respect to potentially non-steady-state and non-equilibrium thermal deflections such as disc coning (2.3.1.1.)

5.2. Characterisation of N.A.O. Friction Materials

It is well appreciated within the industry that the properties of powder-based friction materials are anisotropic and that the microstructures of these components may not generally be described as homogeneous. Much has been attempted to improve this situation although many of those processing techniques capable of introducing improved microstructural uniformity are deemed prohibitive on grounds of cost (e.g. electrostatic dispersion and alignment of individual constituents, microstructural

assembly of components, etc.). In attempting to characterise such materials metallographically, it is therefore important to realise that the results should be weighed against the repeatability and reproducibility of the material's functional or tribometric characteristics (160 – 162).

5.2.1. Abrasive Constituent Characterisation

Firstly, particle size analyses were commissioned in order to establish the range and proliferation of different sized particles (figure 35). The particle size descriptors for the alumina particulates can be seen to roughly equate to US grit sizes with the alumina 200 showing 90 % of all particles being smaller than 70 μm (wide spread). However, the zirconium silicate particulates were seen not to equate to the US grit size scales, the zirconium silicate 200 showing 90 % of all particles being smaller than 55 μm (wide spread) and the zirconium silicate 100 (nominally described as grade 'D') appearing smaller in all respects.

The differences between the two abrasive's grade 200 can be attributed to particle morphology. The zirconium silicates are pebble-like, i.e. smooth, elliptical spheres exhibiting aspect ratios close to unity (*cf.* sizing methodologies by sieving) whereas the alumina is coarse and angular displaying a much greater variation in aspect ratio enabling a 200 gauge sieve to let high aspect ratio particles through via their minimum cross-sections.

The alumina 800 is much more readily characterised since 80 % of all particles are shown to be within 4 and 14 μm mean grain diameter. However, 80 % of the zirconium silicate 100 show a much wider particle size range of 1 – 30 μm diameters.

Plate 8 shows secondary electron micrographs of some popular abrasive friction modifiers. The fused alumina pictured corresponds to a typical mean diameter of 8 – 10 μm or alumina 800. The calcined alumina is of the same size grade but was not included in the model pads AB 1 – 12. The zirconium silicate pictured corresponds to a typical mean diameter of 120 – 150 μm and is referred to in the model pads as zircon sand. Plate 9 shows two bright-field O.L. micrographs, one showing zircon sand particles

and the second showing the same variety of particle seated within the friction material matrix of pad AB 12.

5.2.2. Abrasive Constituent Distribution & Dispersion

The natures of certain abrasive friction modifiers used in the formulation of friction materials readily lend themselves to the assessment of particle distribution surveys by O.L.M. Bright green chromia particles contrast starkly with the colours of virtually all other commonly used friction material constituents, while fused alumina is birefringent, i.e. exhibits two different refractive indexes, making it similarly distinctive. Zirconium silicate particles are generally visible in the form of large glassy pebbles. However, since the model pads could be formulated to avoid characteristic X-ray peaks of components coinciding with those of the abrasive, the distributions of these particles were assessed using thermographic-scale, elemental digimapping in the A.S.E.M.

Suitable areas were randomly selected from the prepared samples and magnifications were applied to suit the particle size being examined. The numbers of particles detected per digimap were then incorporated into a simple mathematical model (appendix 11.10.) to give a volume fraction of abrasive constituent, which could then be compared with the actual volume fraction (2.0 volume % in each case) to show the uniformity of the friction surface assessed. These results are shown in table 19.

Plate 10 shows digimaps of the Al distribution (i.e. effectively the alumina) at metallographically prepared surfaces of pads AB 1 – 3 and AB 7 – 9. Plate 11 shows the digimaps of the Zr distribution (i.e. effectively the zirconium silicate) at metallographically prepared surfaces of pads AB 4 – 6 and AB 10 – 12. By way of a control, each of the two abrasive-bearing materials were digimapped for the elemental constituents of the absent abrasive, i.e. those pads containing alumina abrasives were mapped for the presence of Zr-bearing compounds in order to check that those materials containing zirconium silicate only indicated that abrasive, not being corrupted by the presence of other Zr compounds, and vice-versa.

Table 19:

Particle distribution of abrasive friction modifiers within model materials AB 1 – 12.

Friction material:	Mean abrasive size, \varnothing (μm):	Particles per unit area (mm^2):	Equivalent vol. % through pad:
AB 1	35.8	24.8	3.33
AB 2	10	272.0	2.85
AB 3	8.8	353.6	2.87
AB 4	13.9	143.8	2.91
AB 5	23.3	47.6	2.71
AB 6	135	1.24	2.37
AB 7	35.8	21.3	2.86
AB 8	10	259.2	2.71
AB 9	8.8	309.6	2.51
AB 10	13.9	92.9	1.88
AB 11	23.3	34.3	1.95
AB 12	135	0.91	1.74

There would appear to be a slight but notable difference in the quantity of zirconium silicate abrasive observed in the two resin systems, the phenolic resin binder system showing a higher concentration than that of the system modified with nitrile rubber. A reduced, but similar variation is apparent in the alumina-bearing pads.

With respect to the correlation between the formulated and observed concentrations, the distributions are unexpectedly similar. Indeed, all of the concentrations observed could be manipulated to 2.0 % if the mean particle diameters were varied by -23 % / +8 %, i.e. all of the observations are accommodated by a 31 % mean particle size variation. The ultimate accuracy of these mathematical model assessments is restricted by the following errors:

- Real particles are not ideal spheres.
- The mean particle diameter does not take into account, or does simply not accurately represent actual size distributions or preferred orientations.

- Particles may be unevenly dispersed throughout the matrix.
- Particles, or clusters of particles, may be unevenly distributed throughout the matrix.
- Particle distribution at the surface may not be representative of the bulk material.

Of particular note is the quite disproportionate quantity of sub- 10 μm particles observed in the digimaps illustrating the alumina distribution in pads AB 1 and 7, i.e. alumina 200 grade. It is clear that these smaller particles are not represented in the original laboratory assessments of particle size distribution and their inclusion in the figures would have yielded volume proportions of $\approx 50\%$ alumina (which is clearly not the case). It is evident from the micrographs of fused alumina shown in plate 8 that accretions of smaller, sub-micron particles do adhere to the larger, nominal-sized grains, it being possible that these particles become detached during mixing in a way that may not be detected by particle size assessments. However, more likely is that such particles are caused by the partial fracture of larger particles during either friction material manufacture (in this case, on a pilot plant scale) or tribological contact (in this case, by metallographic preparation).

Although the figures presented in table 19 suggest better overall distribution than expected, the dispersion of these particles was not ideal with $> 50\%$ of all abrasive particles being in physical contact with a nearest neighbour.

5.3. Thermochemistry of Friction Material Constituents

The following tables qualitatively describe the detected thermochemical interactions of the friction material ingredients selected for assessment. Explanations, evidence and the potential tribological implications of those effects observed, along with more quantitative comment, follow each table.

Table 20:

The thermochemical interactions of a powder preform of commercial grade graphite (MNS 1).

<i>Base constituent:</i>	<i>S.T.P.:</i>	<i>200 °C:</i>	<i>400 °C:</i>	<i>600 °C:</i>	<i>800 °C:</i>
Graphite (C)	Graphite	Graphite	Graphite	Graphite	

Although graphite was detected within the pellet throughout the range of assessable temperatures, the strong clear signal, still unaffected at reaching 400°C, diminishes markedly on attaining 600°C where the pellet clearly loses some of its mass and much of its physical strength. Upon heat-treatment at 800°C, all practical strength was lost and the material remaining was unsuitable for repelletisation and analysis.

Plates 12 – 13 show clearly how, in the surface 0.100 mm of a mixed, but graphite-bearing pellet, graphite is distinctly present and evenly distributed at 400°C, but by 600°C the primary carbon signal has dropped off to background levels. By 800°C the mixed sample is correspondingly more friable. A similar illustration can be observed in figure 36 where samples of rotor material have been soaked at temperatures increasing by 100°C increments for 24 hours. From these X.R.D. data it can be seen that the graphite flakes present within the material are apparent within the detectable depth range of the technique only up to about 400°C, after which the peak is no longer distinguishable from background radiation.

According to the Ellingham-type diagram plotted in figure 22, pure graphite heated in air forms CO₂ at temperatures up to 720°C, after which CO becomes the preferred gaseous oxide. Shortly afterwards, the formation reaction for CO becomes so thermodynamically favourable that, in the continued presence of

O₂, the reaction strips carbon from the majority of carbonaceous compounds. From a tribological standpoint it is therefore clear that graphite only fulfils its principal function at relatively low temperatures but that its inherent propensity to yield at cohesive junctions minimises the flash temperatures to which it might be exposed.

Table 21:

The thermochemical interactions of a powder preform of commercial grade black iron oxide (MNS 2).

<i>Base constituent:</i>	<i>S.T.P.:</i>	<i>200 °C:</i>	<i>400 °C:</i>	<i>600 °C:</i>	<i>800 °C:</i>
Black iron oxide (Fe ₃ O ₄)	Fe ₃ O ₄	Fe ₃ O ₄ Fe ₂ O ₃	Fe ₂ O ₃ Fe ₃ O ₄	Fe ₂ O ₃ Fe ₃ O ₄	Fe ₃ O ₄

According to figure 22, the formation of Fe₃O₄ is consistently more energetically favourable than that of Fe₂O₃ throughout the temperature range being considered. However, the partial conversion of Fe₃O₄ to Fe₂O₃ is supported by the colour changes taking place within the specimens between 200°C and 600°C, which redden upon ever greater conversion to Fe₂O₃ but become matt black and slightly swollen on re-formation of Fe₃O₄.

The analogous process of oxidation in metals and alloys is similarly complex although certain simplifications can be made in reference to the ferrous portion of a grey cast iron surface. Iron exhibits numerous oxidation states and, as a result, forms a multi-layer stratified oxide in air (158, 163 – 165, etc.). These oxides, which are usually continuous and adherent up to 800°C, are arranged such that the one richest in oxygen sits at the gas-oxide interface and the one richest in iron sits at the metal-oxide interface:



The equilibrium phase diagram for the iron-oxygen system shows that, at atmospheric oxygen levels, magnetite should be the preferred oxide form up to 570°C, beyond which wustite predominates. However, in the majority of dry steel sliding scenarios oxidation follows those transitions described in figure 37, the predominant wear debris oxide varying from α -Fe₂O₃ to Fe₃O₄ to FeO with increasing sliding velocity or temperature. It is this order of transitions that are being observed in table 21. Oxide films generally continue to grow parabolically with increasing time and temperature by mechanisms of diffusion and / or interconnecting cavities in the film itself. However, beyond 900°C the relative thickness of the three iron oxide layers becomes independent of time and of temperature, remaining approximately 95 % Fe_{0.945}O, 4 % Fe₃O₄ and < 1 % Fe₂O₃. It would therefore follow that upon isothermal holding of a pellet at 1,000°C, FeO would predominate.

The key to interpreting the transitions described in table 21 rely on both the oxidation kinetics of iron oxides and the depth resolution of the X.R.D. process, i.e. 3 nm – 10 μ m (162). Thermodynamically speaking, since the oxides are not stoichiometric (appendix 11.7.), once formed, the conversion of Fe₃O₄ to Fe₂O₃ is favourable from 0 – 1,000°, e.g.



This reaction takes place on the immediate surface of a ferrous substrate or at any magnetite particle exposed to an oxidative environment. Fe₂O₃ is an n-type, i.e. metal-excess semiconductor that allows O²⁻ transfer from the gas-oxide interface toward the Fe₃O₄ layer. Thus, in the first instance Fe₃O₄ is converted to Fe₂O₃ on the most readily analysed surfaces. Fe₃O₄ is a mildly p-type semiconductor that allows Fe²⁺ and Fe³⁺ cationic diffusion via tetrahedral and octahedral vacancies and electron migration toward the Fe₂O₃ layer (although anionic diffusion is also possible through Fe₃O₄). With respect to the tribological characteristics of the various active oxide forms, Fe₃O₄ forms a relatively ductile and coherent film that exhibits a lower coefficient of friction than that of Fe₂O₃.

Fe_{0.945}O is a p-type, i.e. metal-deficit semiconductor containing vacant cation sites and allows Fe²⁺ and electron migration from the metal toward the Fe₃O₄ layer. Wustite, although essentially homogeneous, precludes stoichiometric composition oxides and therefore contains an unusually high concentration of

lattice defects which, with high temperature and continued oxidation migration, leads to increasing incoherence and void formation at the oxide-metal interface, which in turn leads to spalling and extremely high wear.

The extremely low solubility of O in solidified Fe dictates that internal oxidation as a result of frictional heating is unlikely. The turbulent nature of the velocity-accommodating region of the T.B.L. suggests that the development of stable subscales is also improbable as a result of tribological interaction. The occurrence of iron oxides (especially wustite) can be suppressed, either partially or completely by the presence of certain alloying additions, one of which is Cr. However, the concentrations required to have a significant suppressing effect are not normally found in grey irons.

Table 22:

The thermochemical interactions of a powder preform of commercial grade red iron oxide (MNS 3).

Base constituent:	S.T.P.:	200 °C:	400 °C:	600 °C:	800 °C:
Red iron oxide (Fe ₂ O ₃)	Fe ₂ O ₃	Fe ₃ O ₄			
	Graphite			Fe ₃ O ₄	

Red iron oxide was found to contain significant levels of graphite in its raw, commercial grade state (at least 5 % given the analytical sensitivity afforded by X.R.D.). The colour changes observed in the different pellets were consistent with the transformations detected in table 21.

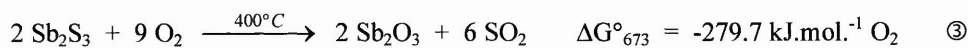
Table 23:

Thermochemical interactions of a powder preform of commercial grade antimony trisulphide (MNS 4).

Base constituent:	S.T.P.:	200 °C:	400 °C:	600 °C:	800 °C:
Antimony trisulphide (Sb ₂ S ₃)	Sb ₂ S ₃	Sb ₂ S ₃	Sb ₂ O ₃		

This smooth, dark grey pellet remained aesthetically unchanged until, at 400°C, it turned white with areas of mild discoloration. By 600°C the pellet was essentially liquefied leaving a brown residue out of which protruded fine, acicular, crystalline fibres, a decomposition product usually associated with the sublimation of volatile oxides. The alumina crucible also contained a fine, white, powdery residue. By 800°C there is evidence suggesting that some element of the brown residue puddle had reached its boiling point and only a small quantity of crystallites remain. No white powders were evident.

At 550°C, pure Sb₂S₃ melts. However, as we can see, by 400°C the sulphide, which is one of the least stable sulphides present at the tribointerface, has already decomposed to form a relatively stable, white, insoluble oxide:



The stability of this oxide is relatively short-lived and, upon increasing the temperature, a phase transformation occurs at 572°C and ultimate liquefaction at 656°C (which explains the absence of white powders at 800°C). However, it was observed that a significant proportion of the specimen had already melted by 600°C, this being due to the retention of a significant volume of unconverted Sb₂S₃.

The residues of the specimens treated at 600°C and 800°C were unsuitable for reconstitution although a candidate for the remaining solid matter is antimony pentoxide, a yellow, acidic, slightly soluble solid exhibiting similar, but inferior thermodynamic stability to that of antimony trioxide:

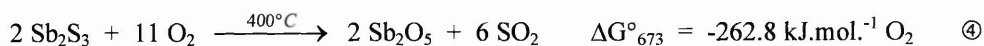


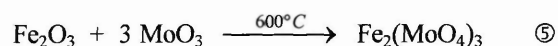
Table 24:

Thermochemical interactions of an equal mixture of red iron oxide & molybdenum disulphide (MNS 5).

<i>Base constituent:</i>	<i>S.T.P.:</i>	<i>200 °C:</i>	<i>400 °C:</i>	<i>600 °C:</i>	<i>800 °C:</i>
Red iron oxide (Fe ₂ O ₃)	Fe ₂ O ₃	Fe ₂ O ₃	Fe ₂ O ₃	Fe ₂ O ₃ Fe ₃ O ₄	Fe ₃ O ₄
Molybdenum disulphide (MoS ₂)	MoS ₂	MoS ₂	MoS ₂ MoO ₃	MoS ₂ MoO ₃	
Complex interaction		FeMoO ₃ FeMoO ₄	FeMoO ₃ FeMoO ₄	Fe ₂ (MoO ₄) ₃ FeMoO ₃ FeMoO ₄	

The critical nature of these compound's interactions prompted additional pellets to be treated at 550°C and 700°C. The original, untreated pellet was smooth and dark red, this condition persisting up to 550°C when the pellet became red with beige speckling. Closer inspection of the pellet treated at 400°C revealed that sub-surface (after mild abrasion), the interior of the pellet was paler than the exterior. By 600°C the pellet is both red and beige, smooth but embrittled. No change occurs at 700°C but by 800°C its appearance has radically altered; dark grey, matt, swollen and textured.

The individual thermochemical progress of both Fe₂O₃ and MoS₂ upon heating to increasingly higher temperatures in air mimicked precisely those indicated by the consideration of the constituents in isolation. However, in addition, the presence of several ferrous molybdate complexes were detected, one of which was also noted in earlier research (96):



In addition to this reaction, two other ferrous molybdates were encountered between 200°C and 600°C:



Since the chemical equations for the combination of these two molybdates can only be balanced when reacting with MoS₂, it is conceivable that these compounds are formed only in the presence of the sulphide. Since thermochemical data is available for FeMoO₄, we can theorise as to whether or not the reaction in the forward direction would continue to remain more energetically favourable than that of the reverse reaction at 600°C:



which shows the reaction to be energetically favourably at 600°C and beyond. This is of course no guarantee that the same thermodynamic stability could be implied to FeMoO₃ (in the absence of appropriate thermochemical data) but it is important to note that the compound would not demand so high an enthalpy of formation to demonstrate comparable stability given its reaction equilibria. Similarly, the preference for MoS₂ to react directly with the available oxygen cannot be ignored:



which suggests that not only is a considerable oxygen excess necessary for the observed interactions to proceed, it is likely that specific reactant proportions and physical proximity requirements would need to be satisfied for the two molybdate complexes to be detectable at the friction interface.

Although X.R.D. has only been applied qualitatively, it is notable that the formation of these complexes does not appear to have influenced the physical appearance of the test pellets beyond what might have been imagined in the absence of thermochemical interaction. That is with the exception of the beige speckling apparent at 550°C which suggests some form of thermochemical interaction as nascent, subliming (MoO₃) escapes from the pellet through micro-fine pores, simultaneously reacting through interconnecting vacancies to produce a discontinuous colour change in the exterior of the specimen as reaction ⑨ is initiated.

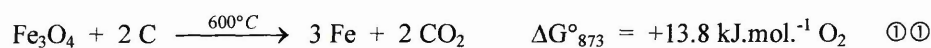
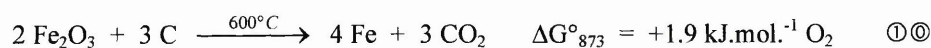
Table 25:

Thermochemical interactions of an equal mixture (by mass) of black iron oxide and graphite (MNS 6).

<i>Base constituent:</i>	<i>S.T.P.:</i>	<i>200 °C:</i>	<i>400 °C:</i>	<i>600 °C:</i>	<i>800 °C:</i>
Black iron oxide (Fe ₃ O ₄)	Fe ₃ O ₄	Fe ₂ O ₃ Fe ₃ O ₄	Fe ₂ O ₃ Fe ₃ O ₄	Fe ₂ O ₃ Fe ₃ O ₄	Fe ₃ O ₄
Graphite (C)	Graphite	Graphite	Graphite	Graphite	Graphite

At room temperature and at 200°C, the pellet is dark grey, predominantly matt in finish and speckled with glossy, coal-black, graphite particles. At 400°C the specimen takes on a reddish sheen due to the transformation to Fe₂O₃, a conversion advanced upon heating to 600°C, whereupon the specimen again becomes very powdery due to CO₂ evolution and requires reconstitution.

Again, graphite appeared to behave much as in isolation, its signal decaying significantly beyond 400°C. Upon its gradual gaseous decomposition, neither of the ferrous oxides appear to have been permanently reduced to metallic iron, direct thermodynamic assessments indicating even temporary reductions of such vigour are theoretically unfeasible below 600°:



By 800°C, however, the direct reduction of the apparently stable magnetite is quite feasible, albeit in an absence of most of the finite original graphite and the presence of an effectively infinite excess of oxygen facilitating the immediate reoxidation of the nascent metallic:



The partial conversion of Fe₃O₄ to Fe₂O₃ between 200°C and 600°C occurs by the same processes noted in the behaviour of Fe₃O₄ in isolation although the transition would be temporarily combated by graphitic reduction:

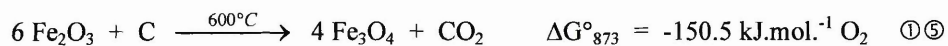
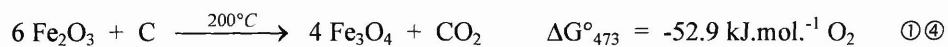


Table 26:

The thermochemical interactions of an equal mixture of black iron oxide and copper powder (MNS 7).

Base constituent:	S.T.P.:	200 °C:	400 °C:	600 °C:	800 °C:
Black iron oxide (Fe ₃ O ₄)	Fe ₃ O ₄	Fe ₂ O ₃ Fe ₃ O ₄	Fe ₂ O ₃ Fe ₃ O ₄	Fe ₃ O ₄ Fe ₂ O ₃	Fe ₃ O ₄
Copper powder (Cu)	Cu	Cu ₂ O Cu	CuO Cu	CuO Cu	CuO

Black and smooth at ambient temperatures, the pellet reddens slightly at 200°C and, upon closer inspection, is brown internally. By 600°C the pellet has become very dark grey, persisting to 800°C, by which time the pellet has swollen. Counter-productively, the changes in the physical appearance of the pellets with increasing temperature could be explained by the interactions of either the cuprous or ferrous species in isolation. However, since similar behaviour has already been encountered and described to reflect the interactions of a powder mix originally containing Fe₃O₄, attention here will be paid to elucidate the kinetic behaviour of copper oxides.

The kinetics concerned with the growth of oxide films have been much studied but are still not yet fully understood (158). The ion-transport phenomena involved in the development of porous, cracked or essentially discontinuous (i.e. non-protective) films are frequently very much more complicated than the growth of continuous films exhibiting essentially uniform thickness. It is known however, that when considering the oxidation of copper, the following reaction is initially tenable:



metallic copper + gaseous oxygen → cuprous oxide (insoluble red powder)

The reaction of metallic copper with excess oxygen to form CuO (copper II oxide) is also tenable but not when in competition with the formation of Cu₂O (copper I oxide) since its forward reaction is less energetic, and remains so to high temperatures (i.e. in excess of 1,000°C):



metallic copper + gaseous oxygen → cupric oxide (basic black solid)

However, the presence of the Cu₂O oxide is usually short-lived since once it has formed a continuous layer, even only a single monolayer thick, its formation ceases and is supplanted by:



Cupric oxide then persists as the preferred oxide up to its melting point (which is beyond the range of temperatures usually experienced during friction braking). Copper continues to be detected up to 600°C when the combined oxide thickness exceeds the depth resolution of the analysis technique.

Table 27:

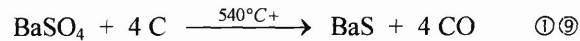
The thermochemical interactions of an equal mixture (by mass) of barytes and graphite (MNS 8).

Base constituent:	S.T.P.:	200 °C:	400 °C:	600 °C:	800 °C:
Barytes (BaSO ₄)	BaSO ₄				
Graphite (C)	Graphite	Graphite	Graphite	Graphite	Graphite

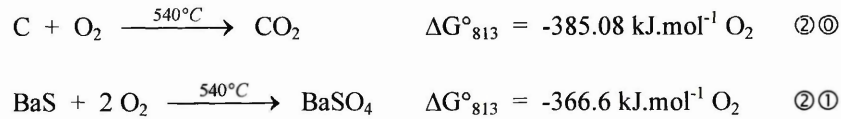
The physical appearance of this series of pellets was dark grey and smooth up to 400°C but by 600°C the specimen was matt and dirt-brown with pink tinges. This pellet was extremely fragile and collapsed

upon removal from the furnace, thus requiring reconstitution (and thereby, homogenisation) prior to analysis. At 800°C the pellet was seen to be in a similar physical condition, the exterior of the pellet being peach-coloured and the interior exhibiting dirt-brown regions indicating the retention of unoxidised graphite.

Given the colour changes involved it is conceivable that, in the presence of carbonaceous material and at temperatures in excess of 540°C, it becomes thermodynamically feasible for barytes to be reduced to its sulphide form:



However, given that the reaction is carbon-intensive and, as we have already observed, carbon is by this point already heavily involved in direct combination with an excess of oxygen, the nascent BaS readily converts back to BaSO₄ in the absence of further reducing agents.



Tribologically this might suggest that barytes is not as thermodynamically stable at the atmospherically-sheltered frictional interface as previously envisaged enabling the formation of formerly ‘energetically-unfeasible’ chemical complexes. The significance of potential reactions such as these should not be underestimated given the reliance of friction material manufacturers on ‘inert’ mineral fillers.

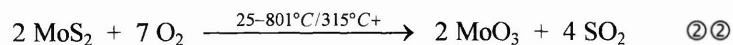
Table 28:

The thermochemical interactions of a powder preform of commercial molybdenum disulphide (MNS 9).

Base constituent:	S.T.P.:	200 °C:	400 °C:	600 °C:	800 °C:
Molybdenum disulphide (MoS ₂)	MoS ₂	MoS ₂	MoS ₂ MoO ₃	MoS ₂ MoO ₃	

As with the MNS 5 series of tests, the MoS₂ pellets were given additional heat-treatments subsequent to their original four. The control (unheated) specimen was dark grey in colour and glossy in appearance. Upon heating to 200°C, the specimen takes on a bluish sheen that is typical of the characteristic wear debris of the solid lubricant. If sufficiently large, wear particles generated and separated from a friction material within this temperature range are smeared, thus becoming integrated into the T.B.L. active at the frictional interface. Heating through 315°C sees a commencement in the conversion of MoS₂ to its primary oxidation product; MoO₃. This may be illustrated by a whitening of the specimen at 400°C, which becomes completely white but remains smooth in appearance upon arriving at 500°C. From 400°C upwards, the sulphide dominates the X.R.D. trace with only very limited MoO₃ perceptible. By 600°C, the pellet has taken on a pale yellow colouring, appears roughened and has experienced significant distortion. Of more interest is the crown of radially protruding acicular crystals, which indicate widespread MoO₃ sublimation. Reconstituting this sample reveals some fibrous constituent and identifies the residual presence of unaffected, bluish MoS₂ at the core of the pellet. Increasing the soak temperature to 650°C results in increased yellowness, friability and acicular appendages. Mass loss is apparent and the pellet has started interacting with the alumina crucible. By 700°C, only 10 % of the original pellet mass remains, this being yellow, heavily distorted and browned at its extremities. By 800°C, no specimen remains, the remaining matter likely simply to have melted (m.p. = 801°C) and to have been absorbed into the crucible, which is stained.

The overall transition scheme is a straightforward oxidation followed by sublimation.



This decomposition, which is included in figure 22 in its own right, is energetically feasible at all temperatures up to the liquefaction point of molybdenum trioxide at 801°C. Figures 22 and 23 show that in competition with other elements for sulphur or oxygen alone, MoS₂ and MoO₃ represent relatively stable compounds.

According to classical oxidation theory, the growth of oxide layers are quasi-linear in the early stages of the process but volatile oxides such as WO₃, and including MoO₃, should never form a continuous stable

layer. The detection of MoO₃ using X.R.D. is therefore, as perhaps with the earlier detection of Cu₂O, unexpected.

Table 29:

The thermochemical interactions of a powder preform of commercial grade barytes (MNS 10).

<i>Base constituent:</i>	<i>S.T.P.:</i>	<i>200 °C:</i>	<i>400 °C:</i>	<i>600 °C:</i>	<i>800 °C:</i>
Barytes (BaSO ₄)	BaSO ₄				

Commercial-grade barytes is a pale yellow mineral at room temperature (higher purity grades being white) and remained ostensibly unchanged at all temperatures. As mentioned in appendix 11.7., the theoretical approach applied for predicting thermochemical behaviour is inappropriate for comparing the stability of barytes with other mineral fillers at varying temperature. However, at S.T.P., BaSO₄ is thermodynamically more stable than the majority of friction material fillers including calcium carbonate, magnesia and magnetite.

It is crucially important that barytes remains stable at the frictional surface interface, but as has already been discussed following table 27, this may well not be the case. Similarly, further concerns are raised since another of barytes' primary decomposition products; BaO, is an effective lubricious oxide and readily capable of introducing fade phenomena at temperatures up to 800°C. Fortunately in this case, even in the reducing presence of graphite, the decomposition of BaSO₄ to BaO appears energetically impossible up to 1,192°C:

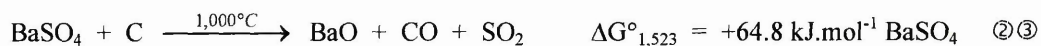


Table 30:

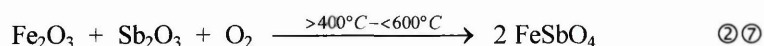
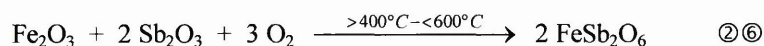
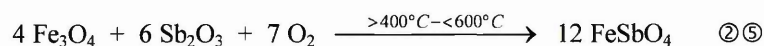
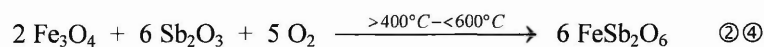
Thermochemical interactions of an equal mixture of black iron oxide & antimony trisulphide (MNS 11).

Base constituent:	S.T.P.:	200 °C:	400 °C:	600 °C:	800 °C:
Black iron oxide (Fe ₃ O ₄)	Fe ₃ O ₄	Fe ₃ O ₄ Fe ₂ O ₃	Fe ₃ O ₄ Fe ₂ O ₃	Fe ₃ O ₄ Fe ₂ O ₃	Fe ₃ O ₄
Antimony trisulphide (Sb ₂ S ₃)	Sb ₂ S ₃	Sb ₂ S ₃	Sb ₂ O ₃	FeSb ₂ O ₆ FeSbO ₄ Sb ₂ O ₄	FeSbO ₄ FeSb ₂ O ₆

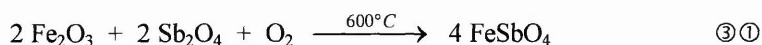
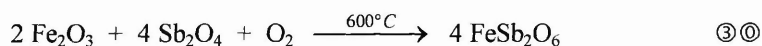
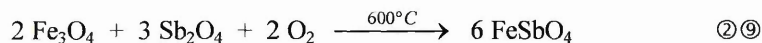
The pellet appeared black and smooth up to 200°C. At 400°C the pellet has 'greyed' a little and at 600°C there is some dark red / brown surface staining due to the melting of retained antimonides. By 800°C the sample is heavily swollen and distorted, typical now of the regeneration of magnetite from previously nascent hematite. Its colour is generally dark grey, as would be expected from the presence of Fe₃O₄ but also exhibits a lustrous avocado and beige hue, which strengthens the arguments for the presence of adventitious complex oxides.

The sulphurous content of the solid lubricant is lost irrevocably via the formation of gaseous SO₂ since the affinity of oxygen for available sulphur is far in excess of both that of Fe (FeS and FeS₂) and Sb.

The presence of the two ferrous antimonates and a subsequent antimonide, Sb₂O₄, can neither be confirmed nor dispelled by thermodynamic modelling due to the shortage of appropriate data for these compounds. However, if these complex interactions are truly tenable, which might be suggested by the attendant colour changes not observed in the absence of either one of the reactants, the corresponding reactions all require excess oxygen:



5.0. Results & Discussion



In the absence of appropriate thermochemical data and considering purely the predominance of reaction products and the availability and surface proximity of the potential reactants, the most tenable reaction scheme might suppose reaction ②⑦ to take place in preference to that of equation ②⑥ between 400° and 600°, and at 600° and beyond, reactions ②⑧ – ③① may occur albeit with either reaction ②⑧ or ③⑩ being preferred. It is also conceivable that FeSb₂O₆ forms directly from FeSbO₄.

Table 31:

The thermochemical interactions of an equal mixture of barytes, copper powder and graphite (MNS 12).

<i>Base constituent:</i>	<i>S.T.P.:</i>	<i>200 °C:</i>	<i>400 °C:</i>	<i>600 °C:</i>	<i>800 °C:</i>
Barytes (BaSO ₄)	BaSO ₄	BaSO ₄	BaSO ₄	BaSO ₄	BaSO ₄
Copper powder (Cu)	Cu	Cu ₂ O Cu	CuO	CuO	CuO
Graphite (C)	Graphite	Graphite	Graphite	Graphite	Graphite

The pellets used in this series of heat-treatments remained dark grey throughout but their textures started smooth, became partially matt at 400°C as CuO is detected, predominantly matt at 600°C as a significant proportion of the graphite is lost and is finally wholly matt by 800°C. It therefore appears that the various reaction schemes duplicate those observations of earlier powder combinations.

Table 32:

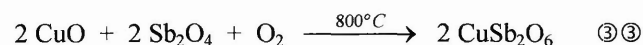
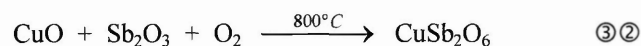
The thermochemical interactions of an equal mixture (by mass) of barytes, copper powder and antimony trisulphide (MNS 13).

Base constituent:	200 °C:	400 °C:	600 °C:	800 °C:
Barytes (BaSO ₄)	BaSO ₄	BaSO ₄	BaSO ₄	BaSO ₄
Copper powder (Cu)	Cu	CuO	CuO	CuO
Antimony trisulphide (Sb ₂ S ₃)	Sb ₂ S ₃	Not perceptible	Possibly Sb ₂ O ₄	CuSb ₂ O ₆
Nature of original constituents confirmed	Sb ₂ S ₃ resembles synthetic form	BaSO ₄ dominates spectrum	Strong CuO presence	Reaction products clearly perceptible

The clarity of the barytes peaks throughout the temperature range examined, but especially at 800°C, reinforces its thermodynamic stability but only in the absence of an aggressive reducing agent.

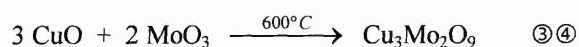
The earlier reactions of Fe₃O₄ and Cu powder showed no permanent interaction between the two constituents but did show the presence of Cu₂O and detectable Cu at 200°C, complete Cu₂O conversion to CuO at 400°C (still registering some shrouded metallic Cu), and full conversion of the detectable surface region to CuO by 800°C. A similar story is told when Cu powder is heated in combination with both graphite and barytes (table 31).

By replacing the graphite in table 31 with Sb₂S₃ in table 32, the temporary transition to Cu₂O ceases to be perceptible. What is significant is the clarity and predominance of the CuO signal beyond 400°C. However, although CuO (copper (II) oxide) dominates as the preferred oxidation product of metallic Cu at 800°C, Cu (II) readily forms complexes in the presence of appropriate ligands which is clearly indicated by the co-ordination and combination of oxidised copper (Cu²⁺) and an available antimonide:



Since thermodynamic data is again unavailable for either the copper antimonate complex or the Sb₂O₄ (which was not clearly the antimony oxide predominating) it is not possible to determine which of /

confirm whether all of these reactions take place. However, the presence of CuSb_2O_6 was clearly present within the X.R.D. trace. Furthermore, when the same powder mixture was heat-treated in 100°C steps on a rotor surface substrate (table 33), Sb_2O_3 was seen to form at 200°C , dominate as the stable oxide to some point beyond 300°C whereupon Sb_2O_4 is detectable and recurrent, although not strongly from 400°C up to 700°C whereupon, once again, CuSb_2O_6 appears. However, tables 35 – 36 show that the presence of MoS_2 (replacing Sb_2S_3) and its attendant oxide product have a potentially significant effect on the reactions of copper and its oxides showing the generation of Cu_2O briefly at 500°C and the generation of copper molybdates at $600 - 700^\circ\text{C}$, after which cupric oxide dominates.



Generally, cupric oxide would be expected to reduce to metallic copper in the presence of gaseous hydrogen or carbon monoxide, such as might be encountered during the decomposition of organic constituents, or by physical combination with carbon (166). This may well explain why, in the graphite-bearing mixture, the appearance of CuO synchronises with the disappearance of non-graphitic carbon between $700 - 800^\circ\text{C}$. CuO is stable up to its melting point whereas Cu_2O is generally oxidised to CuO upon heating in air.

Relating such thermochemical interactions directly to tribological performance is by no means straightforward. CuO and a specific variety of copper molybdate (CuMoO_4) are however used as friction modifying particulates in high temperature friction braking applications, especially aircraft braking (167), their role being seen as to provide high temperature lubrication.

Table 33 shows the effect on the temperature-dependent interactions of the same mixture of friction material constituents when introduced into contact with a grey cast iron, rotor material substrate. As has been stated, the Cu antimonate complexes are again detected, as are the Fe antimonate complexes identified in table 30.

Table 33:

The thermochemical interactions of an equal mixture (by mass) of barytes, copper powder and antimony trisulphide (MNS 13), heated on a cast iron substrate.

Base constituents:	S.T.P.:	100 °C:	200 °C:	300 °C:	400 °C:	500 °C:	600 °C:	700 °C:	800 °C:	900 °C:	1,000 °C:
Copper powder (Cu)	Cu	Cu	Cu	CuO	CuO	CuO	CuO CuSb ₂ O ₆	CuO	CuO CuSb ₂ O ₆	CuO CuSb ₂ O ₆	CuO
Antimony trisulphide (Sb ₂ S ₃)	Sb ₂ S ₃	Sb ₂ S ₃	Sb ₂ S ₃	Sb ₂ O ₃	Sb ₂ O ₃	Sb ₂ O ₄ FeSb ₂ O ₆	FeSb ₂ O ₆ FeSbO ₄ Sb ₂ O ₄ CuSb ₂ O ₆	FeSbO ₄ FeSb ₂ O ₆ Sb ₂ O ₄	FeSbO ₄ FeSb ₂ O ₆ CuSb ₂ O ₆	BaSb ₂ O ₆ FeSbO ₄ FeSb ₂ O ₆ CuSb ₂ O ₆	BaSb ₂ O ₆
Barytes (BaSO ₄)	BaSO ₄	BaSO ₄	BaSO ₄ BaFeO ₃	BaSO ₄	BaSb ₂ O ₆ BaSO ₄	BaSb ₂ O ₆ BaSO ₄					
Trace compounds									SiO ₂	SiO ₂	SiO ₂

Table 34:

The thermochemical interactions of an equal mixture (by mass) of barytes, copper powder, graphite and black iron oxide (MFM 1).

Base constituents:	S.T.P.:	100 °C:	200 °C:	300 °C:	400 °C:	500 °C:	600 °C:	700 °C:	800 °C:	900 °C:	1,000 °C:
Barytes (BaSO ₄)	BaSO ₄	BaSO ₄	BaSO ₄	BaSO ₄	BaSO ₄	BaSO ₄	BaSO ₄	BaSO ₄	BaSO ₄	BaSO ₄	BaSO ₄
Copper powder (Cu)	Cu	Cu Cu ₂ O	Cu Cu ₂ O	Cu Cu ₂ O	CuO Cu	CuO	CuO	CuO	CuO	CuO	CuO
Graphite (C)	Graphite	Graphite	Graphite	Graphite	Graphite	Graphite	Graphite	Graphite	Graphite	Graphite	Graphite
Black iron oxide (Fe ₃ O ₄)	Fe ₃ O ₄ Fe ₂ O ₃	Fe ₃ O ₄ Fe ₂ O ₃	Fe ₃ O ₄ Fe ₂ O ₃	Fe ₂ O ₃ Fe ₃ O ₄	Fe ₂ O ₃	Fe ₂ O ₃	Fe ₂ O ₃	Fe ₃ O ₄ Fe ₂ O ₃	Fe ₃ O ₄	FeO Fe ₃ O ₄	FeO

Table 35:

The thermochemical interactions of an equal mixture (by mass) of copper powder, graphite, molybdenum disulphide and black iron oxide (MFM 2).

Base constituents:	S.T.P.:	100 °C:	200 °C:	300 °C:	400 °C:	500 °C:	600 °C:	700 °C:	800 °C:	900 °C:	1,000 °C:
Copper powder (Cu)	Cu	Cu	Cu	Cu		Cu ₂ O	Cu ₃ Mo ₂ O ₉	Cu ₃ Mo ₂ O ₉ Cu ₂ MoO ₅	CuO	CuO	
Graphite (C)	Graphite	Graphite	Graphite	Graphite	Graphite	Graphite	Graphite	Graphite	Graphite	Graphite	Graphite
Molybdenum disulphide (MoS ₂)	MoS ₂	MoS ₂	MoS ₂	MoS ₂	MoS ₂ MoO ₃	MoS ₂ MoO ₃	Cu ₃ Mo ₂ O ₉	Cu ₃ Mo ₂ O ₉ Cu ₂ MoO ₅			
Black iron oxide (Fe ₃ O ₄)	Fe ₃ O ₄ Fe ₂ O ₃	Fe ₃ O ₄ Fe ₂ O ₃	Fe ₃ O ₄ Fe ₂ O ₃	Fe ₂ O ₃ Fe ₃ O ₄	Fe ₂ O ₃	Fe ₂ O ₃	Fe ₂ O ₃	Fe ₂ O ₃ Fe ₃ O ₄	Fe ₃ O ₄ Fe ₂ O ₃	FeO Fe ₃ O ₄	

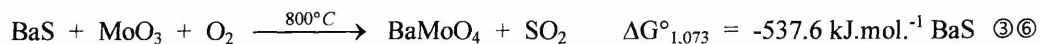
5.0. Results & Discussion

Table 36:

The thermochemical interactions of an equal mixture (by mass) of barytes, copper powder, graphite, molybdenum disulphide and black iron oxide (MFM 3).

Base constituents:	S.T.P.:	100 °C:	200 °C:	300 °C:	400 °C:	500 °C:	600 °C:	700 °C:	800 °C:	900 °C:	1,000 °C:
Barytes (BaSO ₄)	BaSO ₄	BaSO ₄	BaSO ₄	BaSO ₄	BaSO ₄	BaSO ₄	BaSO ₄	BaSO ₄	BaSO ₄ BaMoO ₄	BaSO ₄	BaSO ₄
Copper powder (Cu)	Cu	Cu	Cu	Cu		Cu ₂ O	Cu ₃ Mo ₂ O ₉	Cu ₃ Mo ₂ O ₉ Cu ₂ MoO ₅	CuO	CuO	
Graphite (C)	Graphite	Graphite	Graphite	Graphite	Graphite	Graphite	Graphite	Graphite	Graphite	Graphite	Graphite
Molybdenum disulphide (MoS ₂)	MoS ₂	MoS ₂	MoS ₂	MoS ₂	MoS ₂	MoS ₂ MoO ₃	Cu ₃ Mo ₂ O ₉	Cu ₃ Mo ₂ O ₉ Cu ₂ MoO ₅	BaMoO ₄		
Black iron oxide (Fe ₃ O ₄)	Fe ₃ O ₄				Fe ₂ O ₃	Fe ₂ O ₃	Fe ₂ O ₃	Fe ₂ O ₃ Fe ₃ O ₄	Fe ₃ O ₄ Fe ₂ O ₃	FeO Fe ₃ O ₄	

Tables 34 – 36 show the detected thermochemical interactions of the three MFM combinations that were formulated to observe the effects of five constituents known to play a significant role at the friction interface. In general, the same reactions are encountered as in simpler mixtures – tables 35 – 36 see the detectable conversion of MoS₂ to MoO₃ within the range 400 – 500°C and the formation of copper molybdates coincide with the temperature where MoO₃ starts visibly sublimating (table 28). One exception is the appearance of a barium molybdate; BaMoO₄, at 800°C (table 36).



As the number of elemental constituents under consideration increases, so does the difficulty with which individual reaction products can be identified using X.R.D. since its analytical sensitivity (> 5 % of the total interaction volume) hinders the technique's ability to conclusively identify minor crystal phases. Restriction files must be generated so as to limit interpretation to those elements that are, or are likely to be present. Polycrystalline metals tend to be easier to isolate and identify due to their relatively small number of interatomic lattice spacings but such materials rarely persist unaltered when considering those friction material derivatives potentially active within the T.B.L.

Figure 38 shows the X.R.D. traces generated in analysing four of these commercial grade materials; MoS₂, Sb₂S₃, barytes and vermiculite. Upon traversing through 2θ angles of 15 – 70°, these compounds exhibit 16, 29, 26 and 32 characteristic interatomic lattice spacings, respectively. Similarly, Kevlar exhibits 37 such d-values over the same range and FeO, 34. The superimposition of these numerous peaks in multi-component specimens demanded that transparencies be prepared of many raw material and heat-treated standard X.R.D. traces to corroborate or refute the software-based interpretation. These transparencies could then be used as overlays for the X.R.D. traces generated.

In practice, the MFM samples, containing between 6 and 8 elemental constituents, tended to represent the limit in applying X.R.D. successfully. However, despite operating at a limit of the technique, these complex analyses yielded important and significant thermochemical information not apparent from earlier, simpler combinations. (No results are presented of the unpolymerised dry mix samples since it was difficult to confirm the presence of original ingredients.)

Copper molybdates are detected between 600 and 700°C, in preference to those of iron, although it should not be assumed that the generation of these copper complexes suppresses similar reactions with iron since kinetic effects may also be involved. At those temperatures necessary to permit the formation of these molybdates, it is unclear as to whether the potentially lubricious copper complexes would be preferred by the friction material designer given the alleged abrasive properties of $\text{Fe}_2(\text{MoO}_4)_3$ (relative to the functional behaviour of its origin compounds). Although it is generally understood that the dynamic coefficient of friction and wear rate are not interrelated, from an O.B.W. stand-point, it must be assumed that lubricious properties would be preferred, assisted in this respect as CuO clearly dominates at 800°C and beyond.

Ferrous antimonates form between 500 and 900°C, in preference to, but in combination with those of copper that form between 600 and 900°C, although the same qualifying remarks apply as to the various molybdate complexes.

BaSb_2O_4 is detected at temperatures beyond 800°C (i.e. at temperatures greater than those considered with the simpler mixtures) and in greater abundance than all of those antimonates identified to date, i.e. FeSbO_4 , FeSb_2O_6 and CuSb_2O_6 .

One salient feature of these, more complex combinations not yet alluded to was the increasing ease with which Cu and its compounds became identified with increasing temperature, an effect that shall be examined more closely next.

5.4. Kinetics of Friction Material Constituents

By extending some of the thermodynamic characterisations just reviewed, the analysis of certain heat-treated pellets yielded significant variations in the distribution of friction material constituents and their reaction products with temperature. One phenomenon in particular was the migration of Cu and / or its oxides to oxygen-rich surfaces. First identified in the MFM 3 series of samples, it was noted using differing excitation voltages within the A.S.E.M. (and hence, correspondingly differing interaction

volumes) that pellets generated at 400 – 800°C appeared to register a disproportionately high Cu signal at the surface and were correspondingly denuded in Mo-based species.

Figure 39 shows the X-ray spectra collected from the surface of the MFM 1 pelletised samples; ‘control’ and heat-treated at 200°C, 400°C, 600°C and 800°C. The two columns of spectra show data collected at the same area (and magnification) but excited by two different electron beam accelerating voltages.

Carbon produces very low-energy, i.e. easily absorbed X-rays, and is thus best suited to low incident operating energies that limit electron-beam penetration leading to the production of X-rays nearer to the specimen surface. The 10 kV spectra show a significant contribution from allotropic graphite (the principal source of the carbon peak) up to 400°C, which falls dramatically (by circa 70 %) upon heating between 400°C and 600°C, and drops-off completely upon increasing the temperature to 800°C. Elemental oxygen, naturally detected only in combination with other elements, is another low-energy K α X-ray emitter. The 10 kV spectra show a slight increase in the oxygen peak in response to the oxidation of Cu but it is not necessary to rely wholly on this data to demonstrate that the Cu has been oxidised.

The elemental constituents of BaSO₄ (and associated CaF₂), Fe₃O₄ (and its other oxide products), vermiculite and Cu all seem reasonably stable, their intensity increasing at some point after 400°C in response to the C peak decay. These analyses were conducted employing an accelerating voltage of 25 kV so as to allow the monitoring of higher energy peaks.

Figure 40 shows the X-ray spectra collected from the surface of the MFM 2 pellets, the format and scale of the sample series being virtually identical to that of MFM 1, with the exception that heat-treatment at 800°C rendered the sample too friable for subsequent handling or analysis.

In some respects similar to the MFM 1 series, C falls dramatically upon heating, but at an earlier stage, i.e. between 200°C and 400°C. The coincident primary characteristic X-ray peaks of Mo and S are prodigious and clearly dominant up to 200°C, probably suggesting that the constituent was extruded to the immediate surface during pelletisation. However, this situation is reversed above 200°C as the MoS₂ oxidises, with the emission of gaseous SO₂, to MoO₃, the nascent oxide essentially subliming. In contrast, upon increasing the temperature from 200°C, Cu peaks proliferate dramatically; these associated with a notable increase in the oxygen peak. Similarly, from the point at which Cu begins to

predominate, the Fe peaks deriving from the Fe_3O_4 become significantly depressed in the 25 kV spectra and non-existent in the 10 kV column.

Figure 41 shows the X-ray spectra collected from the surface of the MFM 3 pellets, the format and scale of the sample series being identical to that of MFM 1.

It can be seen that the behaviour and interaction of the constituents, as described by variations in the X-ray spectra, are virtually identical to those observed in the MFM 2 samples with the exception that since the MFM 3 sample generated at 800°C survived to the analysis stage, it is clear that the copper oxide coating persists. When considered simultaneously, both MFM 2 and MFM 3 show negligible Mo / S at 400°C, but at 600°C a notable, but not large peak has been restored. This would seem to suggest that upon furnace heating and isothermal holding at 400°C, the anticipated oxidation and sublimation takes place but upon isothermal treatment at 600°C, the elemental constituents survive in solid compounds long enough for stable, higher temperature complexes to form.

In order to better assess the dispersal and diffusional interactions of the friction material constituents involved, cross-sections of the MFM 3 pellets were prepared for digimapping, the pellets being carefully encapsulated in aluminium foil before being bisected and the exposed surface being polished using conventional metallographic procedures (alumina finishing papers being employed such that any entrapped particles would be readily distinguished from those constituents present at the porous surface). Thermographic digital elemental X-ray maps illustrating the diffusional redistribution of MFM 3 constituents at 400°C and 600°C are shown in plates 12 and 13, respectively. Although the exterior surface of the pellet is pictured at the top surface, the pellet was inclined at 45° during heat-treatment. All of the exposed surfaces were examined. Inspection of the untreated pellet showed a random distribution of discrete particles, as did the pellet treated at 200°C. However, the pellet heat-treated at 400°C, and to an even greater extent, that treated at 600°C, showed a distinct and essentially discrete Cu-rich surface skin. Confirmation of the migration of a Cu species, as opposed to say the gaseous reaction and escape of other constituents, was demonstrated by the virtual absence of all constituents other than oxygen at the Cu-rich film. Unfortunately, the 800°C pellet consistently proved too delicate to withstand sectioning and could not be studied.

It can be seen from the collection of 600°C digimaps that, rather than the surface of the pellet being denuded in Fe (deriving from the original Fe₃O₄), Ba (deriving from BaSO₄), Mo (from both MoS₂ and the products of its decomposition) and S (deriving from both BaSO₄ and retained MoS₂), Cu species have migrated to the surface. The uniform and undisturbed distribution of both Fe and Ba within the substrate indicate no diffusional activity on their part. Oxygen distribution shows merely that the mean oxygen content of the copper oxide (/ oxidised Cu) is less than that of the matrix, a case that would be true in the case of either stoichiometry (CuO) or less (Cu₂O, Cu₃Mo₂O₉, Cu₂MoO₅). Other features include the presence of Ca from commercial-grade barytes and the fact that there is a higher residual concentration of C present in the Al foil than remains within the pellet surface. The 400°C digimaps show that graphite is still present within the matrix although the thickness of the Cu-rich scale obviously accounts for the minimal C K α peak, the same being true of the coincident Mo / S.

Importantly, at 400°C, the distribution of Mo / S is much more coherent and is absent from the Cu-rich film. At 600°C, this same distribution is much more diffuse, as might be anticipated from the onset of MoO₃ sublimation, although this time there is clearly some Mo or S signal associated with the film. Returning to the relative affinities of those elements present for thermochemical recombination with S (figure 23), there is no reason to believe that S forms a constituent of the Cu-rich skin since gaseous SO₂ would escape instantaneously upon the oxidation of the solid lubricant. These observations wholly corroborate the observations made in evaluating the thermochemical interactions taking place suggesting the near surface presence of CuO and one or more copper molybdates.

Conventional wide scan *X-ray Photoelectron Spectroscopic* (X.P.S. – appendix 11.11.) surveys were collected from various surfaces of pellets of MFM 3 heat-treated at both 400°C and 600°C. Appropriate narrow scan analyses were also considered to further elucidate the situation at the pellet surfaces. Figure 42 shows narrow scan data of the Mo 3d and S 2p peaks accumulated at three different MFM 3 surfaces. At 400°C, the Signal-to-Noise (*S / N*) ratios of both Mo and S are relatively poor:

$$S / N = \sqrt{\frac{S + B}{F}} \quad \textcircled{3} \textcircled{7} \quad \text{and,} \quad F = \frac{(S / B + 1)(S / B + 2)}{(S / B)^2} \quad \textcircled{3} \textcircled{8}$$

where S = height of a peak above background (intensity, arbitrary but consistent units).

B = background level at 7 eV higher kinetic energy than at which S was measured (intensity).

F = an intensity factor (effectively dimensionless).

A simple review of the relative peak heights (table 37) provides considerable information about the surfaces analysed. At 400°C, peaks are low, of a similar order of S/N , suggesting the trace presence of retained MoS₂. By 600°C, however, the two peaks lose this common proportionality when analysed from the top surface of the specimen suggesting that MoO₃ has formed but has been reincorporated into the mesostructure in a disproportionate abundance to S (which by now exhibits an S/N only just greater than that of average S 2p background-to-background).

Table 37:

Surface-to-Noise (S/N) ratios for the Mo 3d and S 2p peaks accumulated from various surface sections of MFM 3 specimens.

Peak:	S	B	F	S/N:
Molybdenum (MFM 3 @ 400°C)	1392	1314	5.6	22.0
Sulphur (MFM 3 @ 400°C)	1410	1255	5.3	22.5
Molybdenum (MFM 3 @ 600°C - upper surface)	1460	1070	4.3	24.3
Sulphur (MFM 3 @ 600°C - upper surface)	1122	1045	5.5	19.8
Molybdenum (MFM 3 @ 600°C - lower surface)	1410	1018	4.2	24.0
Sulphur (MFM 3 @ 600°C - lower surface)	1820	900	3.0	30.2
Mean Mo 3d background	1134	1134	6.0	19.4
Mean S 2p background	1067	1067	6.0	18.9

This again points to the formation of a Cu complex and was repeatedly indicated during thermodynamic evaluations of the system. The lower surface of the same sample again suggests the retention of significant quantities of MoS₂ which, albeit different from the sweep of the upper surface, is likely to

have experienced some liquefaction in response to both the soak temperature and exothermic reactions (*cf.* table 28 and the reactions of MNS 9). Its proximity within the specimen is therefore attributed to gravitational rather than migrational effects.

Returning our attention to the interactions of Cu, figure 43 shows narrow scan data of the Cu 2p and Cu LMM peaks. Despite not inconsiderable specimen charging, the strong presence of the shake-up satellites in the Cu 2p spectrum, together with the location of the Cu LMM Auger peak indicated that Cu was present in the form of CuO and likely a copper molybdate of a variety identified earlier. Both of the copper molybdates identified earlier involved the complex interaction of Cu^{2+} , a relatively common phenomenon in an excess of copper (II) oxide. However, only two signals could be deconvoluted from the peak seen between 940 eV and 950 eV, these being Cu 1 at 944.0 eV (height = 92 %, area = 61 %) and Cu 2 at 946.5 eV (height = 60 %, area = 39 %), *Full-Width, Half-Maximum* (F.W.H.M.) being 2.47. The author was not able to isolate the individual complex involved.

G.D.O.E.S. (appendix 11.3.) depth profiling was also applied to the pellets up to 400°C in order to quantify the elemental variation in surface constitution. G.D.O.E.S. depth profiles showing the variation in the relative concentration of Cu-rich species are shown in figure 44. The salient features of these profiles are that firstly, the surface region of the unheated specimen is actually denuded in Cu, this being due in the main to the near-surface extrusion of more plastic constituents (this having been seen to be true for graphite, for example). Secondly, migration can be seen to have partially commenced at 200°C although the absolute surface concentration appears to drop sharply, and thirdly, the uniformity of the concentration curves toward the bulk of the specimen suggests isotropic distribution of species but also some local stratification behaviour within the near-surface (< 1 μm) layers (at both 200 and 400°C). The influence of the inherently imperfect surface geometry of the specimens analysed was deemed sufficient to consider the definitive interpretation of this near surface stratification imprudent.

Although it is not necessarily correct to assume that such ion-transport mechanisms will automatically take place within the F.H.A.L. of a friction material (given the differences between the friction couple environment and the heavily oxidising atmosphere of a muffle furnace), the phenomenon described might well compliment other mechanisms by which the uppermost layers of the friction material surface become enriched in the inorganic, and in particular, metallic species present in the pad bulk (appendix

11.1.). Also important to note is that the phenomenon was not observed in MFM 1, possibly in the absence of a suitable carrier, namely a solid lubricant acting in such a way as to significantly improve pellet density and intergranular contact area between particles.

Scope exists for considerable further work in this area including investigations incorporating more refined atmospheric control, the replacement of MoS₂ with alternative transport media, e.g. Sb₂S₃, and the replacement of Cu powder with zinc chips, Zn having been observed to occupy the uppermost layers of the F.H.A.L. by a disproportionately high level relative to, say, metallic iron constituents of the friction material bulk (118).

As was described in section 4.3., several of the powder mixtures featured in table 8 were sprinkled onto grey cast iron substrates prior to their heat-treatment in order to assess their thermo-chemical interactions with the countersurface. As a supplement to the study it was decided to examine whether or not the presence of these materials exerted any influence on the oxidation characteristics of either the base grey cast iron or surface-impinging graphite flakes.

Samples of friction ring grey cast iron were heat-treated at 200 – 1,000°C, in steps of 100°C, for a duration of 24 hours. Upon cooling, the samples were sectioned to reveal a cross-section of the oxidised surface generated at each temperature. The mean oxide film thickness was evaluated by averaging ten thicknesses measured at 1 mm intervals. The procedure was then repeated with the surface of each sample dusted with a 0.5 mm layer of powdered friction material constituents. Results (figure 34), show the effect of Cu powder alone, MNS 13 (Cu + Sb₂S₃), MFM 3 (Cu + MoS₂) and dry mixes; DM 24 / 3264 and DM 24 / 3353. The plot shows the variation in the mean total thickness of the oxide layers formed on the samples with increasing temperature. As would be expected, the level of oxidation in each case is parabolic and governed by an Arrhenius relationship (see 5.5.3.).

The presence of foreign species deriving from a friction material reservoir were observed not to exert an influence on the oxidation penetration of a pearlitic, grey cast iron rotor surface in the absence of mechanical perturbation via friction (which would have increased the effective *activities* (appendix 11.7.) and hence the interaction potential of the materials). Similarly, while measuring the thickness of oxide layers prepared from the various heat-treated specimens, attention was paid to examine whether

any of the powder mixtures influenced the degree to which surface-impinging and near-surface graphite flakes were oxidised. No evidence could be found to suggest that their oxidation was either accelerated or exacerbated by the presence of transfer materials.

5.5. Disc Thickness Variation Evaluation rig Testing

Tentative, pre-analysis inspections of the rotors run on the D.T.V. evaluation rig revealed significant variations in the appearance of the regions exposed to maximum and minimum L.I.P. generated on either side of the friction ring. These variations were more readily distinguished on earlier, i.e. non-preburnished, discs where the 'lower-to-zero' pressure contact zones were clearly seen to retain the original machining scroll. In later tests using preburnished rotors, the lower overall surface roughness facilitated greater overall coverage accompanied by seemingly less abrupt transitions in the appearance of the resulting T.B.L.

C.M.M.-assessed, D.T.V. generation in the earlier discs was perceived as being fairly high, this being due, at least in part, to the ready removal of machining mark crowns (alluded to in **2.3.2.4.**), this frequently being associated with accentuated friction material transfer making accurate interpretation difficult given the wide variety of adventitious phenomena being seen to operate. The variability encountered with these discs (D.T.V. test rotors nos. 2, 3, 4 and 5) ultimately proved more constructive in the refinement of the test rig and L.I.P. schedules by highlighting several mechanical difficulties, e.g. the gradual decay in contact pressure with increasing O.B.W. and the uneven contact pressures attained on alternate sides of the friction ring.

Table 38 shows the D.T.V. generated around concentric circles of the friction ring of each disc, the outer diameter considered being 5 mm from the disc O.D. Figures 45 – 56 show the actual thicknesses (and hence, the circumferential variation in that thickness) of all of the 12 rotors featured in table 38 (including a virgin, as-machined rotor for reference), for each of four diameters considered. (The scales of the ordinate axes are identical in each case for ease of comparison.)

Table 38:

The extent of D.T.V. on concentric circles of the solid friction ring of various test rotors.

<i>D.T.V. test rotor no.:</i>	<i>D.T.V. (μm) @ \varnothing 140 mm:</i>	<i>D.T.V. (μm) @ \varnothing 170 mm:</i>	<i>D.T.V. (μm) @ \varnothing 200 mm:</i>	<i>D.T.V. (μm) @ \varnothing 230 mm:</i>
Virgin	6	7	8	7
2	21	31	20	27
3	20	11	16	25
4	13	20	27	25
5	13	13	17	27
6	8	6	8	10
7	13	12	11	12
9	9	10	18	26
10	9	6	7	17
11	43	56	59	55
12	10	7	18	24
13	14	27	29	26

For the sake of ready interpretation, levels of D.T.V. of 10 μm or less should be considered benign, between 10 and 25 μm cold judder becomes increasingly possible but is still extremely sensitive to the relevant characteristics of the respective vehicle, and beyond 25 μm cold judder can be considered a probability (based on observations quoted in section 2.3.2.1.).

5.5.1. Tribological Characteristics of Burnished Rotors

Although not exposed to L.I.P. schedules, the inspection of D.T.V. test rotors nos. 6 and 7 provided the requisite foundation upon which to base the assessment of subsequent test rotors. In each case, the tribological environment encountered by both rotors resulted in the plastic deformation of matrix material over the 'heads' of previously surface-impinging graphite flakes and uniformly polished rotor surfaces (exemplified in plates 14 – 15); the degree of polishing being comparable to, say, a grade 240 grit preparation for material; N, and a slightly finer, perhaps grade 400 grit for material; S.

Neither rotor exhibited noteworthy D.T.V. (figures 50 – 51), thereby resembling an as-machined circumferential geometry. Material S effected greater rotor wear than material N where machining scrolls were still evident. Microstructural analysis, discussed later, revealed that only very small quantities of material had been transferred, or integrated into the surface layers in either case, although plate 16 shows the effect of accelerating voltage on the perception of T.B.L. thicknesses.

Disc 6 showed most topographically-elevated artefacts to be oxide-based but the very low intensity signals of C, Cu, Al, Sb, Cr and Mn made it impossible to definitively identify their chemical association. Sulphurous material was also detectable at the surface and although the friction material originally contained both MoS₂ and Sb₂S₃, no obvious correlation was apparent. One possible explanation is that the antimony from Sb₂S₃ has been displaced by the thermodynamically-favoured FeS. This supposition is supported by the fact that MoS₂ also forms a component on the countermember mated with rotor no. 7 but no discrete pattern of any sulphurous species is perceptible.

Rotor no. 7 shows a coherent distribution of siliceous matter which, upon inspection of a virgin, as-machined surface using the same techniques and operating conditions (plate 17), represents a signal from the underlying substrate rather than from supplementary (deposited or migrated) material. The areas denuded in Si can be seen to be masked directly by the Cu distribution, which effectively forms a negative image of that for Si.

In general however, a minimal quantity of material can be seen to have been transferred to the cast iron surface in either case and the X-ray spectra are quite similar, other than in those respects already mentioned.

With respect to the general form of wear to which both rotors have been exposed, during bedding-in (figures 50 – 51), the greatest rotor wear occurs not at the outer diameter considered but consistently at the diameter in from that (\varnothing 200 mm), i.e. approximately coincident with the rubbing radius where the stator presents its longest arc of tribocontact. This could be due to flexural and compressive effects in the pad and backing plate relative to the position of the load-applying pistons, higher interfacial temperatures due to increased shielding / insulation or tribocontact with the pad, or simply due to an increased contact period. It is likely that all of these explanations play a role to differing degrees.

Since both materials invoked maximum wear at a point other than at the O.D., i.e. at a radial coordinate where the excited *Brake Torque Variation* (B.T.V.) was likely to at a maximum, D.T.V. generation at this diameter was considered extensively.

5.5.2. Tribomechanical Interactions and D.T.V. Generation

In contrast to those observations of friction material interactions under the circumstances for which they were designed (i.e. braking, *cf.* burnishing procedures), D.T.V. test rotors nos. 9 – 13 all showed significant material transfer after exposure to differing L.I.P. cycles. Plate 18 shows the physical appearance of rotor nos. 10 – 13. It would be very difficult to say whether it were possible to differentiate between the physical characteristics of those discs rubbed against differing materials, but it is clearly reasonable to state that the majority of the surfaces exhibit pronounced banding, these bands varying in their appearance, essentially chromatically at this stage, across the friction ring.

However, although during burnishing both friction materials N and S generated maximum rotor wear at a point where the tribocontact parameter (**160**) was at its greatest, $\epsilon_{1(\max)}$, upon applying L.I.P. this ceased to always prove the case. Material N tends to induce minimum rotor thicknesses and maximum D.T.V. at the O.D. whereas material S continues to retain the maximum thickness variation at $\epsilon_{1(\max)}$. These observations highlight the importance of pad compressibility and backing plate flexure in the

stressed state, and pad rigidity and the rigidity of its supporting elements in the unapplied brake, as factors in accommodating load transfer.

Both N and S were observed to generate circumferential D.T.V., the overall extent of which was greater for the aggressive material; S. Perhaps more importantly, material N caused a more regular, sinusoidal variation whereas the variations induced by contact with material S were more abrupt. However, these thickness variations, and the plots describing them, fail to adequately describe the rotors' geometrical variations.

Figures 57 – 61 show the form variations of rotors 9 – 13, respectively. In each case the resultant form at both an inner (\varnothing 140 mm) and outer diameter (\varnothing 230 mm) was evaluated. The resultant profile, which shows a generally sinusoidal form due to both inherent runout and the fact that the C.M.M. was not programmed to compensate for axial S.R.O. relative to the datum face, is compared with an ideal friction ring geometry (of comparable alignment) to highlight the transformations affecting the discs. The direction of rotor rotation during testing was from 0 – 360° in each case, i.e. relative motion of the stator was from 360 – 0°.

Some difficulties arise in using form variations and superimposed, so-called 'ideal' friction ring geometries to evaluate the extent of simulated O.B.W. Discs that have retained significant proportions of their original circumferential profile are readily compared with the ideal circumferential profile. However, on discs that have encountered wear to such a degree that the original form may be considerably disfigured, e.g. 13, the level of wear described by the friction ring form variation must partially be considered conjecture.

A principal reason for needing to consider the form variation of a disc at the same time as its D.T.V. is to ensure that the level of D.T.V. attained is not due to disparities between the rubbing regimes encountered by each side of the disc. For example, if one face were to wear exactly as described in figure 6 and the opposite face not experience any O.B.W. due to severely imbalanced L.I.P. (as is generally the case on the vehicle (2.3.2.)), the rotor would eventually show extremely high D.T.V. (\approx original T.I.R.) although this would not reflect the friction material's potentially excellent capacity for rotor-truing. Another important reason is to highlight differences in the pattern of O.B.W. generated by varying pad formulations.

Figure 57 shows the form variation of D.T.V. test rotor no. 9 after L.I.P. cycling against pad material; N. The extent of the L.I.P. wear on the two faces is very different, suggesting a lack of precision in achieving equal contact regimes on either sides of the friction ring during testing. The regions where the rotor profile (black) overlaps that of the ideal geometry (white) show areas perceived as being heavily deposited to the naked eye.

Some deviant geometry is evident at the prow on the outboard friction face. Upon traversing radially across the friction ring, three descending peaks transform into two ascending peaks. Conversely, the inboard face shows the onset of intermittent wear at the innermost diameter and heavy, well-defined, disproportional wear at the O.D. (The effect of this region on the overall D.T.V. is clearly evident in figure 52.) It should be remembered that these profiles represent the dimensional characteristics of the dismounted, unshimmed disc and so it should not be assumed that the high pressure contact prow remains in tact. By raising the profile to the shimmed level of S.R.O. presented upon commencement of L.I.P. testing (figures 62 – 63) it can clearly be seen that wear is more pronounced directly prior to reaching the higher pressure contact prow at maximum S.R.O. During a single revolution, it can therefore be stated that as the friction material starts to exert increasing L.I.P., material is removed during the ascent of the contact prow up to a point close to the maximum pressure (pre-set at 40 N), this prow ascent being characterised by an abrasive, low deposition-oriented friction mode that essentially ends a short way after clearing the crest. Thereafter, the prow descent towards and including the minimum pressure zone appears to be characterised by a mildly adhesive, high deposition-oriented friction mode. It would therefore follow that the pad transfers material up to a point where the abrasive friction modifier is activated whereupon the interfacial temperature is increased sufficiently to reduce the coverage of transferred material and generate considerable, preferential wear. (The shimmed geometry also dispels concerns about the ‘deviant’ form of the outboard face described earlier.)

Figure 58 shows the variation in D.T.V. test rotor no. 10, again after L.I.P. cycling against pad material; N. Again, the convention of an overlapping, ideal rotor geometry is applied to indicate deposition. The figure provides further evidence of minimal form error at the I.D. and significant, diametric O.B.W. at the O.D.

Thick T.F. coverage characterises the lower pressure L.I.P. contact zones but this only persists for 60 – 90° beyond the minimum contact pressure trough. Maxima in friction ring thickness occur at 50 – 60° after the high pressure contact prow on the inboard face and at 75 – 105° after the high pressure prow on the outboard side. Generally, these maxima are simultaneously defined by the decay in the preferential wear effect experienced by one side and the onset of the same effect on the other. By referring again to figure 53, the minima in friction ring thickness occurs at 200 – 210°, approximately 15° prior to the maximum contact pressure area of the outboard face, and at 0°, approximately coincident to the maximum contact pressure peak of the inboard face.

Summarising, mildly abrasive friction material; N, starts to abrade the disc most on the approach to the higher pressure prow, i.e. slightly out-of-phase with the original runout geometry. As wear is allowed to continue, the prow becomes eroded away and is effectively ‘pushed’ against the direction of rotation.

One major anomaly distinguishes the wear patterns generated on D.T.V. test rotor no. 10 from those generated on no. 9. At the O.D., pictured in figure 58, the inboard friction face of rotor 10 shows significant wear after the contacting stator has passed the higher pressure crest, i.e. almost equal wear has occurred both on the ascent and descent of the pad over the prow. The inboard friction face of rotor 9, however, clearly only shows preferential wear on the ascent of the pad. Upon examining this area more closely using A.S.E.M., it was determined that it coincided with a transfer-free arc (plate 19) occupying the outer 12 – 13 mm of the friction ring. This highly polished surface clearly reveals the graphite flakes present at the surface, the degree to which they are exposed being similar to that due to the abrasive action of a very fine metallographic surface preparation (applying third-body abrasion with nominally \varnothing 1 μ m diamond grit (*cf.* plate 5)). This area is evidence of at least one temperature- / pressure- / speed-dependent threshold where the wear regime acting on the rotor surface alters dramatically. The appearance of this area is also markedly different from that of the bedded surface suggesting the existence of an additional tribological transition occurring under non-design-intent operating conditions.

Since out of discs 9 – 13, no. 10 was exposed to a lower level of axial S.R.O., but still to the overall mean pad load of 40 N, it is conceivable that when an L.I.P. load is introduced more evenly it becomes possible, upon passing the higher pressure crest, for the abrasive particles within the friction material

matrix to relax, protrude from their immediate surroundings to some point beyond the previously interacting matrix, and exert a purely abrasive wear component leading to the physical phenomenon described.

The concept that an abrasive friction component should arise out of increasing L.I.P. is an unconventional suggestion. More typically, it is envisaged that at very light normal pressures, abrasive particles protrude from the matrix exerting an essentially abrasive, high friction, high wearing effect. With increasing pressure it has been suggested that the tribological interactions of the matrix become more significant, the friction coefficient sinking to a stable level and optimum conditions for minimum wear arrived at. Following this to its natural conclusion, it is usually imagined that either decreasing the size of the abrasive particles, or reducing the stiffness of the friction material matrix serves to accelerate the progression to uniform friction behaviour (figure 64). However, comparing these tenets with the experimental observations of Jeacock (80, 2.3.2.2., figure 10) suggests that it is more likely that the dynamic friction level starts off below that of the equilibrium level at pressures less than 100 N and then rises unsteadily as a series of thermochemical and thermophysical tribomechanisms are gradually activated at the frictional interface. This is supported by simple mathematical models describing the individual contributions of adhesion and abrasion to the overall dynamic friction level of a friction pair comprising one harder and one softer metal (168), where $\mu_{\text{ABRASION}} > 0.10$ and $\mu_{\text{ADHESION}} \approx 0.2$. Since friction level and wear rate are not interrelated, it is likely that the yellow curve represents the true friction variation in figure 64 and that several high wearing mechanisms are active while μ is low.

D.T.V. test rotor no. 12, also coupled with material N, is complicated a little by the fact that the rotor was shimmed at a location displaced from that of the maximum inherent S.R.O. (figure 60) but exhibited the same metrological characteristics as its two predecessors. This was true both in terms of geometric variation and overall D.T.V. (figure 55, *cf.* figures 52 – 53) although no polishing descent wear was observed (*cf.* disc 10).

D.T.V. test rotors nos. 11 and 13, both of which were rubbed against aggressive friction material; S, both exhibited significant D.T.V., pictured in figures 54 and 56, and severely disfigured form variations (figures 59 and 61 (63)). In considering these figures collectively, the first important point to make is that although rotor 11 shows virtually double the D.T.V. of rotor 13, this should not be taken to suggest

that rotor 11 has been exposed to greater wear. Indeed, the shimmed profile of disc 13 (figure 63) clearly indicates that it has reached a far more advanced stage in the truing of the rotor. It can also be seen that the high levels of D.T.V. exhibited by rotor 11 are partially circumstantial in that the area of maximum thickness coincides with the fall-off in preferential wear on the outboard side of the disc and an area just prior to the onset of preferential wear on the inboard side. Another exacerbating factor is the dissimilar level of wear from one face of the disc to the other. The profile of disc 13 suggests that if the D.T.V. test schedule had been longer in duration, e.g. doubled to 160 hours, or were modified so as to include intermittent full braking applications, e.g. one every hour, the dimensional profile of rotor 11 would have appeared much more linear. Such hypotheses introduce the importance of characterising not only the D.T.V. generation-potential of a given friction material, but also the clean-up characteristics of that friction material, an issue not dealt with during this study.

Of the form variations shown, the inner rubbing radius of disc 13 (figure 63) shows the least D.T.V. at only 14 μm and certainly appears to have been axially planed. Taking a more holistic view, it is important to consider at this stage how much cold judder might a typical driver be expected to tolerate while waiting for the high levels of D.T.V. to be planed down to a minimum. A warranty claim that might, with time, have corrected itself remains a costly failing and detriment to the customer's perception of the product, be that of the car or of individual components. Similarly, differing rotor materials start to play a significant role in this context. Softer, less durable rotor materials, such as high carbon grades containing a minimum of hard-wearing constituents (such as titanium carbonitride or phosphide eutectic), coupled with aggressive pads materials are, for example, preferred in the German market where consumers prefer rapid-bedding friction couples. However, certain features of the results suggest that market preferences do not provide an ultimate solution. Even if the inboard face of test rotor 13 had been perfectly planed, the outboard face would retain 0.020 mm D.T.V. at the O.D. occurring between 120° (minimum) and 75° (maximum), i.e. over a period of 45° or 80 % of the pad width. More importantly, the area of minimum thickness evident between 120° and 150° is not coincident with the region of lowest L.I.P. rubbing but appears to have been 'over-eroded' at the higher L.I.P. region. The onset of this effect is also perceptible from the outboard face of rotor 11. This over-erosion is attributed to both the dynamic and temperature-dependence influences known to affect in-service, axial S.R.O.,

discussed at length in section 2.3.2.1. This behaviour is of paramount significance since it wholly castigates the aggressive friction material solution to the cold judder issue.

With respect to the levels of D.T.V. generated by materials N and S, figure 65 does much to define the differential wear behaviour of the two commercial N.A.O. friction materials. Upon traversing four rubbing radii, the levels of maximum D.T.V. generated by each material have been presented as a function of the S.R.O. perceived by the pads at each of these rubbing radii (these being shown as white lines illustrating O.D. S.R.O. values at 0.090 mm, 0.110 mm and 0.120 mm). Neither of the two materials show D.T.V. as being a proportional function of axial S.R.O. with varying rubbing radii, but a clear trend is apparent. Material N, represented by test rotors 9, 10 and 12 in various shades of blue, shows disproportionately lower D.T.V. generation with reduced rubbing radii. In exact contrast, material S, represented by test rotors 11 and 13 in various shades of red, shows disproportionately higher D.T.V. generation with reduced rubbing radii. (The fundamental tenet in appreciating this point is in remembering that the T.I.R. measured at any point on the friction ring increases tangentially with the radius considered.) The radial flatness of the friction surface may also be superimposed onto the tangential runout variation, dependent on caliper alignment, and thereby serve to exacerbate the impression of pressure variations from one side of the disc to the other. This highlights another significant importance of the bedding schedule, which gradually converts the radial flatness of the friction ring from a positive, potentially misaligned gradient (traversing outward), to a negative, potentially aligned gradient profile.

Therefore, when exposed to L.I.P. testing, aggressive material; S, has been shown to induce heavy, but relatively even wear across the centre of the friction ring. Milder material; N, only generates notable D.T.V. towards the outer diameter of the disc. This is very much in keeping with the formulation strategy applied to the two materials – the function of material S being to plane the geometry of the rotor true, and the function of material N being to minimise D.T.V. generation. However, in practice, both materials have failed to wholly accomplish their overall objectives with respect to the eradication of cold judder. Material S generates high rotor wear, large levels of D.T.V. and is capable of producing ‘over-eroded’ regions during extended off-brake running, and material N, while being kind to the rotor in the

majority of instances, encounters a transition with increasing rubbing radii that exacerbates its wear behaviour.

Certain aspects of these conclusions are more readily quantified while considering figures 66 – 67 which show the approximate maximum and minimum wear track profiles for both materials. It is clear how much more abrasive material S has been, and, that material N has been less sensitive to changes in rubbing radii than material S.

A notable difference in the form variations of rotors tested against material S, apart from the overall levels of wear, which in terms of volume of rotor material removed is considerably greater than that experienced against material N, is the fact that L.I.P. wear is also very considerable at the inner diameters. This characteristic results from the larger abrasive particulates found in material S; \varnothing 50 – 75 μm (*cf.* \varnothing 10 μm – table 9). Indeed, even assuming a perfectly rigid, inflexible pad in minute contact at the O.D., i.e. at maximum axial S.R.O., a \varnothing 50 μm abrasive particle protruding from the idealised friction material surface to its mid-point at a rubbing radius of 70 mm would be in simultaneous contact with the rotor surface. This would suggest that abrasive friction modifiers are both load-bearing and play a principal role in the generation of O.B.W.

5.5.3. Tribochemical Interactions and D.T.V. Generation

The virgin rotor surface (plate 17) shows many of the features discussed in detail in section 5.1.1.. Mn and S X-ray signals tally to show the distribution of MnS inclusions, concentrated regions of P show the dispersion of small lakes of ternary phosphide eutectic, and residual traces of Al indicate its inclusion as a melt deoxidant. Surface oxidation is minimal, oxygen concentrations tending to coincide with retained machining debris and similar extraneous artefacts. Si, the second major alloying addition to the Fe, is uniformly distributed, deviations reflecting the effect of surface topography on X-ray escape rather than constitutional inhomogeneity. C is, of course, highly concentrated in the form of graphite flakes, their true morphology being heavily disguised by the destructive influence of the turning process. The

machining grooves are clearly visible indicating a feed rate of around 0.30 mm per revolution during facing. The radial surface roughness (as shown in 3-D in plate 2) needs to be sufficiently low so as to avoid both the introduction of scrolling effects on the contacting stator and the accelerated generation of perceived D.T.V. In analysing test rotors 9 and 10, the machining marks were generally obliterated by the higher L.I.P. contact but were frequently still visible in lower pressure zones.

All of the surfaces examined were rich in oxygen relative to the bedded surfaces (5.5.1). Early experiences in attempting to accurately interpret varying levels and chemical forms of transferred materials showed that a thorough appreciation of the thermomechanical influences to which the various surfaces had been exposed was critical. Therefore, constant reference will be made throughout the following section to those observations reported previously (5.5.2).

Plates 20 and 21 show the higher and lower L.I.P. regions of the inboard surface of rotor no. 9. Although in the previous section, significant differences were noted between the levels of preferential wear generated on either side of rotor 9, the surfaces were surprisingly similar. Visually, the higher L.I.P. zones were described as having encountered low levels of material transfer, the opposite of the situation encountered by the lower L.I.P. zones.

The high L.I.P. zone is characterised by a relatively uniform dispersion of discrete islands of ferrous oxide. These islands are apparent in the backscattered electron image but not to the extent that they are in the O digimap. In general, however, friction material transfer is negligible; any Sb signal is indistinguishable above the level of background noise, and sulphurous or Mo-based species are indecipherable between the MnS inclusions. Ba is also virtually absent except in the form of small speckles occupying topographical recesses and cavities. The graphite flake structure is clear, pronounced and varies from that of the bedded appearance. Indeed, the graphite visibility is comparable with that of a \varnothing 1 μm , diamond-lapped surface (*cf.* plate 5) suggesting the action of a reasonably abrasive component to the wear, albeit a polishing rather than a ploughing or scoring wear mode.

The low L.I.P. surfaces show a more continuous, and thicker, O distribution. This is supported by the poorer graphite visibility. By comparing the S / Mo map with that of the Sb, it can be seen that Sb_2S_3 has dissociated to an oxide form, likely Sb_2O_3 according to the earlier studies. Cu-rich species are also attendant in very limited quantities but do not directly coalesce with either S or O. S represents an

anomaly from one side of the disc to the other being coincident with Sb on the outboard (less worn) side and dissociated from it on the inboard (more worn) surface. This is in keeping with previous observations which suggested that significantly greater wear had been experienced by the inboard face, albeit that these deposited regions hail from the low L.I.P. sections of the disc. The tribointerfacial breakdown of the solid lubricant may have been either a contributing factor to, but more likely an effect of, the higher wear regime encountered at the high L.I.P. zone of the inboard face. Also of interest is the delineative transfer of Cr from the stainless steel fibres present in the friction material. The Cr signal, although not being disparate from that of the oxygen (Cr_2O_3), was also clearly coincident with S and with the strings of deposited material apparent in the compositional micrograph shown in figure 21. (Although not considered experimentally as a potential thermochemical interaction, the formation of chromium sulphide (CrS) is not energetically favourable in this environment.) The graphite flake structure is almost imperceptible and more closely resembles that of the bedded surface than that of the higher L.I.P. zone.

The association of increased rotor wear with increased oxidative effects points strongly to the principal wear mechanism by which the countersurface is eroded during O.B.W. Although under static, non-friction conditions at temperatures below 500°C the oxide thickness of iron is very much less than $1\ \mu\text{m}$ (even with quite long incubation periods), mild wear tends to predominate since the oxide films are relatively coherent and strongly bonded. Surface oxidation occurs much more rapidly under dry sliding conditions than would be expected from static oxidation, especially at low temperature (table 39). Film thicknesses developed by thermal oxidation under static conditions may take periods $10^3 - 10^{10}$ longer than those developed by oxide growth during dynamic sliding. This rapid oxide growth may result from accelerated ionic diffusion rates in response to the greater abundance of voids, vacancies and dislocations inherent during mechanical perturbation, augmenting static oxidation mechanisms. Similarly, the scaling of iron is accelerated by the presence of graphite, especially at temperatures up to 500°C (169), a situation exacerbated by the fact that graphite may well be being supplied to the interface by both triboelements simultaneously. Nevertheless, all oxidation rates are governed by an Arrhenius relationship:

$$k_p = A \cdot \exp \frac{-Q}{R \cdot T} \quad \text{③③}$$

where k_p = parabolic rate constant for oxide film growth.

A = Arrhenius constant, or pre-exponential factor ($\text{kg}^2 \cdot \text{m}^{-4} \cdot \text{s}^{-1}$).

Q = activation energy, i.e. a function of the growth rate temperature dependence ($\text{J} \cdot \text{mol}^{-1}$).

R = gas constant (= $8.31441 \text{ J} \cdot \text{mol}^{-1} \cdot \text{K}^{-1}$).

T = absolute temperature (K).

Table 39:

Typical values of the Arrhenius constant, A , and activation energy, Q , for the oxidation of self-mating steels under both static and dry sliding conditions (adapted from 170; cited in 168).

Temperature range \Rightarrow	< 450 °C	450 - 600 °C	> 600 °C
Arrhenius constant, A ($\text{kg}^2 \cdot \text{m}^{-4} \cdot \text{s}^{-1}$) under static oxidation	1.5×10^6	3.2×10^{-2}	1.1×10^5
Arrhenius constant, A ($\text{kg}^2 \cdot \text{m}^{-4} \cdot \text{s}^{-1}$) under sliding conditions	10^{16}	10^3	10^8
Activation energy, Q ($\text{J} \cdot \text{mol}^{-1}$) under static oxidation	208×10^3	96×10^3	210×10^3

In addition, the flash temperatures experienced at asperities during dry sliding friction are strongly dependent on the rubbing velocity (168), 700°C being encountered at only $1 \text{ m} \cdot \text{s}^{-1}$ between self-mating steels. The intrinsically high surface speeds associated with *in situ* D.T.V. generation (10 – 40 $\text{m} \cdot \text{s}^{-1}$ dependent upon rubbing radius and vehicle speed) therefore account for extremely high rates of oxidation over areas considerably greater than that of the asperity contact. However, the clean, oxide-deficient wear regions appear to have been polished, demonstrating the action of a ‘oxidation-scrape-reoxidation’ mechanism acting at the areas of maximum L.I.P., oxide wear matter agglomerating by a mechanism similar to that described in figure 21. This is confirmed by the retained clumps of Fe oxide clearly visible in plate 20.

The lower L.I.P. region of the outboard face of D.T.V. test rotor no. 10 (plate 22) shows many similarities with corresponding regions in rotor no. 9; uniform, heavy oxidation, indistinguishable flake structure and comparable levels of siliceous matter. However, significant differences accompany these similarities. This time, the oxidation is partially blotchy, these concentrations being associated with Cu and S / Mo. Sb and delineated chromia no longer feature in the mapped area.

The higher L.I.P. region selected for analysis (plate 23) appears to represent a transitional surface condition between that of the lower L.I.P. zone and the very highly polished wear zone discussed earlier in section 5.5.2. (plate 19). It is similar to its counterpart on disc 9 in that oxidation is discontinuous and discrete but is dissimilar in that these islands now appear to be strongly associated with Cu (CuO). Unlike 9, the graphite flake structure is not clearly evident although the compositional image suggests an intermediate stage of transition from the coarse, over-scored flakes of the lower L.I.P. zone and the highly polished, deposition-free crescent encountered on approaching the O.D. Indeed, this is supported by the low magnification compositional image that shows a marked transition in the level of deposition with increasing rubbing radii.

A major and consistent difference between the surfaces of test rotors 9 and 10 is the absence of CuO on the surfaces of disc 9 and the surfeit of CuO on the higher pressure regions of no. 10. One possible explanation is that once the original lubricious sulphides have been rendered ineffective by oxidation and decomposition as a result of high speed, oxygen-rich, asperity interactions, Cu / CuO readily transfers to the countersurface. An alternative explanation might be that the virtual absence of graphite at the tribointerface means that its accelerating effect on the oxidation of the ferrous matrix is negated (169) and CuO is allowed to form in its absence and transfer to the surface (referring to the discussions succeeding table 32 and reference 166).

Examination of figures 55 and 60 illustrates that rotor no. 12 experienced greater L.I.P. wear loss from its inboard face. Plates 24 – 25 show the higher and lower L.I.P. rubbing regions of this face. Disc 12 shows stronger oxygen signals on the high L.I.P. surfaces, combined with Cu, S and Mg; S to a lesser extent in the lower L.I.P. zones. Otherwise, rotor 12 shows characteristics of both 9 and 10.

Examination of figures 54 and 59 illustrate that rotor no. 11, rubbed against N.A.O. friction material; S, clearly experienced greater L.I.P. wear loss from its outboard face. However, even when comparing the

high L.I.P. region of the outboard friction face (plate 26) with the low L.I.P. region of the inboard friction face (plate 27), it is instantly apparent that the two surfaces are considerably more alike than any of those test rotors coupled with material N. Rotor 11 bears much broader, better defined wear scars than any of the counter member surfaces mated to material N, these wear scars being characterised by high iron signals from the underlying matrix material, low oxidation (relative to their surroundings) and low material transfer. Both high and low L.I.P. regions show oxygen-rich bands of tightly agglomerated islands of oxidised matter, reasonable graphite flake resolution albeit slightly more evident at higher L.I.P., negligible P- and barytes-retention and comparable levels of Cu, Mg and sulphurous species, these tending more to be associated with the oxygen-rich part of the T.B.L. The positive thermographic presence of silicon in plate 27 should not be interpreted as suggesting a signal very much greater than that of background noise given the poor spatial resolution of the image.

As has already been commented upon, D.T.V. test rotor no. 13 experienced considerable material loss from both inboard and outboard friction faces. Plates 28 – 29 show the virtually identical high and low L.I.P. regions, which is not particularly unexpected given the level to which the faces were planed during the 80 hour test cycle. Unlike rotors 9, 10, and 12, no. 13 is indistinguishable from its counterpart, no. 11. The most notable feature of both rotor 11 and 13 is the difference in the clarity of the graphite flake structure between the higher and lower L.I.P. regions. As was the case with material N, material S produces a more pronounced polishing effect at the high L.I.P. region, albeit to a lesser extent, perhaps comparable with a 6 μm metallurgical preparation (*cf.* plate 5). Figure 68 shows four X-ray spectra collected from the surfaces of rotor 13. These spectra corroborate the virtually identical tribochemical nature of both high and low L.I.P. in terms of elemental distribution within a relatively small analysis region. Given the advanced stages of surface planing already encountered by these test components, these similarities are wholly to be expected. These observations neither support nor dispel the ‘over-erosion’ mechanism ventured earlier for the tribomechanical perpetuation of D.T.V. (5.5.2.).

What is particularly poignant in comparing the tribochemical response of friction couples under D.T.V.-generating conditions and their in-service-type, bedding frictional surface interactions, is the virtual absence of oxidation at the on-brake interface and the wide-scale oxidation evident at the off-brake interface. The environment that is generated by the L.I.P. test schedules described has been seen to be

one that supplies sufficient atmospheric oxygen to the friction interface to make it a highly oxide-rich environment. This, combined with an equilibrium bulk rotor temperature monitored consistently at around 150°C, but with flash temperatures likely to be well in excess of 700°C, introduces an array of both thermochemical and thermomechanical frictional interactions for which commercial friction materials were not designed. The instability of lubricious sulphides under such conditions is also clearly significant, a factor that adversely affects material N to a greater extent than material S, the tribological behaviour of which is considerably more predictable, stable but unavoidably destructive.

5.5.4. Supplementary Observations and D.T.V. Generation

Friction material; Exp. A, rubbed against D.T.V. test rotor no. 4, was formulated with a graphitic solid lubricant in preference to metallic sulphides in an attempt to increase the transfer potential of both barytes and carbonaceous char matter (table 9 (4.4.), 2.3.2.4., 90 – 91).

Plate 30 shows, with the virtual exclusion of all other off-brake surfaces studied, coherent bands rich in both barytes and carbonaceous material. However, plate 30 shows the lower L.I.P. region whereas plate 31, showing the corresponding higher pressure region, can be seen to be devoid of either retained carbon (as a surface deposit) or Ba-rich species other than the typical seams associated with surface cavities.

Plate 32 shows the higher pressure region of the opposite, inboard face. This region combines aspects of both the lower and higher L.I.P. regions of the outboard face. In many respects the area examined illustrates a fundamental difficulty experienced with the early, manually controlled L.I.P. contact. Wear has commenced in the higher pressure L.I.P. mode exposing a mildly polished, readily-resolvable graphite flake structure, but as wear has continued to diminish the effective normal pressure, the oxide layer has apparently been lost and relatively large surface artefacts of undeformed wear debris have adhered to the surface. From the compositional images it can be seen that the underlying countermember substrate is very similar in respect of the abrasive wear component to which it has been exposed. However, the low magnification topographical image clearly shows that the barytes / carbonaceous /

vermiculite-composed artefacts have only adhered with diminishing contact pressure as off-brake wear continued.

Section 2.3.2.4. reported how T.F.s rich in barytes and carbonaceous char had been noted as being considerably more resistant to L.I.P. wear than those containing Cu-derived compounds and metallic sulphides (90 – 91). However, the relative cohesive properties of friction material constituents were discussed in section 3.3. and it established that both carbonaceous char matter and ceramics such as barytes required an oxide film of reasonable integrity in order to transfer and be retained by the countermember surface. Similarly, as we saw in section 5.5.3., the L.I.P. tribological regime is one persistently exposed to heavily oxidising influences but in the virtually complete absence of either barytes transfer or the formation of a stable carbonaceous char. The factors affecting the absence of these two constituents are likely divergent, carbonaceous matter being lost as gaseous decomposition products. Materials such as barytes are unlikely to form strongly adhesive bonds with metals but may bond to other materials if lattice parameters and orientations coincide. However, $BaSO_4$ shows zero lattice parameter coincidence with Fe, minimal coincidence with Fe_2O_3 and negligible coincidence with Fe_3O_4 but is of course part of the ionic and covalently bonded family of species capable of bonding to the countermember surface in the presence of a tenacious oxide substrate. Unfortunately, as has been commented on earlier, all of the evidence accumulated to date indicates the principal mechanism by which O.B.W. proceeds to be by the removal of oxidised countersurface, a situation that precludes the development of a suitably coherent substrate.

5.5.5. Influence of Abrasive Friction Modifier Additions

Much attention has already been paid to the particle size of abrasive friction modifiers and the influence of their tribological interaction with the countersurface during O.B.W. With respect to the formulation of friction materials to attain adequate levels of braking torque, it is well appreciated that the introduction of smaller abrasive particles reduces the overall friction level and a minimum particle size threshold does appear to exist, after which the abrasive addition ceases to be effective. Concomitantly, when smaller abrasive particulates are selected they tend to be of the hardest / most fracture resistant varieties, i.e. Moh's hardness values of 8.5+ (table 40).

Table 40:

Moh's hardness values of pertinent friction material constituents.

<i>Friction material constituent:</i>	<i>Moh's hardness:</i>	<i>Generic hardness:</i>	<i>Specific gravity (g.cm⁻³):</i>
Molybdenum disulphide (MoS ₂)	1 - 1.5	Very soft	4.7
Graphite (C)	1 - 2	Very soft	2.23
Antimony trisulphide (Sb ₂ S ₃)	2	Soft	4.6 - 4.7
Vermiculite (Mg, Fe, Al) ₃ (Al, Si) ₄ O ₁₀ (OH) ₂ .4H ₂ O	2 - 3	Soft	2.4 - 2.7
Copper particulates (Cu)	2.5 - 3	Fairly soft	8.93 - 8.95
Calcium carbonate (CaCO ₃)	3	Semi-hard	2.71
Barium sulphate (barytes, BaSO ₄)	2.5 - 3.5	Semi-hard	4.48
Copper oxide (CuO)	3.5	Semi-hard	4.03 - 5.8
Calcium fluoride (fluorite, CaF ₂)	4	Semi-hard	3.1 - 3.3
Red iron oxide (hematite, Fe ₂ O ₃)	5.5 - 6.5	Hard	5.2 - 5.3
Black iron oxide (magnetite, Fe ₃ O ₄)	5.5 - 6.5	Hard	5.2
Silica quartz (α -SiO ₂)	7	Very hard	2.65
Zirconium silicate (zircon, ZrSiO ₄)	7.5	Very hard	3.9 - 4.8
Fused alumina (α -Al ₂ O ₃)	9	Very hard	3.97
Silicon Carbide (α -SiC)	9+	Very hard	3.22
Chromia (Cr ₂ O ₃)	9+	Very hard	

In part, this has been substantiated by laboratory studies considering the effect of hard particle size on both the abrasion and erosion of metals although such studies have shown that even sub-micron particles continue to exert wearing effects, albeit by alternative modes of wear. In general however, the wear rate induced at the countersurface drops markedly upon decreasing the particle size from \varnothing 100 μm , this being illustrated in figure 69. The reason for this is most convincingly attributed to the fact that the flow stress of a small volume of countersurface material is higher than that encountered in a large volume, possibly because of the difficulty in either nucleating or displacing dislocations within a small volume. This higher local flow stress, which results from the fundamental contact mechanics of smaller particles, is more resistant to deformation and thereby reduces the wear rate attainable through plastic processes.

In considering the T.B.L. present on the rubbing countermember, with respect to its potential resistance to O.B.W., the hardness of other friction material constituents and their reaction products may also be significant. Harder materials such as the oxides of Fe may provide overall wear resistance while retained on the rotor countersurface by the avoidance of severe, metal-to-metal, adhesive wear but contribute strongly to the destruction of the T.F. when particles become loose in the velocity accommodating zone. In addition, L.I.P. tribotesting has shown abrasive particle size to be extremely significant in determining the O.B.W. performance of N.A.O. friction materials. Zirconium silicate, a relatively soft abrasive, readily removes ferrous scales in addition to those lubricious films, such as CuO, that might under certain circumstances have been imagined to provide some O.B.W. resistance.

In other work not forming a direct component of this programme of research, the chemical nature and particle morphology of very hard abrasive friction modifiers have been seen to exert a critical role in affecting the tribochemistry of many of those compounds active at the frictional interface (98 – 100). However, their role in the generation of D.T.V. is clearly overwhelming and highly detrimental to the dimensional integrity of the disc brake rotor.

It has been shown that the role of abrasive friction modifiers is critical in determining the tribological performance of friction couples in automotive braking systems. It is clear, for example, that their particle size, size distribution, morphology, hardness / chemical nature and volume fraction within the triboelement all exert significant influences.

Under specific circumstances it is possible to consider the frictional influence of abrasive and adhesive friction material constituents as acting independently. According to classical refinement theories whereby abrasive contact gives rise to the generation of D.T.V., which certainly appears to be the case based on the evidence accumulated during this research programme, and adhesive contact lends itself to slip-stick, noise-inducing interactions, it is apparent that the balance to be attained between abrasive and adhesive frictional interaction is extremely important. We can express these relations as follows:

$$\mu_{ABRASION} = \frac{F_{ABRASION}}{F} \quad \text{④②} \qquad \mu_{MATRIX} = \frac{F_{MATRIX}}{(F_N - F)} \quad \text{④①}$$

where,

$\mu_{ABRASION}$ = dynamic coefficient of friction due to abrasive friction modifiers (dimensionless).

$F_{ABRASION}$ = friction force acting at the abrasive particles in contact with the countersurface (N).

F = normal force acting through abrasive particles in contact with the countersurface (N).

μ_{MATRIX} = dynamic coefficient of friction due to the friction material matrix (dimensionless).

F_{MATRIX} = friction force acting at the friction material matrix in contact with the countersurface (N).

F_N = normal force acting on the entire friction material (N).

The balance attained between abrasive and adhesive contributions to the overall friction behaviour is significantly easier to manipulate by abrasive particulate selection than it is by the complex balancing of thermochemically-active, adhesive components.

Considering equations ④② and ④①, it is clear that these relations can only hold over a limited range of operating conditions. Just as is the case when attempting to formulise the durability of automotive friction materials, threshold criteria need to be identified and defined with respect to the environment (including the atmosphere and the partial pressures of the components thereof), the rubbing speed, pressure, tribochemistry and, of course, the temperature. D.T.V.-generation studies have shown that several such thresholds (or transition points) exist between the off- and on-brake situations, and, if the causal mechanisms of cold judder are to be overcome, much greater attention needs to be paid to the balance between abrasive and adhesive friction components in the off-brake, L.I.P. condition.

Unfortunately, the practicability of discriminating between the contributions of abrasive and adhesive components to the overall friction level is relatively limited. In time, and with increasing knowledge of their interrelation, the situation will no doubt improve. While pin-on-disc-type tribotesting is generally not considered meaningful in the evaluation of the effectiveness of automotive friction couples, the field could benefit from a more fundamental appreciation of the frictional surface interactions of individual friction material constituents and the tribological characteristics of their decomposition / interaction products, e.g. Fe₂O₃, Fe₃O₄, CuO and various complexes of interest identified during this study.

Under unusual circumstances where friction level ceases to be significant to the function of the friction couple, such as during off-brake motoring, abrasive and adhesive components exert their potential influence on the brake exclusively in the form of wear. Subjectively speaking then, it is possible to show qualitative variations in the balance between abrasive and adhesive wear components of commercial automotive braking friction couples under varying, simulated, operating conditions.

Table 41 shows some typical examples selected from the results of section 5.5.2.. From the table, it is possible to attribute all of the abrasive characteristics of the two materials under the three rubbing conditions to the size of abrasive friction modifier particulate contained within those friction materials.

Table 41:

Example of the qualitative variations in the balance between abrasive and adhesive wear components.

① = Very low ② = Low ③ = Medium ④ = High

<i>Friction</i>	<i>'Normal' braking wear:</i>		<i>High L.I.P. wear:</i>		<i>Low L.I.P. wear:</i>	
<i>Material:</i>	<i>Abrasion:</i>	<i>Adhesion:</i>	<i>Abrasion:</i>	<i>Adhesion:</i>	<i>Abrasion:</i>	<i>Adhesion:</i>
N	②	②	③	④	①	④
S	③	①	④	③	④	③

Note 1: The abrasive component referred to represents the wear loss experienced by the rotor.

Note 2: The adhesive component referred to represents the perceived level of transfer material retained by the surface of the rotor upon separation of the friction couple.

6.0. Conclusions

It has been shown that the thermochemical interactions of *Non-Asbestos Organic* (N.A.O.) friction material constituents with atmospheric oxygen, countersurface-derived ferrous compounds and other friction material constituents are both varied and complex. Many of these reactions will not exert a significant influence over the tribological behaviour of the automotive braking friction couple. It has also been seen that many will.

Empirical studies supported by thermodynamic modelling, in addition to thoroughly characterising the physico-chemical interactions of friction material constituents, have noted the formation of several adventitious chemical complexes coinciding with the breakdown of metallic sulphide solid lubricants, these including ferrous molybdates (e.g. FeMoO_3 , FeMoO_4 and $\text{Fe}_2(\text{MoO}_4)_3$) and antimonates (e.g. FeSb_2O_6 and FeSbO_4), cupric molybdates (e.g. $\text{Cu}_3\text{Mo}_2\text{O}_9$ and Cu_2MoO_5) and antimonates (e.g. CuSb_2O_6) and even a high temperature barium molybdate (BaMoO_4).

Evidence has also been presented illustrating how many friction material constituents in common use can generate reaction products that are potentially deleterious to the function of the friction pair at elevated temperature, e.g. the ready oxidation of metallic copper to highly lubricious copper (II) oxide (CuO) at temperatures of 400°C and beyond, and the graphitic reduction of barytes to barium sulphide (BaS) in excess of 540°C .

The *condensation* or concentration of metallics at the interacting surface of the friction material does not result solely due to the loss of other interfacial constituents by the formation of gaseous oxidation products. Plates 12 – 13 illustrate that CuO and other Cu-rich species can form at an oxygen-rich surface via diffusional mechanisms, i.e. the condensation phenomenon is exacerbated by the kinetics of the species involved.

Significant *Disc Thickness Variations* (D.T.V.) do result from the preferential wearing effects of intermittent stator / rotor contact at *Low Interfacial Pressures* (L.I.P.). (By 'significant' it is intended to mean levels and dimensional forms of D.T.V. capable of causing *Brake Torque Variations* (B.T.V.) and thereby, cold judder.) For both milder and more aggressive friction material formulations, *Off-Brake Wear* (O.B.W.) occurs by an essentially oxidative wear mechanism (termed 'oxidation-scrape-

reoxidation') characterised by a polished rotor surface appearance whereas on-brake wear involves much more plasticity-dominated wear (although oxidational effects remain significant).

Since the effectiveness with which boundary lubricants actively reduce the shear strength of interfacial asperity contacts is severely diminished at those sliding velocities encountered during L.I.P. contact, the level of O.B.W. generated tends to depend heavily on abrasive particle size. However, the smaller the abrasive particulate borne by the friction material, the more sensitive the friction pair is to the physico-chemical interactions of lubricious sulphides. In general, the characteristics of the abrasive particulate added to a friction material, in particular that of particle size, dominate its potential for the generation of D.T.V.

N.A.O. friction materials loaded with smaller abrasives ($< \varnothing 20 \mu\text{m}$) generate disproportionately lower O.B.W. with reduced levels of axial *Side-face RunOut* (S.R.O.), this having been determined by consideration of the axial S.R.O. perceived by the friction material at differing rubbing radii on the same friction ring. Conversely, N.A.O. friction materials loaded with larger abrasives ($> \varnothing 30 \mu\text{m}$) generate disproportionately higher O.B.W. with reduced levels of axial S.R.O. Materials containing the smaller variety of abrasive particulate discussed have demonstrated numerous wear mode transitions in response to a variety of factors, but especially sliding velocity and its affect on the thermochemistry of solid lubricants.

When a disc brake rotor is paired with an aggressive pad material, excessive periods of exposure to L.I.P. can lead to an 'over-eroded' form of O.B.W., i.e. the friction ring is not planed to an ideal circumferential geometry, rather one that perpetuates the effects of cold judder. This is attributed to the influence of dynamic and temperature-dependent effects on the level of axial S.R.O. presented to the stators.

The use of graphite as a solid lubricant serves to promote the retention of transferred barytes and similar ceramics fillers at an oxidised countersurface. However, given the conditions under which D.T.V. is generated, even a heavily oxidised rotor surface does not promote the retention of tribologically active layers of either barytes or carbonaceous char, two T.B.L. constituents that have been suggested to provide O.B.W. resistance. As would be expected of a thermosetting binding agent, little evidence exists

to suggest that polymeric compounds play a significant role in the constitution of the T.B.L. generated on the surfaces of automotive friction couples.

The coupling of triboelement-derived geometrical data (such as that gathered by a *Co-ordinate Measuring Machine* (C.M.M.)) with the findings of surface analytical techniques (e.g. *Analytical Scanning Electron Microscopy* (A.S.E.M.)) provides a very useful tool in the assessment of frictional surface interactions and their effect on D.T.V. generation.

6.1. Suggestions for Future Research

With the increasing complexity of *Finite Element Models* (F.E.M.) and both the software and hardware that support such analyses, techniques like these can contribute greatly to the understanding of fundamental tribological interactions by the simultaneous modelling of physico-chemical interactions and the *spring and dashpot*-type elastic and non-elastic deformations acting between an abrasive friction modifier and both its supporting matrix and the friction interface. Empirical data relating to such physico-chemical phenomena might be derived from studies such as that conducted during this programme of research or, non-empirically by the coupling of the model with a metallurgical thermochemistry databank. The time-dependence of those elastic and non-elastic interactions experienced by abrasive friction modifiers, could, in the first iteration, be empirically investigated by examining the microscopic loading / unloading behaviour of real particles in real friction material matrices using a nanoindenter hardness tester.

While pin-on-disc type tribotesting is generally not considered meaningful in the evaluation of the effectiveness of automotive friction couples, the field could benefit from a more fundamental appreciation of the frictional surface interactions of friction material constituents and the tribological characteristics of their decomposition / interaction products, e.g. Fe_2O_3 , Fe_3O_4 , CuO and various complexes of interest identified during this study.

Having identified that D.T.V. takes different forms and may be most pronounced at differing radii on the friction ring, dependent upon the friction material, the D.T.V. evaluation rig should be adapted further so that once D.T.V. has been generated, the influence of that D.T.V. on judder excitation can be assessed. Concomitantly, although early studies have focused on characterising a friction material's propensity for D.T.V. generation, similar attention needs to be paid to examine the clean-up characteristics of friction materials once normal braking is re-established.

An additional characteristic of the braking system not having received consideration during the author's programme of research is that of caliper alignment. During normal braking there is a certain amount of self-centralisation and equalisation of the contact regimes from one side of the rotor to the other. This is not the case during off-brake running where abutment interactions within the caliper assembly and misaligned stator contact may play a significant role in determining the form of D.T.V. generated. These effects must be studied in depth to determine the influence of these characteristics on the causes of cold judder.

Plates 20 – 32 have been used to elucidate those physico-chemical interactions active at the friction interface during L.I.P. running but more could be learnt about the actual conditions under which rotor material is removed by detailed studies of the chemical nature of the wear debris expelled from the friction couple during O.B.W.

Future studies examining the nature of the T.B.L. generated between automotive friction pairs could be assisted by the use of components that facilitate accelerated bedding-in, rapid brake face clean-up and increased *Transfer Film* (T.F.) consistency. An example of such components might include brake rotors incorporating either grooves or drilled holes at the friction interface, these features being available in a variety of novel arrangements such as are shown in figure 70.

1. **MACNAUGHTAN, M.** - Extracts from: *The history, design and production of cast iron brake discs*, Foundryman, Volume 91, Part 11, page 363, November 1998.
2. **JIMBO, Y.; MIBE, T.; AKIYAMA, K.; MATSUI, H.; YOSHIDA, M. & A. OZAWA** - *Development of high thermal conductivity cast iron for brake disc rotors*, S.A.E. (Society of Automotive Engineers) Technical Paper Series no. 900002, 1990.
3. **METZLER, H.** - *The brake rotor - friction partner of brake linings*, S.A.E. (Society of Automotive Engineers) Technical Paper Series no. 900847, 1990.
4. **EYRE, T.S.** - *Friction and wear of cast irons*, A.S.M. Handbook - Volume 18; *Friction, Lubrication and Wear Technology*, ISBN 0-87170-380-7, pages 695 - 701, October, 1992.
5. **COYLE, J.P. & P.H.S. TSANG** - *Microstructural changes of cast iron rotor surfaces and their effects on brake performance and wear resistance*, S.A.E. (Society of Automotive Engineers) Technical Paper Series no. 830534, 1983.
6. **RHEE, S.K.; DuCHARME, R.T. & W.M. SPURGEON** - *Characterisation of cast iron friction surfaces*, S.A.E. (Society of Automotive Engineers) Technical Paper Series number 720056, 1972.
7. **RHEE, S.K. & R.T. DuCHARME** - *The friction surface of gray cast iron brake rotors*, Short communication - *Wear*, Volume 23, pages 271 - 273, 1973.
8. **RHEE, S.K.** - *Influence of rotor metallurgy on the wear of friction materials in automotive brakes*, S.A.E. (Society of Automotive Engineers) Technical Paper Series no. 710247, 1971.
9. **MACNAUGHTAN, M.P. & J.G. KROSNAR** - *Cast iron - a brake disc material for the future?* 2nd International Seminar on *Automotive Braking: Recent developments and future trends*, Leeds, UK, ISBN 1-86058-131-5, pages 177-190, 14-15 May 1998.
10. **VANSTEENKISTE, R.H. & E.K. BUYZE** - *All steel brake disc development*, S.A.E. (Society of Automotive Engineers) Technical Paper Series no. 710590, 1971.
11. **TSUJIMURA, T. & S. MANABE** - *Suitability of austempered cast iron as brake disc material*, Quarterly Review of the R.T.R.I., Volume 30, no. 4, pages 220 - 226, November, 1989.

12. **WYCLIFFE, P.** - *Friction and wear of Duralcan reinforced aluminium composites in automotive braking systems*, S.A.E. (Society of Automotive Engineers) Technical Paper Series no. 930187, 1993.
13. **NEITZL, B.; BARTH, M. & M. MATIC** - *Weight reduction of disc brake systems with the utilisation of new aluminium material*, S.A.E. (Society of Automotive Engineers) Technical Paper Series no. 940335, 1994.
14. **DWIVEDI, R.** - *Performance of M.M.C. rotors in dynamometer testing*, S.A.E. (Society of Automotive Engineers) Technical Paper Series no. 940848, 1994.
15. **de SANCTIS, A.M.; EVANGELISTA, E.; FORCELLESE, A. & A. FUGANTI** - *Forging of a M.M.C. for an automotive component*, Institute of Materials Symposium: *Materials for Lean Weight Vehicles*, University of Warwick, pages 73 - 82, 1995.
16. **GRIEVE, D.G.; BARTON, D.C.; CROLLA, D.A.; BUCKINGHAM, J.T. & J. CHAPMAN** - *Investigation of light weight materials for brake rotor applications*, Institute of Materials Symposium: *Materials for Lean Weight Vehicles*, University of Warwick, pages 73 - 82, 1995.
17. **GRIEVE, D.G.; BARTON, D.C.; CROLLA, D.A.; CHAPMAN, J. & J.T. BUCKINGHAM** - *Alternative disc brake materials*, I.Mech.E. (Institution of Mechanical Engineers) workshop - *Advances in Automotive Braking Technology: Design, Analysis and Materials Development*, University of Leeds, Leeds, 3rd April 1996.
18. **ZEUNER, T.; STOJANOV, P.; SAHM, P.; RUPPERT, H. & A. ENGELS** - *On track with M.M.C. brake discs*, *Materials World* (The Journal of the Institute of Materials), Volume 6, Number 1, pages 17 - 19, January 1998.
19. **CURRAN, G.** - *M.M.C.s: the future*, *Materials World* (The Journal of the Institute of Materials), Volume 6, Number 1, pages 20 - 21, January 1998.
20. **BAKER, C.** - *Metal Matrix Composites VI* (a summary of conference proceedings), *Materials World* (The Journal of the Institute of Materials), Volume 6, Number 1, pages 22 - 23, January 1998.

21. **DENHOLM, M.J.** - *Aluminium metal matrix composite rotors and drums - a future trend*, 2nd International Seminar on *Automotive Braking: Recent developments and future trends*, Leeds, UK, ISBN 1-86058-131-5, pages 205-214, 14-15 May 1998.
22. **A.P. RACING ENGINEERING STAFF** - *Carbon-carbon brakes and clutches - stopping power*, Racecar - Special Report, A.P. (Automotive Products) Racing, 1995.
23. **HUBBARD, D.A.** - *New materials in railway braking*, Presented at the I.Mech.E. workshop: *Advances in Automotive Technology: Design Analysis and Materials Developments*, Leeds, 3rd April, 1996.
24. **FLITCROFT, S.M.** - *The friction and wear characteristics of a sintered metal motorcycle friction braking material, under wet and dry conditions*, Ph.D. Thesis, Brunel University, 1990.
25. **NEWCOMB, T.P. & R.T. SPURR** - *Braking of road vehicles*, Chapman and Hall Ltd. (out of press), page 132, 1967.
26. **HARPER, G.A.** - *Brakes and friction materials - The history and development of the technologies*, Mechanical Engineering Publications (M.E.P.) Ltd., ISBN 1-86058-127-7.
27. **AVRAM, P.** - *Applying the brakes as cars gain speed*, Professional Engineering, Volume 9, Number 19, pages 55 - 56, Wednesday 16th October 1996.
28. **EAST, R.G.** - *Evolution of friction materials for commercial vehicle disc brakes*, I.Mech.E. (Institution of Mechanical Engineers) paper C450/88, 1988.
29. **FERODO TECHNICAL STAFF** - *Friction materials for engineers*, Published by Ferodo Ltd., Publication: 1011/10/61, 1961.
30. **JACKO, M.G.; TSANG, P.H.S. & S.K. RHEE** - *Automotive friction materials evolution during the past decade*, Wear, Volume 100, pages 503 - 515, 1984.
31. **SMALES, H.** - *Friction materials - Black art or science?* I.Mech.E. (Institution of Mechanical Engineers) Automobile Division Chairman's address, University of Leeds, 09.02.1995.
32. **IRESON, R.** - *The Penguin car handbook*, Penguin Books, pages 211 - 226, 1960.

33. **NEWCOMB, T.P. & R.T. SPURR** - *Commercial vehicle braking*, Butterworth & Co. (Publishers) Ltd., pages 8 - 9, 1979.
34. **NEWCOMB, T.P.** - *Interfacial temperatures and the distribution of heat between bodies in sliding contact*, A.S.M.E. (American Society of Mechanical Engineers) International Heat Transfer Conference, Number 77, 1961.
35. **NEWCOMB, T.P.** - *Transient temperatures in brake drums and linings*, Proceedings of the Institution of Mechanical Engineers (Automobile Division), Number 7, pages 227 - 244 (including communications), 1958 - 1959.
36. **NEWCOMB, T.P. & B.R. V.** - *Thermal effects in brakes*, Loughborough University of Technology (Department of Transport Technology) - *Braking of Road Vehicles* course notes, 1993.
37. **ASHWORTH, F.J.; SHERBINY, M.E. & T.P. NEWCOMB** - *Temperature distribution and thermal distortions of brake drums*, Proceedings of the I.Mech.E. (Institution of Mechanical Engineers), Volume 191, Paper number 19/77, pages 169 - 176, 1977.
38. **LIMPERT, R.** - *An investigation of thermal conditions leading to surface rupture of cast iron rotors*, S.A.E. (Society of Automotive Engineers) Technical Paper Series no. 720447, 1972.
39. **LIMPERT, R.** - *The thermal performance of automotive disc brakes*, S.A.E. (Society of Automotive Engineers) Technical Paper Series no. 750873, 1975.
40. **LIMPERT, R.** - *Cooling analysis of disc brake rotors*, S.A.E. (Society of Automotive Engineers) Technical Paper Series no. 751014, 1975.
41. **RAMACHANDRA RAO, V.T.V.S.; RAMASUBRAMANIAN, H. & K.N. SEETHARAMU** - *Simulation of temperature distribution in drum brakes - comparison by measurements*, Proceedings of NUMETA '85 Conference, Swansea, pages 841 - 849, 1985.
42. **RAMACHANDRA RAO, V.T.V.S.; RAMASUBRAMANIAN, H. & K.N. SEETHARAMU** - *Analysis of temperature field in brake disc for fade assessment*, *Warme- und Stoffübertragung*, Volume 24, pages 9 - 17, 1989.

43. **KAYES, W.M. & I.S. BJORKLUND** - *Heat transfer from a rotating cylinder with and without crossflow*, Transactions of the ASME, Paper no. 56-A-71, 1958.
44. **COBB, E.C. & O.A. SAUNDERS** - *Heat transfer from a rotating disc*, Proceedings of the Royal Society A., Volume 236, page 343, 1956.
45. **HAUSEN, H.** - *Wärmeübertragung im Gegenstrom, Gleichstrom und Kreuzstrom (Heat transfer in turbulent flow, laminar flow and cross-flow)*, Springer-Verlag, Berlin, 1950.
46. **SISSON, A.E.** - *Thermal analysis of vented brake rotors*, S.A.E. (Society of Automotive Engineers) Technical Paper Series no. 780352, 1978.
47. **MORGAN, S. & R.W. DENNIS** - *A theoretical prediction of disc brake temperatures and a comparison with experimental data*, S.A.E. (Society of Automotive Engineers) Technical Paper Series no. 720090, 1972.
48. **SECRET, D.A. & R.W. HORNBECK** - *An analysis of heat transfer and fade in disk brakes*, Journal of Engineering for Industry (Transactions of the A.S.M.E. (American Society of Mechanical Engineers)), pages 385 - 390, May, 1976.
49. **HO, T-L.; PETERSON, M.B. & F.F. LING** - *Effect of friction heating on brake materials*, Wear, Volume 30, pages 73 - 91, 1974.
50. **PAVELESCU, D. & M. MUSAT** - *Some relations for determining the wear of composite brake materials*, Wear, Volume 27, pages 91 - 97, 1974.
51. **KAO, T-K.; RICHMOND, J.W. & M.W. MOORE** - *The application of predictive techniques to study thermo-elastic instability of brakes*, S.A.E. (Society of Automotive Engineers) Technical Paper Series no. 942087, 1994.
52. **KAO, T-K.; RICHMOND, J.W. & A. DOUARRE** - *Thermo-mechanical instability in braking and brake disc thermal judder: an experimental and finite element study*, 2nd International Seminar on *Automotive Braking: Recent developments and future trends*, Leeds, UK, ISBN 1-86058-131-5, pages 231 - 263, 14 - 15 May 1998.
53. **CURRY, E.** - *Design, installation and production of brake rotors*, Short Course on the *Braking of Road Vehicles*, University of Bradford, 7 - 11 September 1998.

54. **de VRIES, A. & M. WAGNER** - *The brake judder phenomenon*, S.A.E. (Society of Automotive Engineers) Technical Paper Series no. 920554, 1992.
55. **HAIGH, M.; SMALES, H. & M. ABE** - *Vehicle judder under dynamic braking caused by disc thickness variation*, I.Mech.E. (Institution of Mechanical Engineers) Conference on the 'Braking of Road Vehicles', Paper no. C444/022/93, 1993.
56. **HAIGH, M.; SMALES, H. & M. ABE** - *R.T.V. - A friction material designer's view*, S.A.E. (Society of Automotive Engineers) Technical Paper Series no. 933070, 1993.
57. **ENGEL, H.G.; HASSIOTIS, V. & R. TIEMANN** - *System approach to brake judder*, S.A.E. (Society of Automotive Engineers) Technical Paper Series no. 945041, 1994.
58. **TIEMANN, R. & H.G. ENGEL** - *Flat surface test-stand for investigations on braking dynamics*, Eurotrib' 92, 1992.
59. **INOUE, H.** - *Analysis of brake judder caused by thermal deformation of brake disc rotors*, S.A.E. (Society of Automotive Engineers) Technical Paper Series no. 865131, 1986.
60. **BOSWORTH, R.** - *Investigation of secondary ride aspects of steering wheel vibration (shimmy and judder) using Taguchi methodology*, I.Mech.E. (Institution of Mechanical Engineers) Conference on the 'Braking of Road Vehicles', Paper no. C399/9, 1989.
61. **STRINGHAM, W.; JANK, P.; PFEIFER, J. & A. WANG** - *Brake roughness - disc brake torque variation, rotor distortion and vehicle response*, S.A.E. (Society of Automotive Engineers) Technical Paper Series no. 930803, 1993.
62. **JACOBSSON, A.H.** - *The brake judder phenomenon - problem approach and classification*, 2nd International Seminar on *Automotive Braking: Recent developments and future trends*, Leeds, UK, ISBN 1-86058-131-5, 14 - 15 May 1998.
63. **JACOBSSON, A.H.** - *Wheel suspension related disc brake judder*, Proceedings DETC '97 Conference, VIB-4165, Sacramento, California, 14-17 September 1997 (Modified version).
64. **JACOBSSON, A.H.** - *High speed disc brake judder - The influence of passing through critical speed*, Proceedings of *EUROMECH - 2nd European Non-linear Oscillation Conference*, Prague, Volume 2, pages 75 - 78, September 1996.

65. **JACOBSSON, A.H.** - *Frequency sweep approach to brake judder*, Thesis for the degree of Licentiate of Engineering, Chalmers University of Technology, Göteborg, Sweden, Report no. 1998-06-12, 1998.
66. **ANDERSON, A.E. & R.A. KNAPP** - *Hot spotting in automotive friction systems*, *Wear*, Volume 135, pages 319 - 337, 1990, and source unknown, pages 673 - 680.
67. **BROOKS, P.C.; BARTON, D.; CROLLA, D.A.; LANG, A.M. & D.R. SCHAFER** - *A new approach to disc brake judder using a thermo-mechanical finite element model*, I.Mech.E. (Institution of Mechanical Engineers) *AUTOTECH '93* Conference, Seminar paper C462/31/064.
68. **KREITLOW, W.; SCRODTER, F. & H. MATTHAI** - *Vibration and 'hum' of disc brakes under load*, S.A.E. (Society of Automotive Engineers) Technical Paper Series no. 850079, 1979.
69. **BARBER, J.R.** - *The influence of thermal expansion on the friction and wear process*, *Wear*, Volume 10, pages 155 - 159, 1967.
70. **BARBER, J.R.** - *Thermoelastic instabilities in the sliding of conforming solids*, *Proceeding of the Royal Society - Series A*, Volume 312, pages 381 - 394, 1969.
71. **KAO, T-K.; RICHMOND, J.W. & M.W. MOORE** - *The application of predictive techniques to study thermo-elastic instability of brakes*, S.A.E. (Society of Automotive Engineers) Technical Paper Series no. 942087, 1994.
72. **DOW, T.A. & R.A. BURTON** - *Thermoelastic instability of sliding contact in the absence of wear*, *Wear*, Volume 19, pages 312 - 328, 1972.
73. **STERNE, D.D.** - *Monitoring brake disc distortions using lasers*, I.Mech.E. (Institution of Mechanical Engineers) *AUTOTECH '89* Conference, Seminar paper C399/34.
74. **ANON.** - *Textar internal report on judder as a result of high thermal stress*, (translation), pages 1 - 31.
75. **EGGLESTON, D.** - *Bluespotting and cracking of grey cast irons used in automotive friction couples*, M.Eng. dissertation, Sheffield Hallam University (formerly Sheffield City Polytechnic), June 1992.

76. **ENGEL, H.G.; BACHMANN, T.; EICHHORN, U. & C. SAAME** - *Dynamic behaviour of brake-disc geometry as cause of brake judder*, 4th International E.A.E.C. (European Automobile Engineers Co-operation) Conference, Strasbourg, 16 - 18 June, 1993.
77. **GASSMAN, S. & H.G. ENGEL** - *Excitation and transfer mechanism of brake judder*, S.A.E. (Society of Automotive Engineers) Technical Paper Series no. 931880, 1993.
78. **CROLLA, D.A. & A.M. LANG** - *Brake noise and vibration - the state of the art*, Proceedings of the 17th Leeds-Lyon Symposium on Tribology held at the Institute of Tribology, Leeds University, Leeds, U.K., 4 - 7 September, 1990.
79. **LANG, A.M. & H. SMALES** - *An approach to the solution of disc brake vibration problems*, I.Mech.E. (Institution of Mechanical Engineers) Conference Paper no. C37/83, 1983.
80. **JEACOCK, S.M.** - *Disc brake performance*, Final year project thesis, Sheffield City Polytechnic (now Sheffield Hallam University), 1987.
81. **KEARNS, G.** - *Disc brake wear*, Final year project thesis, Sheffield City Polytechnic (now Sheffield Hallam University), 1988.
82. **BETTERIDGE, M.** - *Disc brake vibrations*, Final year project thesis, Sheffield City Polytechnic (now Sheffield Hallam University), 1989.
83. **AOKI, K.; KIMURA, T. & M. MAEDA** - *Development of a low drag disc brake system for small cars*, S.A.E. (Society of Automotive Engineers) Technical Paper Series no. 800781, 1980.
84. **SHIBATA, K.; GOTO, A.; YOSHIDA, S.; AZUMA, Y. & K. NAKAMURA** - *Development of brake friction material*, S.A.E. (Society of Automotive Engineers) Technical Paper Series no. 930806, 1993.
85. **BASTOW, D.** - *Car suspension and handling*, 2nd edition, Pentech Press, ISBN 0-7273-0316-3, 1987.
86. **GOLDBERG, G.L. & T.N. JAMES** - *An old material meets a new challenge - integral cast iron hub and disc development*, S.A.E. (Society of Automotive Engineers) Technical Paper Series no. 690444, 1969.

87. **MILLER, J.E.; SCHENK, D.E. & G.C. FULKS** - *Motor based brake control technology*, I.Mech.E. (Institution of Mechanical Engineers) *AUTOTECH '95* Conference, Seminar paper C498/12/161.
88. **CARRE, J-J. & L.E. DELP** - *New generation of single pin caliper brakes*, S.A.E. (Society of Automotive Engineers) Technical Paper Series no. 870259, 1987.
89. **ANON.** - *Simple seal doubles brake pad life*, Innovator's Notebook, Eureka on Campus, Summer, 1993.
90. **BORJESSON, M.; ERIKSSON, P.; KUYLENSTIERNA, C.; NILSSON, P.H. & T. HERMANSSON** - *The role of friction films in automotive brakes subjected to low contact forces*, I.Mech.E. (Institution of Mechanical Engineers) Conference on the 'Braking of Road Vehicles', Paper no. C444/026/93, 1993.
91. **HERMANSSON, T.; KUYLENSTIERNA, C.; NILSSON, P.H. & M. BORJESSON** - *Some details concerning the uniformity of disc wear in automotive disc brakes as a function of third-body layer properties*, Proceedings of the 6th International Congress on Tribology - *EUROTRIB '93*, Budapest, Volume 5, pages 422 - 427, 30th August - 2nd September, 1993
92. **WIRTH, A. & R. WHITAKER** - *An energy dispersive x-ray and imaging x-ray photoelectron spectroscopical study of transfer film chemistry and its influence on friction coefficient*, Physics Journal D: Applied Physics, **25**, A38 - A43, 1992.
93. **WIRTH, A. & R. WHITAKER** - *The role of transfer film chemistry in automotive friction couples*, Proceedings of the International Congress on X-ray Optics and Microanalysis, Manchester, (*Inst. Phys. Conf. Ser., No. 130*), 1992.
94. **WIRTH, A.; STONE, K. & R. WHITAKER** - *A study of the relationship between transfer film chemistry and friction performance in automotive braking systems*, S.A.E. (Society of Automotive Engineers) Technical Paper Series no. 922541, 1992.
95. **WIRTH, A. & R. WHITAKER** - Proceedings of Eurotrib' 93, Budapest, Volume 1, pages 341 - 350, 1993.

96. **WIRTH, A.; WHITAKER, R.; TURNER, S. & G. FIXTER** - *X-ray photoelectron spectroscopy characterisation of third body layers formed during automotive friction braking*, Journal of Electron Spectroscopy and Related Phenomena, **68**, p. 675 - 683, 1994.
97. **WIRTH, A.; HALLAM, K.R. & R. WHITAKER** - *An investigation of in-situ chemical changes associated with imaging X.P.S. studies of transfer films*, pages , 1995.
98. **WIRTH, A.; EGGLESTON, D. & R. WHITAKER** - *A fundamental tribochemical study of the third-body layer formed during automotive friction braking*, Proceedings of the 6th Nordic Symposium on Tribology - *NORDTRIB '94*, Uppsala, Sweden, 12th - 15th June, 1994.
99. **WIRTH, A.; EGGLESTON, D. & R. WHITAKER** - *A fundamental tribochemical study of the third-body layer formed during automotive friction braking*, Wear, Volume 179, pages 75 - 81, 1994.
100. **WIRTH, A.; EGGLESTON, D. & R. WHITAKER, R.** - *A study of transfer film formation and its influence on disc thickness variation of grey cast iron used in automotive braking systems*, *AUTOTECH '95* (Seminar 12 - Braking Technology), NEC, Birmingham, 7th - 9th November, 1995 - **ORAL ONLY**.
101. *Dictionary of polymeric materials* - phenolic resins, pages 716 - 719.
102. **ROBINSON, J.W.; MOGENSEN, G.E.; PACKARD, K.D. & J. HERMAN** - *Ceramic fibers for friction applications*, Automotive Engineering, Volume 98, Number 12, pages 47 - 52, December 1990.
103. **ARSENIC, Z.; DUBOKA, C. & J. TODOROVIC** - *Prediction of brake pad life - further development of L.W.H.*, S.A.E. (Society of Automotive Engineers) Technical Paper Series no. 860631, 1986.
104. **CROSA, G.; ENDERLE, N.; LEAL, H.; OLIVEIRA, A.; STEDILE, F.C. & I.J.R. BAUMVOL** - *Study of effect of abrasives in friction material composites*, source unknown.
105. **ANON.** - *Vermiculite - increased capacity encourages optimism but construction still the key to demand*, Industrial Minerals, pages 17 - 31, April, 1977.

106. **LIU, T.; RHEE, S.K. & K.L. LAWSON** - *A study of wear rates and transfer films of friction materials*, *Wear*, Volume 60, pages 1 - 12, 1980.
107. **ARCHARD, J.F. & W. HIRST** - *The wear of metals under unlubricated conditions*, *Proceedings of the Royal Society (London)*, Volume A 236, pages 397 - 410, 1956.
108. **MINEGISHI, H.; SHIMIZU, H.; WAKAMATSU, H. & Y. YOSHINO** - *Prediction of brake pad wear/life by means of brake severity factor as measured on a data logging system*, S.A.E. (Society of Automotive Engineers) Technical Paper Series no. 840358, 1984.
109. **DUBOKA, C. & J. TODOROVIC** - *Linear wear hypothesis for the prediction of brake lining life*, *Proceedings of the I.Mech.E. (Institution of Mechanical Engineers) conference; Braking of Road Vehicles*, London, paper no. C15/83, 1983.
110. **RHEE, S.K.** - *Wear equation for polymers sliding against metal surfaces*, *Wear*, Volume 16, pages 431 - 445, 1970.
111. **RHEE, S.K.** - *Wear-mechanism of asbestos-reinforced automotive friction materials*, *Wear*, Volume 29, pages 391 - 393, 1974.
112. **KAR, M.K. & S. BAHADUR** - *Micromechanism of wear at polymer-metal sliding interface*, *Wear*, Volume 46, pages 189 - 202, 1978.
113. **BOWDEN, F.P. & D. TABOR** - *Friction and lubrication of solids - part 1*, Clarendon Press Ltd., 1950.
114. **BOWDEN, F.P. & D. TABOR** - *Friction and lubrication of solids - part 2*, Clarendon Press Ltd., 1964.
115. **LANDHEER, D. & J.H. ZAAT** - *The mechanism of metal transfer in sliding friction*, *Wear*, Volume 27, pages 129 - 145, 1974.
116. **BRISCOE, B.J.; RAMIREZ, I. & P.J. TWEEDALE** - *Friction of aramid fibre composites*, *I.Mech.E. (Institution of Mechanical Engineers) paper no. C452/88*, 1988.
117. **LUDEMA, K.C.** - *Sliding and adhesive wear*, *A.S.M. Handbook - Volume 18; Friction, Lubrication and Wear Technology*, ISBN 0-87170-380-7, pages 237 - 241, October, 1992.

118. **JACKO, M.G.** - *Physical and chemical changes of organic disc pads in service*, *Wear*, Volume 46, pages 163 - 175, 1978.
119. **BARK, L.S.; MORAN, D. & S.J. PERCIVAL** - *Chemical changes in asbestos-based friction materials during performance - a review*, *Wear*, Volume 34, pages 131 - 139, 1975.
120. **BARK, L.S.; MORAN, D. & S.J. PERCIVAL** - *Inorganic and organic changes during friction material performance*, *Wear*, Volume 53, pages 107 - 113, 1979.
121. **SPURGEON, W.M. & A.R. SPENCER** - *Reliability and durability of automotive friction materials*, *Bendix Technical Journal*, Volume 2 (number 3), pages 57 - 66, 1969.
122. **GATRELL, R.L. & T.P. SCHREIBER** - *Chemical changes at brake wear surfaces*, S.A.E. (Society of Automotive Engineers) Technical Paper Series no. 670511, 1967.
123. **ROWSON, D.M.** - *The chrysotile content of the wear debris of brake linings*, *Wear*, Volume 47, pages 315 - 321, 1978.
124. **ROWSON, D.M.** - *Wear of an asbestos-based friction material*, Ph.D. Thesis, Postgraduate school of Applied Physics, University of Bradford, 1971.
125. **FISHER, G.E. & J.C. NEERMAN** - *Identification of brake lining constituents by pyrolysis gas chromatography*, *Industrial & Engineering Chemistry Product Research & Development*, Volume 5, pages 288 - 292, September, 1966.
126. **GEALER, R.L. & B.H. BIGGERS** - *New chemical test for the characterization of organic brake linings - pyrolytic gas chromatography*, S.A.E. (Society of Automotive Engineers) Technical Paper Series no. 670512, 1967.
127. **SCIESZKA, S.F.** - *Tribological phenomena in steel-composite brake material friction pairs*, *Wear*, Volume 64, pages 367 - 378, 1980.
128. **BROS, J. & S.F. SCIESZKA** - *The investigation of factors influencing dry friction in brakes*, *Wear*, Volume 41, pages 271 - 286, 1976.
129. **HUTCHINGS, I.M.** - *Introduction to sliding wear*, University of Cambridge Programme for Industry - Tribology course, 21 - 23 March, 1994.

130. **GEORGIEWSKIJ, G. & M. OLINA** - *About pick-up in the friction couple brake composite material - cast iron*, Problems of Friction (KRAGELSKII, I.V. (ed.), Nauka, Moscow (in Russian), 1967.
131. **HOLINSKI, R.** - *The interface in dry frictional systems*, Oral presentation, 15th October 1997.
132. *Friction Assessment Screening Test Instruction Manual*, Bush Manufacturing Company, Clawson, Michigan, revised edition, 1967.
133. **ANDERSON, A.E.; GRATCH S. & H.P. HAYES** - *A new laboratory friction and wear test for the characterisation of brake lining*, S.A.E. (Society of Automotive Engineers) Technical Paper Series no. 670079, 1967.
134. **SPENCER, A.R.; SPURGEON, W.M. & J.L. WINGE** - *Four tests for consistency of automotive brake linings*, S.A.E. (Society of Automotive Engineers) Technical Paper Series no. 660412, 1966.
135. **WILSON, A.J. & G.T. BOWSER** - *Machine testing for brake lining classification*, S.A.E. (Society of Automotive Engineers) Technical Paper Series no. 710249, 1971.
136. **ZIMMER, D.** - *ATE friction test machine and other methods of lining screening*, S.A.E. (Society of Automotive Engineers) Technical Paper Series no. 820163, 1982.
137. **G.M. ENGINEERING STAFF** - *General motors engineering staff test procedures for the laboratory evaluation of brake lining materials*, Engineering publication no. A - 2604, September, 1969.
138. **PRESTON, J.D. & R.J. FORTHOFFER** - *Correlation of vehicle, dynamometer and other laboratory tests for brake friction materials*, S.A.E. (Society of Automotive Engineers) Technical Paper Series no. 710250, 1971.
139. **SINCLAIR, D. & W.F. GULICK** - *The dual brake inertia dynamometer*, Paper no. 488C, S.A.E. (Society of Automotive Engineers) National Automobile Week Meeting, Detroit, Michigan, U.S.A., March, 1962.
140. **VON THUN, H-J.** - *A double ended brake test rig with inertia simulation*, S.A.E. (Society of Automotive Engineers) Technical Paper Series no. 800855, 1980.

141. **CHAPMAN, B.J. & D. HATCH** - *Cast iron brake rotor metallurgy*, I.Mech.E. (Institution of Mechanical Engineers) paper no. C35/76, 1976.
142. **EGGLESTON, D.** - *An investigation into the microstructural and compositional uniformity of cast disc brake rotors*, *LINK* programme report, unpublished, 12th June 1993.
143. **BRITISH STANDARDS INSTITUTION (BSI)** - *Founding – Grey cast irons*; BS EN 1561 : June 1997.
144. **BRITISH STANDARDS INSTITUTION (BSI)** - *British standard specification for flake graphite cast iron*; BS 1452 : 1990.
145. **EGGLESTON, D.** - *Structural anomalies in vertically cast brake disc rotors*, *LINK* programme report, unpublished, 16th February 1993.
146. **GOLDSTEIN, J.I.; NEWBURY, D.E.; ECHLIN, P.; JOY, D.C.; ROMIG Jr., A.D.; LYMAN, C.E.; FIORI, C. & E. LIFSHIN** - *Scanning electron microscopy and x-ray microanalysis: a text for biologists, materials scientists and geologists*, 2nd edition, Plenum Press, ISBN 0-306-44175-6, 1994.
147. **CULLITY, B.D.** - *Elements of X-ray diffraction*, 2nd edition, Addison-Wesley Publishers, ISBN 0-201-01174-3, 1978.
148. **SWEETING, F.B.J.; THORPE, W.R. & A.N. PETTITT** - *Fault and cause diagnosis of casting defects: a case study*, *Quality and reliability engineering international*, Volume 8, pages 79 - 91, 1992.
149. **DAWSON, J.V. & A.M. SAGE** - *High strength, high carbon grey irons containing vanadium and their resistance to thermal fatigue cracking*, *Foundry Trade Journal International*, June, 1989.
150. **CHAPMAN, B.J. & G. MANNION** - *Titanium bearing cast iron for automotive brake applications*, *Foundry Trade Journal*, pages 232-246, 1982.
151. **SOROCHEJ, M.** - *The analysis of wear process of the grey cast iron in a technically dry friction conditions*, pages 300 - 301, Source unknown, circa 1981 - 1986.

152. **WIRTH, A. & R. WHITAKER** - *Developments in cast iron rotor metallurgy*, I.Mech.E. (Institution of Mechanical Engineers) workshop - *Advances in Automotive Braking Technology: Design, Analysis and Materials Development*, University of Leeds, Leeds, 3rd April 1996.
153. **ELLIS, K.** - *The effect of cast iron disc metallurgy on friction and wear characteristics*, 2nd International Seminar on *Automotive Braking: Recent developments and future trends*, Leeds, UK, ISBN 1-86058-131-5, pages 191-203, 14-15 May 1998.
154. **INTERNATIONAL STANDARDS ORGANISATION (ISO)** - *Cast iron - designation of microstructure of graphite*; ISO 945 : 1975 (E).
155. *Comparative charts for the assessment of flake graphite size, morphology and formation*, ASTM (American Society for the Testing of Materials) A247.
156. **GLAESER, W.A.** - *Introduction to materials for friction and wear applications*, A.S.M. Handbook - Volume 18; *Friction, Lubrication and Wear Technology*, ISBN 0-87170-380-7, pages 693 - 694, October, 1992.
157. **SMITHELLS, C.J. ;(BRANDES, E.A. (ed.))** - *Smithells metals reference book*, 6th edition, Butterworths & Co. (Publishers) Ltd., ISBN: 0-408-71053-5, pages 21-1 to 21-7, 1983.
158. **KUBASCHEWSKI, O. & B.E. HOPKINS** - *Oxidation of metals and alloys*, 2nd edition, Butterworths Scientific publications, pages 1 - 15, 108 - 114, 1967.
159. **DIGGLE, J.W. (ed.)** - *Oxides and oxide films*, Volume 1, Marcel Dekker Inc., ISBN 0-8247-1143-2, 1972.
160. **CZICHOS, H.** - *Basic tribological parameters*, A.S.M. Handbook - Volume 18; *Friction, Lubrication and Wear Technology*, ISBN 0-87170-380-7, pages 473 - 479, October 1992.
161. **CZICHOS, H.** - *Design of friction and wear experiments*, A.S.M. Handbook - Volume 18; *Friction, Lubrication and Wear Technology*, ISBN 0-87170-380-7, pages 480 - 488, October, 1992.
162. **GEE, M.G.** - *Guidelines for unlubricated sliding wear tests: Part 1, general approach* - National Physical Laboratory (N.P.L., D.T.I.), April 1993.

163. **ROLLASON, E.C.** - *Metallurgy for engineers*, 4th edition, Edward Arnold, a division of Hodder & Stoughton Ltd., ISBN: 0-7131-3282-5, pages 149 -151, 1986.
164. **GILBERT, G.N.J.** - *The growth and scaling of cast irons in air and steam*, BCIRA Journal, Volume 7, pages 478 - 566, 1959.
165. **PALMER, K.B.** - *Design with cast irons at high temperatures, Part 1: Growth and scaling*, Report 1248, BCIRA.
166. **DAINTITH, J. (ed.)** - *Dictionary of chemistry*, Intercontinental Book Productions Ltd., ISBN 0-85047-936-3, page 58, 1981.
167. **HO, T.L.** - *Development and evaluation of high-energy brake materials*, Rensselaer Polytechnic Institute, Ph.D. thesis, 1974.
168. **HUTCHINGS, I.M.** - *Tribology - friction and wear of engineering materials*, Edward Arnold, a division of Hodder & Stoughton Ltd., ISBN 0-340-56184-x, 1992.
169. **DAVIS, J.R. (ed.)** - *ASM Speciality Handbook: Cast Irons*, ASM International, ISBN: 0-87170-564-8, September, 1996.
170. **QUINN, T.F.J.** - *Proceedings of International Conference on Tribology – Friction, Wear and Lubrication*, I.Mech.E. (Institution of Mechanical Engineers) Conference Series 1987-5, pages 253 – 259, 1987.
171. **BRIGGS, D. & M.P. SEAH** - *Practical surface analysis: Volume I - Auger and X-ray photoelectron spectroscopy*, 2nd edition, John Wiley & Sons, ISBN 0-471-92081-9, 1990.
172. **VIKULOV, K.; TRON, B. & P. BUONFICO** - *Brake vibration and disc thickness variation (D.T.V.)*, 2nd International Seminar on *Automotive Braking: Recent developments and future trends*, Leeds, UK, ISBN 1-86058-131-5, pages 77 - 84, 14 - 15 May 1998.

The following articles and publications represent documents not referenced directly in the text but worthy of attention when investigating frictional surface interactions and their effect on brake judder.

1. **MISRA, A. & I. FINNIE** - *Wear*, Volume 65, pages 359 - 373, 1981.
2. **NEWCOMB, T.P. & R.T. SPURR** – *Automobile brakes and braking systems*, 2nd edition, Chapman and Hall, ISBN 0-412-14020-9, 1975.
3. **LIMPERT, R.** – *Brake design and safety*, S.A.E. (Society of Automotive Engineers) US, ISBN 1-56091-261-8, 1992.
4. **BAKER, A.K.** – *Vehicle braking*, Pentech Press, ISBN 0-7273-2202-8, March, 1986.
5. **GOODAY, L.; SCANLON, M. & J. DEVINE** – *Brakes and braking: Information update 1*, Information and Library Service, I.Mech.E. (Institution of Mechanical Engineers), March, 1994.
6. **LIBSCH, T.A. & S.K. RHEE** – *Microstructural changes in semi-metallic disc brake pads created by low temperature dynamometer testing*, *Wear*, Volume 46, pages 203 - 212, 1978.
7. **RHEE, S.K.; JACKO, M.G. & P.H.S. TSANG** – *The role of friction film in friction, wear and noise of automotive brakes*, S.A.E. (Society of Automotive Engineers) Technical Paper Series no. 900004, 1990 / *Wear*, Volume 146, pages 89 - 97, 1991.
8. **JACKO, M.G.; TSANG, P.H.S. & S.K. RHEE** – *Wear debris compaction and friction film formation of polymer composites*, *Wear*, Volume 133, pages 23 - 38, 1989.
9. **RHEE, S.K.; TSANG, P.H.S. & Y.S. WANG** – *Friction-induced noise and vibration of disc brakes*, *Wear*, Volume 133, pages 39 - 45, 1989.
10. **HO, T.L.; PETERSON, M.B. & F.F. LING** – *Effect of frictional heating on brake materials*, *Wear*, Volume 30, pages 73 - 91, 1974.
11. **McLOUGHLIN, W.T. & B.H. PRATT** – *The measurement and analysis of brake performance under service conditions*, Conference Proceedings of the I.Mech.E. (Institution of Mechanical Engineers), 1983-2.

12. **TIROVIC, M. & A.J. DAY** – *Disc brake interface pressure distributions*, Conference Proceedings of the I.Mech.E. (Institution of Mechanical Engineers), Number 205, 1991.
13. **WANG, N.** – *The evolution of the pad guided disc brake caliper*, S.A.E. (Society of Automotive Engineers) Technical Paper Series no. 940332, 1994.
14. **SAMIE, F. & D.C. SHERIDAN** – *Contact analysis for passenger car disc brakes*, S.A.E. (Society of Automotive Engineers) Technical Paper Series no. 900005, 1990.
15. **KAO, R.G.; KUO, E.Y. & M.L. ADELBERG** – *A new tyre model for vehicle N.V.H. analysis*, S.A.E. (Society of Automotive Engineers) Technical Paper Series no. 870424, 1987.
16. **BROOKS, P.C.; BARTON, D.; CROLLA, D.A.; LANG, A.M. & D.R. SCHAFER** - *A study of disc brake judder using a fully coupled thermo-mechanical finite element model*, S.A.E. (Society of Automotive Engineers) Technical Paper Series no. 945042, 1994.
17. **MURAKAMI, H.; TSUNADA, N. & T. KITAMURA** - *A study concerned with a mechanism of disc brake squeal*, S.A.E. (Society of Automotive Engineers) Technical Paper Series no. 841233, 1984.
18. **LIMPERT, R.; GAMERO, F.E. & R. BOYER** – *An investigation of brake balance for straight and curved braking*, S.A.E. (Society of Automotive Engineers) Technical Paper Series no. 741086, 1974.
19. **MILLNER, N.** – *An analysis of disc brake squeal*, S.A.E. (Society of Automotive Engineers) Technical Paper Series no. 780332, 1978.
20. **CULP, J.S.** – *Lightweight brake system*, S.A.E. (Society of Automotive Engineers) Technical Paper Series no. 760255, 1976.
21. **ANDERSON, A.E.** – *Truck brake block swell, growth and thermal instability*, S.A.E. (Society of Automotive Engineers) Technical Paper Series no. 902248, 1990.
22. **FLAIM, T.A.** – *Vehicle brake balance using objective brake factors*, S.A.E. (Society of Automotive Engineers) Technical Paper Series no. 890804, 1989.

23. **GARRO, A.** – *Thermal transient analysis of disc brake problems concerning a mathematical model*, S.A.E. (Society of Automotive Engineers) Technical Paper Series no. 811328, 1981.
24. **HIGHLEY, F.H.** – *Techniques for determining the thermal characteristics of brake drums and discs*, S.A.E. (Society of Automotive Engineers) Technical Paper Series no. 710589, 1971.
25. **HARTER, L.L.** – *Evaluation of copper alloy brake discs by thermal modelling*, S.A.E. (Society of Automotive Engineers) Technical Paper Series no. 740560, 1974.
26. **LIMPERT, R.** – *Proportional braking of solid-frame vehicles*, S.A.E. (Society of Automotive Engineers) Technical Paper Series no. 710047, 1971.
27. **NOYES, R.N. & P.T. VICKERS** – *Prediction of surface temperatures in passenger car disc brakes*, S.A.E. (Society of Automobile Engineers) Technical Paper Series no. 690457, 1969.
28. **RHEE, S.K.** – *A comparative study of four alloys for automotive brake drums*, S.A.E. (Society of Automobile Engineers) Technical Paper Series no. 690443, 1969.
29. **RHEE, S.K.** – *An inertial dynamometer evaluation of three alloys for automotive brake drums*, S.A.E. (Society of Automobile Engineers) Technical Paper Series no. 700138, 1970.
30. **SCHWARTZ, H.W.** – *Brake dynamometer evaluation of the Detroit traffic road test*, S.A.E. (Society of Automobile Engineers) Technical Paper Series no. 770026, 1977.
31. **SCHWARTZ, H.W. & L. HARTTER** – *Evaluation of gray iron brake discs for trucks by thermal modelling*, S.A.E. (Society of Automobile Engineers) Technical Paper Series no. 751014, 1975.
32. **STOCKS, A.I.; GIEZENDANNER, H. & H. van den HURK** – *Asbestos-free clutches and brakes reinforced with Kevlar aramid fibres*, International Journal of Vehicle Design, Volume 6, Numbers 4 – 5, July – September 1995.
33. **ROSS, G.A.** – *Asbestos replacement in friction materials*, Conference: *Asbestos Replacement*, U.M.I.S.T. (University of Manchester Institute of Science & Technology), 3rd – 4th April 1984.
34. **WASHABAUGH, F.J.** – *Emcor 66 ultra-short fibers for asbestos-free friction materials*, S.A.E. (Society of Automotive Engineers) Technical Paper Series no. 860630, 1986.

35. **FLETCHER, L.S.; ANDERSON, A.E.; RABINS, M.J.; FOBIAN, J.; RADLINSKI, R.; McCOLLOUGH, J.; RABINOWICZ, E.; NELSON, R.; BARBER, S.; HOESS, J.; FRANCIS, J.; GRATCH, S.; HADEN, J. & K. DUFRANE** – *Analysis of replacing asbestos in automobile and truck brakes*, A.S.M.E. (American Society of Mechanical Engineers), New York, NY, USA, 1988.
36. **AINSCOUGH, T. & G. HESKETH** – *Non wearing braking (a blend to the end?)*, Conference: *Brakes and Braking Systems*, I.Mech.E. (Institution of Mechanical Engineers), 28th April 1993.
37. **WILSON, A.J.; BELFORD, A.J. & G.T. BOWSER** - *Scaled vehicle brake installations for friction material assessment*, Lucas engineering review, Volume 4, Number 1, January 1968.
38. **HARDING, P.R.J. & T. FOWLER** - *The determination of brake lining friction coefficients*, Paper XII (iii), pages 349 - 359.
39. **RUNSAK, R.M.; SPURGEON, W.M. & F.W. ALDRICH** - *Friction material testing*, S.A.E. (Society of Automotive Engineers) Technical Paper Series no. 700517, 1970.
40. **LANDON, G.W.** - *Model 10 brake test instrument*, S.A.E. (Society of Automotive Engineers) Technical Paper Series no. 700374, 1970.
41. **BURKMAN, A.J. & F.H. HIGHLEY** - *Laboratory evaluation of brake lining materials*, S.A.E. (Society of Automotive Engineers) Technical Paper Series no. 670510, 1967.
42. **TIEMANN, R.** - *Investigations to optimize the braking behaviour on uneven roads*, 3rd International E.A.E.C. (European Automobile Engineers Co-operation) Conference, Strasbourg, E.A.E.C. no. 91026, 1991.
43. **RAKOWSKI, W.A.** - *The surface layer of friction plastics*, *Wear*, Volume 65, pages 21 - 27, 1980.
44. **STEIJN, R.P.** - *Metals Engineering Quarterly*, Volume 7 (number 2), page 9, 1967.
45. **TARR, W.R. & S.K. RHEE** - *Static friction of automotive friction materials*, Short Communication, *Wear*, Volume 33, pages 373 - 375, 1975.
46. **GILBERT, G.N.J.** - *The growth and scaling of cast irons in air and steam*, BCIRA Journal, Volume 7, pages 478 - 566, 1959.

47. **PALMER, K.B.** - *Design with cast irons at high temperatures, Part 1: Growth and scaling*, Report 1248, BCIRA.
48. **KUBASCHEWSKI, O.; ALCOCK, C.B. & P.J. SPENCER** - *Materials Thermochemistry* (formerly: *Metallurgical Thermochemistry*), 6th edition (revised), Publisher: Pergamon Press Ltd., 1993.
49. **MONDADORI, A. (ed.)** - *The Macdonald encyclopaedia of rocks and minerals*, Macdonald & Co. Ltd., ISBN 0-356-09147-3, 1988.
50. **WATERS, W.C.** - *General purpose automotive vehicle performance and economy simulator*, S.A.E. (Society of Automotive Engineers) Technical Paper Series no. 720043, 1972.
51. **WINKLER, C.B. & R.D. ERVIN** - *A braking efficiency test technique*, S.A.E. (Society of Automotive Engineers) Technical Paper Series no. 750398, 1975.
52. **TIMTNER, K. & D. DUCHSTEIN** - *Establishment of vehicle braking behaviour patterns with special reference to U.S. and European test procedures*, S.A.E. (Society of Automotive Engineers) Technical Paper Series no. 810311, 1981.
53. **JACKO, M.G. & R.T. DuCHARME** - *Simulation and characterization of used brake friction materials and rotors*, S.A.E. (Society of Automotive Engineers) Technical Paper Series no. 730191, 1973.
54. **OEHL, K-H. & H-G. PAUL** - *Brake linings for road vehicles: development and testing*, Verlag Moderne Industrie A.G. & co., 1990.
55. **KISSANE, M.J.** - *High performance brakes for Ceru-III*, S.A.E. (Society of Automotive Engineers) Technical Paper Series no. 910576, 1991.
56. **SAENGER, K. & K. STEINMETZ** - *No putting the brakes on amborite*, Industrial Diamond Review, Volume 42, Number 493, pages 350 – 355, June 1982.
57. **ABENDROTH, H. & W.F. FAGAN** - *New optical method of testing vibration, strain and heat distribution on rotating automotive components*, ISATA 84050, pages 839 – 851 / S.A.E. (Society of Automotive Engineers), 1984.

58. **LAIGHT, D.J.; PHILLIPS, M.; GENWAY-HADEN, R. & D. ADAMS** – *Improvement of low frequency vibration front wheel drive cars*, **AUTOTECH '95**, I.Mech.E. (Institution of Mechanical Engineers), C498/13/125, 1995.

59. **RHEE, S.K. & P.A. THESIER** - *Effects of surface roughness of brake drums on coefficient of friction and lining wear*, S.A.E. (Society of Automotive Engineers) Technical Paper Series no. 720449, 1972.

60. **DAY, A.J.** - *Modern friction materials*, pages 1 - 5, original source unknown.

61. **BRANDWOOD, D. & R. WHITAKER** - *Metallurgical study of blue spotting in cast iron*, B.B.A. Friction Ltd. (formerly Mintex Don Ltd.) Research and Development Report no.: MD 1116, October 1987.

62. **YANG, H.H.** - *Kevlar aramid fiber*, John Wiley & Sons Ltd., ISBN 0 471 93765 7, 1993.

Figure 1:

Interaction diagram showing the factors involved in automotive braking. Duplicated from reference 25, courtesy of Ferodo Ltd.

The factors involved in automotive braking and their interactions



Figure 2:

Common modes of thermo-mechanical distortion affecting disc brake rotor geometry and hence friction pair coupling during automotive friction braking. Note: Distortion magnitudes have been exaggerated for ease of visualisation; typical axial displacements <math>< 250 \mu\text{m}</math>.

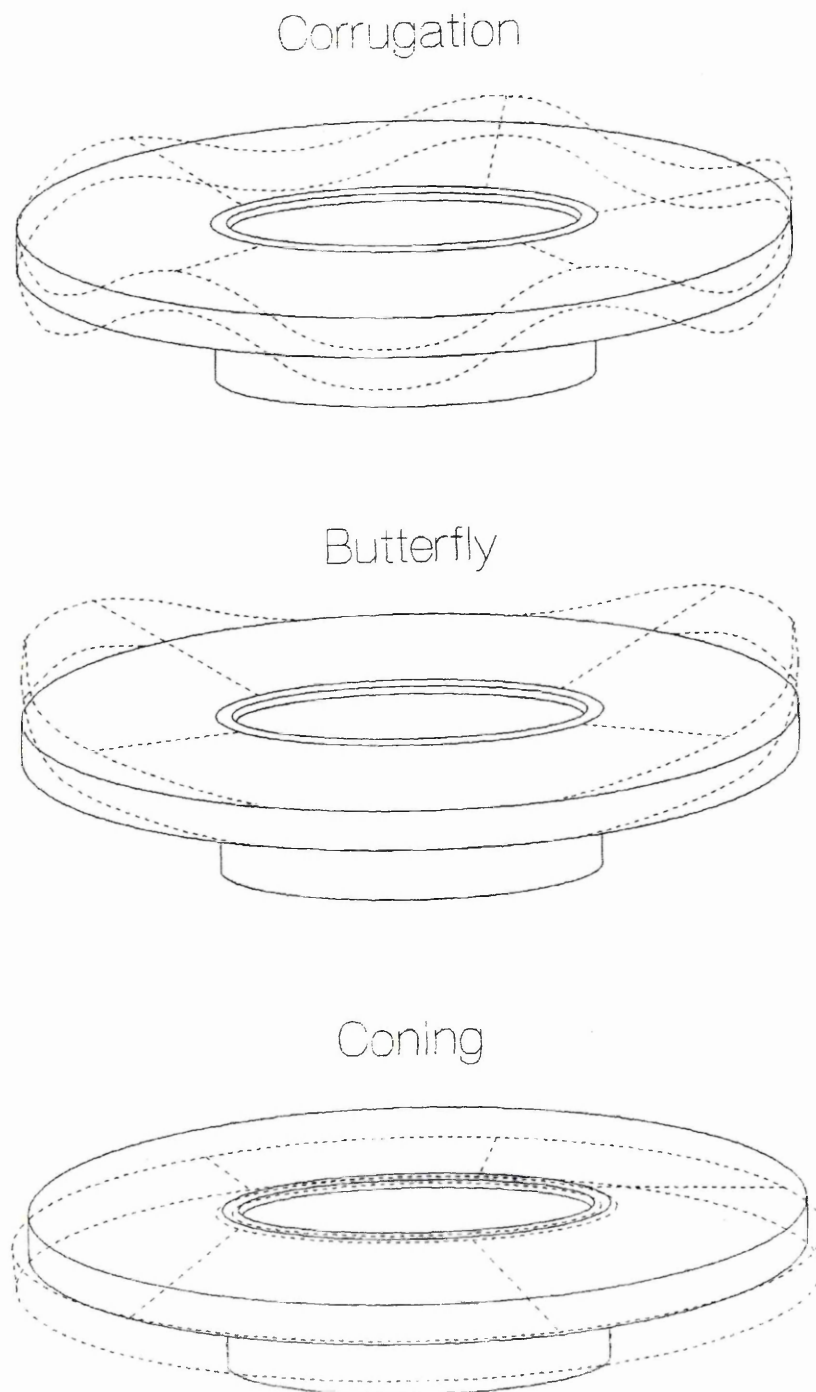


Figure 3:

Hardness variations through the cross-section of a critical focal hot spot, i.e. bluespot, as a result of microstructural phase transformations. Modified from reference 75.

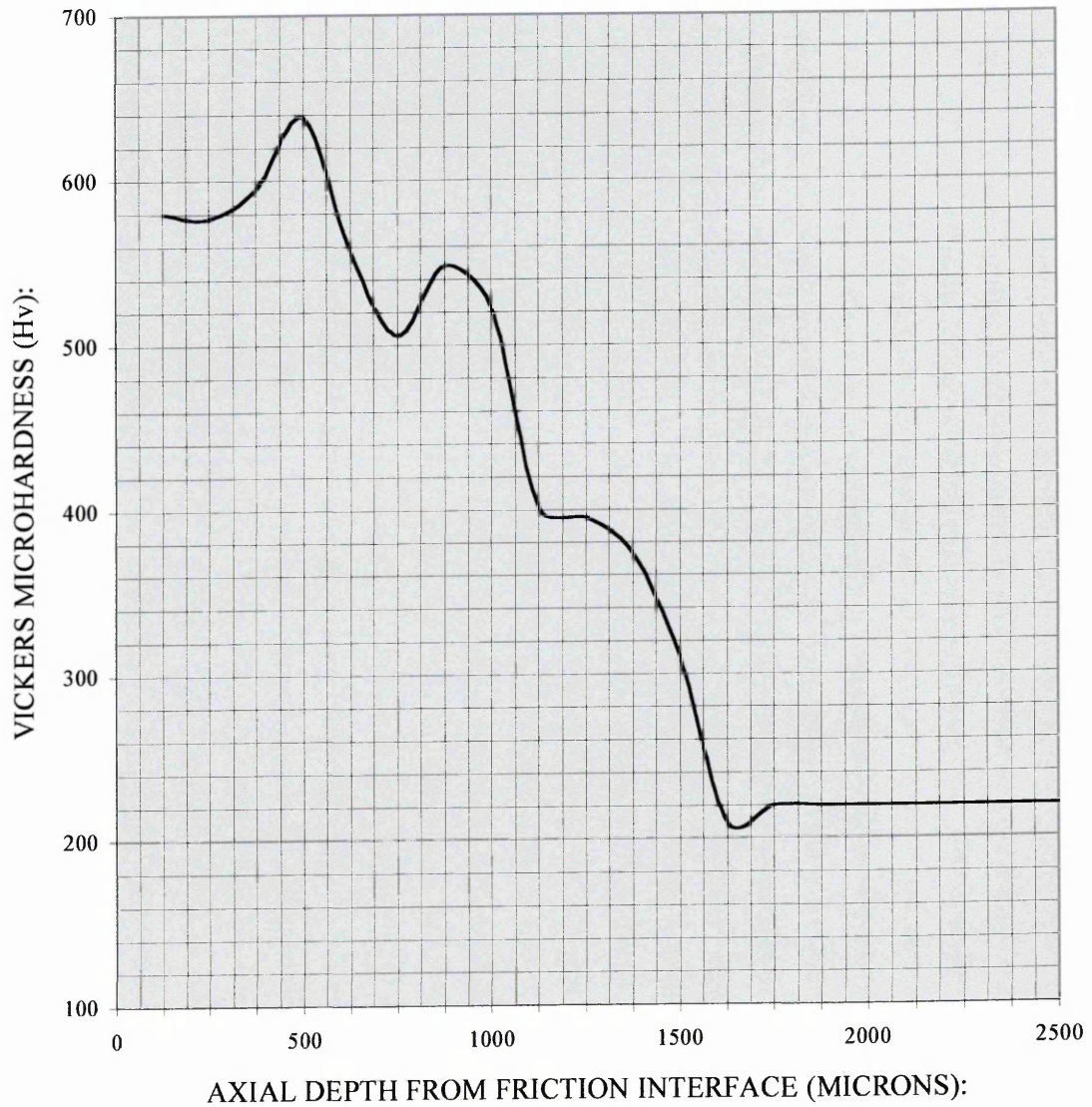


Figure 4:

Commonly manufactured non-conformities contributing to the causes of cold judder. Those characteristics pictured are, from the top; inherent rotor runout, inherent disc thickness variation and inherent hub-face runout. (For each example, the effect has been significantly exaggerated.)

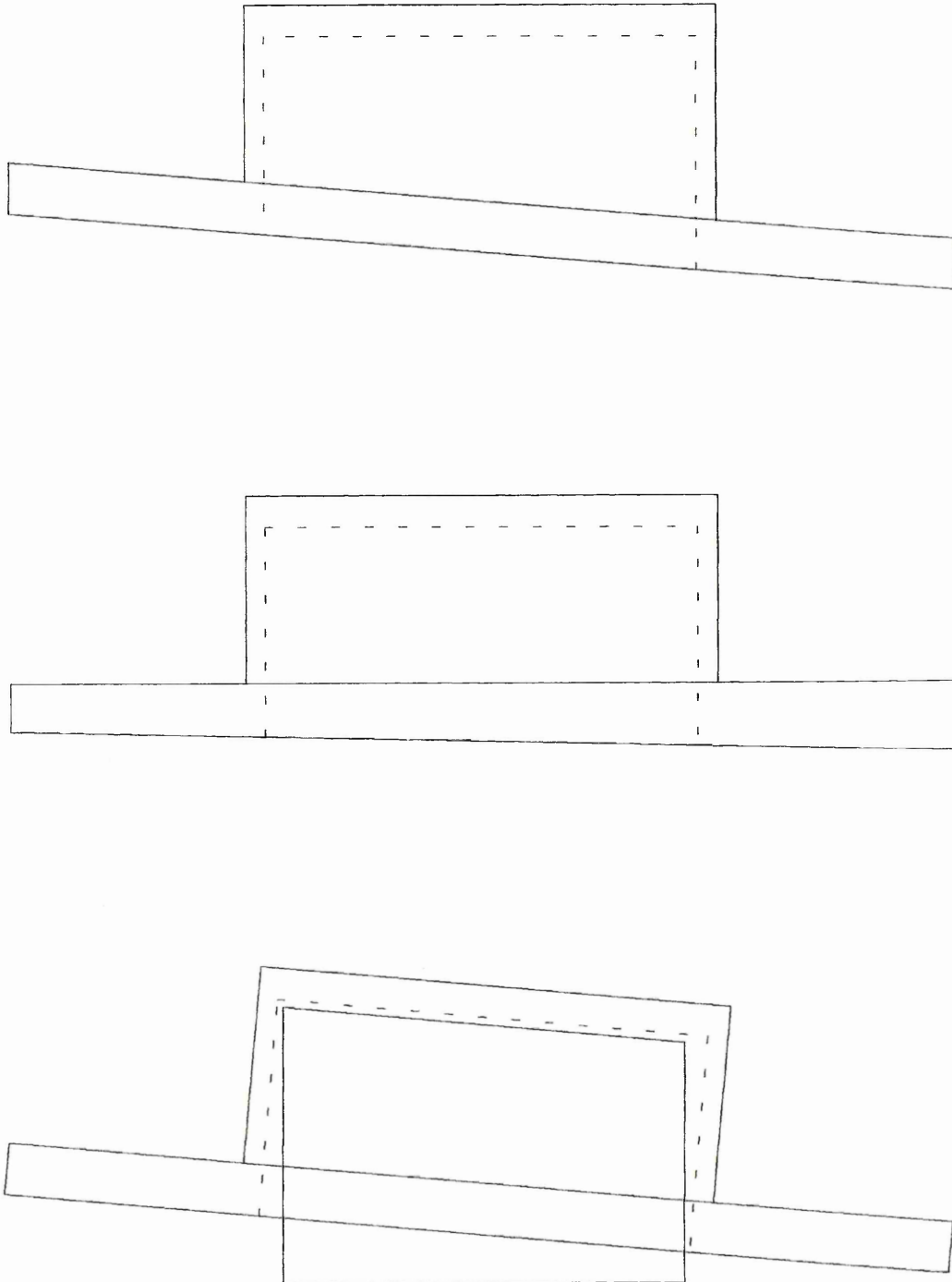


Figure 5:

Schema illustrating the nature and scale of values of peak-to-peak or Total Indicated Runout (T.I.R.) as a result of axial side-face rotor runout.

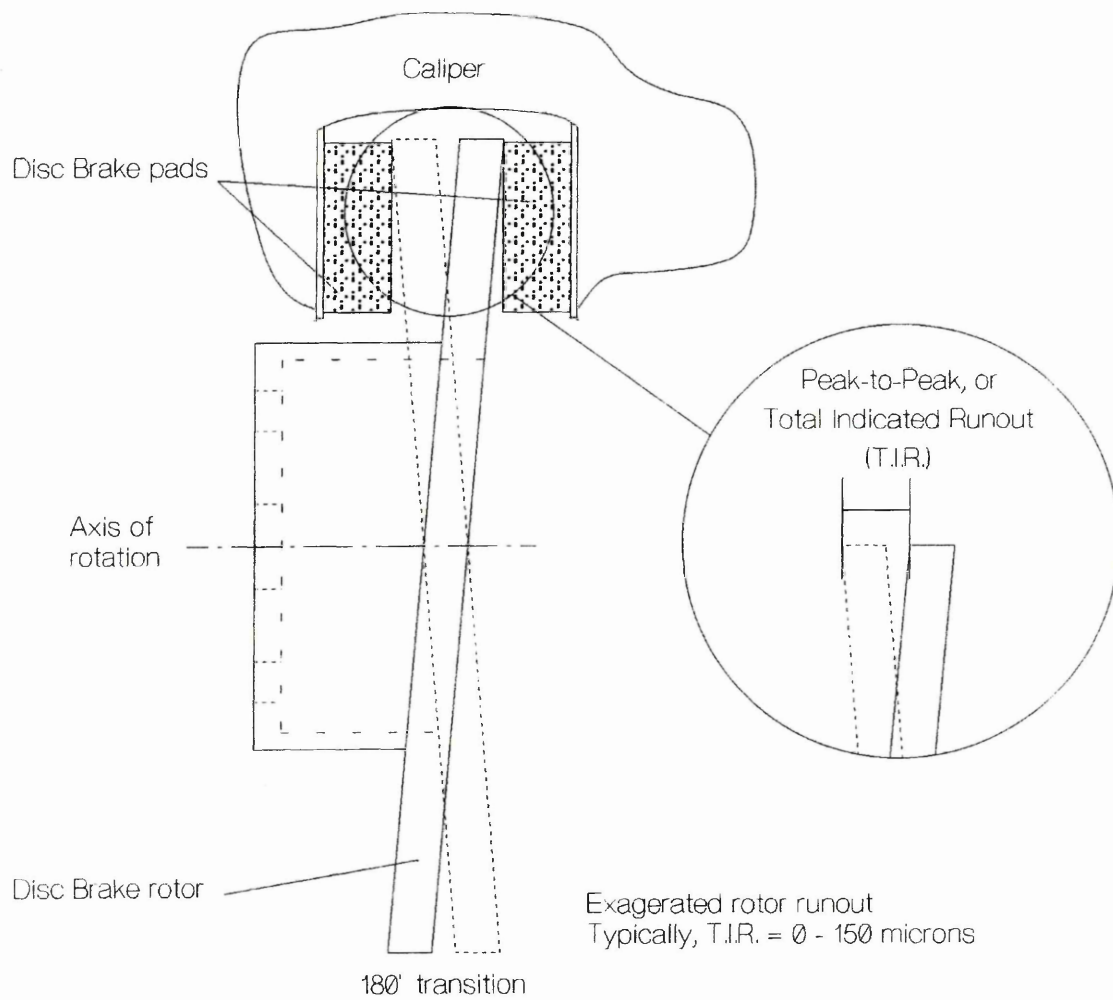


Figure 6:

Schema illustrating the anticipated, uncorrected wear effect of cyclic, intermittent abrasive contact between friction material stator and disc brake rotor as a result of axial side-face rotor runout.

Duplicated and modified from references 55 and 56.

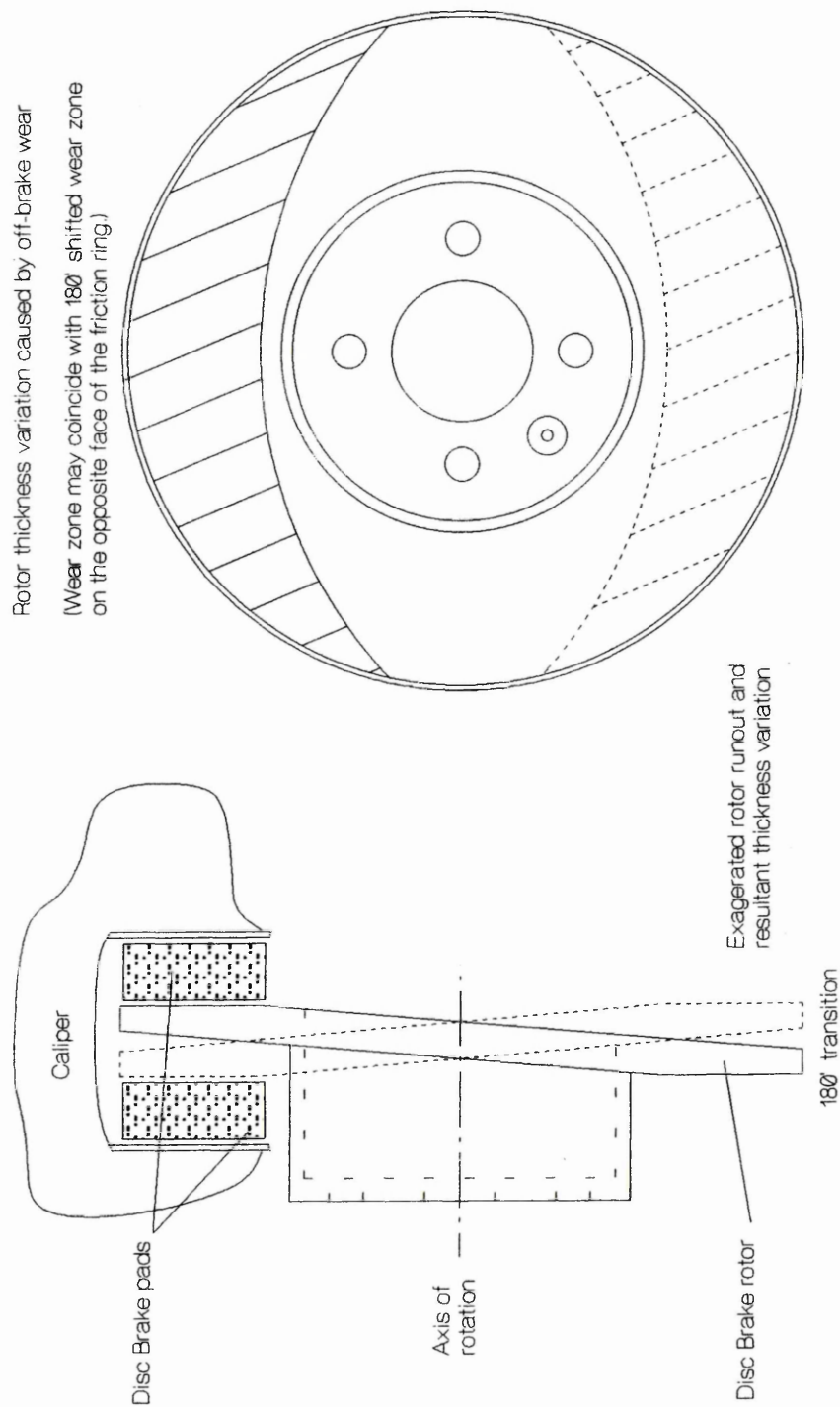


Figure 7:

Plot illustrating the nominal relationship between Total Indicated Runout (T.I.R.) and Disc Thickness Variation (D.T.V.) with increasing off-brake driving distance. Note: The indicated judder sensitivity may vary markedly and is vehicle dependent.

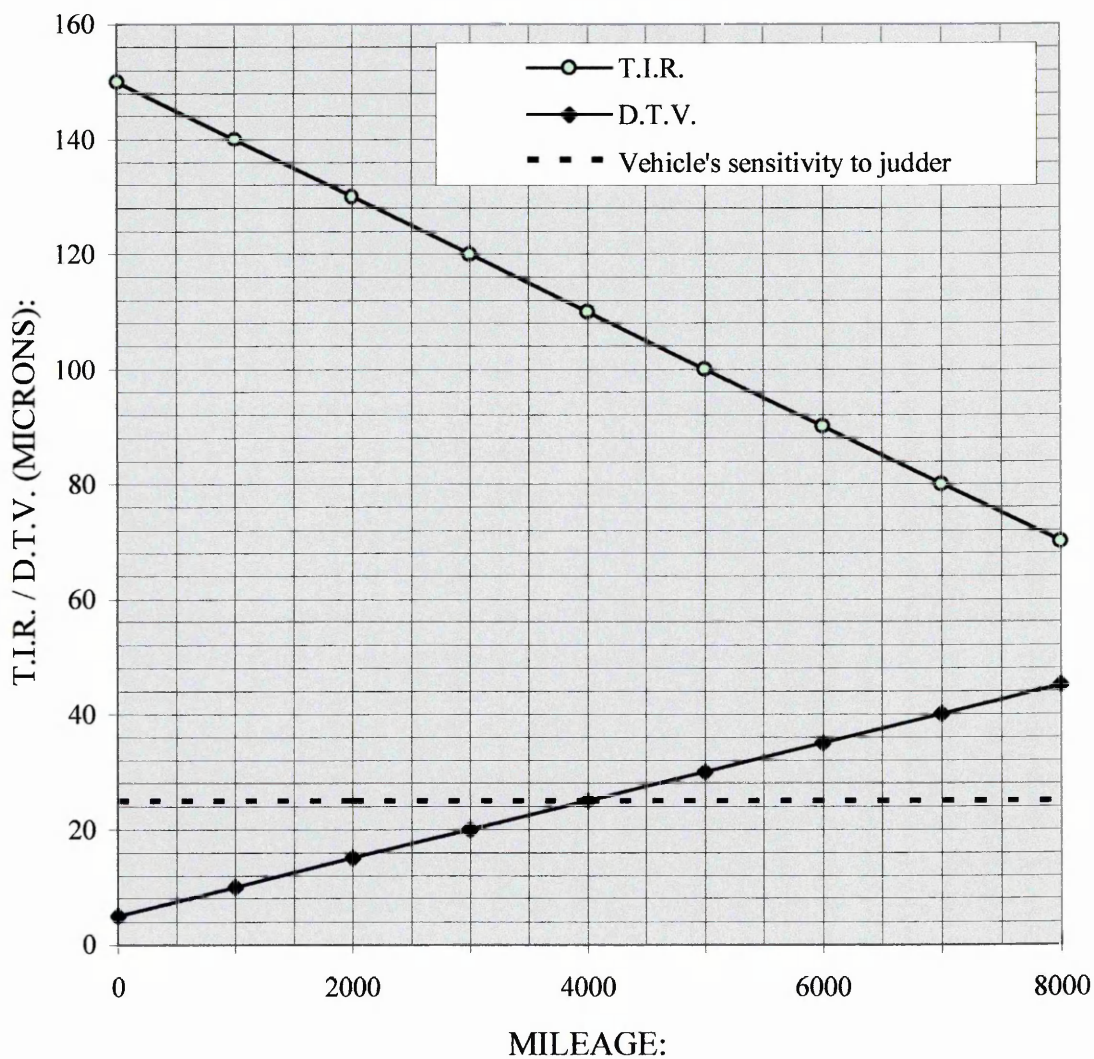


Figure 8:

Schema illustrating a virtual contribution to static D.T.V. as perceived by the friction material pads and caliper. Duplicated from reference 77.

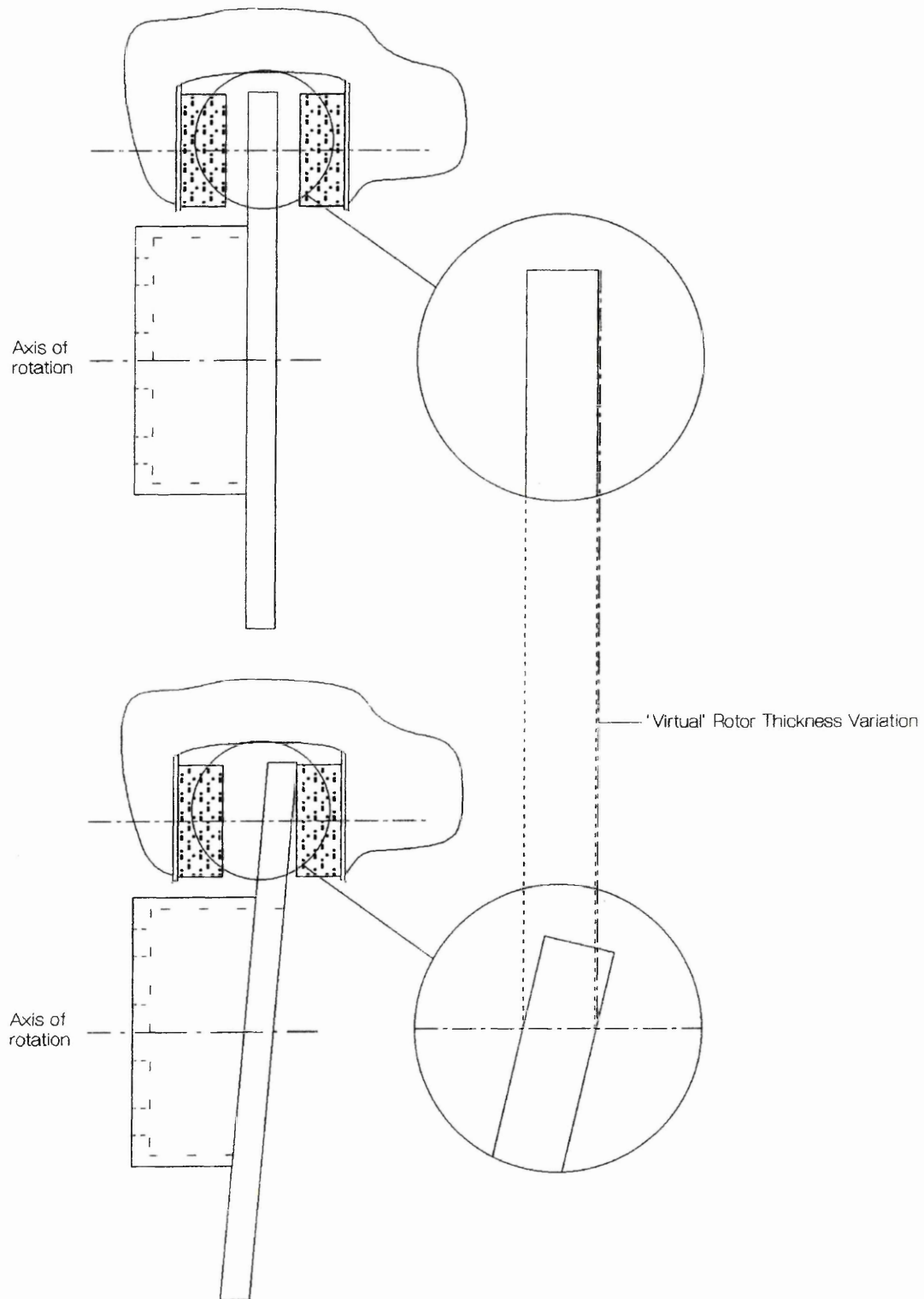


Figure 9:

Schema of acting forces affecting dynamic S.R.O. and apparent D.T.V. as perceived by the friction material pads and caliper. Duplicated from reference 77.

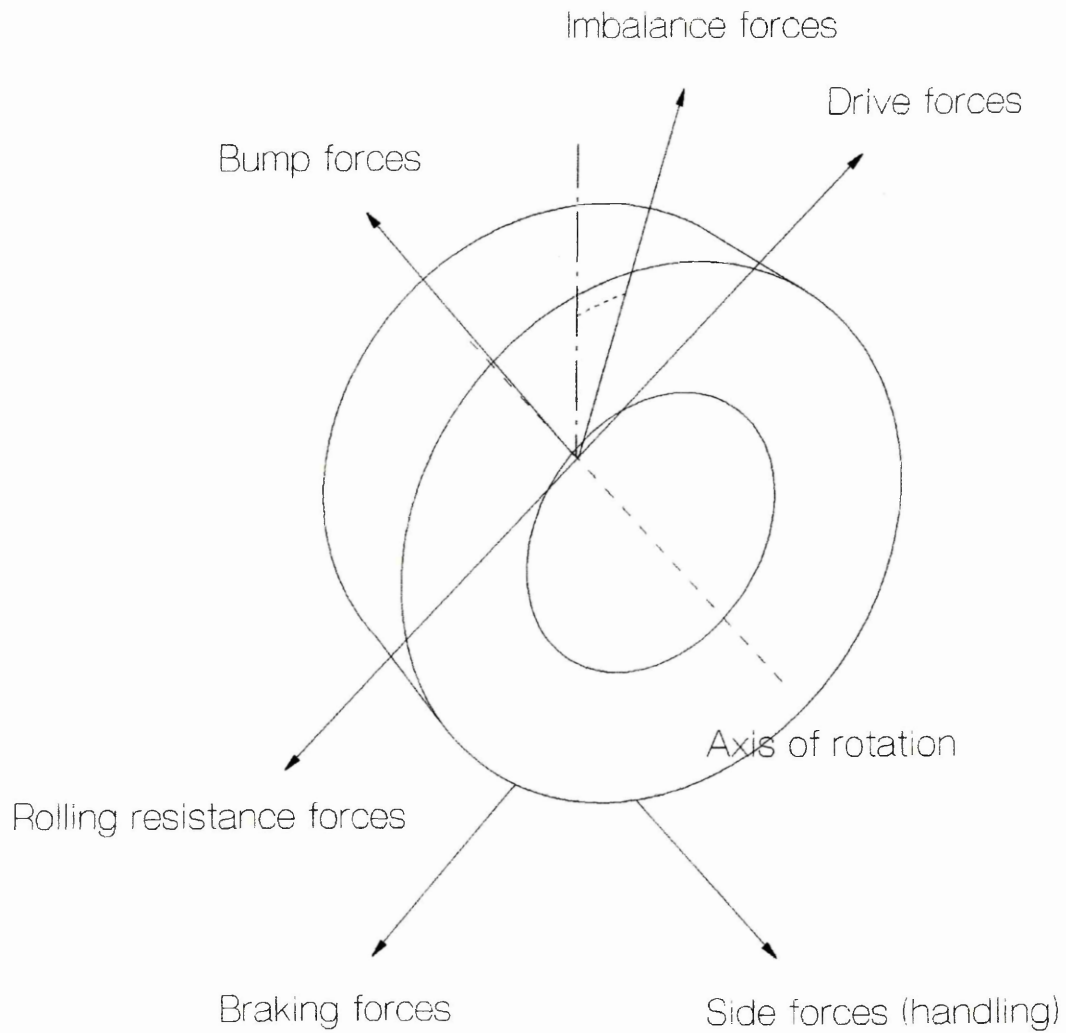


Figure 10:

Plot showing the apparent variation in dynamic coefficient of friction as a function of rubbing velocity with increasing normal brake force. Note: The limiting step function noted to operate between 100 N and 300 N was speculatively attributed to abutment losses within the test rig caliper. Adapted from reference 80.

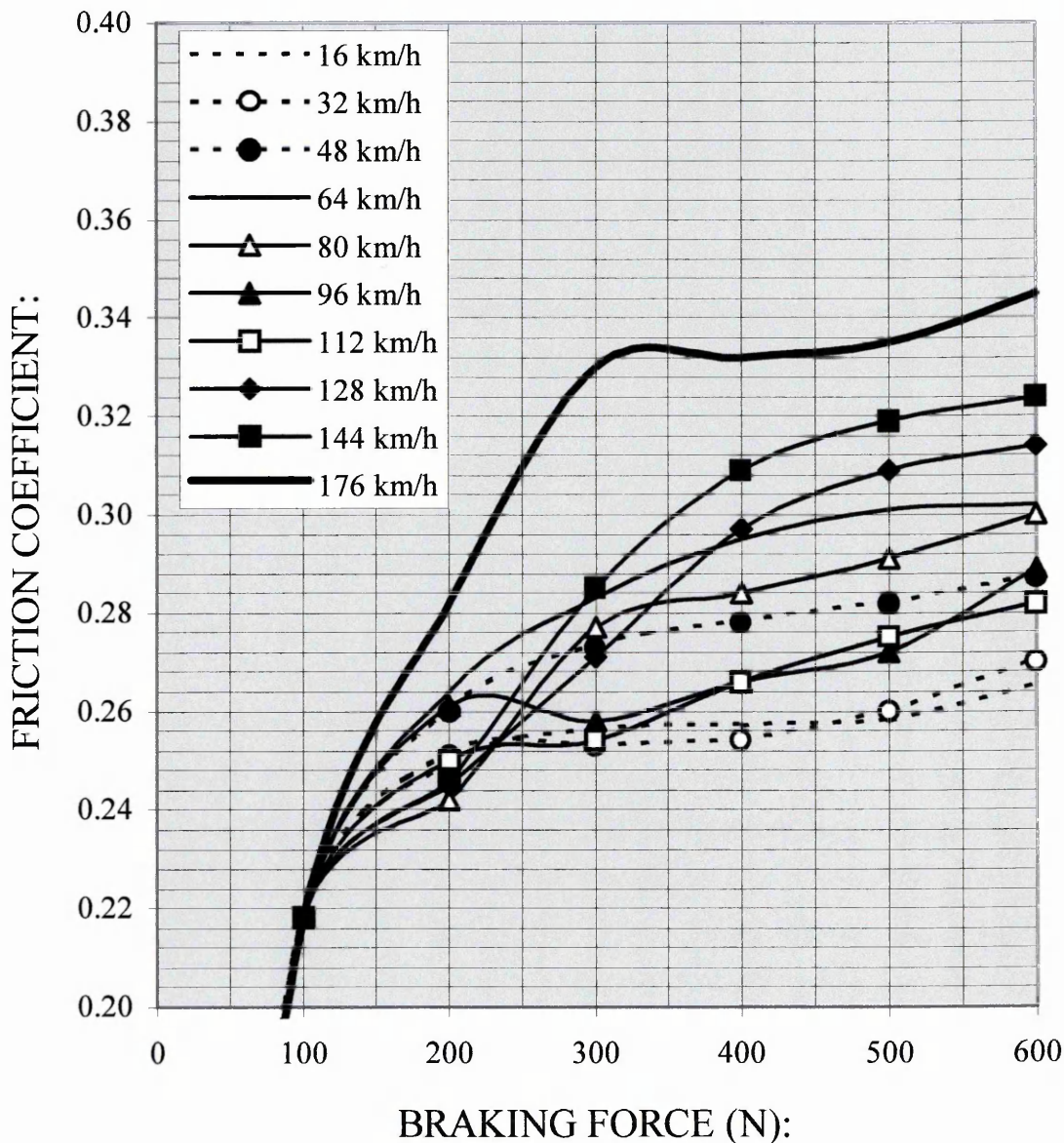


Figure 11:

Plot showing the suggested relation between Disc Thickness Variation (D.T.V.) and the product of abrasive friction modifier hardness and volume fraction. Duplicated from reference 84.

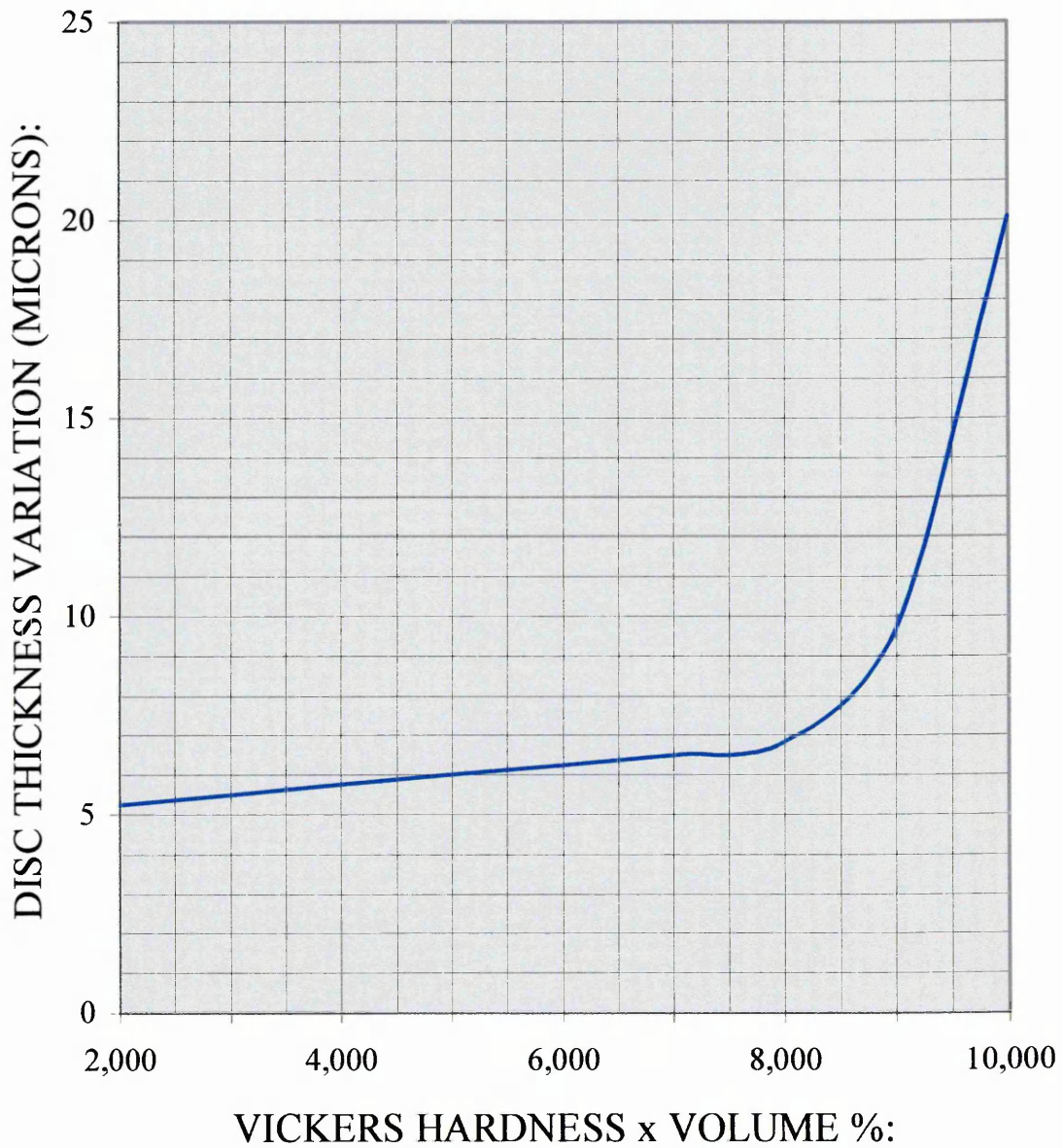


Figure 12:

Schema of the principal component elements and sub-systems of the potential vibration transmission path in a light passenger vehicle.

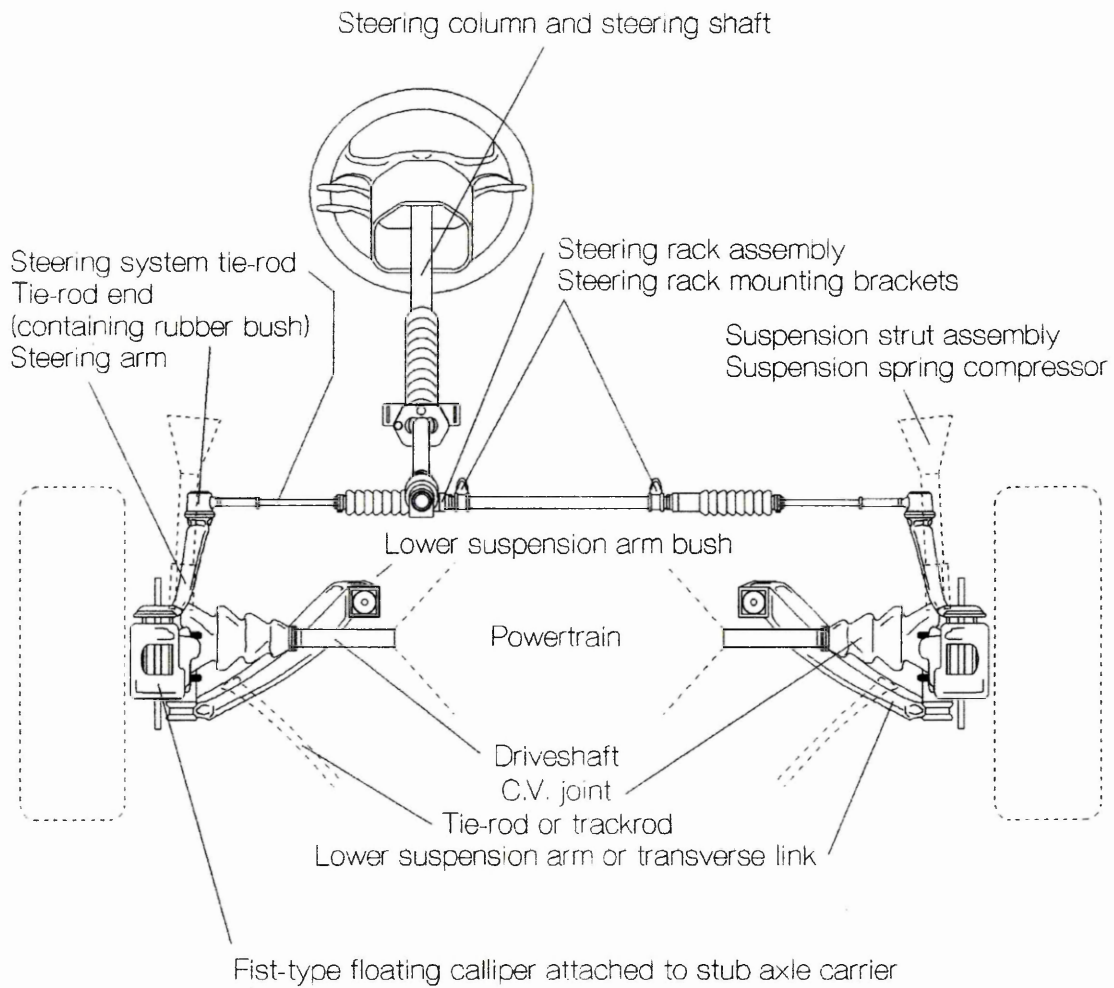


Figure 13:

Vibration transmission diagram determined via Taguchi methodology and computerised vehicular response modelling (60).

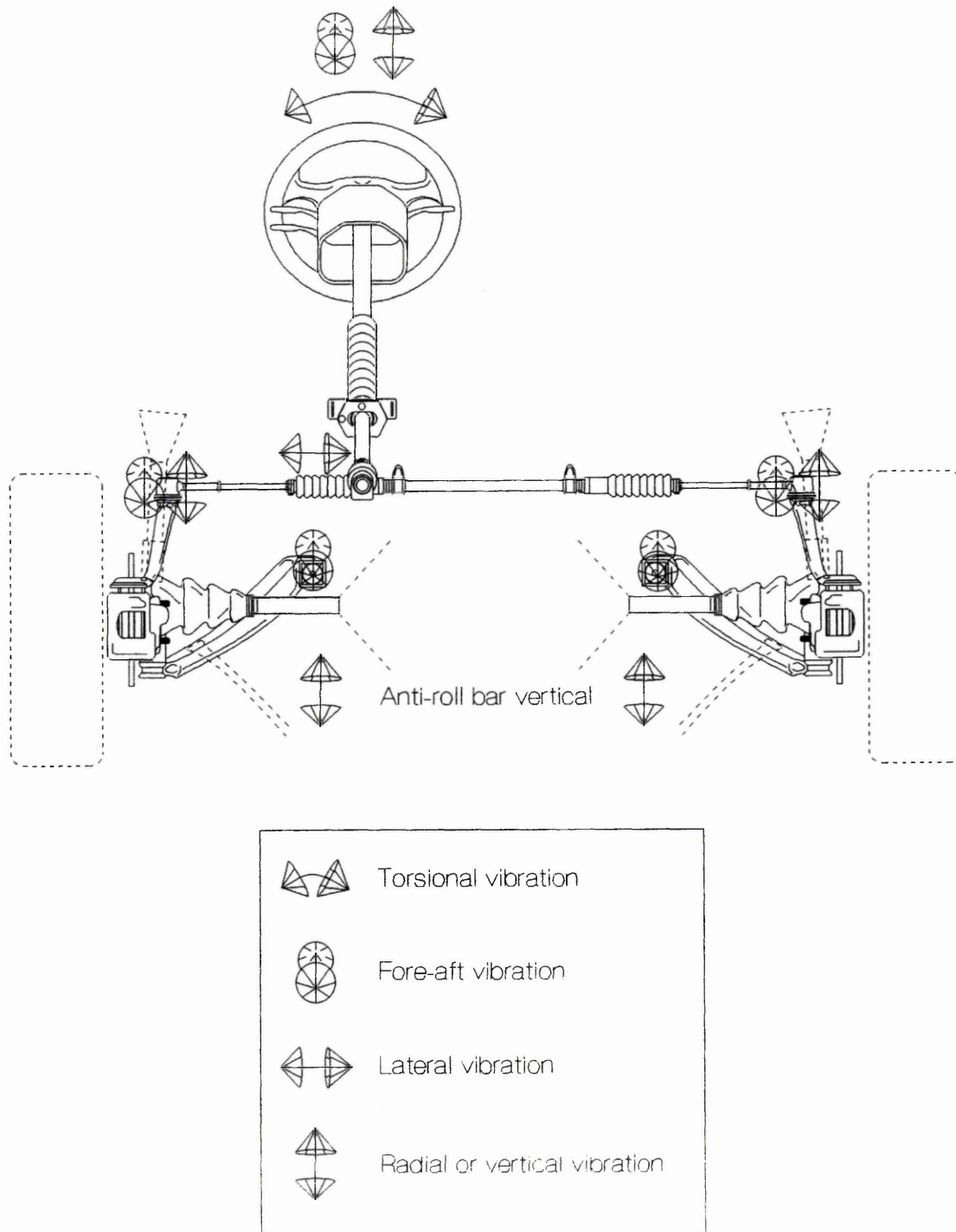


Figure 14:

Vibration transmission diagram determined via physical elasto-kinematic motion sensors during vehicle-based field trials (77).

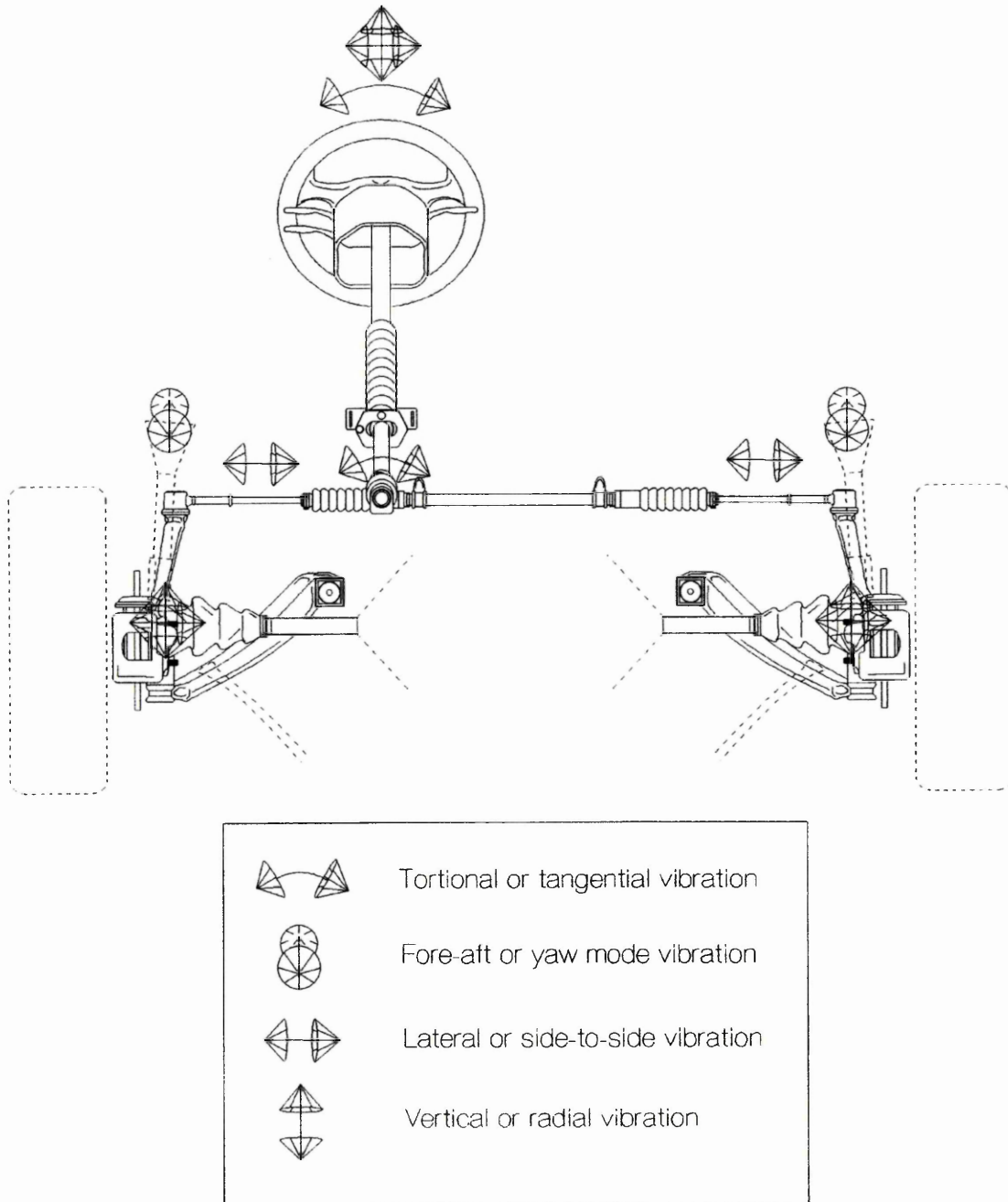


Figure 15:

Schematic representation of a 'cut-away' caliper manifesting androgynous (floating and stationary) characteristics illustrating the arrangement of hydraulic piston chamber, cylinder, fully retracted piston-seal (rectangular cross-section) and associated seating groove. During Off-Brake Wear (O.B.W.) the piston-seal is not fully retracted and the piston cylinder rests on the friction material backing plate, hence the elastic response of the lining is partially dependent upon the elastic response of the piston-seal.

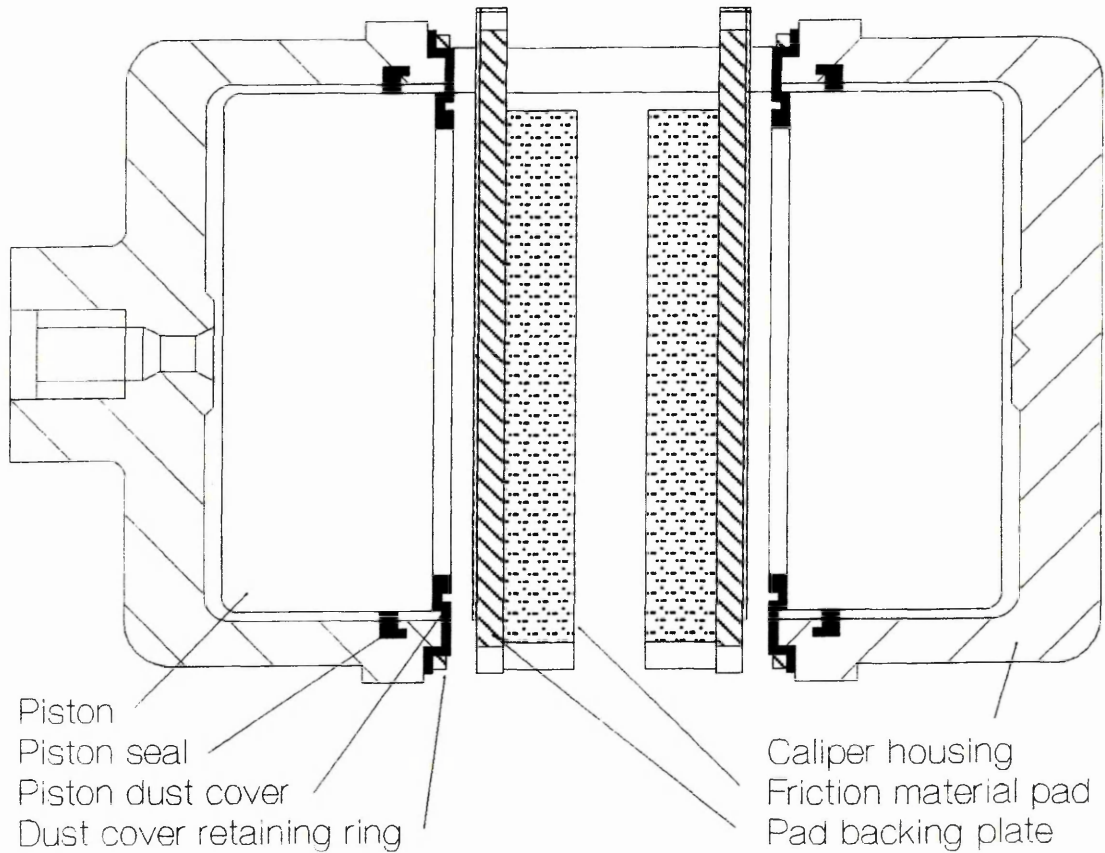
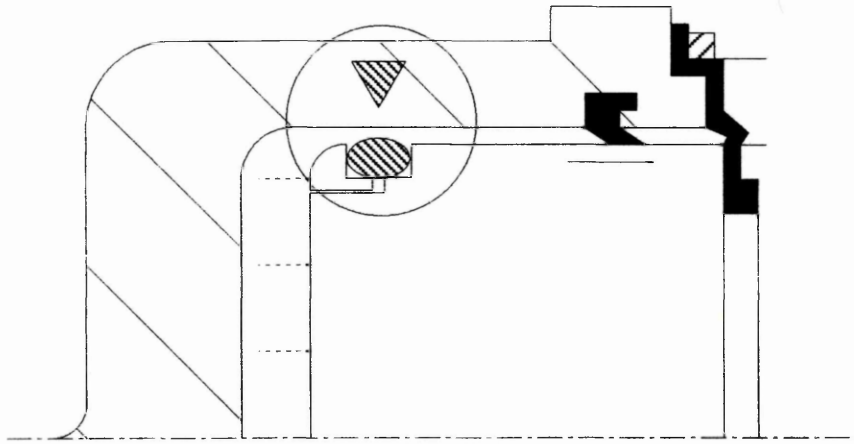


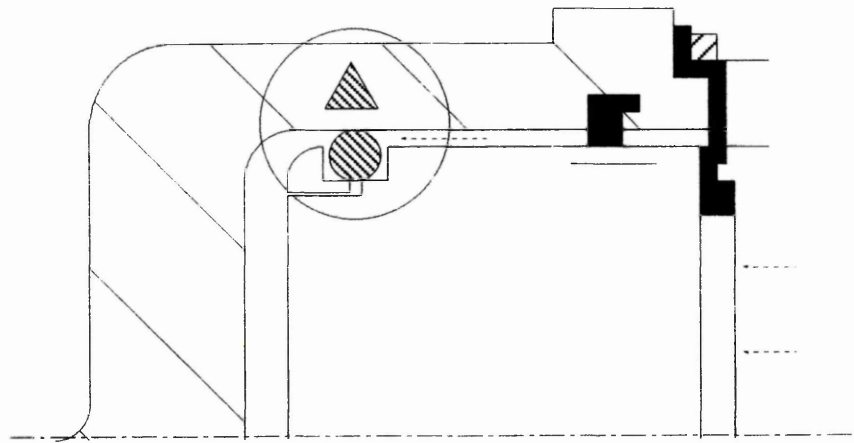
Figure 16:

Schematic representation of a 'cut-away' caliper piston (floating or stationary format) illustrating a mechanical solution to improved piston-seal rollback and hence pad retraction as proposed in reference

89.



Pressure-distorted O-ring



Restored, undistorted O-ring

Figure 17:

Plots showing the variation in both disc brake rotor (top) and stator (bottom) wear, as a function of bulk rotor temperature, in comparative friction pairs employing passive (lightly abrasive) and aggressive (heavily abrasive) pad formulations (unpublished data generated by **Ford Motor Company**).

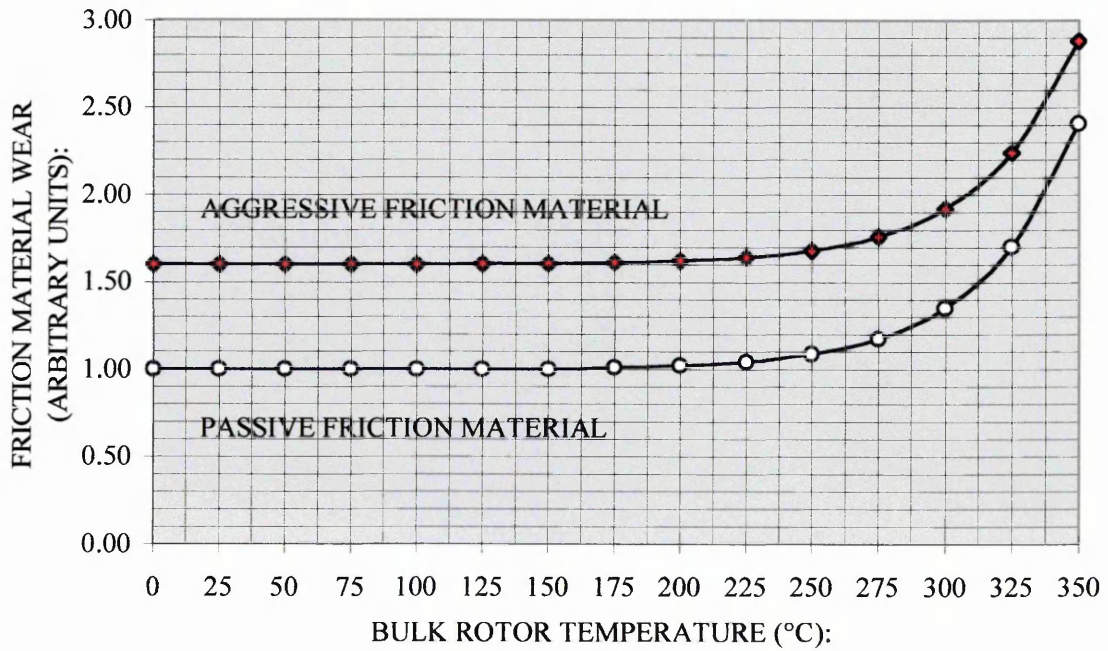
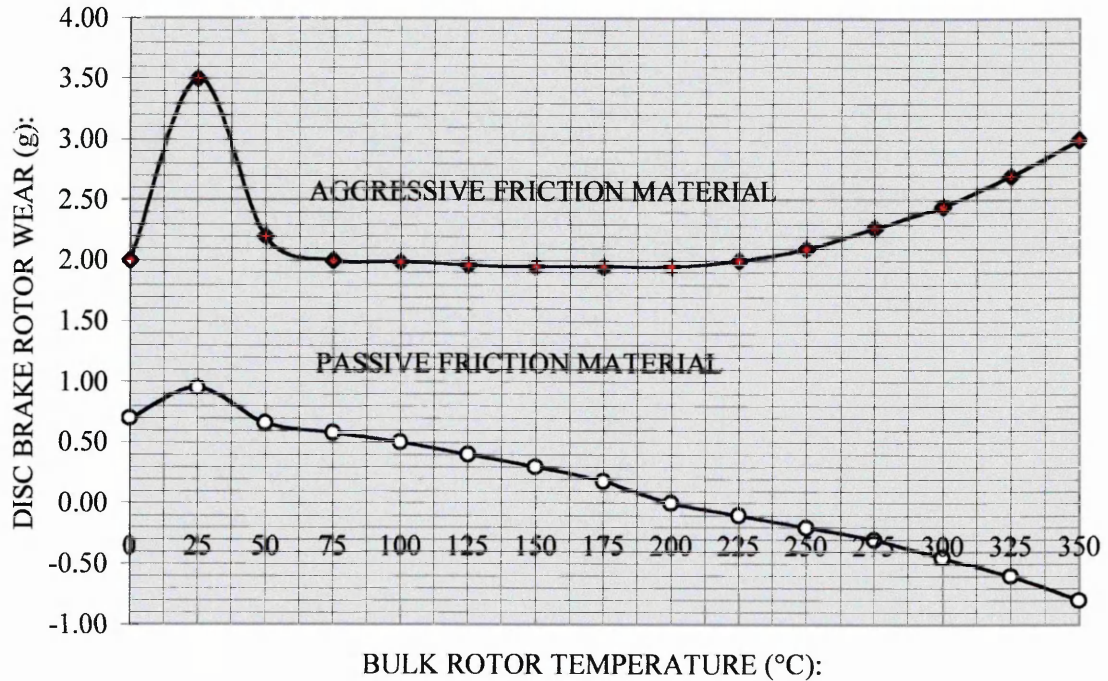


Figure 18:

The phenolic family of thermosetting resins used as the binding agent constituent in automotive friction materials. Duplicated from reference 84.

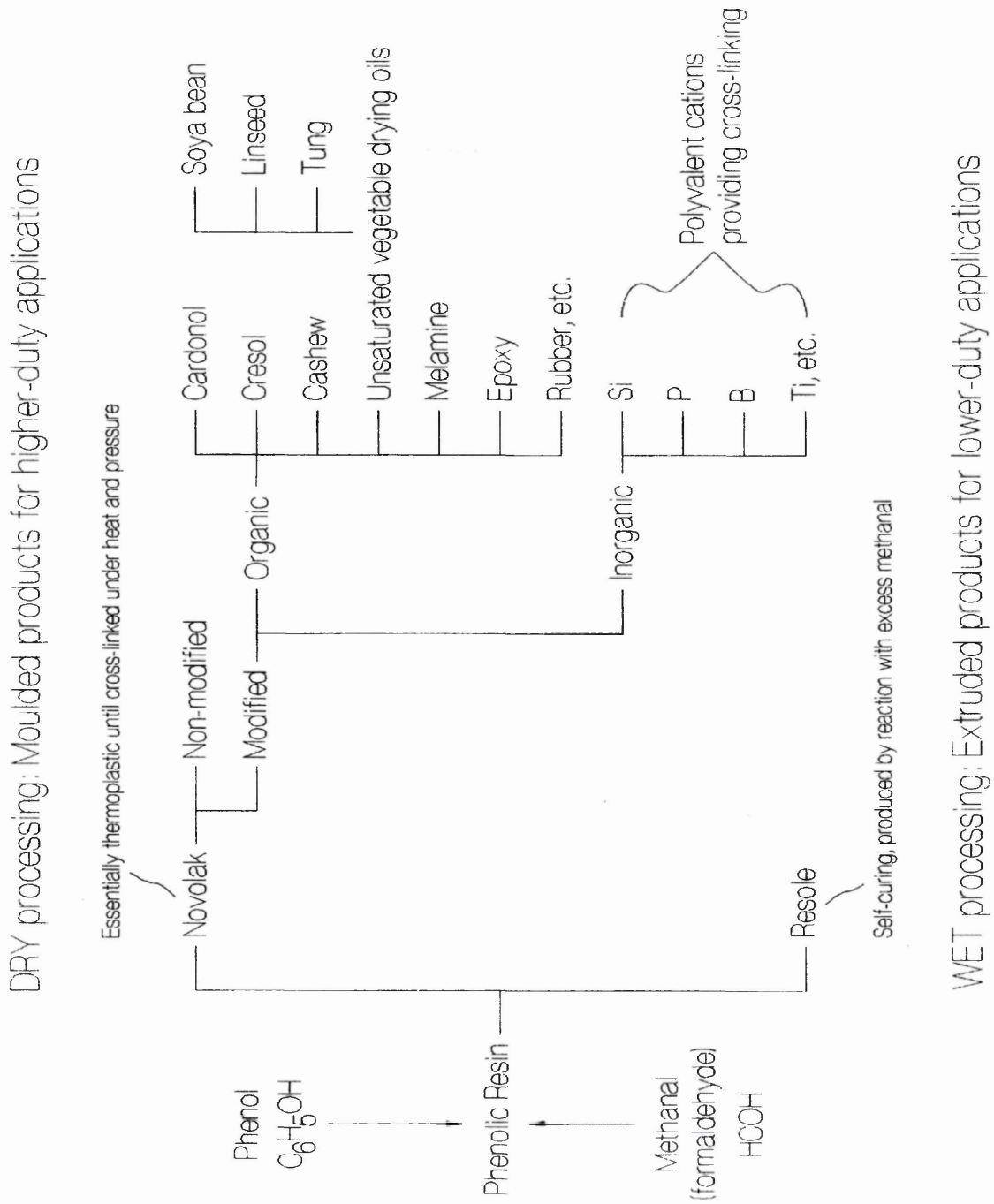


Figure 19:

Plot showing the transition from a combined abrasion-adhesion friction material wear regime to an essentially ablative wear regime in response to increasing interfacial temperature. Duplicated from reference 117.

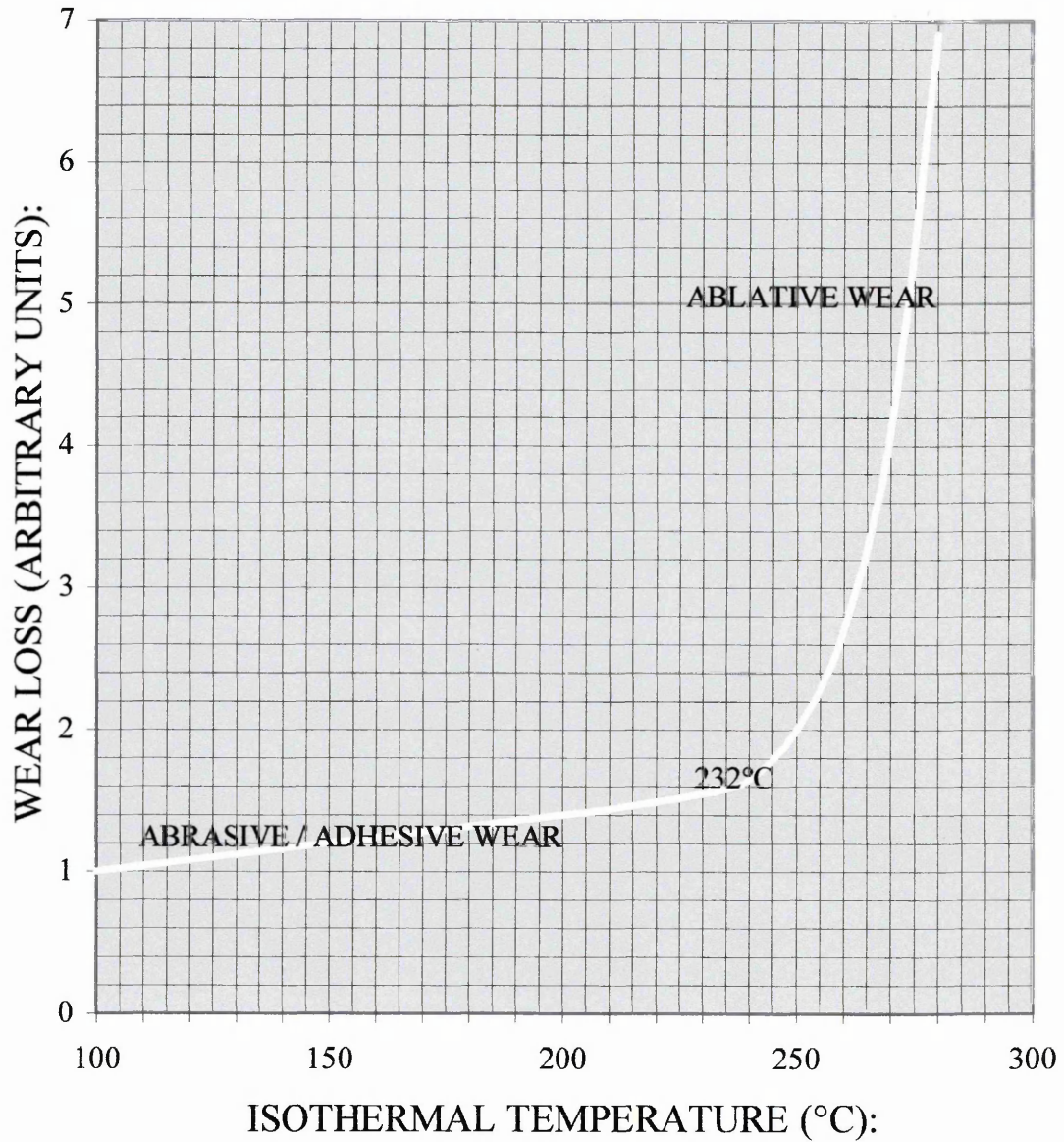


Figure 20:

The onset of material transfer and the effect on dynamic friction coefficient in relation to the bedding-in period in dry sliding contact. Adapted from reference 129.

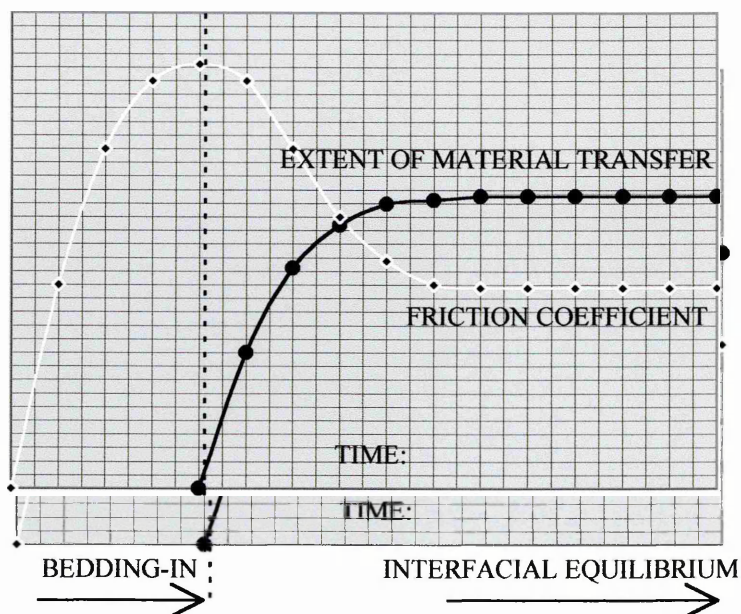


Figure 21:

The micromechanical process by which transfer films are generated between surfaces in sliding contact.

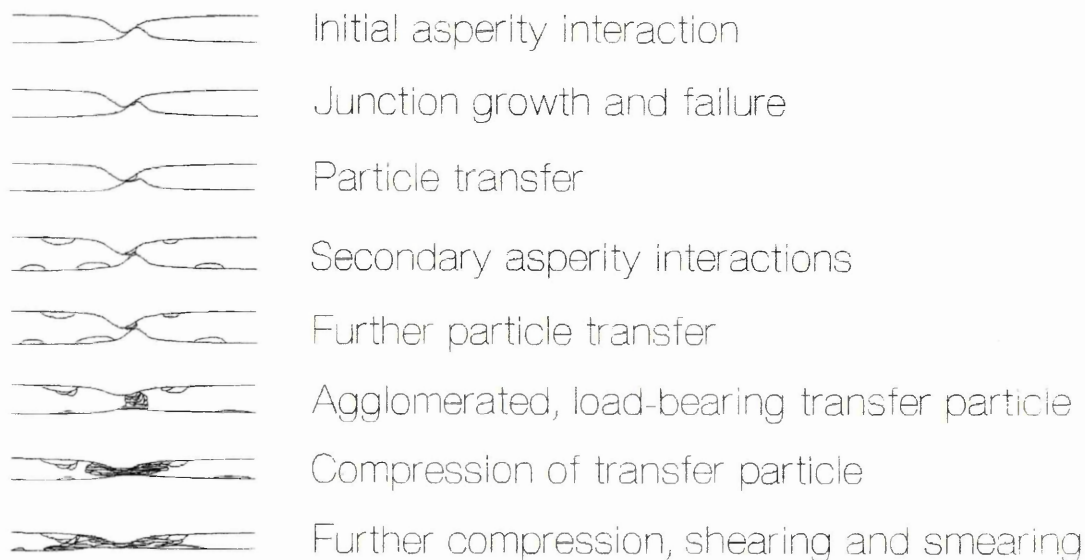


Figure 22:

Ellingham-type diagram showing the relative affinities, in terms of Gibbs energy of formation / reaction, of various tribointerfacial constituents for one mole of gaseous oxygen in an atmosphere of air.

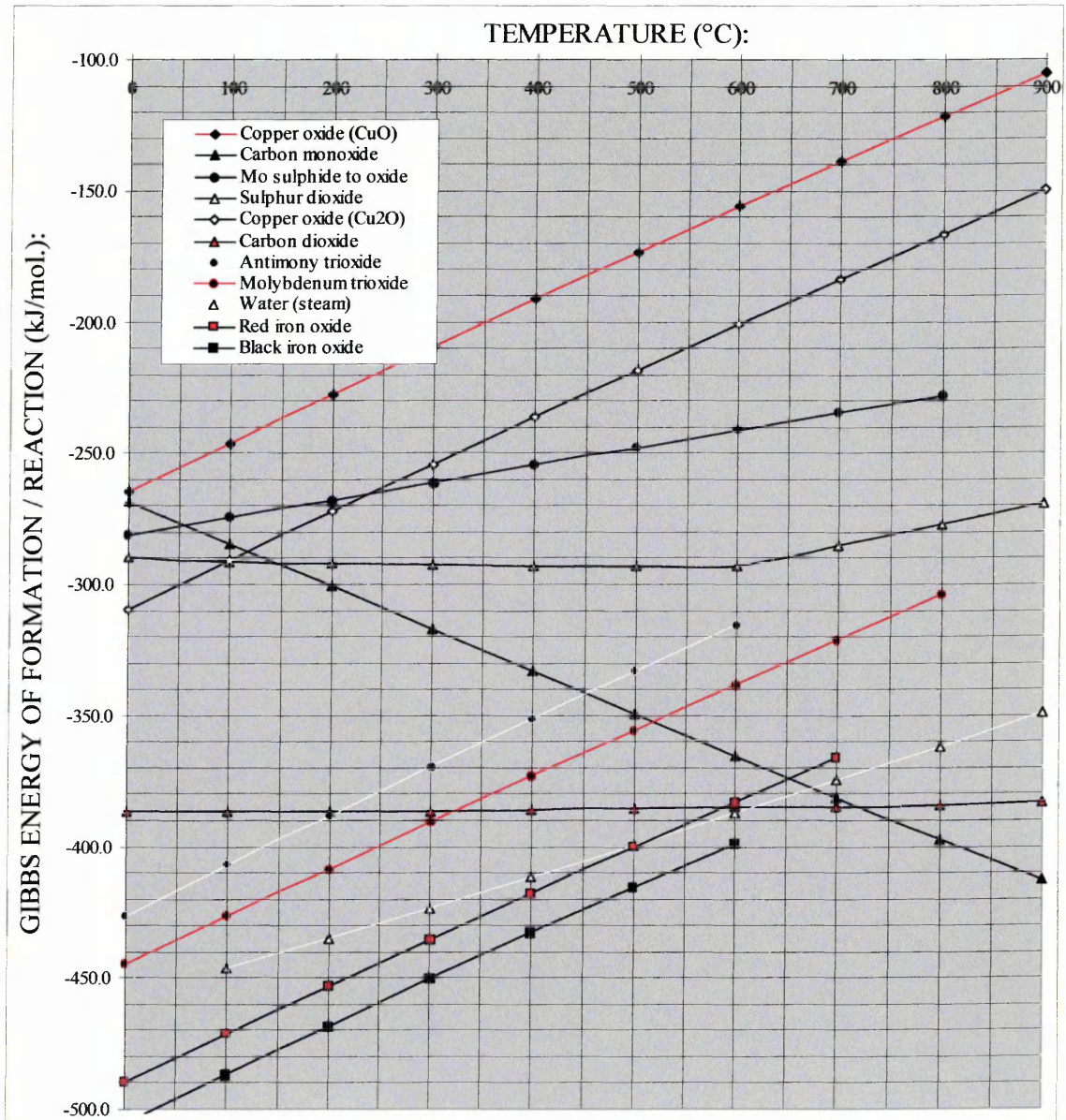


Figure 23:

Ellingham-type drawing showing the relative thermodynamic stability, in terms of Gibbs free energy of reaction per mole of gaseous S_2 , of lubricious metallic sulphides either used in the formulation of friction materials or potentially active at the tribointerface.

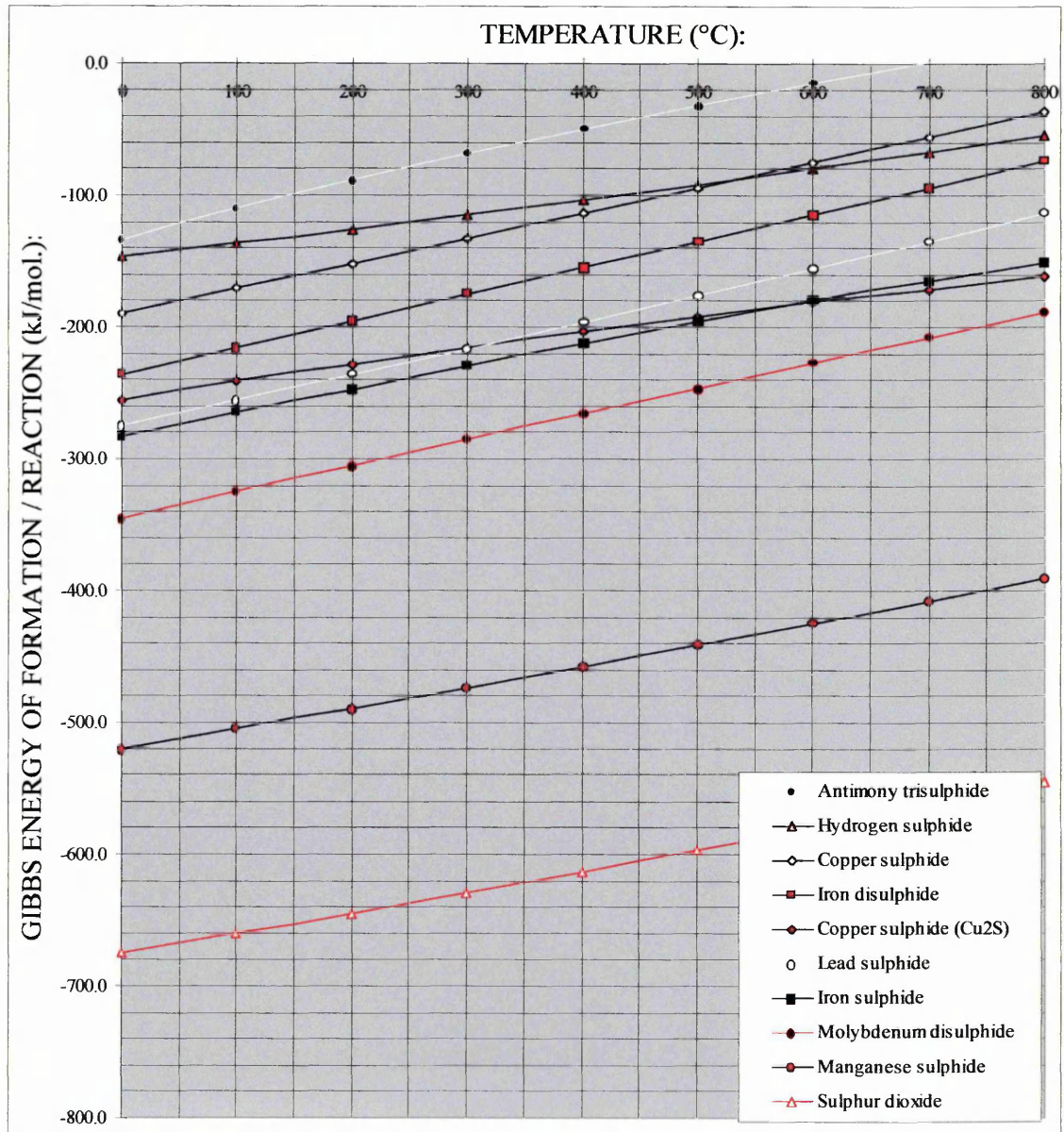


Figure 24:

Schematic systems layout of the Disc Thickness Variation Evaluation rig.

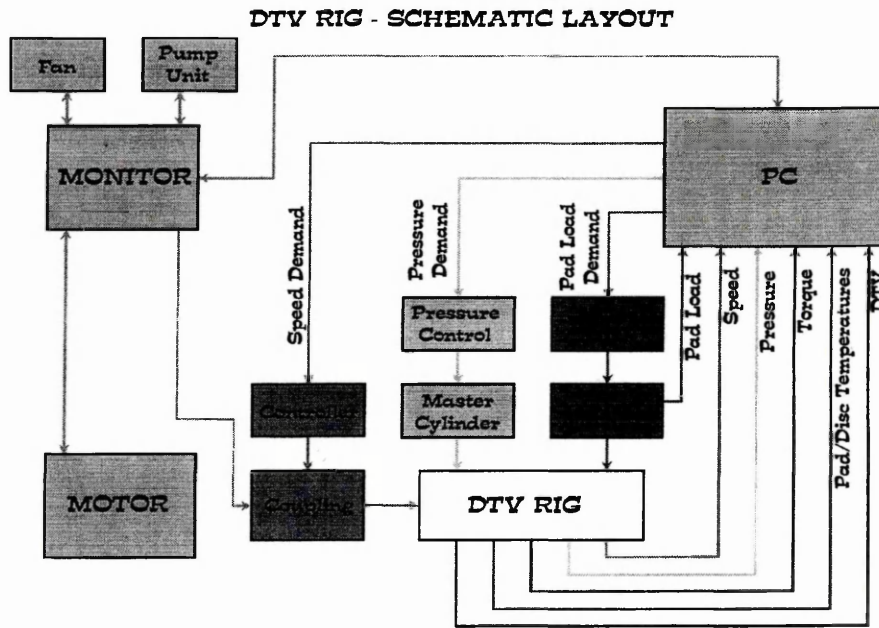


Figure 25:

Functional data-flow and operations diagram of the Disc Thickness Variation Evaluation rig.

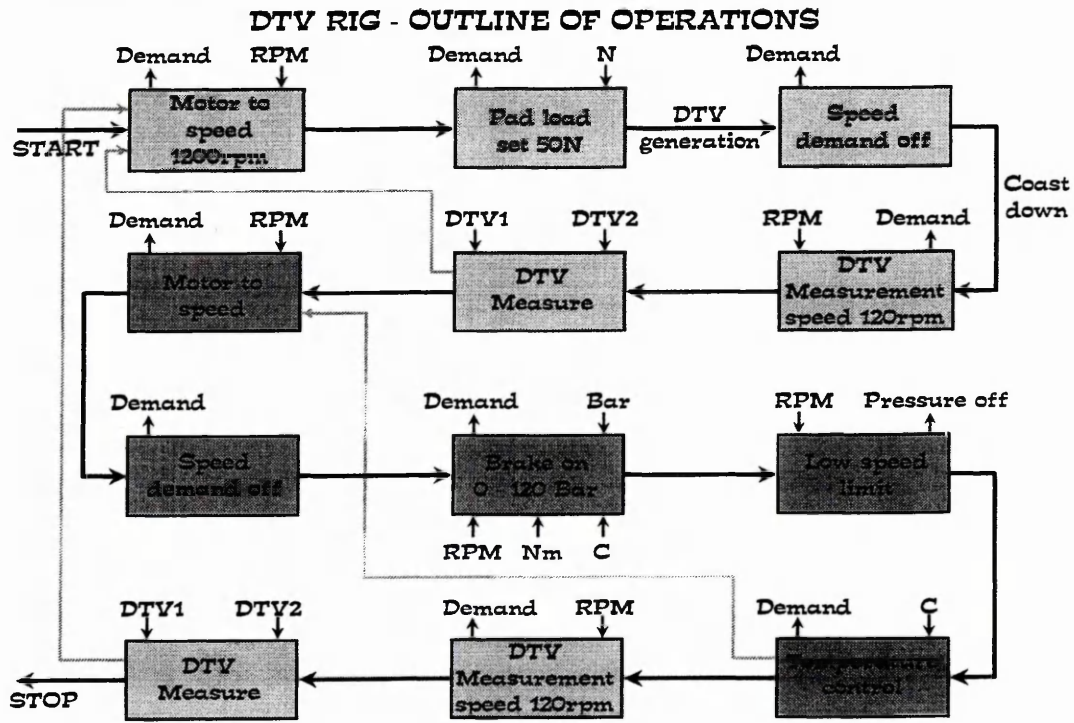


Figure 26:

Computerised Monte-Carlo trajectory simulation of the electron interaction volume generated when an electron beam of 25 kV, 20 kV, 15 kV, 10 kV and 5 kV impinge on an oxidised iron substrate bearing a micron-thick oxide film.

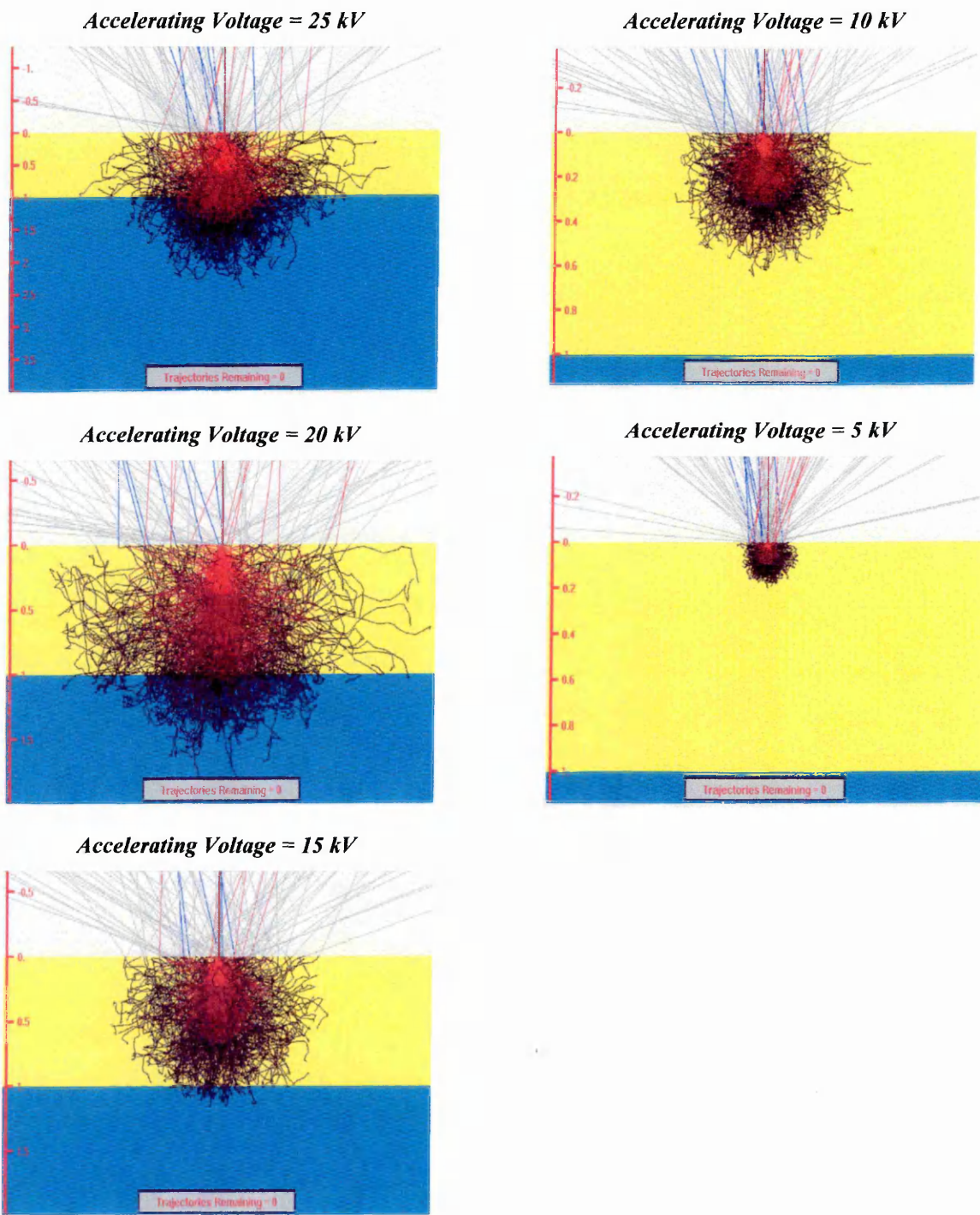


Figure 27:

Plot showing the variation in the exposure of surface-impinging graphite (expressed relatively in terms of characteristic X-ray nominal count rate) with surface roughness (expressed in terms of Ra) when rotor material surfaces are metallographically polished using increasingly fine grain-sized abrasives.

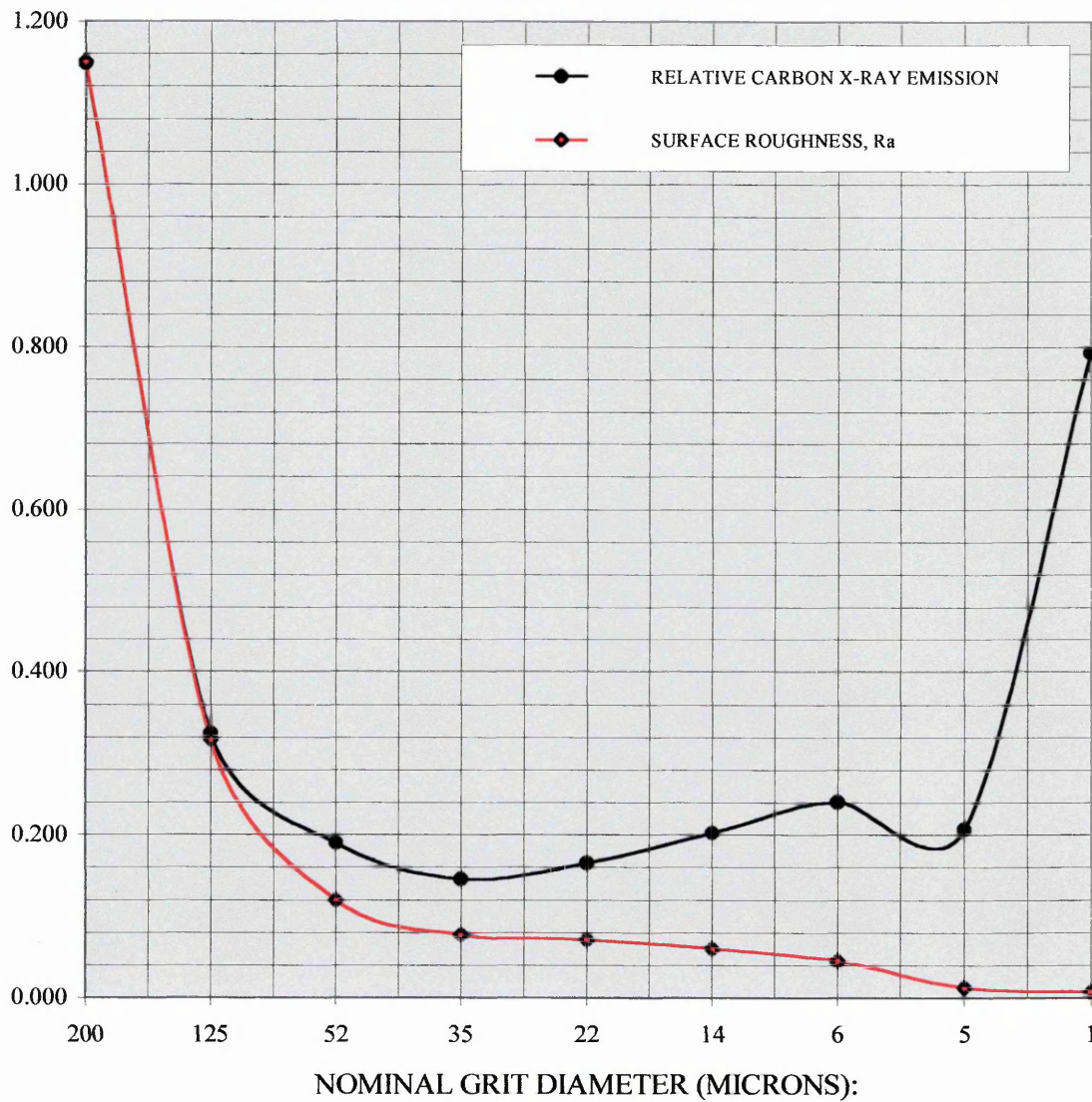
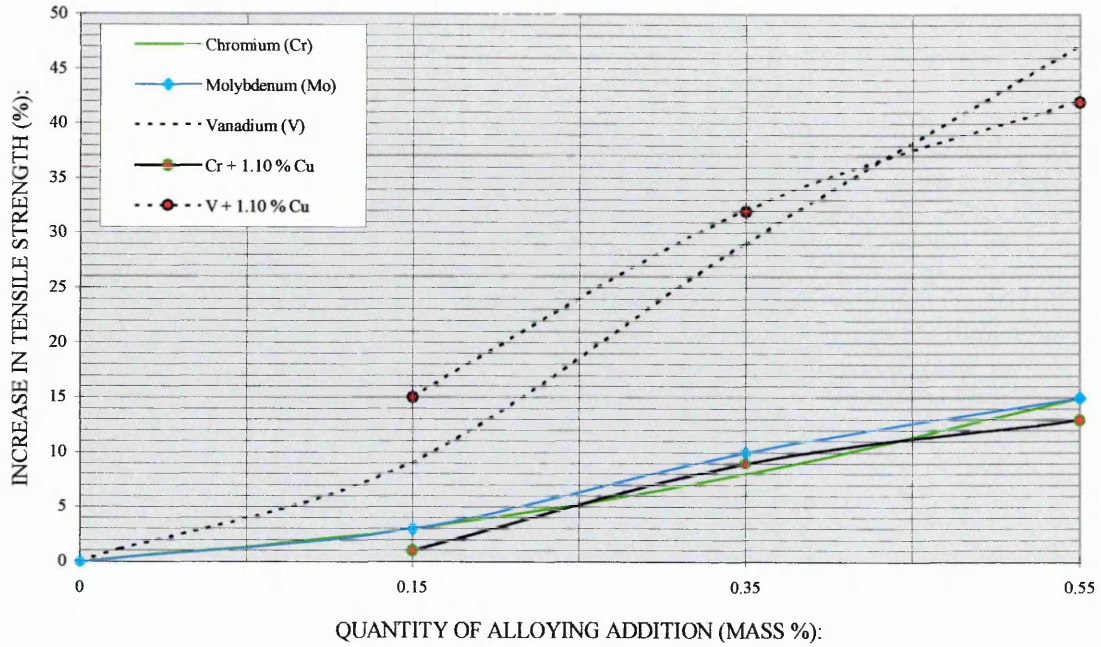
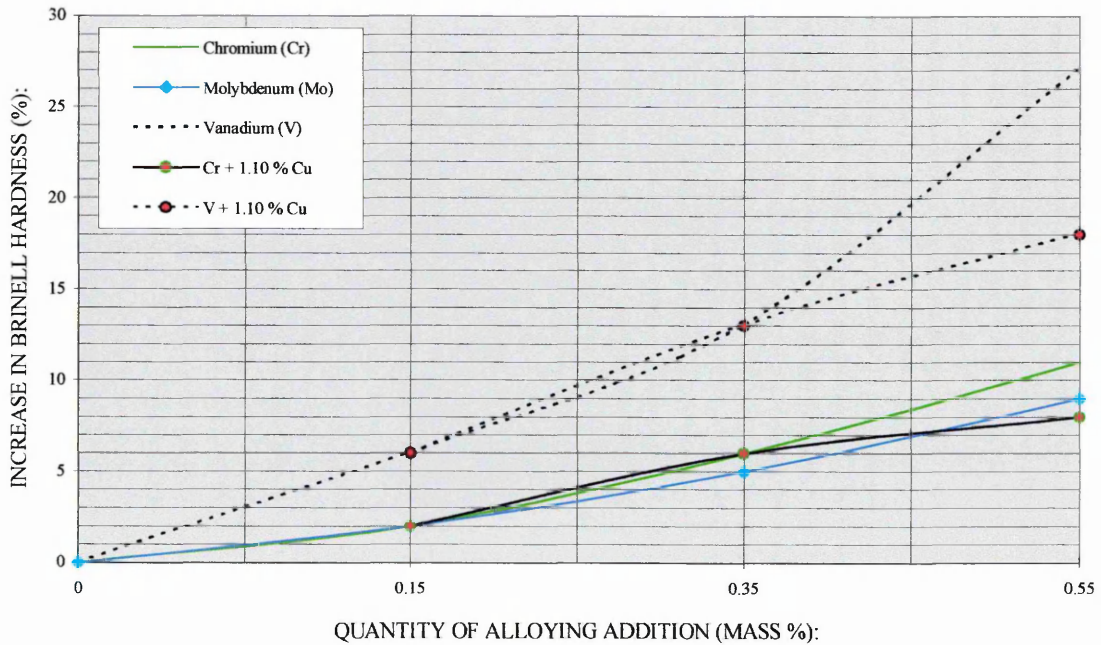


Figure 28:

Plot showing the influence of various alloying additions on the tensile strength of grey cast irons.

**Figure 29:**

Plot showing the influence of various alloying additions on the Brinell hardness of grey cast irons.



Note the partial non-linearity of the ordinate axis. (Data derived and adapted from reference 149.)

Figure 30:

Plot showing the influence of alloying additions of titanium to pearlitic, grey cast iron on friction coefficient, disc brake rotor wear and friction material wear. The shape of the curve is typical for many rotor / lining friction couples. Duplicated from reference 141.

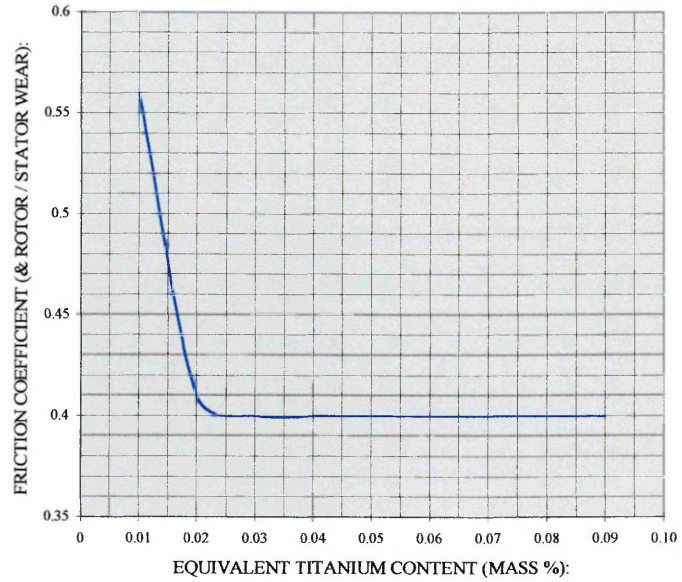


Figure 31:

Plot showing the friction performance level for a range of friction materials tested against both low and high titanium grey cast iron brake rotors. Duplicated from reference 152.

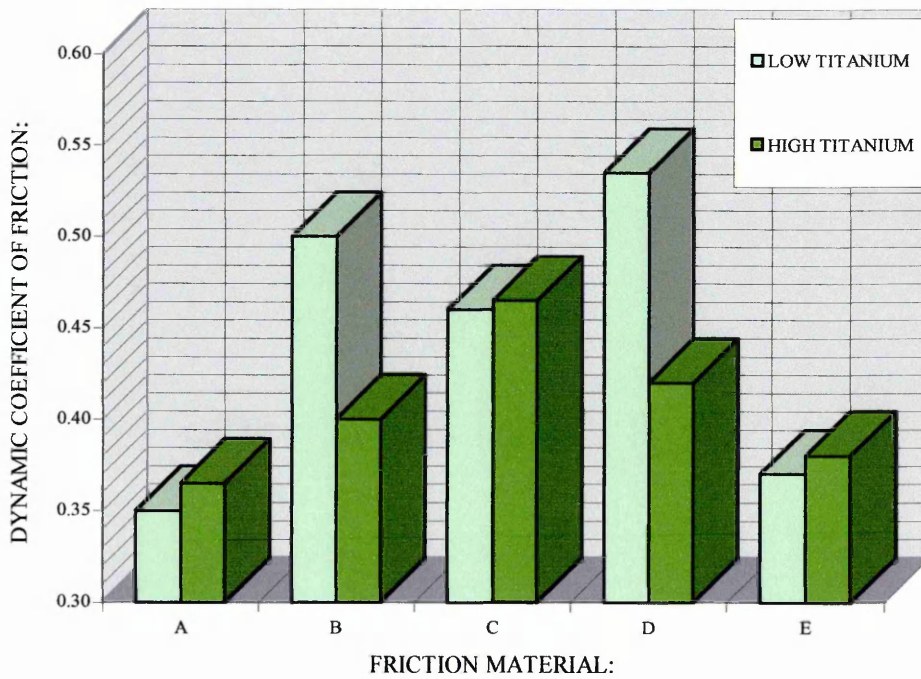


Figure 33:

The before and after surface profiles of a pearlitic, grey cast iron, solid, disc brake rotor exposed to a 580°C stress-relieving heat-treatment for a duration of 5 hours.

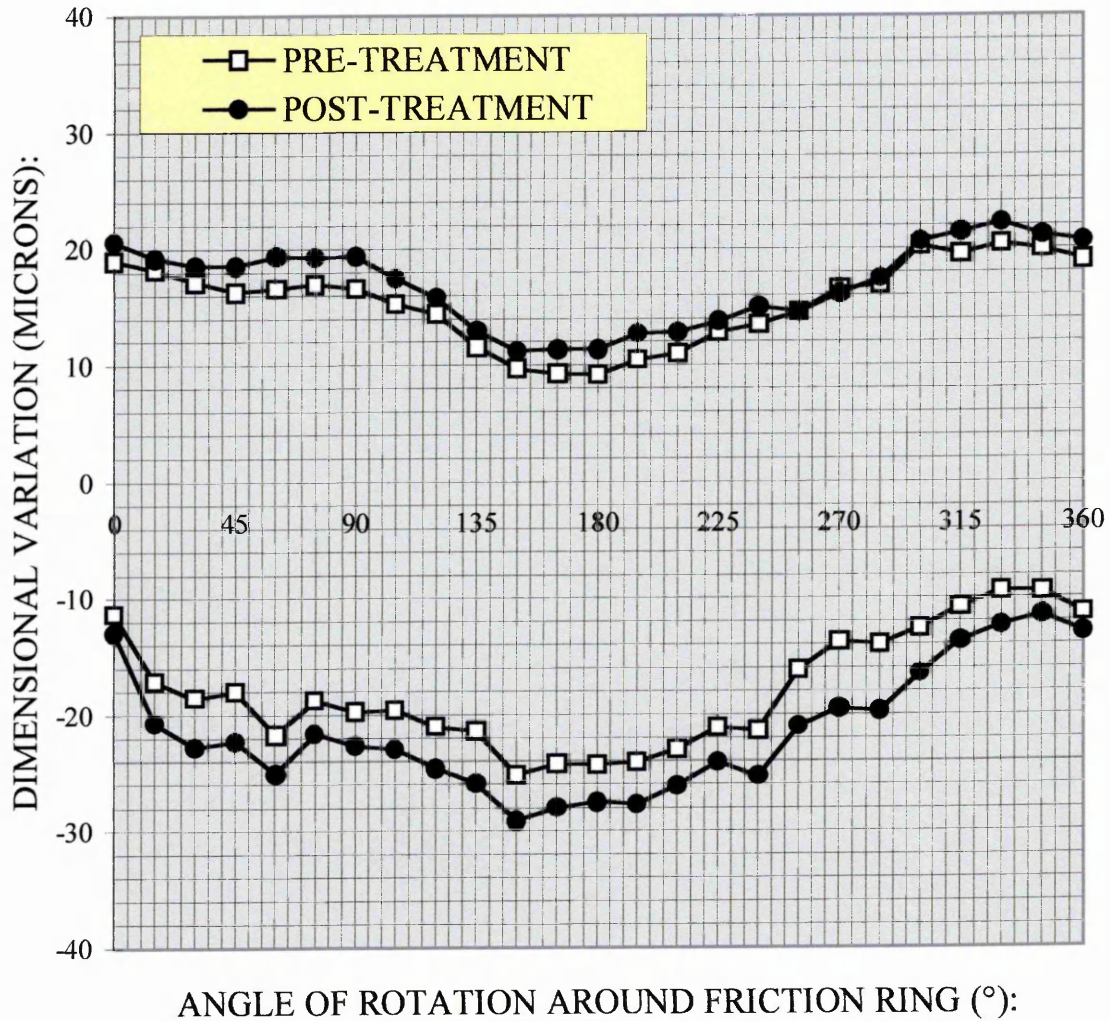


Figure 34:

Plot showing the cumulative thicknesses of the iron oxide layers grown on an automotive grey cast iron substrate deliberately contaminated with surface layers of friction material constituent combinations. Samples were heat-treated from room temperature to 1,000°C in steps of 100°C for a duration of 24 hours.

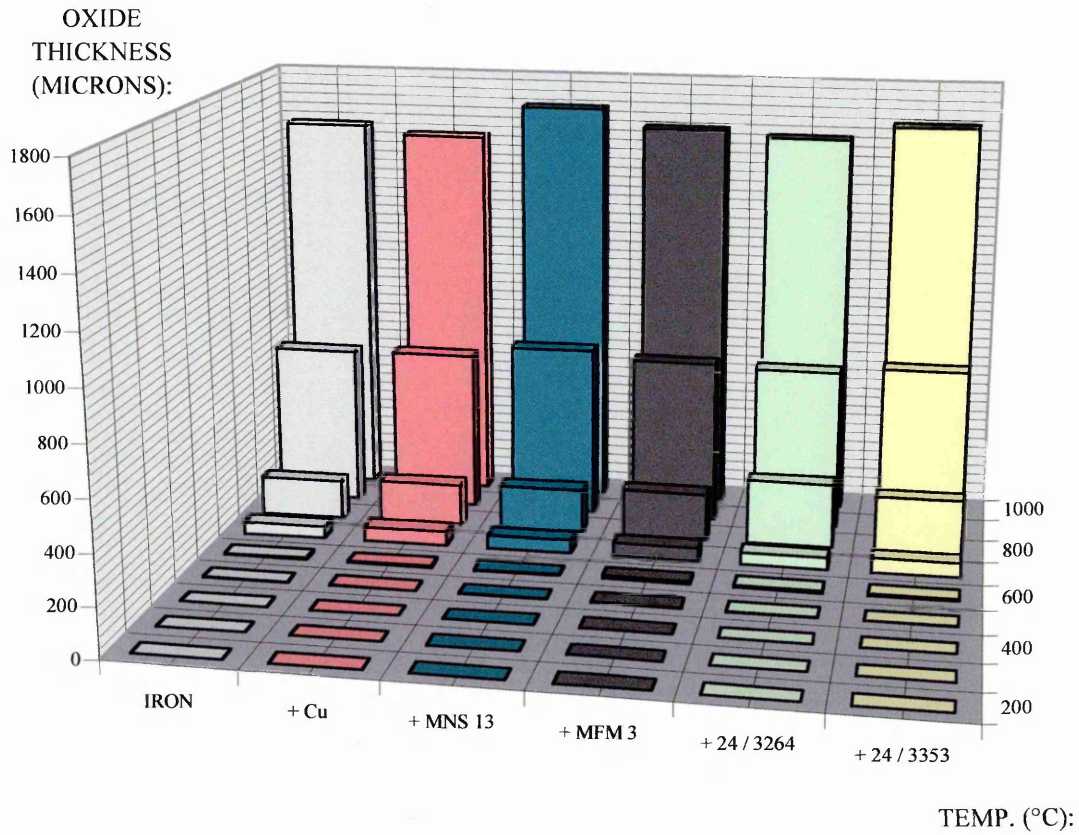


Figure 35:

Particle size analyses showing the particle size ranges and distributions of four of the principal abrasive friction modifiers (commercial grades) used to formulate friction materials AB 1 - AB 12.

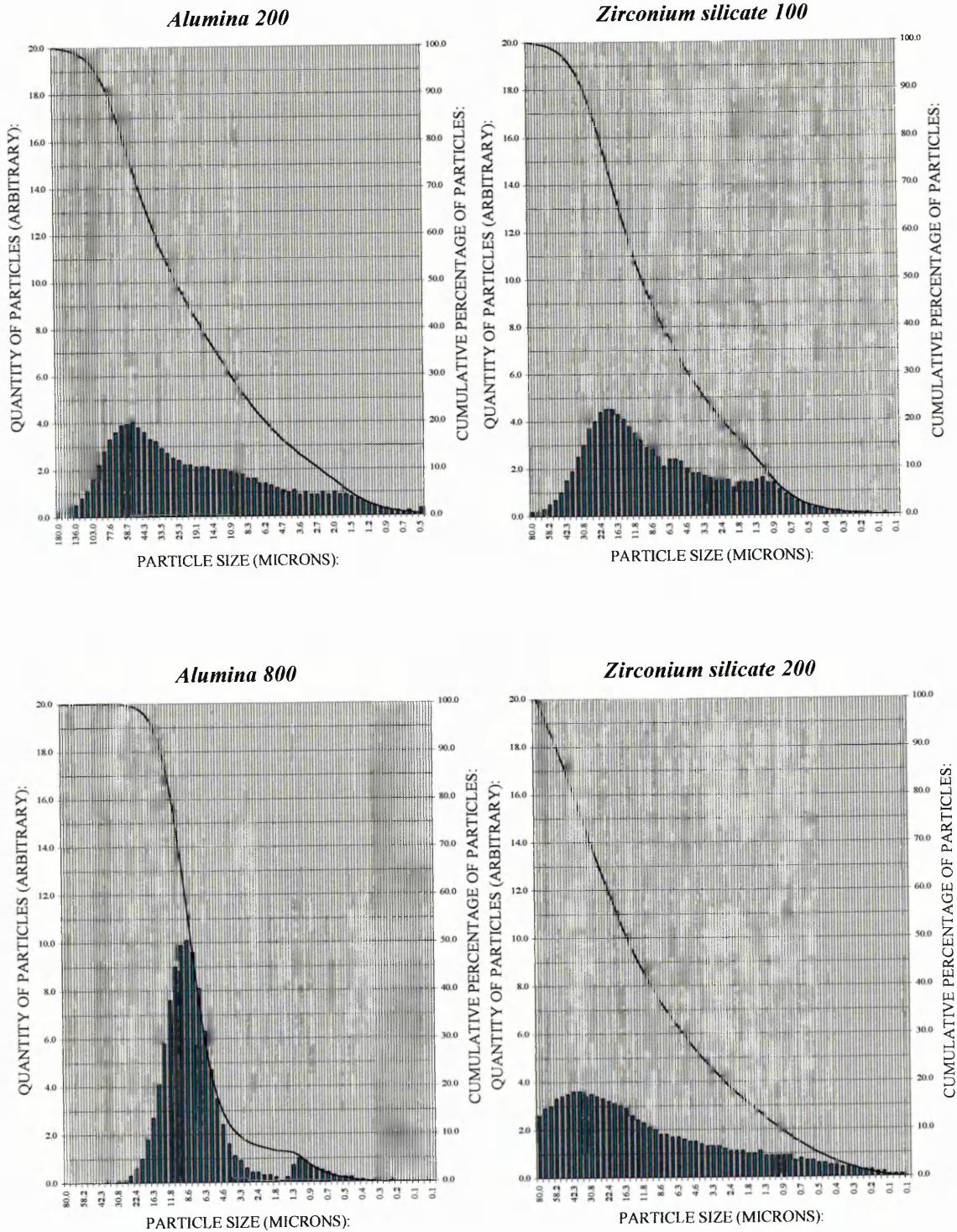
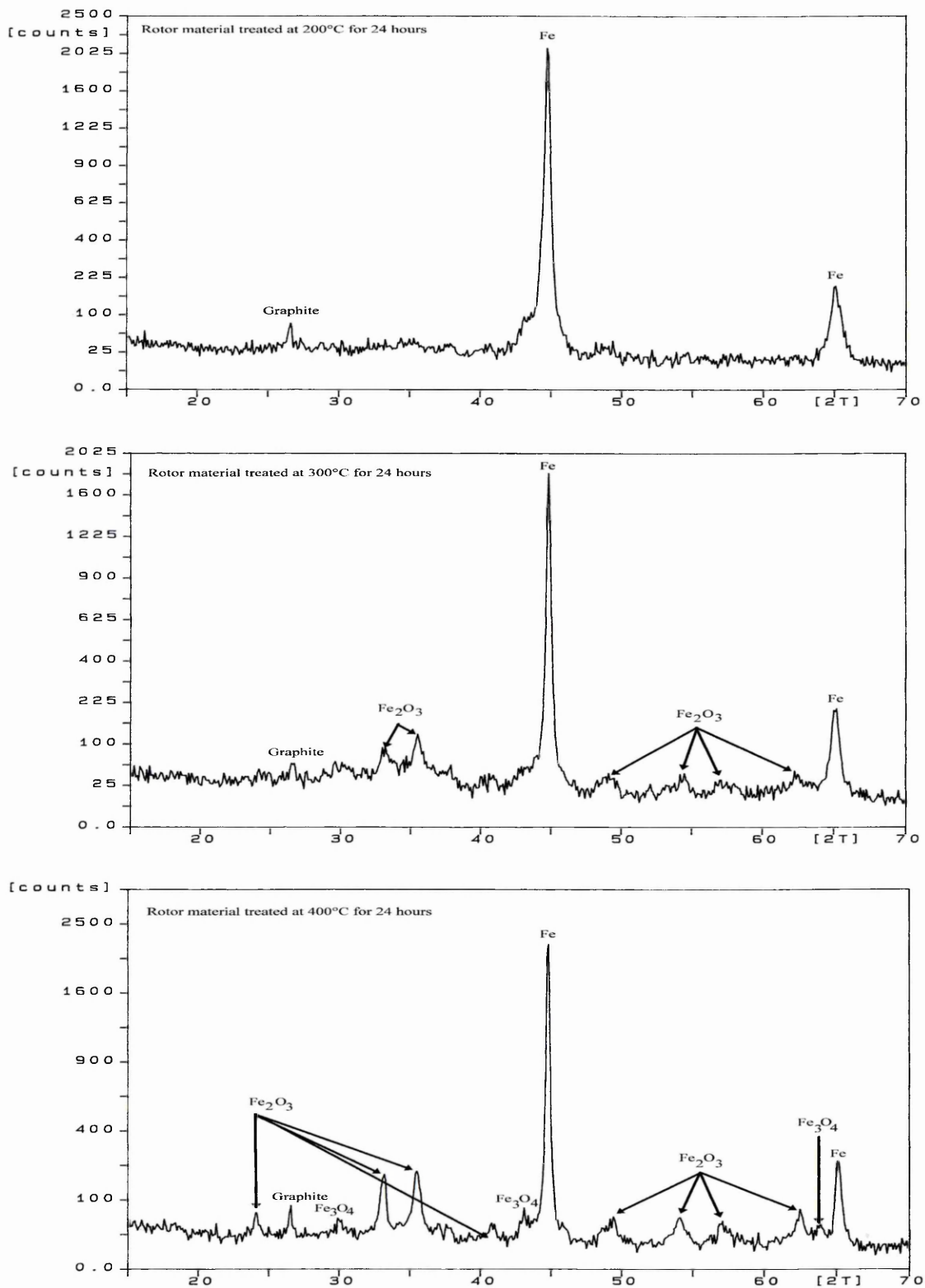


Figure 36:

X-Ray Diffraction traces of pearlitic, grey cast iron, rotor material samples heated between 200 °C and 700 °C in steps of 100 °C.



9.0. Figures

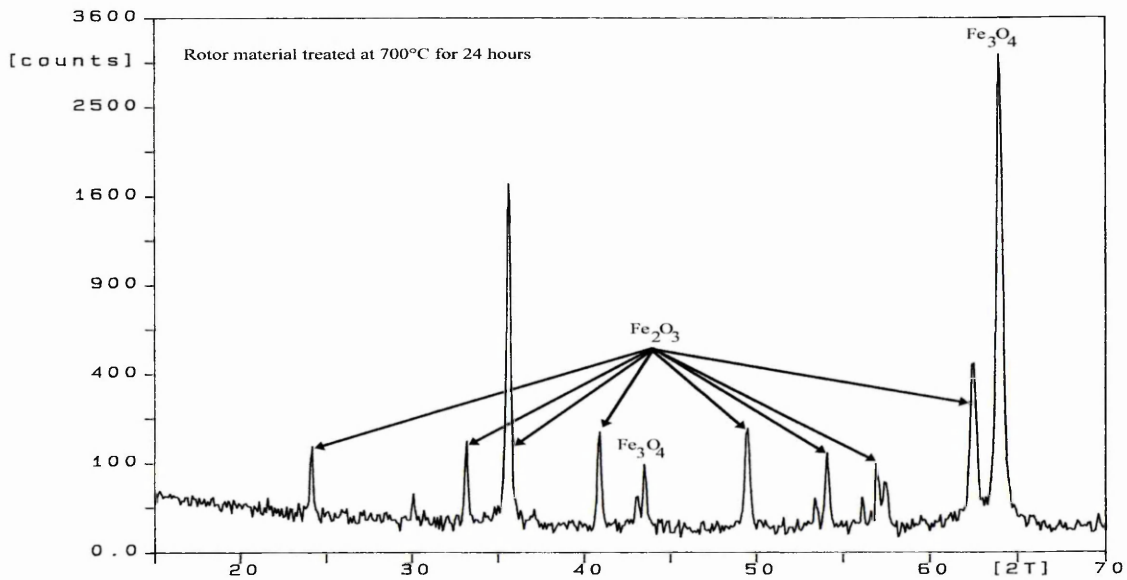
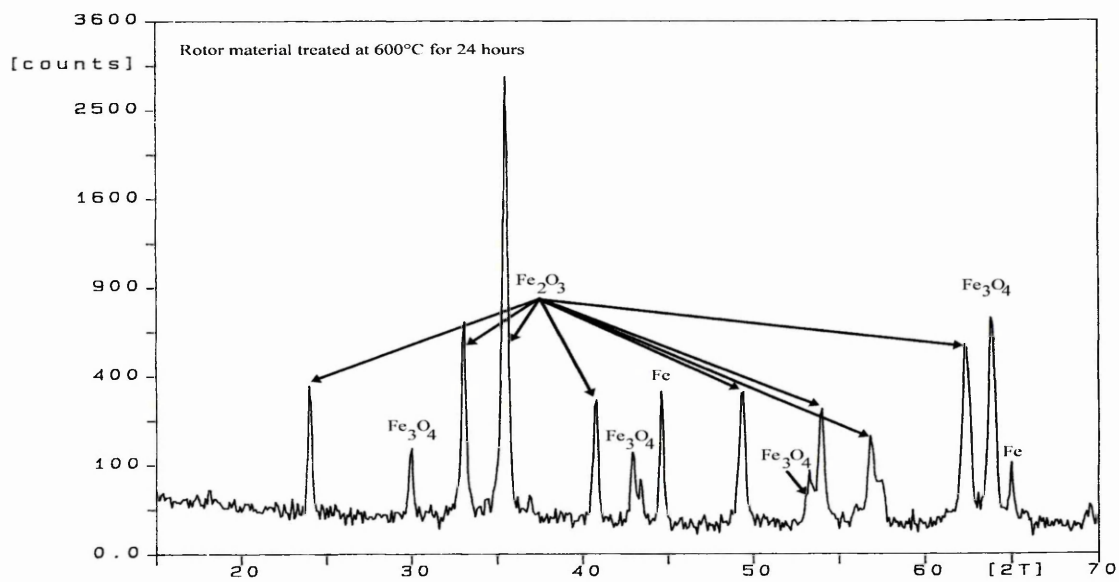
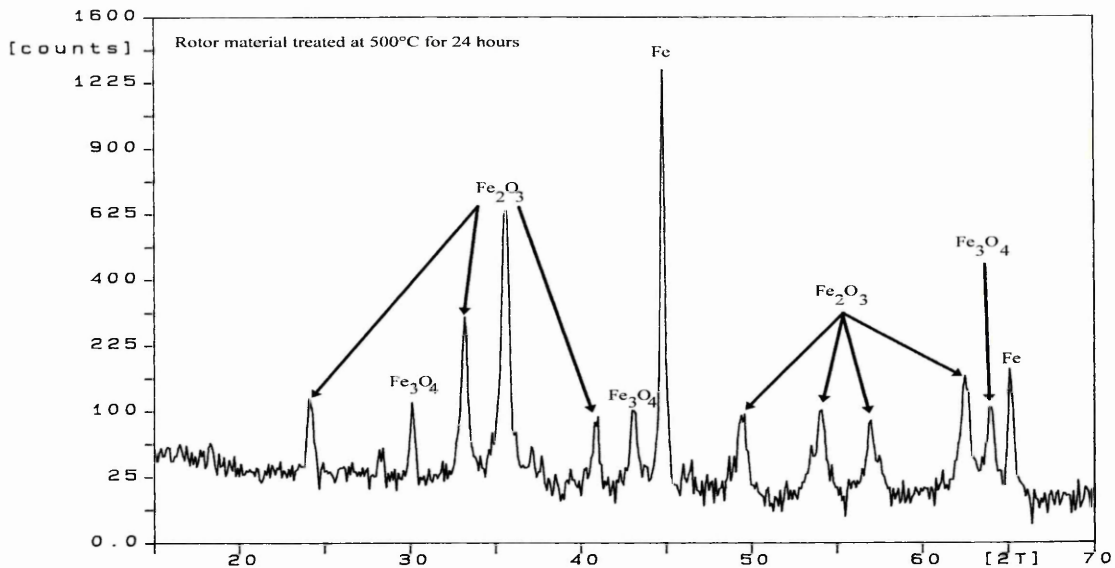
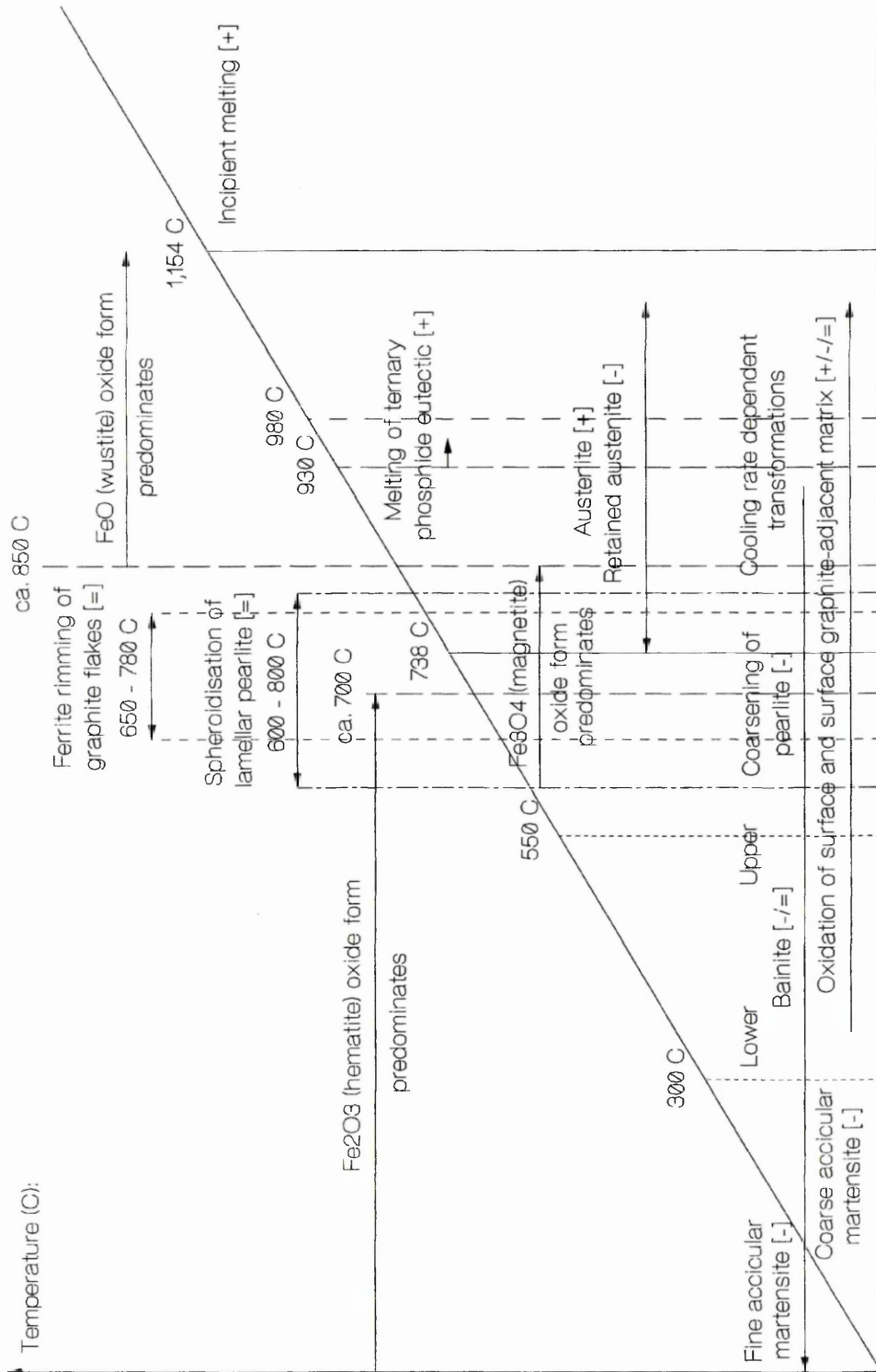


Figure 37:

Schema illustrating the potential phase transformations and modifications taking place in grey cast irons when subjected to frictional heating in automotive friction braking systems.



Potential phase transformations/modifications upon heating [+], cooling [-] or cycling/isothermal holding [=]:

Figure 38:

X-ray diffraction traces of commercial grade friction material constituent standards of (top to bottom) molybdenum disulphide, antimony trisulphide, barytes and vermiculite.

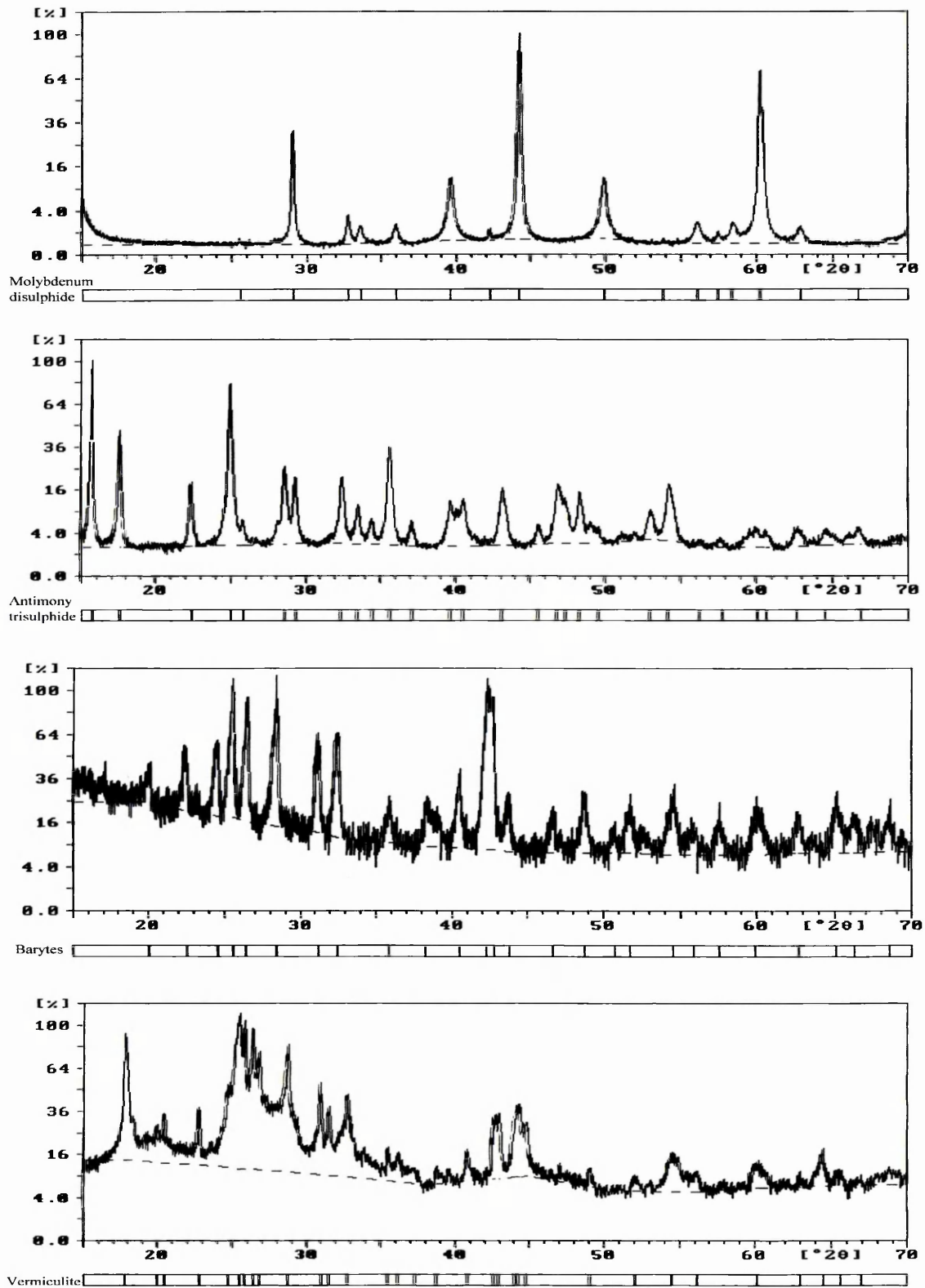


Figure 39:

X-ray spectra, generated at accelerating voltages of 10 and 25 kV, of a central surface area of compressed pellets of MFM 1, unheat-treated and heat treated between 200 °C to 800 °C in steps of 200 °C.

PAGE 199

Figure 40:

X-ray spectra, generated at accelerating voltages of 10 and 25 kV, of a central surface area of compressed pellets of MFM 2, unheat-treated and heat treated between 200 °C to 600 °C in steps of 200 °C.

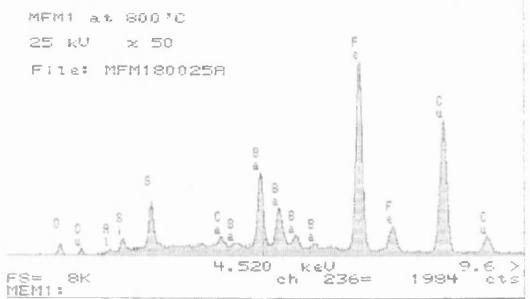
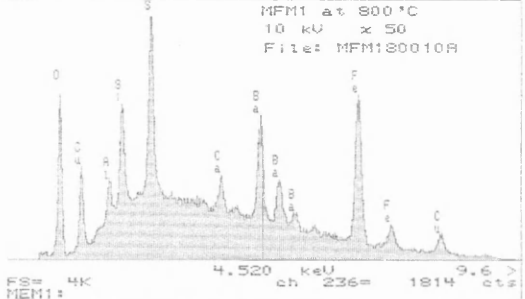
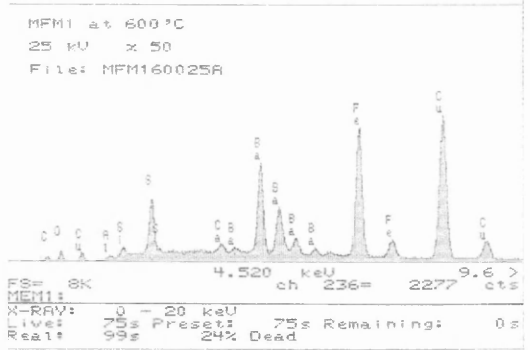
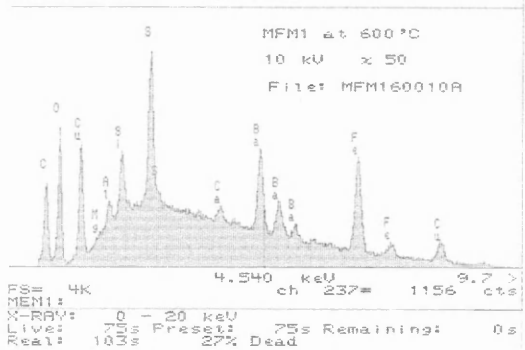
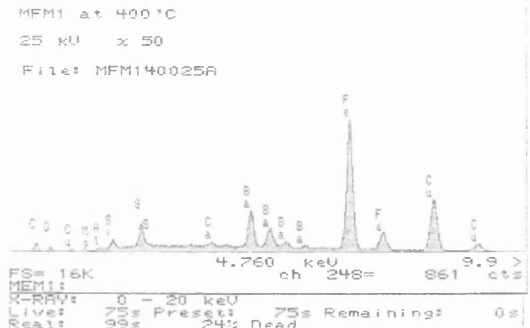
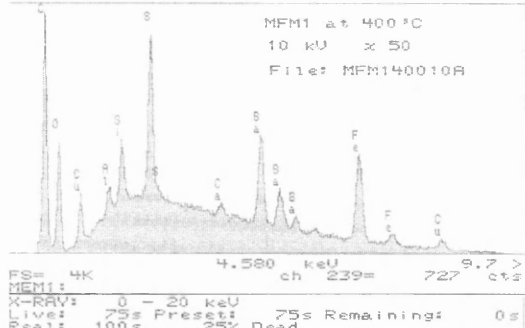
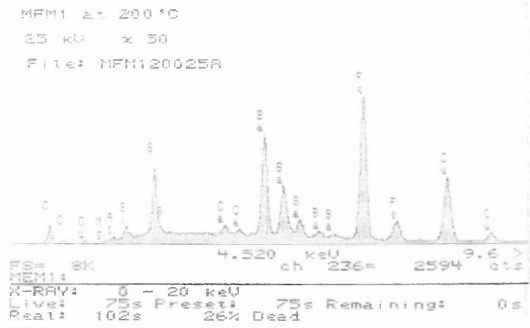
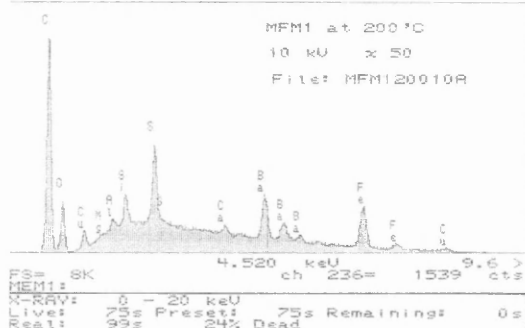
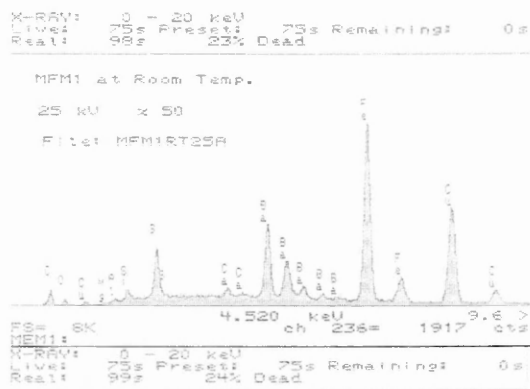
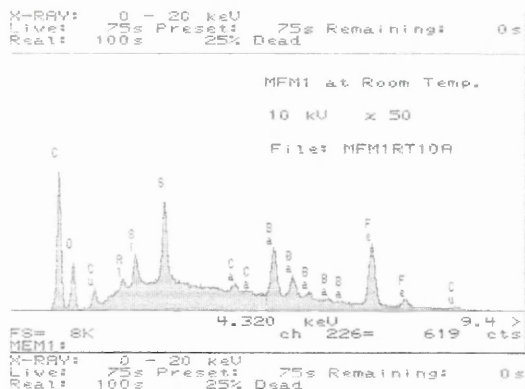
PAGE 200

Figure 41:

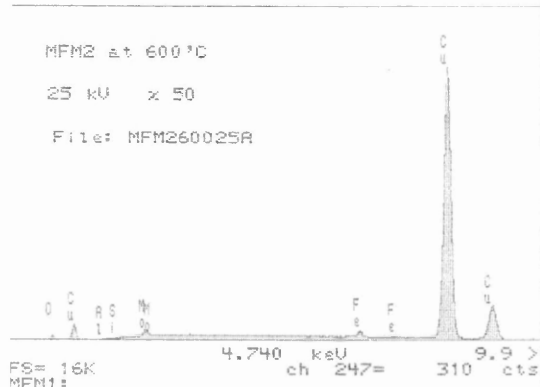
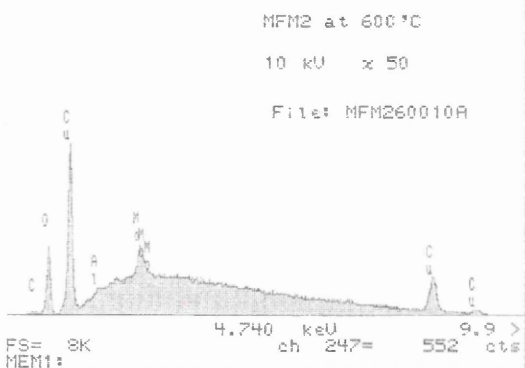
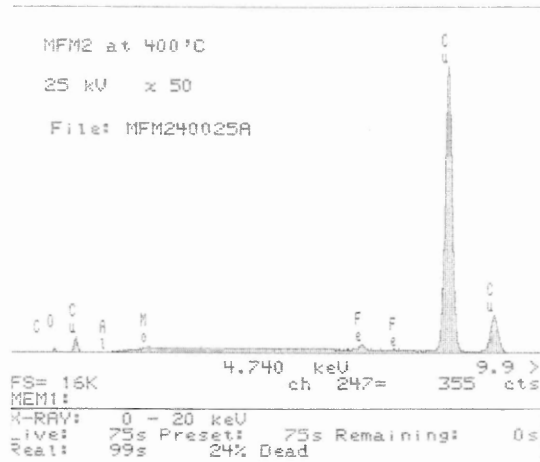
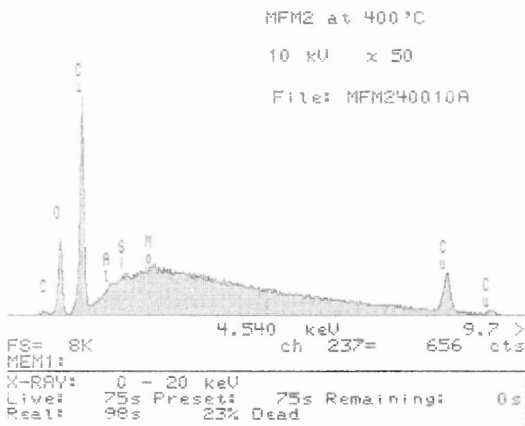
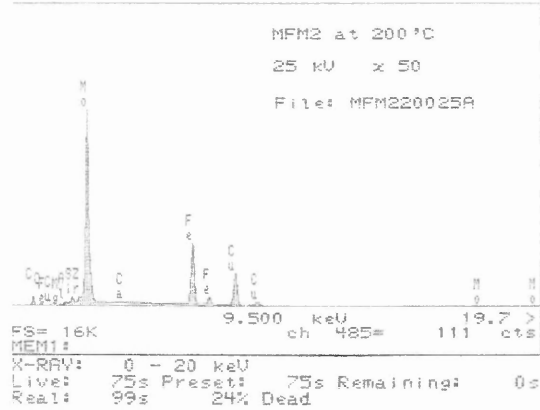
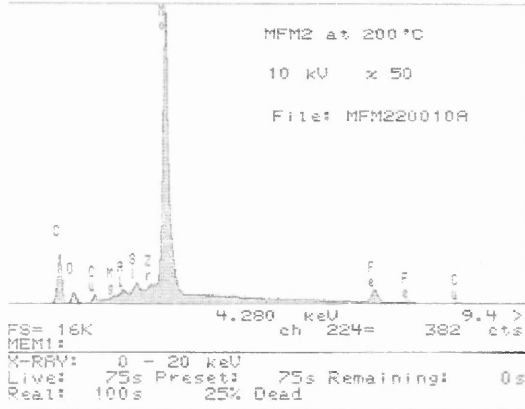
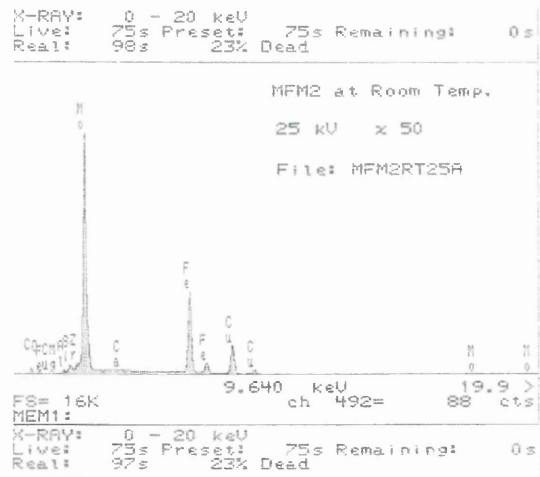
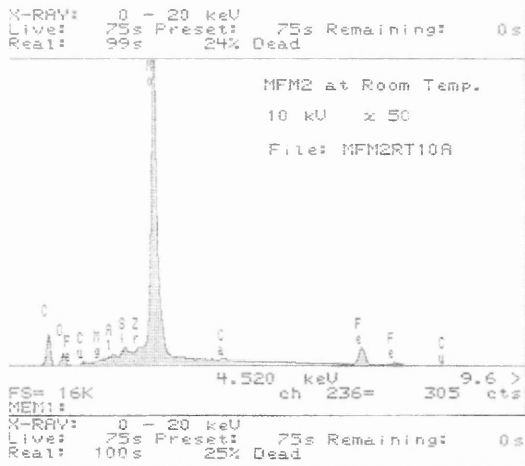
X-ray spectra, generated at accelerating voltages of 10 and 25 kV, of a central surface area of compressed pellets of MFM 3, unheat-treated and heat treated between 200 °C to 800 °C in steps of 200 °C.

PAGE 201

9.0. Figures



9.0. Figures



9.0. Figures

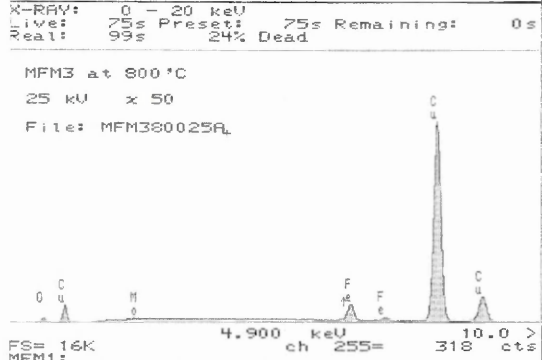
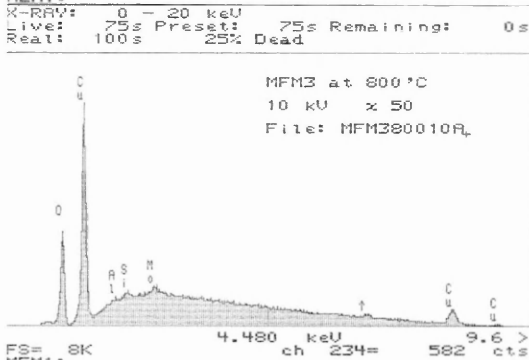
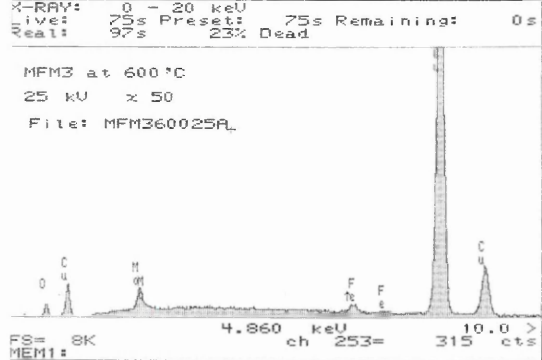
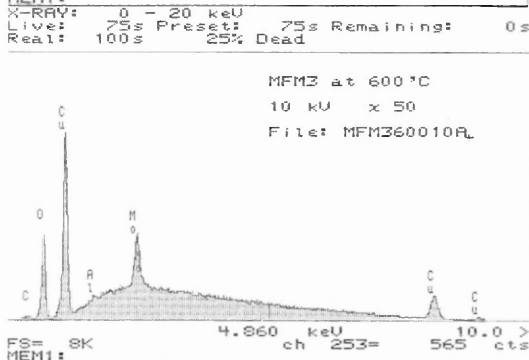
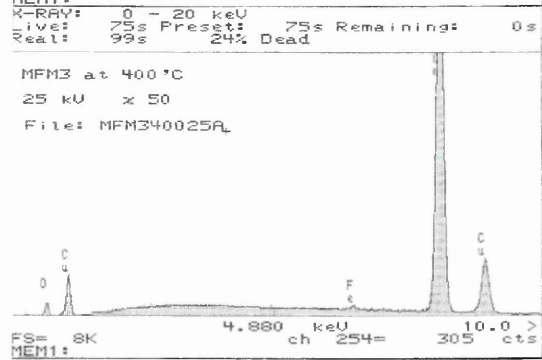
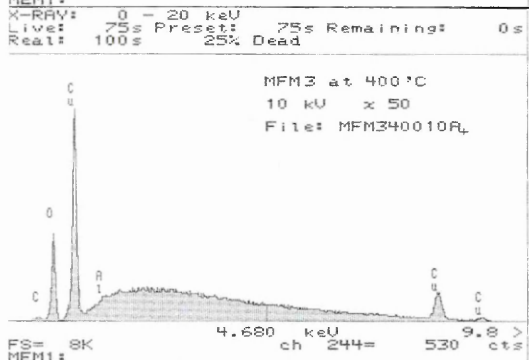
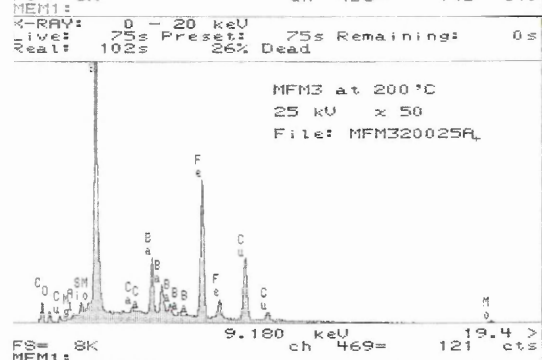
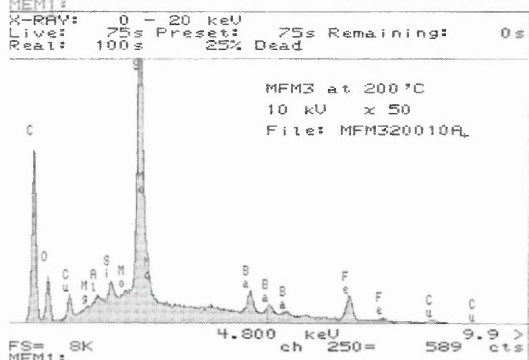
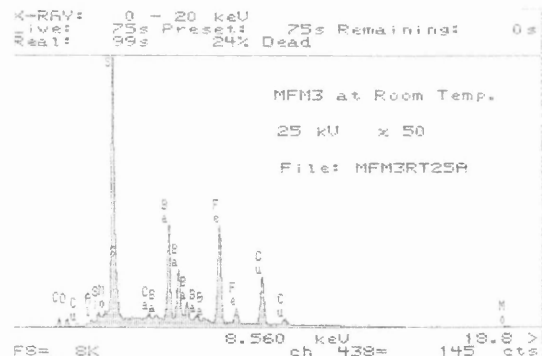
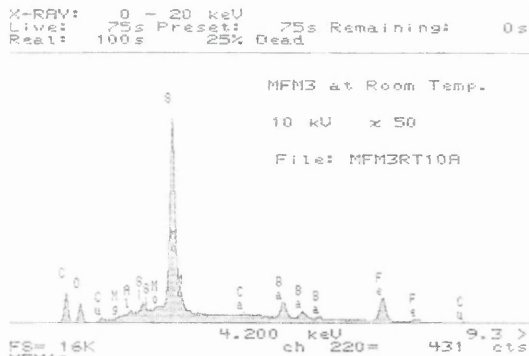


Figure 42:

Narrow scan X.P.S. data showing the Mo_{3d} and S_{2p} peaks of a surface scan of MFM 3 heat-treated at 400°C (top row) and of the upper and lower surfaces of MFM 3 heat-treated at 600°C (middle and bottom rows, respectively). (Abscissae = binding energy (eV), ordinate axes = intensity (counts).)

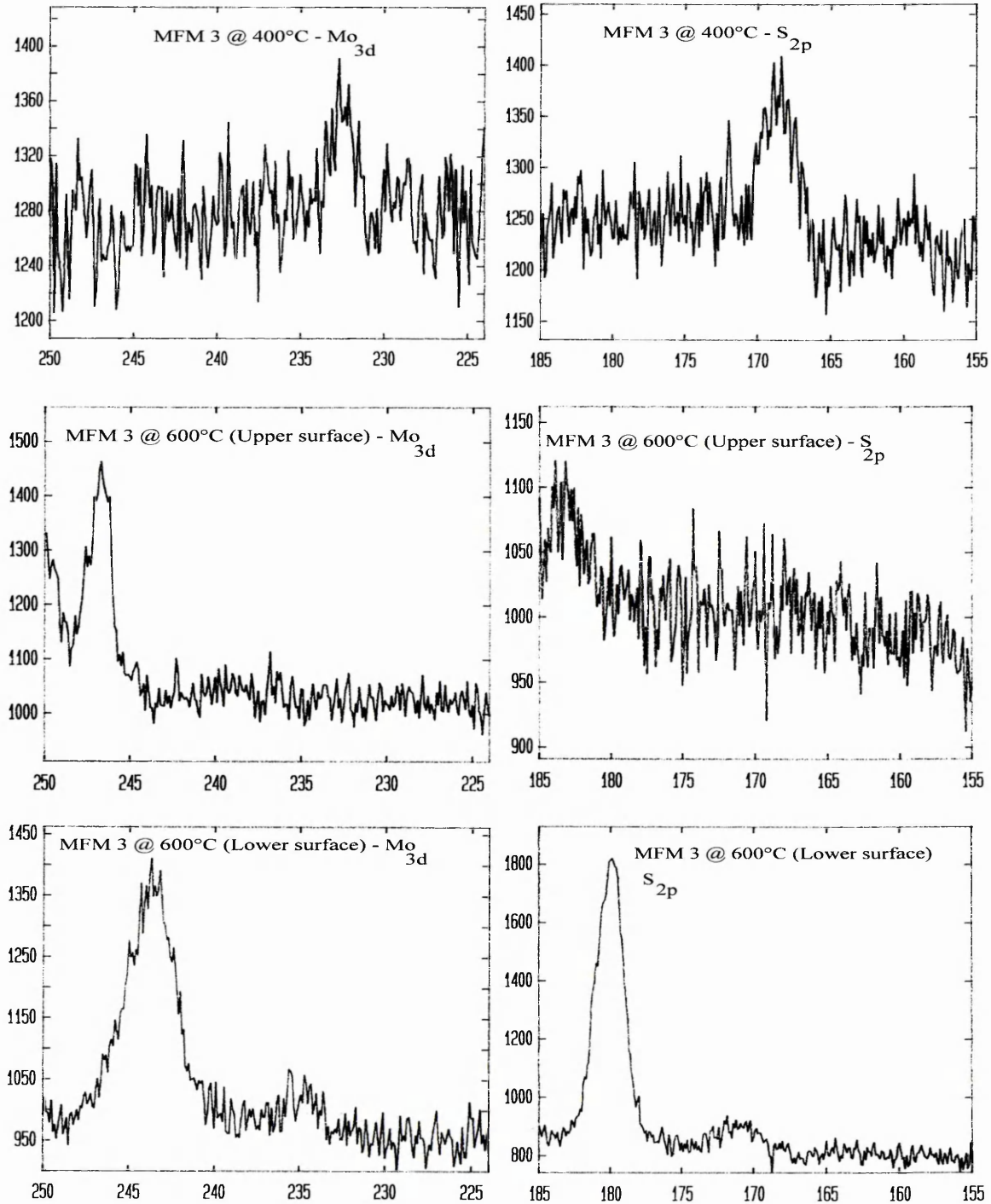


Figure 43:

Narrow scan spectroscopic data showing the X-ray photoelectronic (top) and Auger electron (bottom) peaks for copper from a surface scan of MFM 3 heat-treated at 600 °C. (Abscissae = binding energy (eV), ordinate axes = intensity (counts).)

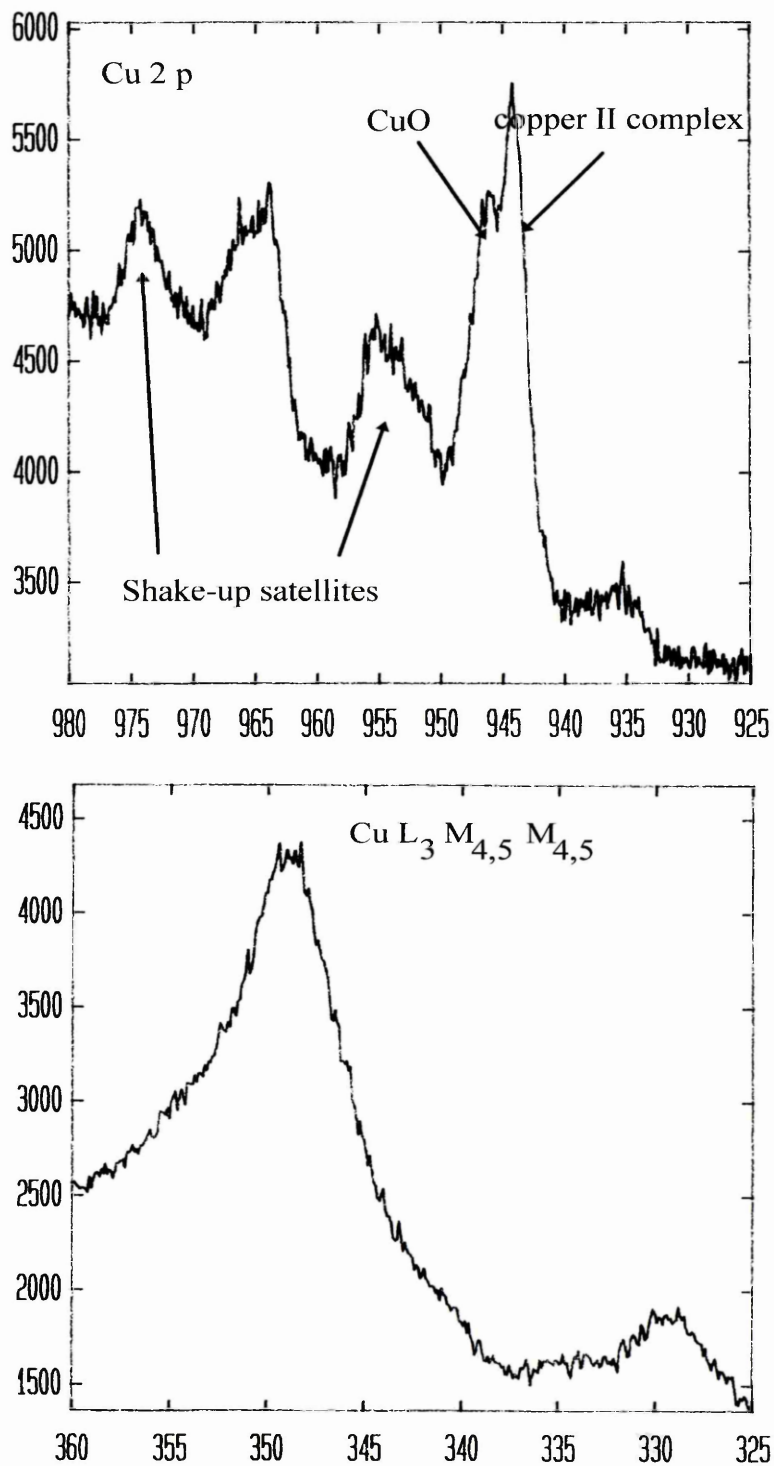


Figure 44:

G.D.O.E.S. depth profiles showing the relative concentration of copper-rich species at the surface of three MFM 3 pelletised powders; without heat-treatment (top), heat-treated at 200°C for 24 hours (middle) and heat-treated at 400°C for 24 hours (bottom).

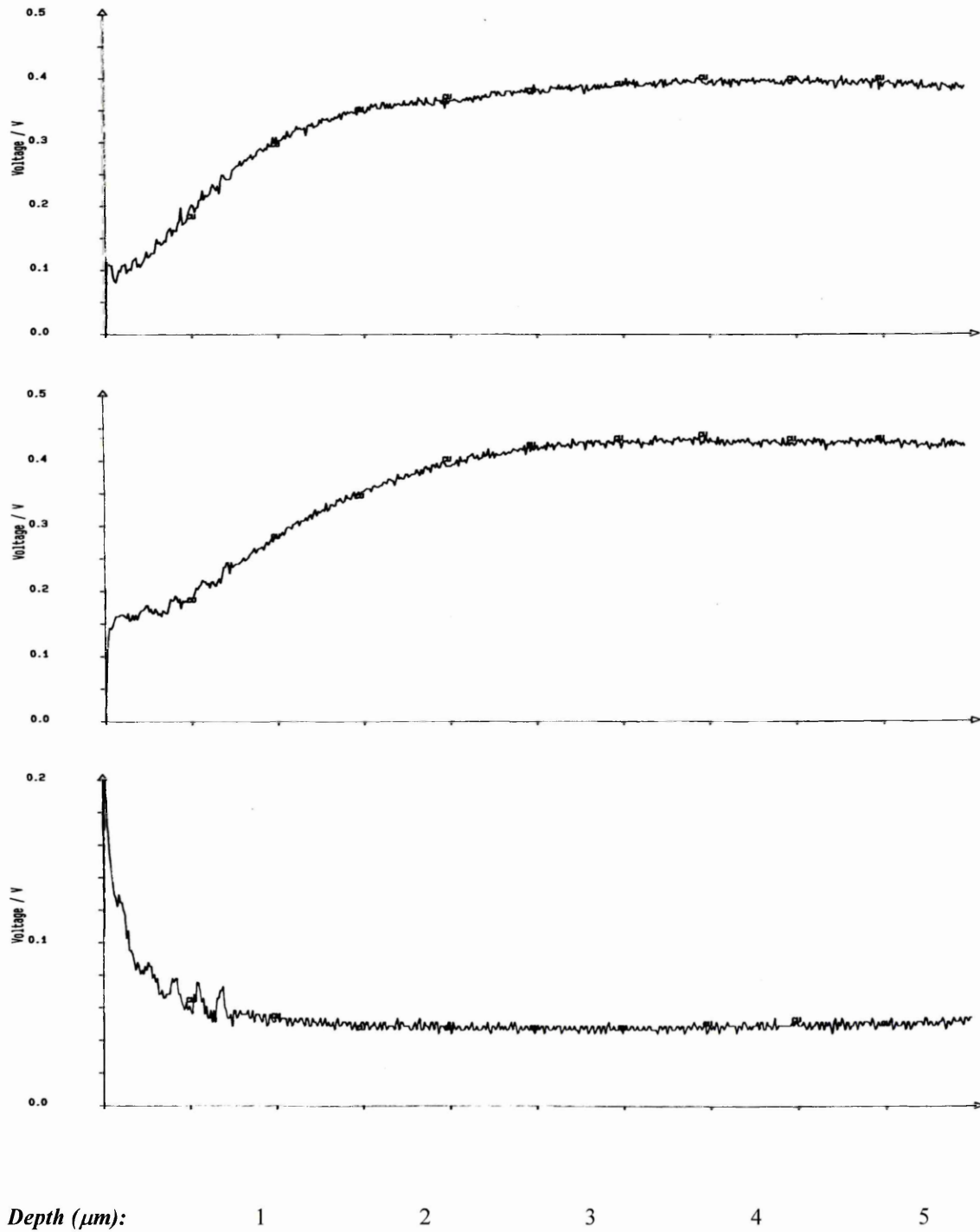


Figure 45:

Three-dimensional plot showing the Disc Thickness Variation (D.T.V.) around the solid friction ring of a virgin, i.e. unused, as-machined disc brake rotor.

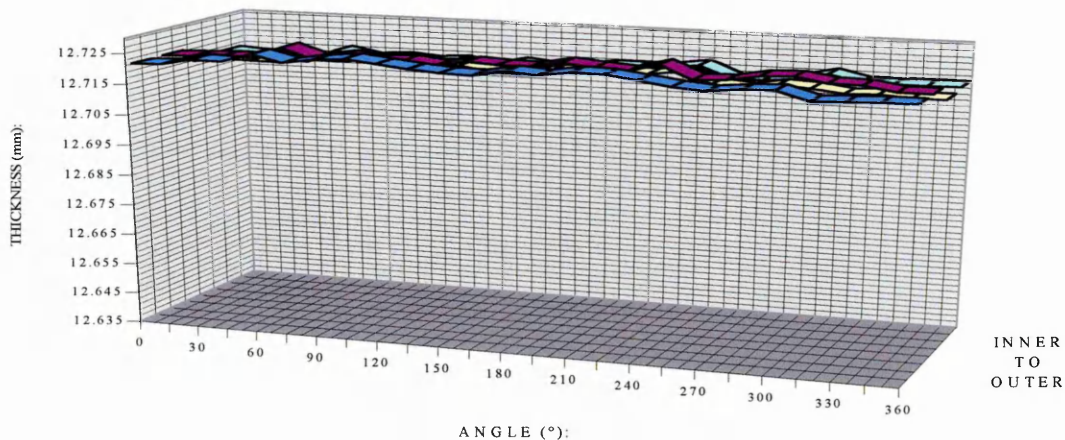


Figure 46:

Three-dimensional plot showing the Disc Thickness Variation (D.T.V.) around the solid friction ring of D.T.V. test rotor number 2.

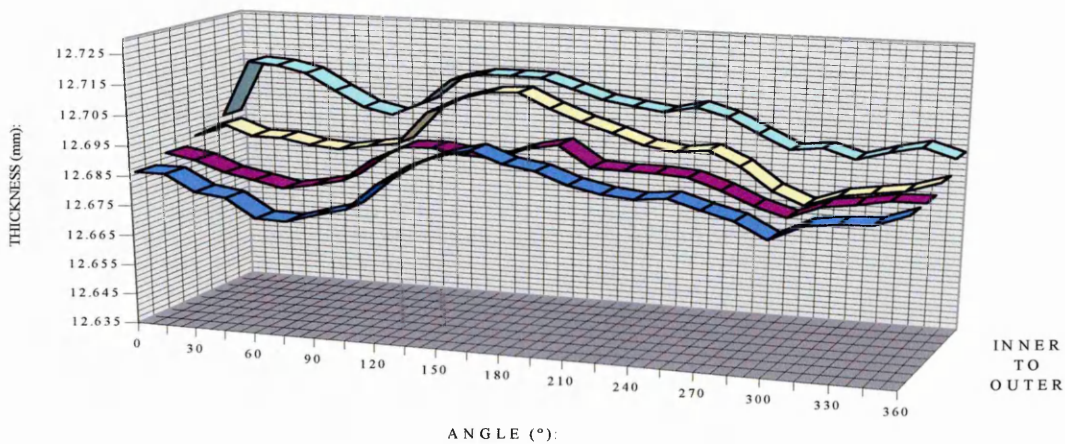


Figure 47:

Three-dimensional plot showing the Disc Thickness Variation (D.T.V.) around the solid friction ring of D.T.V. test rotor number 3.

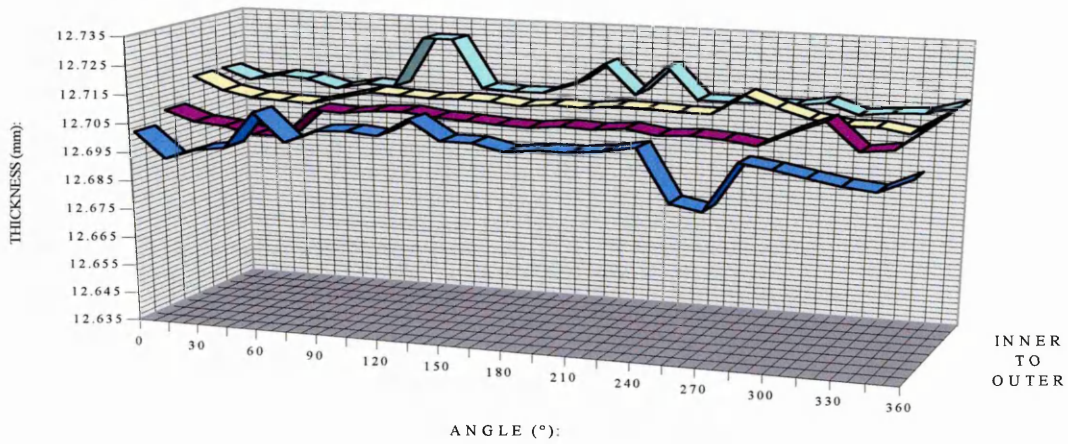


Figure 48:

Three-dimensional plot showing the Disc Thickness Variation (D.T.V.) around the solid friction ring of D.T.V. test rotor number 4.

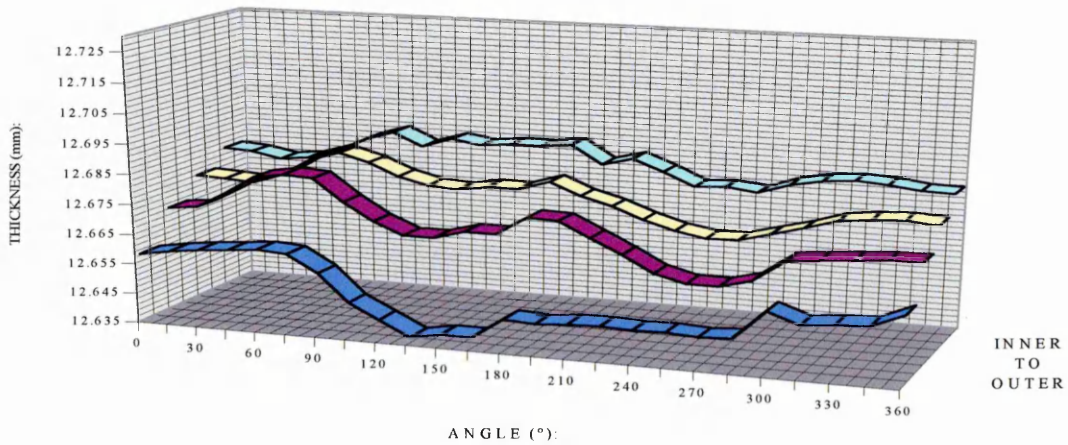


Figure 49:

Three-dimensional plot showing the Disc Thickness Variation (D.T.V.) around the solid friction ring of D.T.V. test rotor number 5.

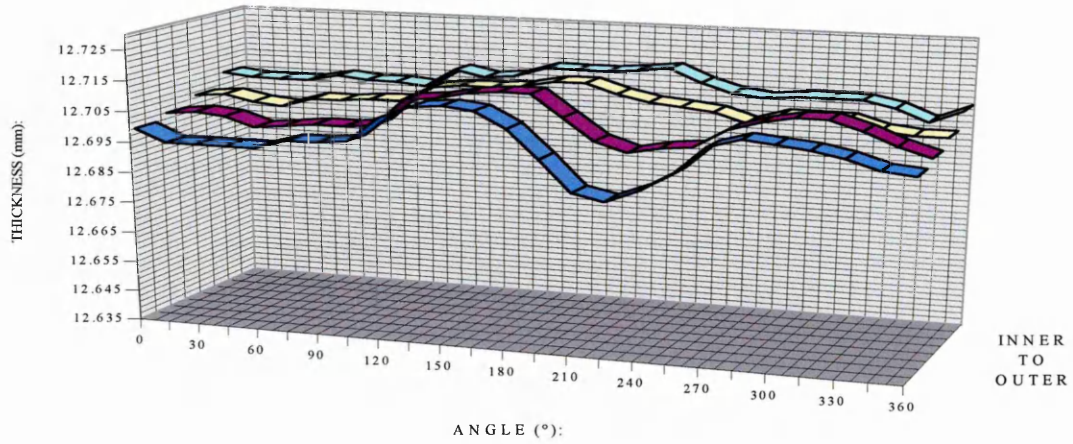


Figure 50:

Three-dimensional plot showing the Disc Thickness Variation (D.T.V.) around the solid friction ring of D.T.V. test rotor number 6.

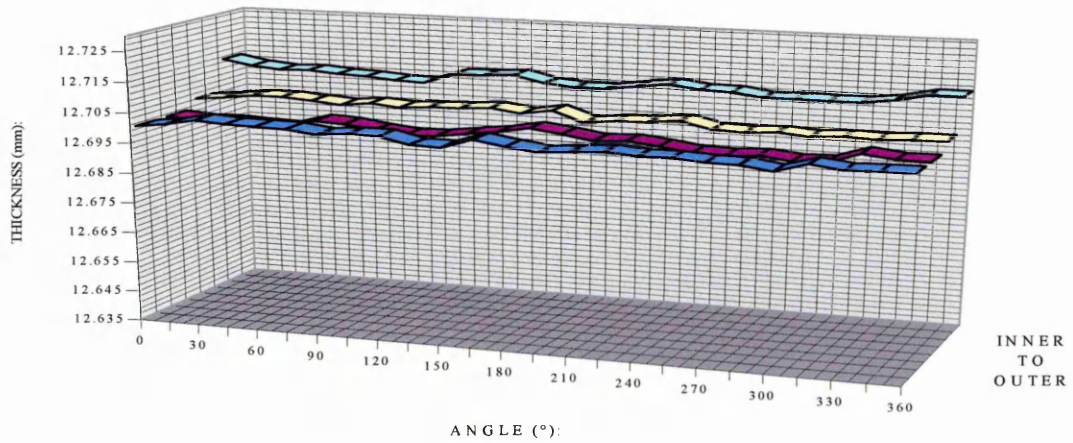


Figure 51:

Three-dimensional plot showing the Disc Thickness Variation (D.T.V.) around the solid friction ring of D.T.V. test rotor number 7.

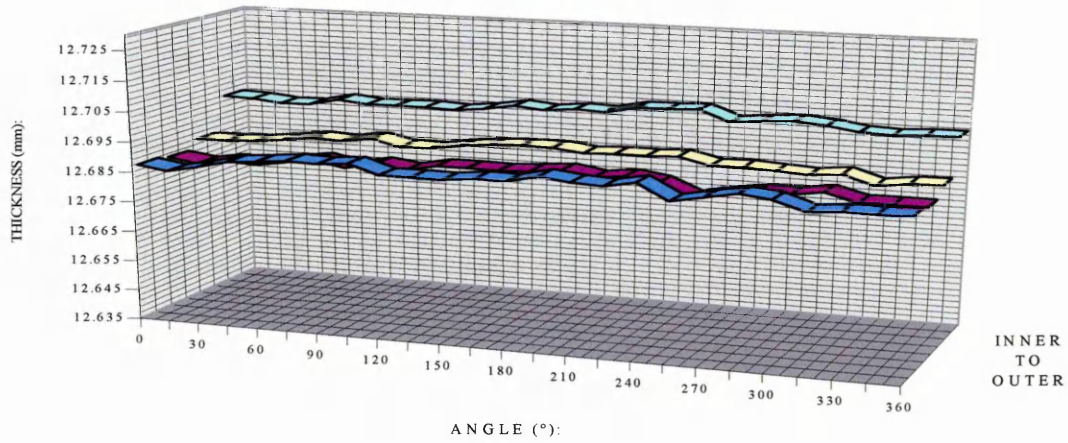


Figure 52:

Three-dimensional plot showing the Disc Thickness Variation (D.T.V.) around the solid friction ring of D.T.V. test rotor number 9.

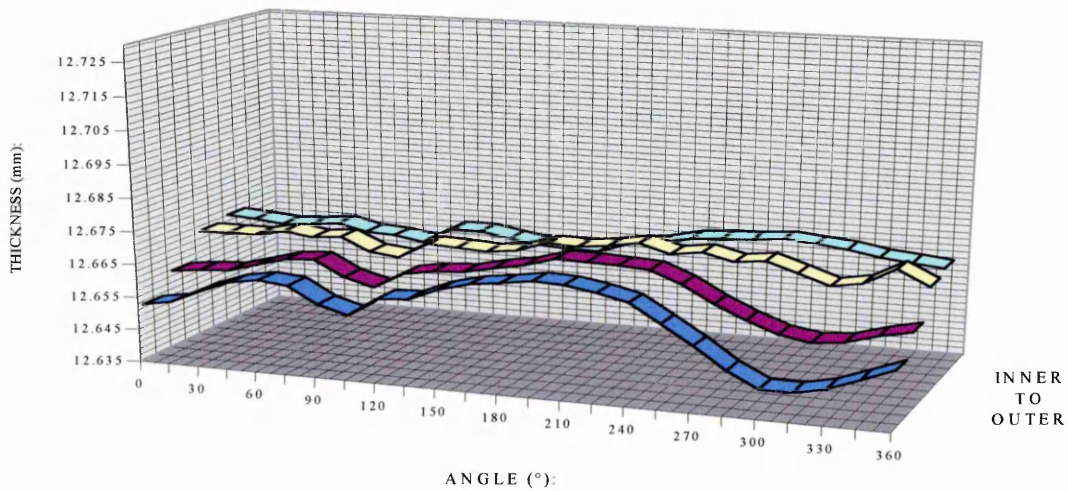


Figure 53:

Three-dimensional plot showing the Disc Thickness Variation (D.T.V.) around the solid friction ring of D.T.V. test rotor number 10.

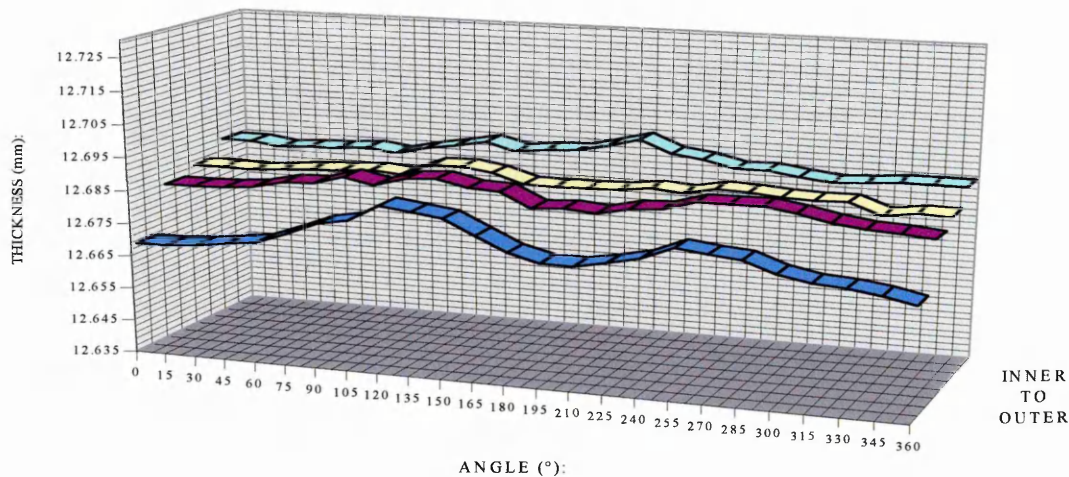


Figure 54:

Three-dimensional plot showing the Disc Thickness Variation (D.T.V.) around the solid friction ring of D.T.V. test rotor number 11.

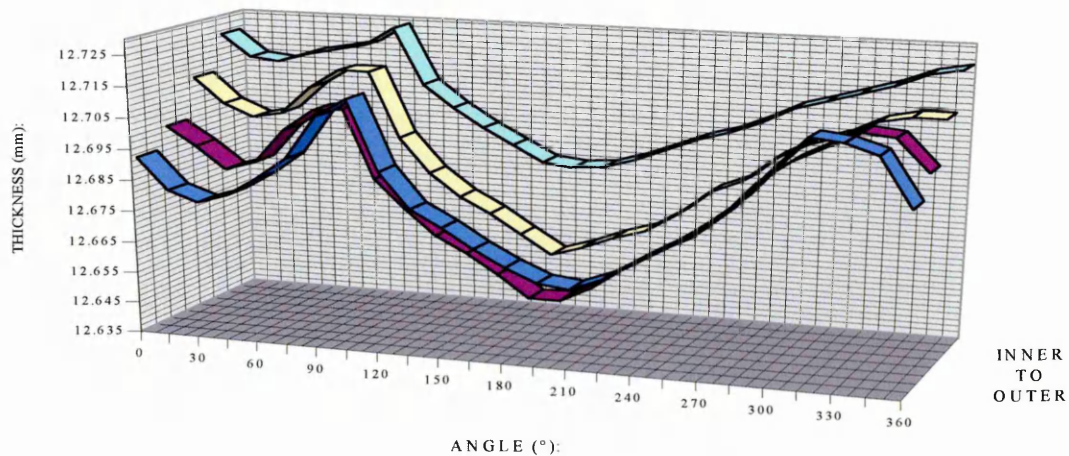


Figure 55:

Three-dimensional plot showing the Disc Thickness Variation (D.T.V.) around the solid friction ring of D.T.V. test rotor number 12.

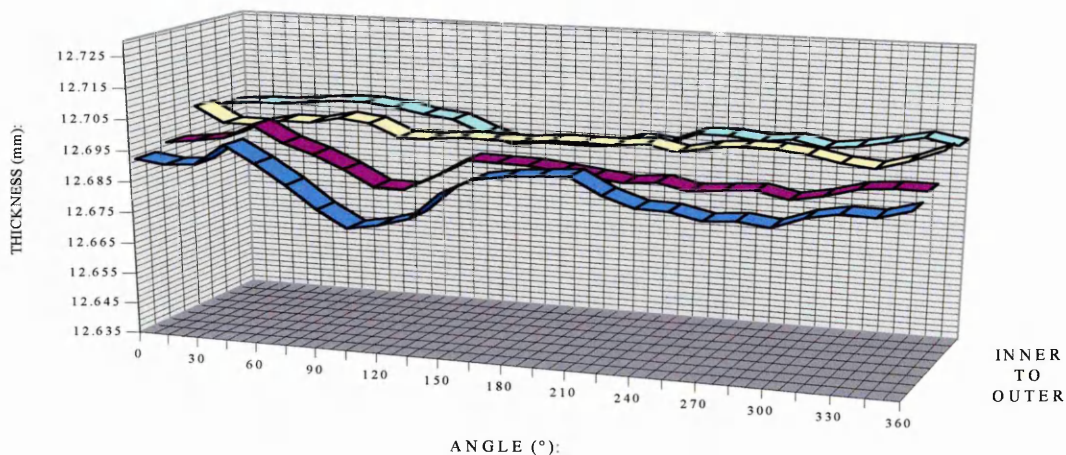


Figure 56:

Three-dimensional plot showing the Disc Thickness Variation (D.T.V.) around the solid friction ring of D.T.V. test rotor number 13.

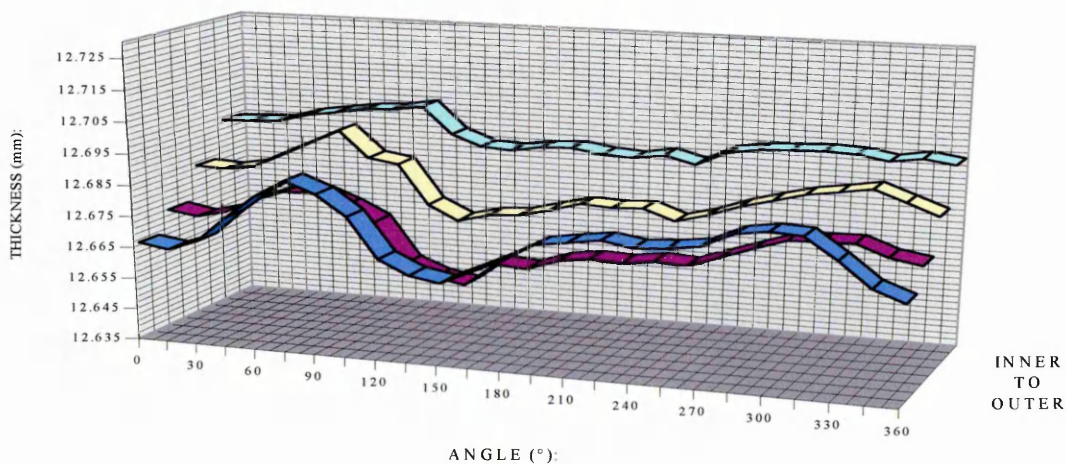


Figure 57:

Form variation of D.T.V. test rotor no. 9, rubbed against commercial friction material; N, at $\varnothing 140$ mm (inner diameter - top) and at $\varnothing 230$ mm (outer diameter - bottom).

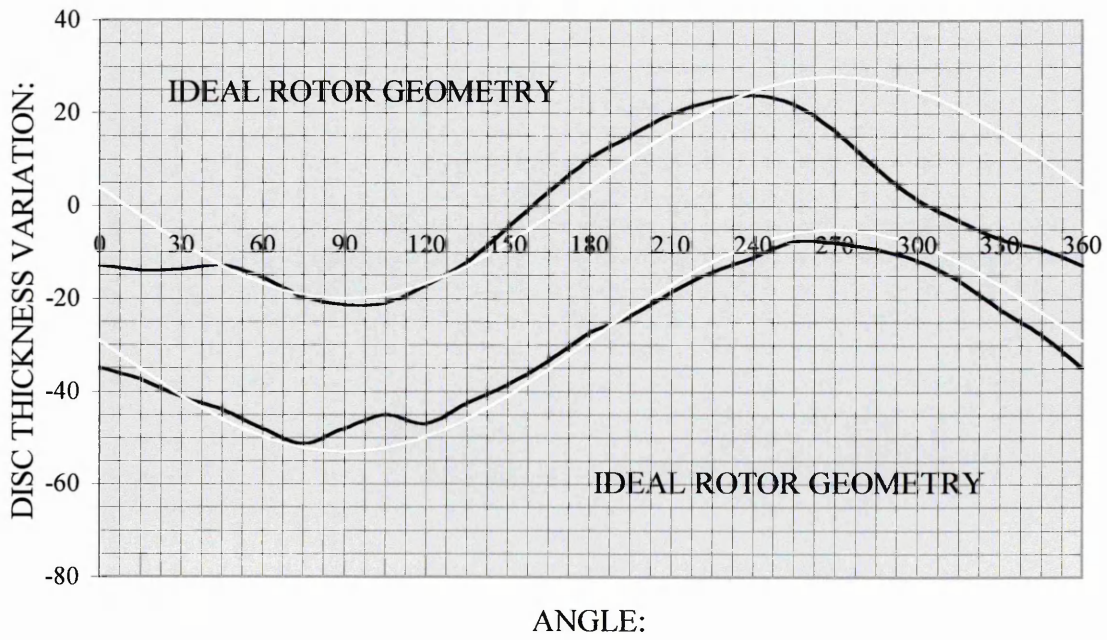
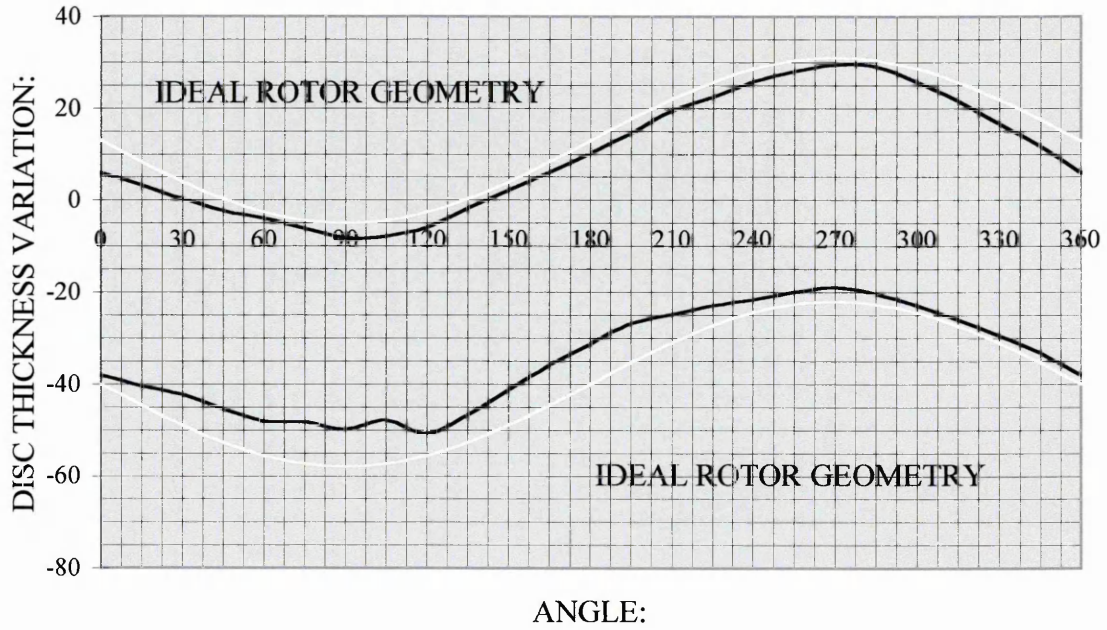


Figure 58:

Form variation of D.T.V. test rotor no. 10, rubbed against commercial friction material; N, at \varnothing 140 mm (inner diameter - top) and at \varnothing 230 mm (outer diameter - bottom).

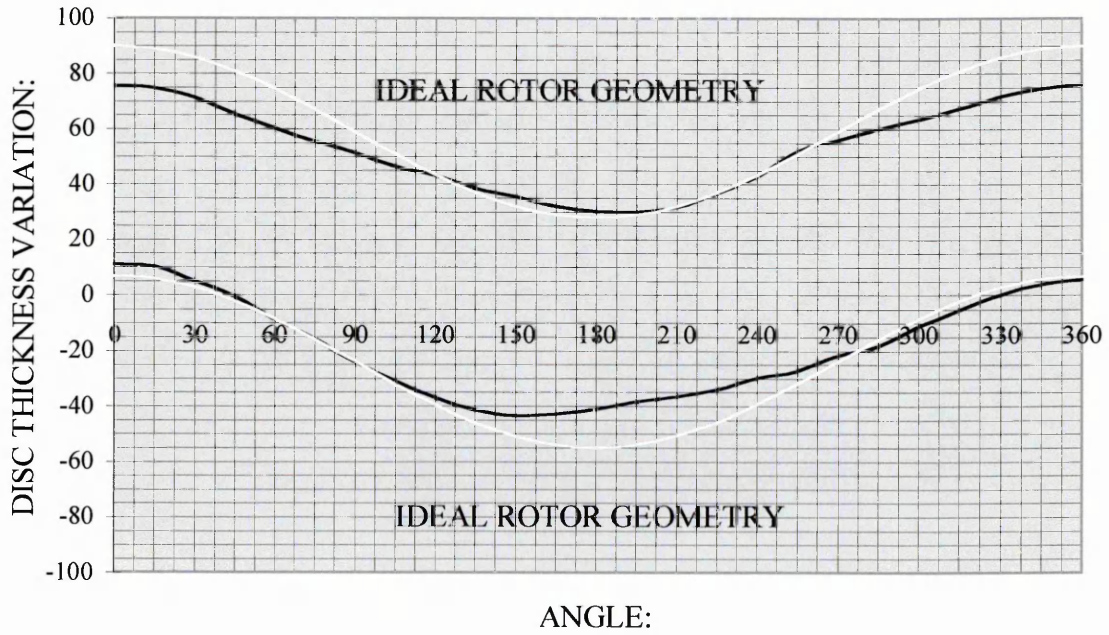
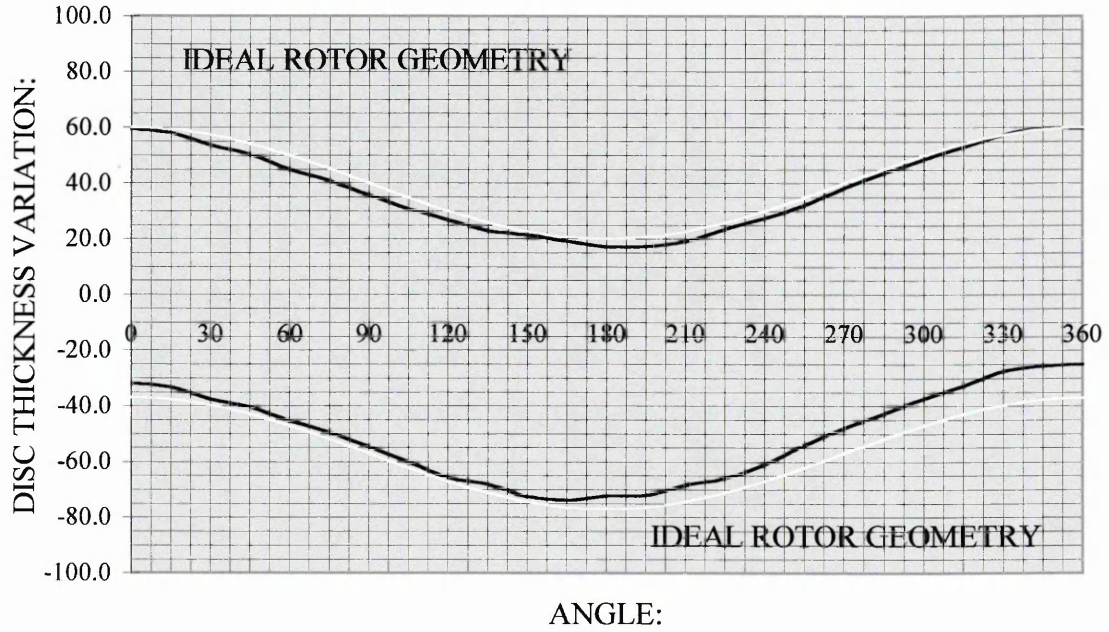


Figure 59:

Form variation of D.T.V. test rotor no. 11, rubbed against commercial friction material; S, at \varnothing 140 mm (inner diameter - top) and at \varnothing 230 mm (outer diameter - bottom).

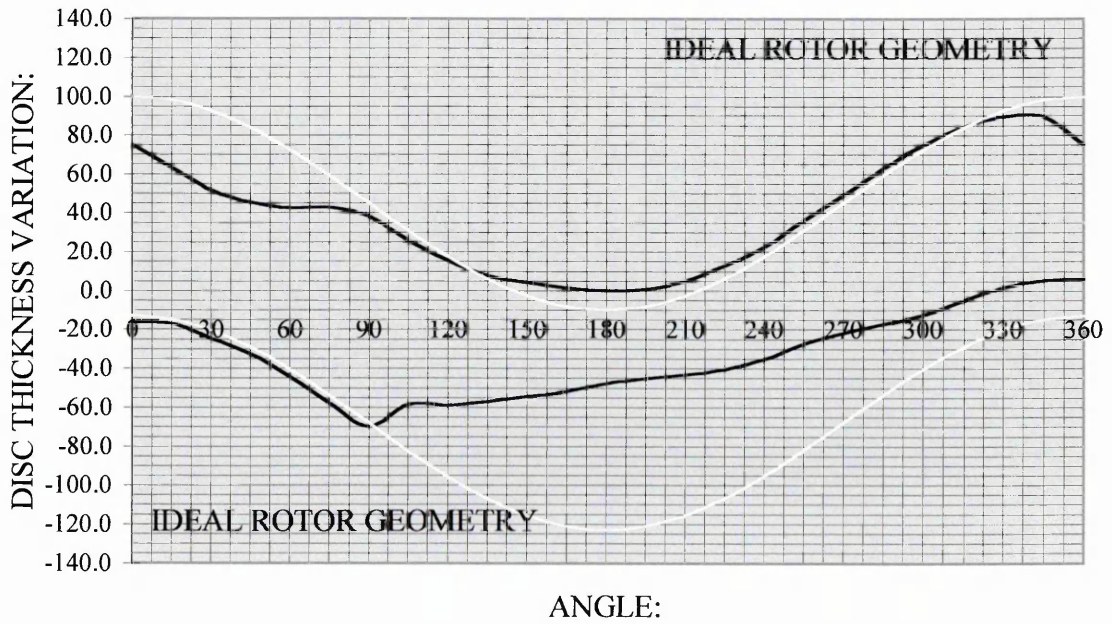
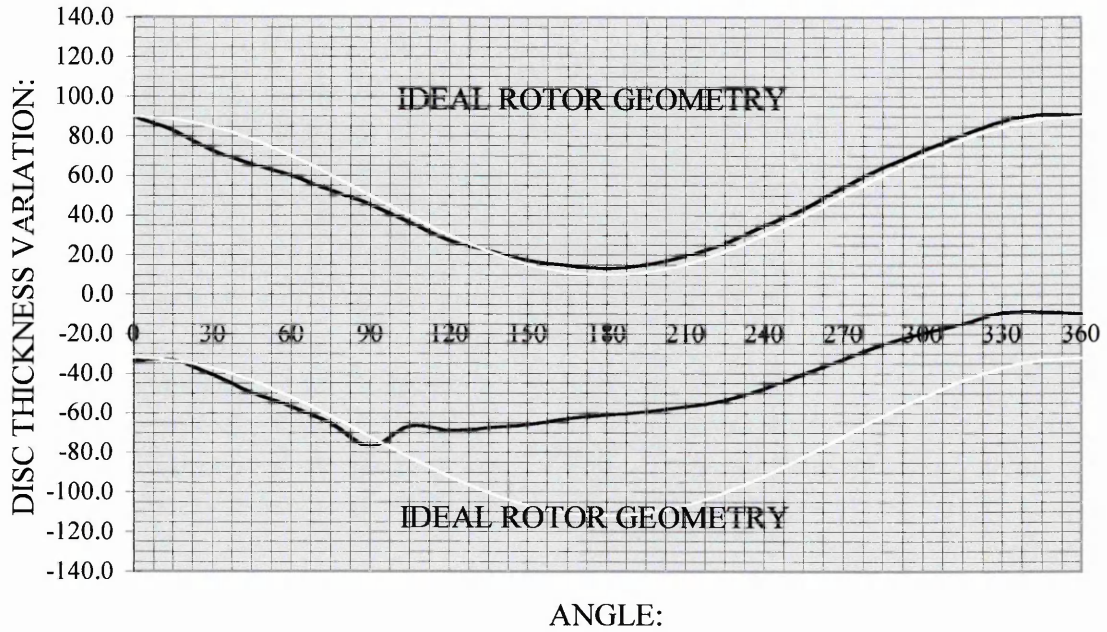


Figure 60:

Form variation of D.T.V. test rotor no. 12, rubbed against commercial friction material; N, at \varnothing 140 mm (inner diameter - top) and at \varnothing 230 mm (outer diameter - bottom).

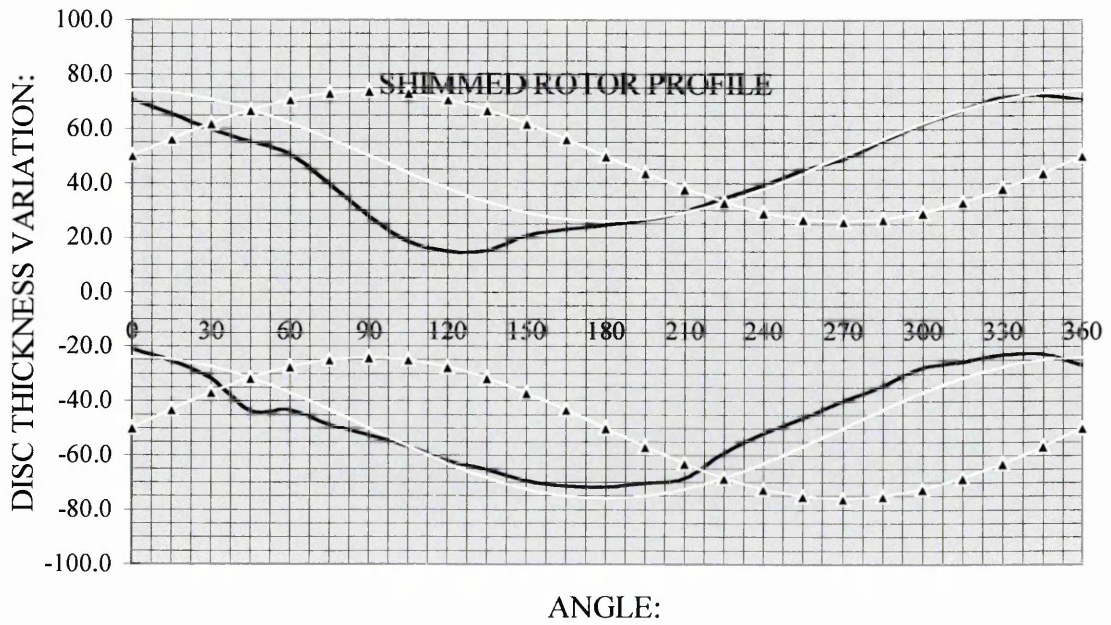
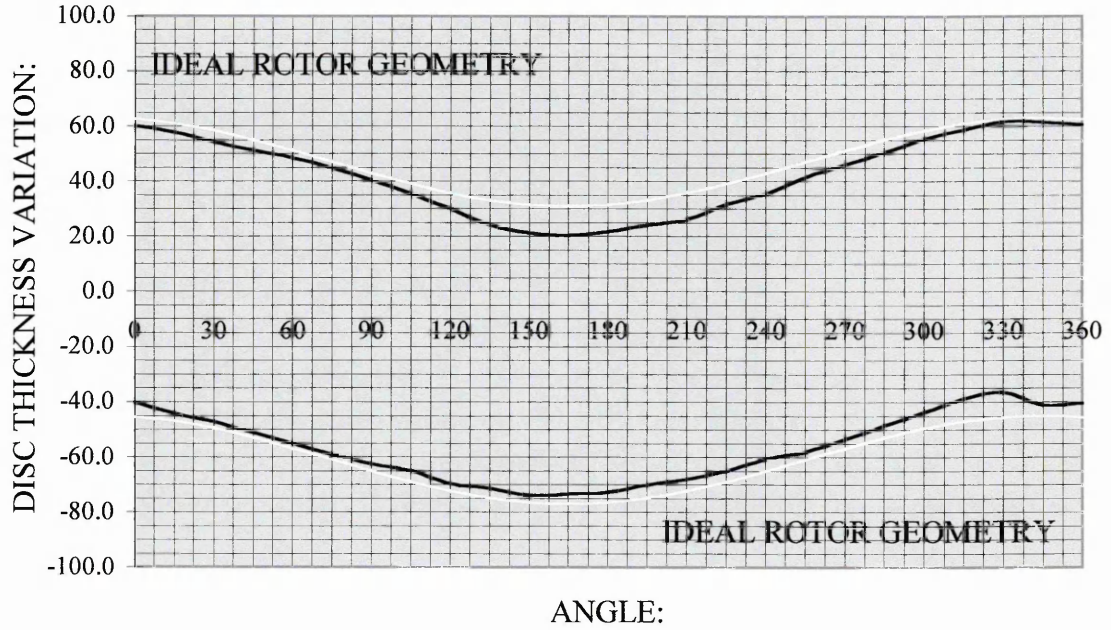


Figure 61:

Form variation of D.T.V. test rotor no. 13, rubbed against commercial friction material; S, at \varnothing 140 mm (inner diameter - top) and at \varnothing 230 mm (outer diameter - bottom).

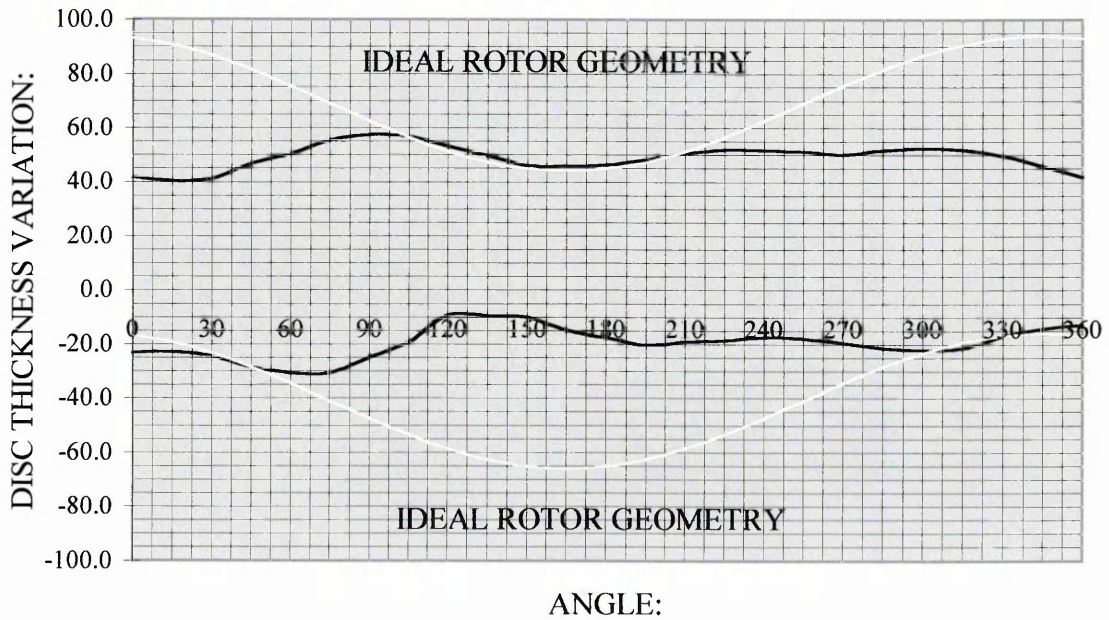
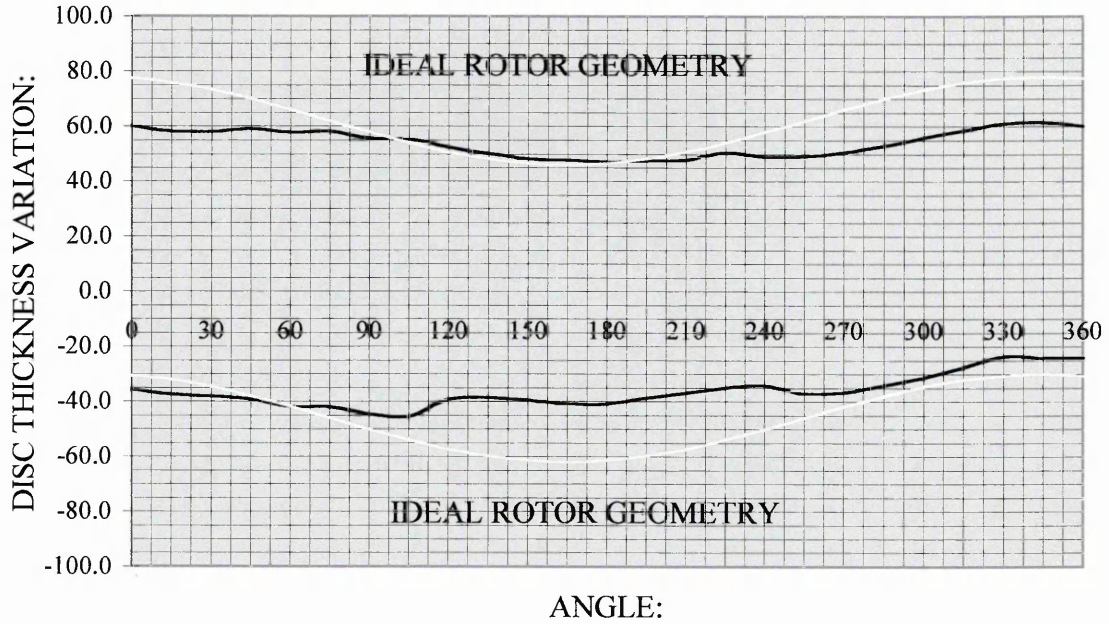


Figure 62:

Form variation of D.T.V. test rotor no. 9, rubbed against commercial friction material; N, in the shimmed condition (simulated axial S.R.O. = 120 μm) at \varnothing 140 mm (inner diameter - top) and at \varnothing 230 mm (outer diameter - bottom).

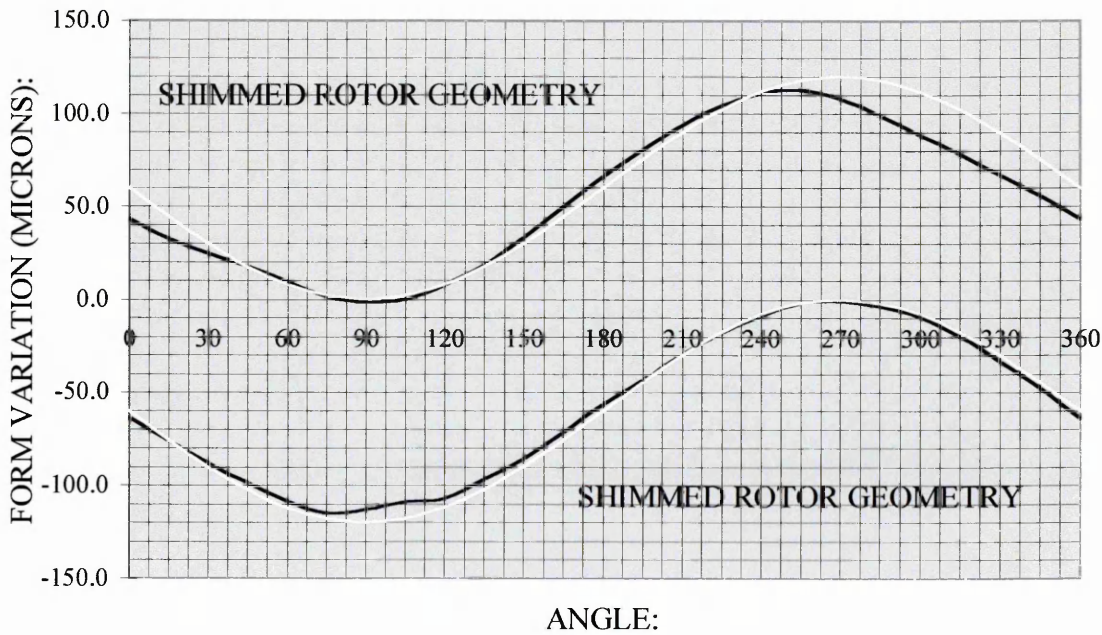
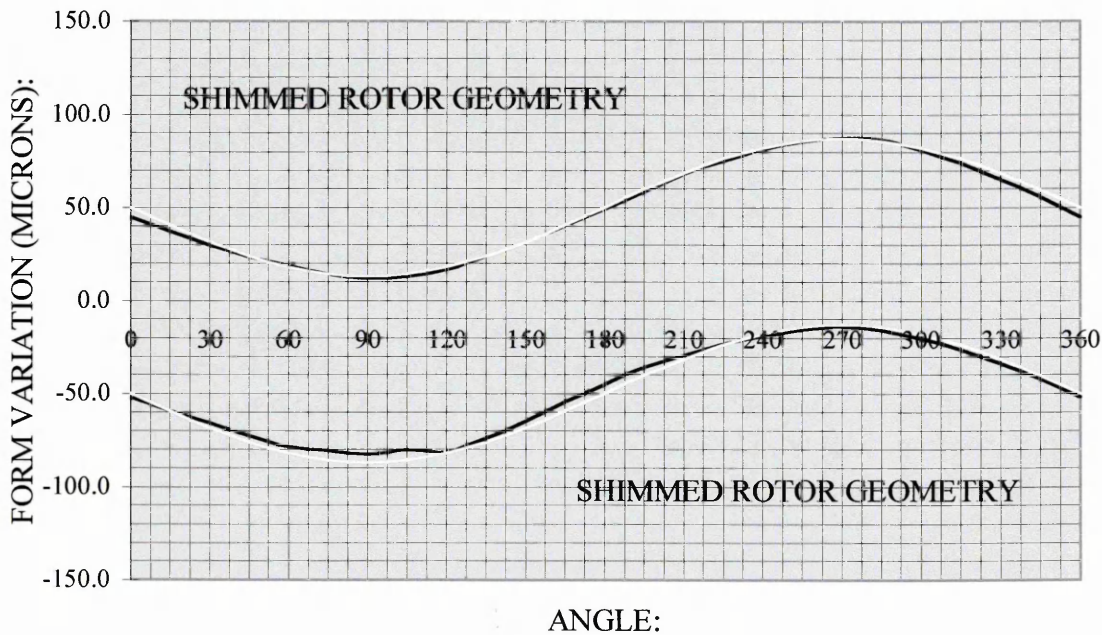


Figure 63:

Form variation of D.T.V. test rotor no. 13, rubbed against commercial friction material; S, in the shimmed condition (simulated axial S.R.O. = 120 μm) at $\varnothing 140$ mm (inner diameter - top) and at $\varnothing 230$ mm (outer diameter - bottom).

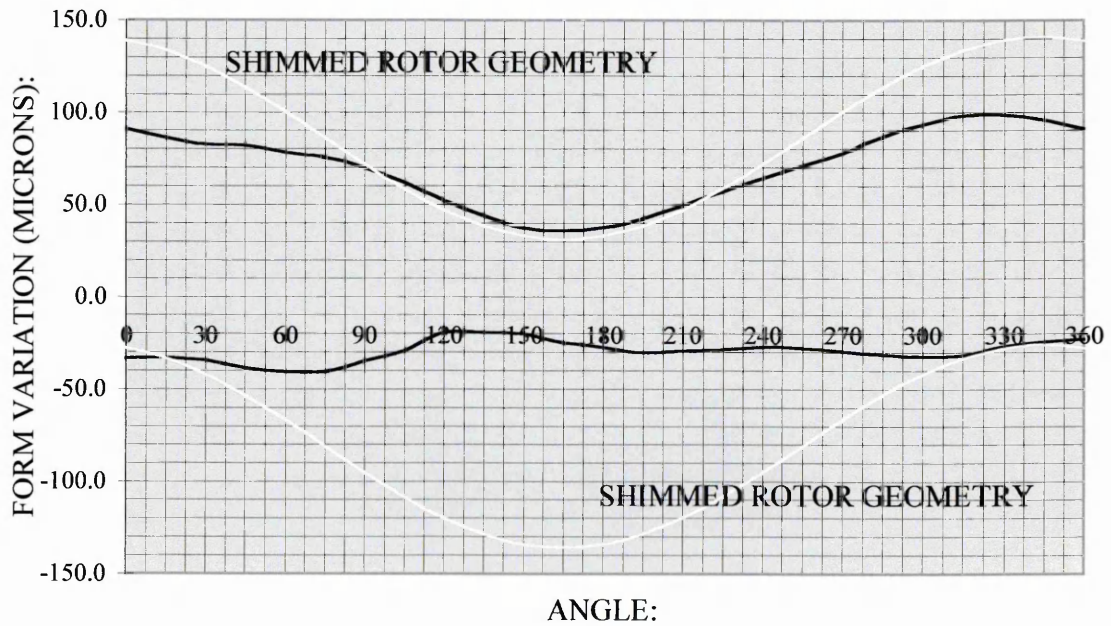
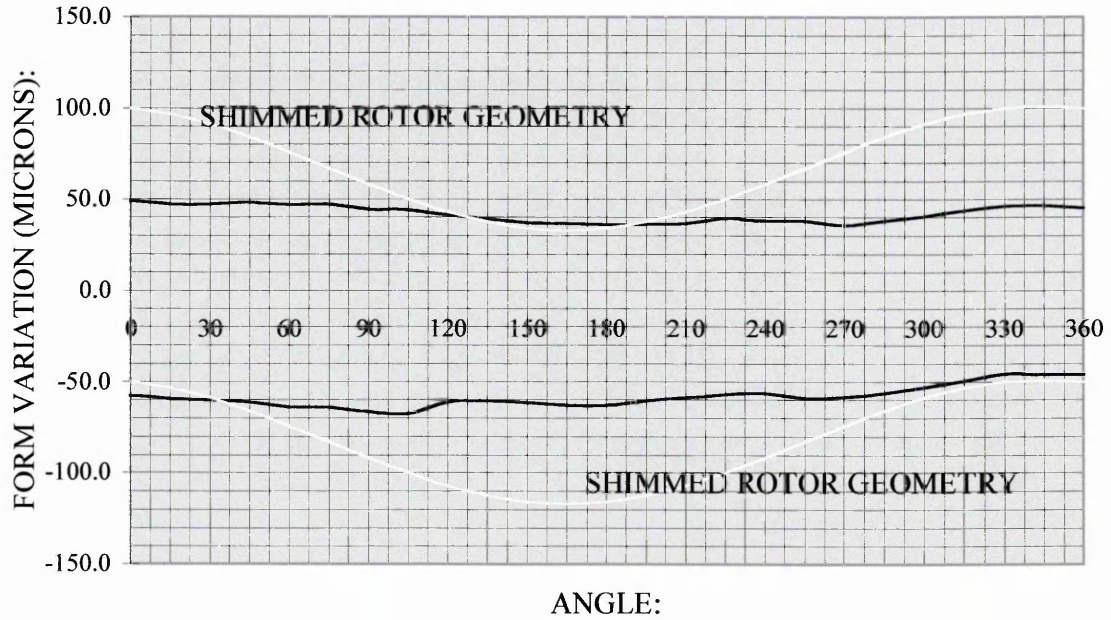
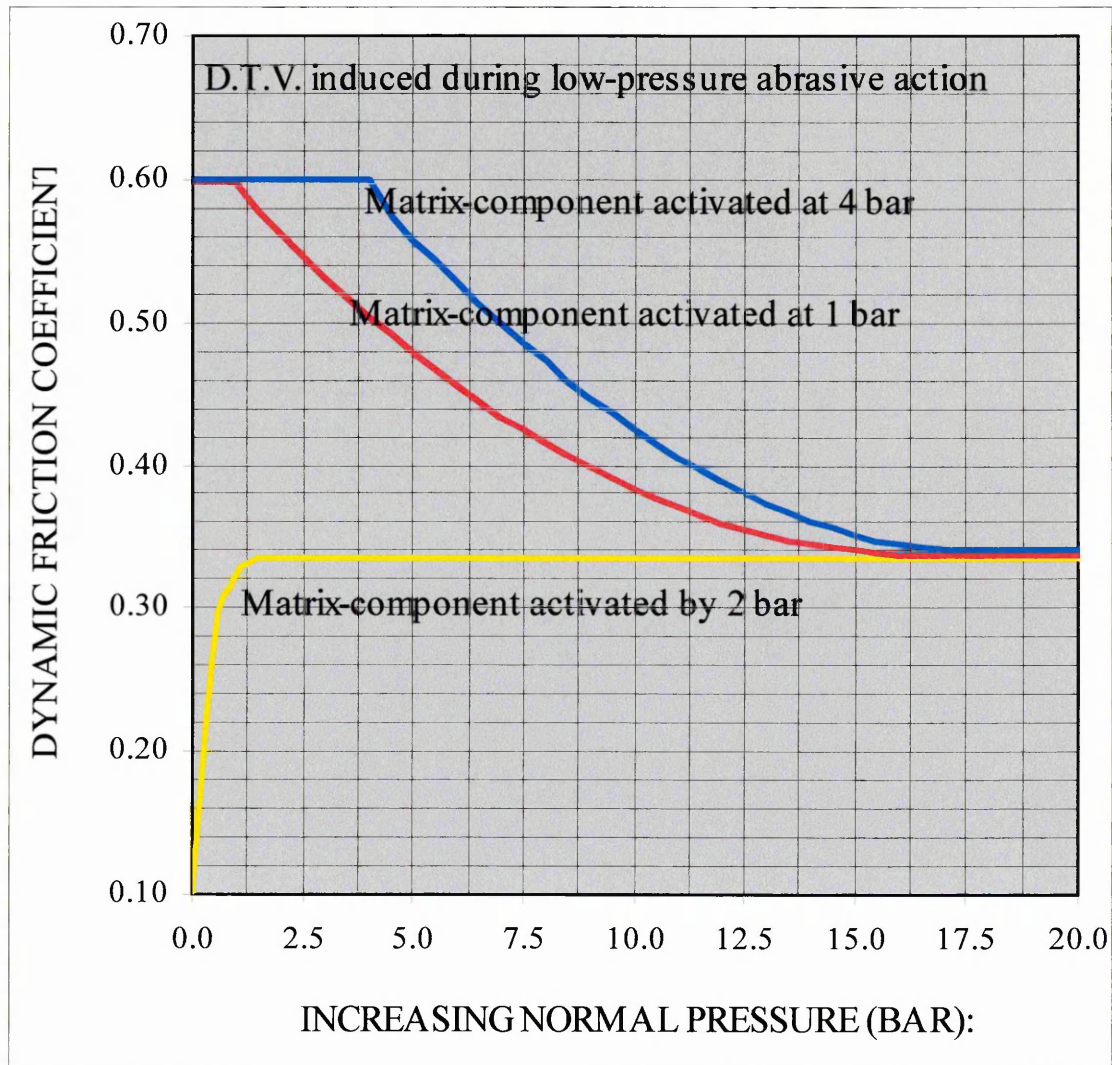


Figure 64:

Plot showing the suggested tribological pressure threshold between abrasive particle friction and matrix friction for three theoretical friction materials.



The friction material in which the matrix component of friction is introduced at a normal force of 4 bar (blue) is intended to describe a matrix of higher stiffness, or containing larger abrasives, than that activated at 1 bar (red). The friction material showing a rapidly ascending friction level (yellow) represents the author's view of standard behaviour.

Figure 65:

Plots showing the proportionality of D.T.V. generated at varying rubbing radii on the friction rings of D.T.V. test rotors 9 - 13 (top), and the same characteristic corrected to account for manufactured D.T.V. and measurement uncertainty (bottom).

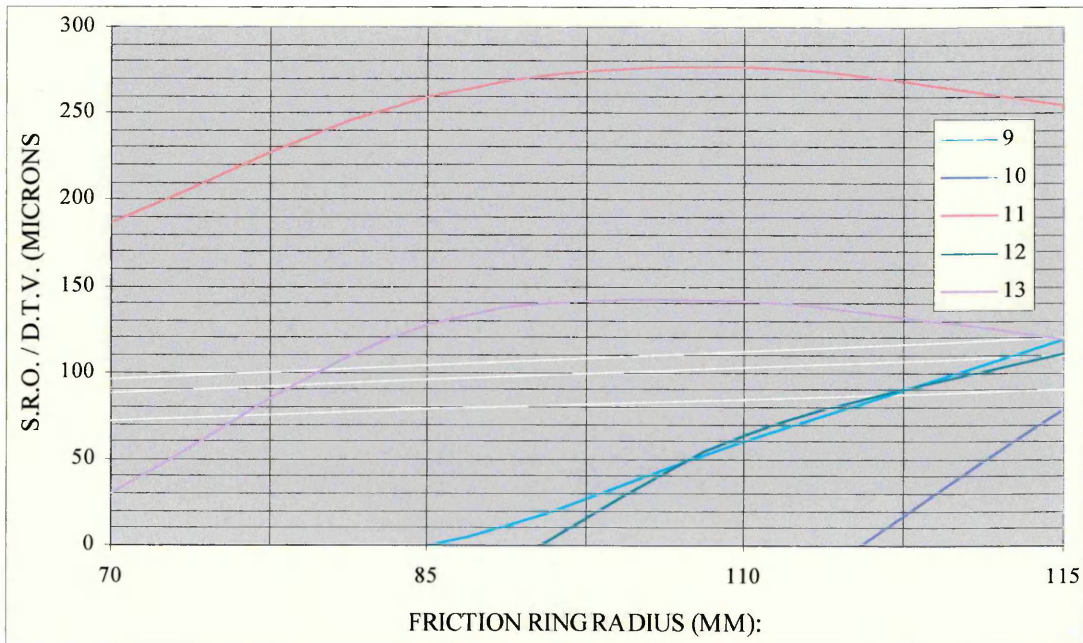
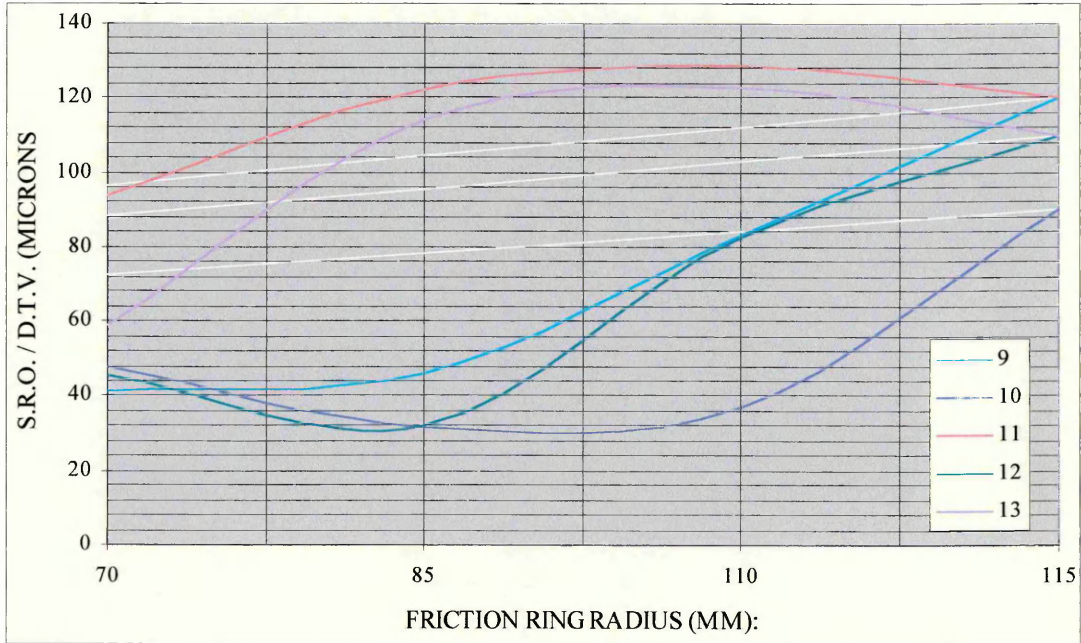


Figure 66:

Wear depth profiles showing the level of D.T.V. generation at two positions on the friction ring of D.T.V. test rotor no. 10. Rather than being perfectly diametrically opposed, the sections are opposed by 173°.

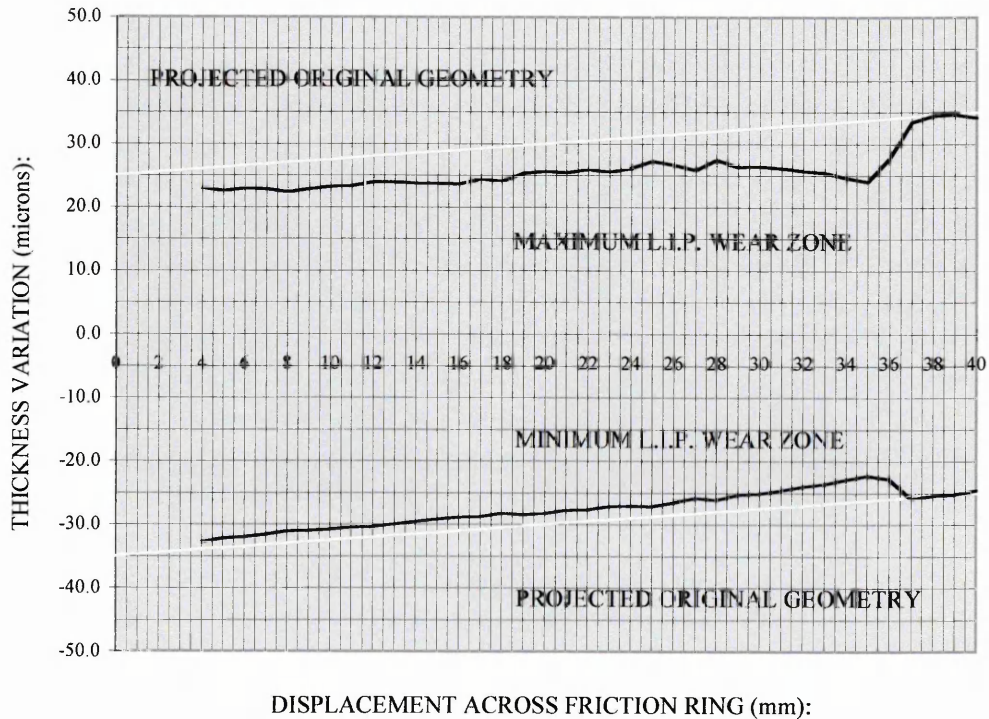
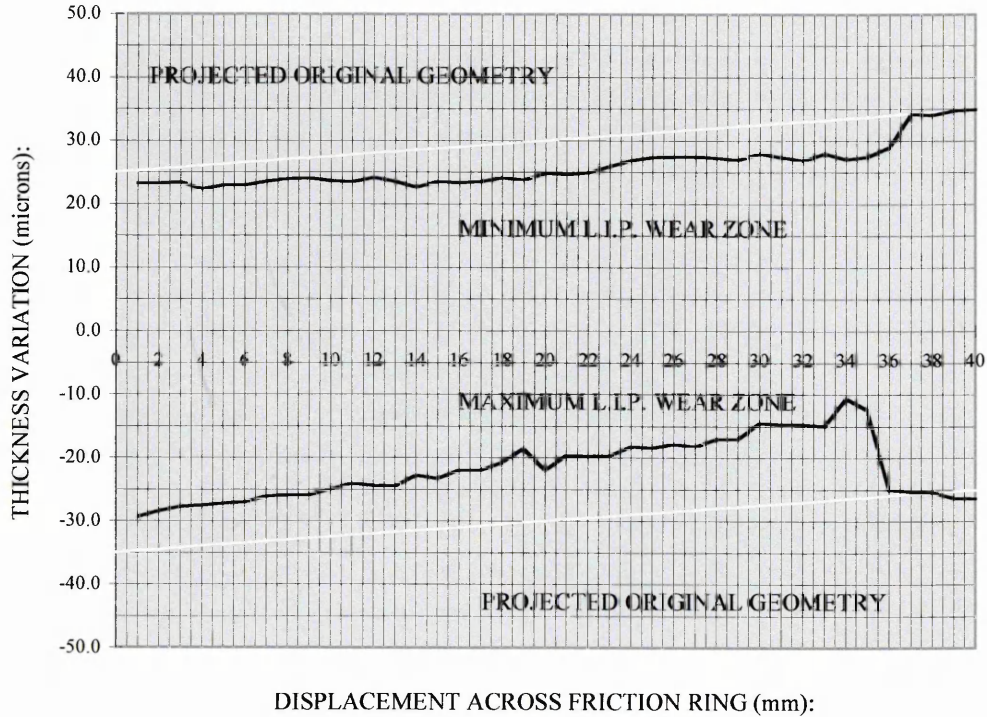


Figure 67:

Wear depth profiles showing the level of D.T.V. generation at two positions on the friction ring of D.T.V. test rotor no. 11. Rather than being perfectly diametrically opposed, the sections are opposed by 170°.

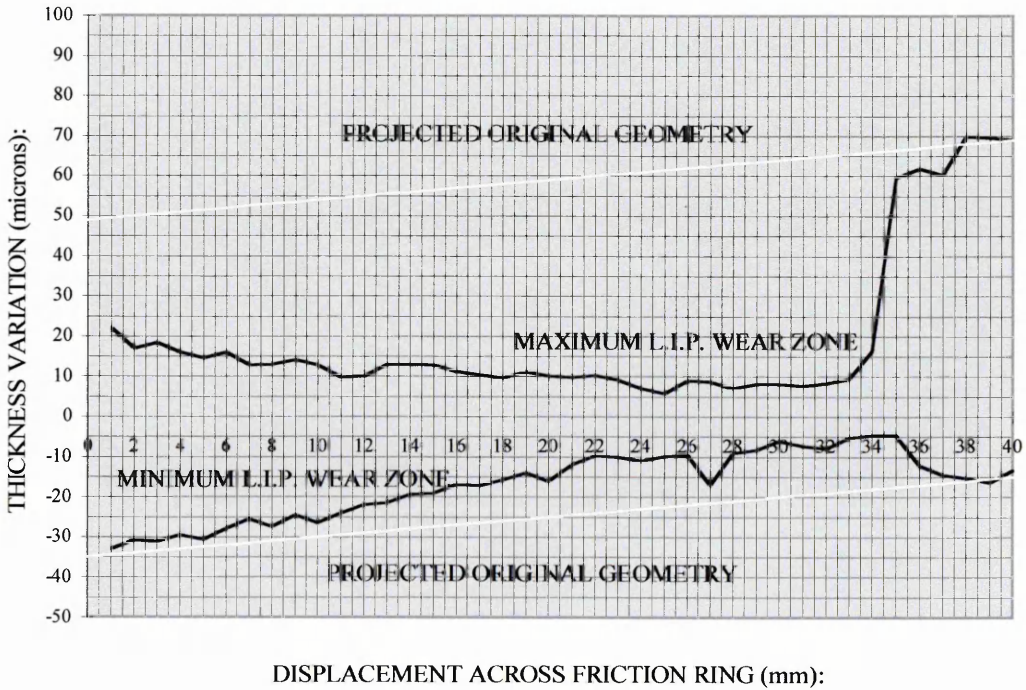
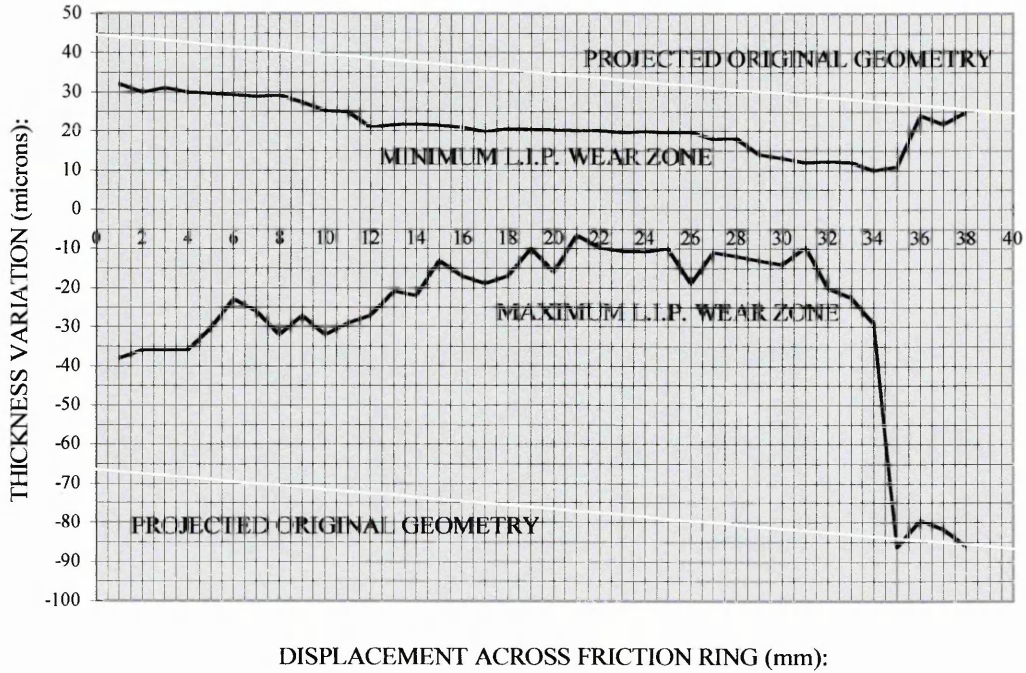


Figure 68:

X-ray spectra collected from equal areas of D.T.V. test rotor no. 13 having been rubbed against commercial N.A.O. friction material; S, under simulated off-brake conditions for 80 hours.

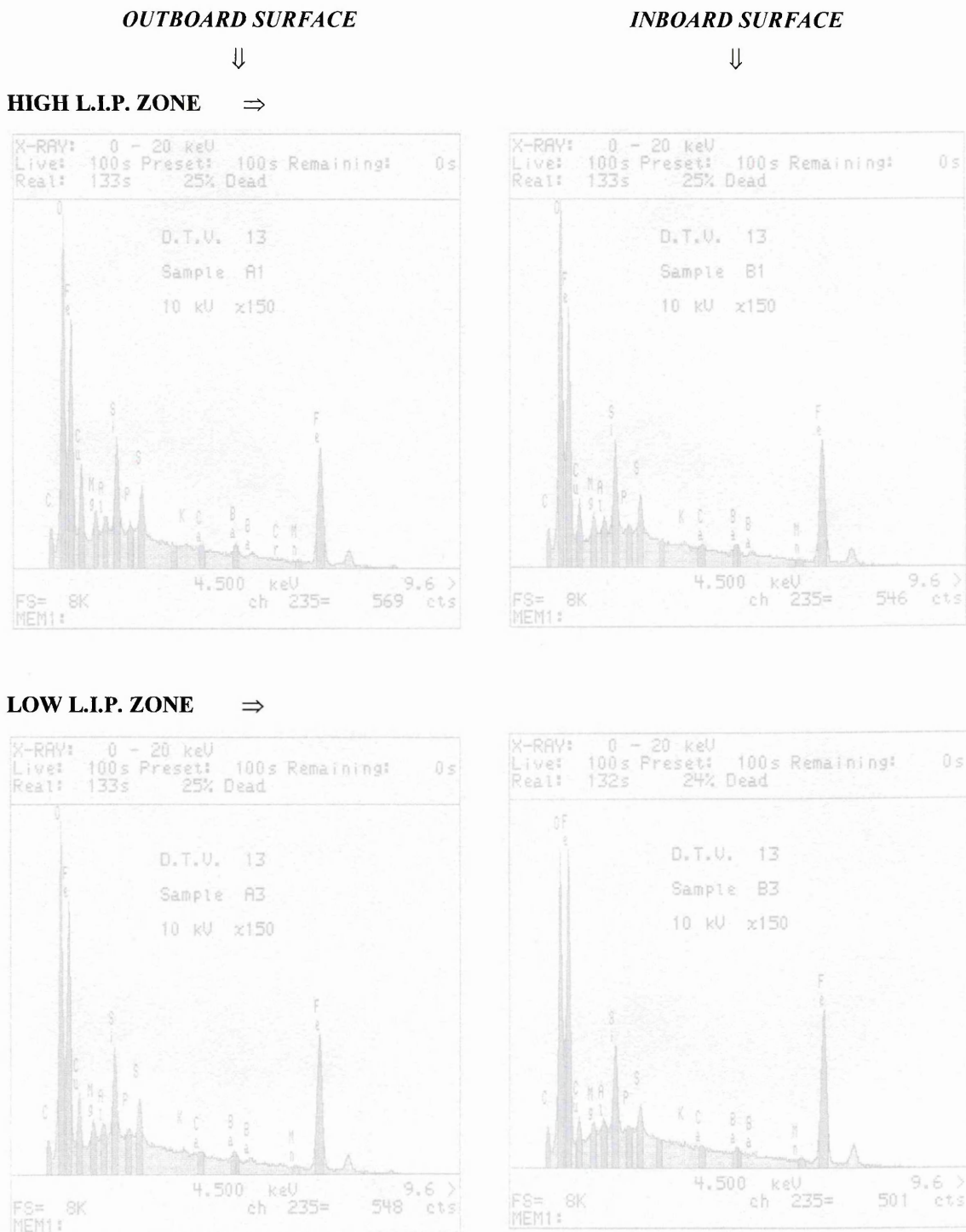


Figure 69:

Wear rates of copper under conditions of two-body and three-body abrasion and erosion, due to silicon carbide particles of different sizes. Duplicated from reference 168.

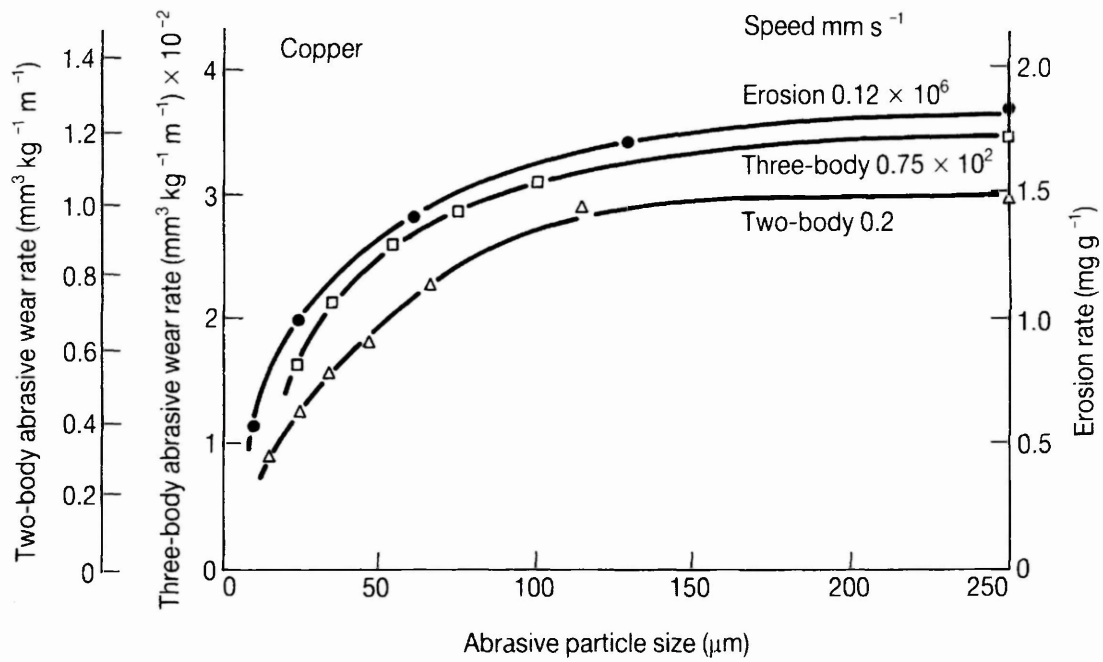


Figure 70:

Grooved / perforated disc brake rotors potentially capable of facilitating the generation of uniform transfer films.

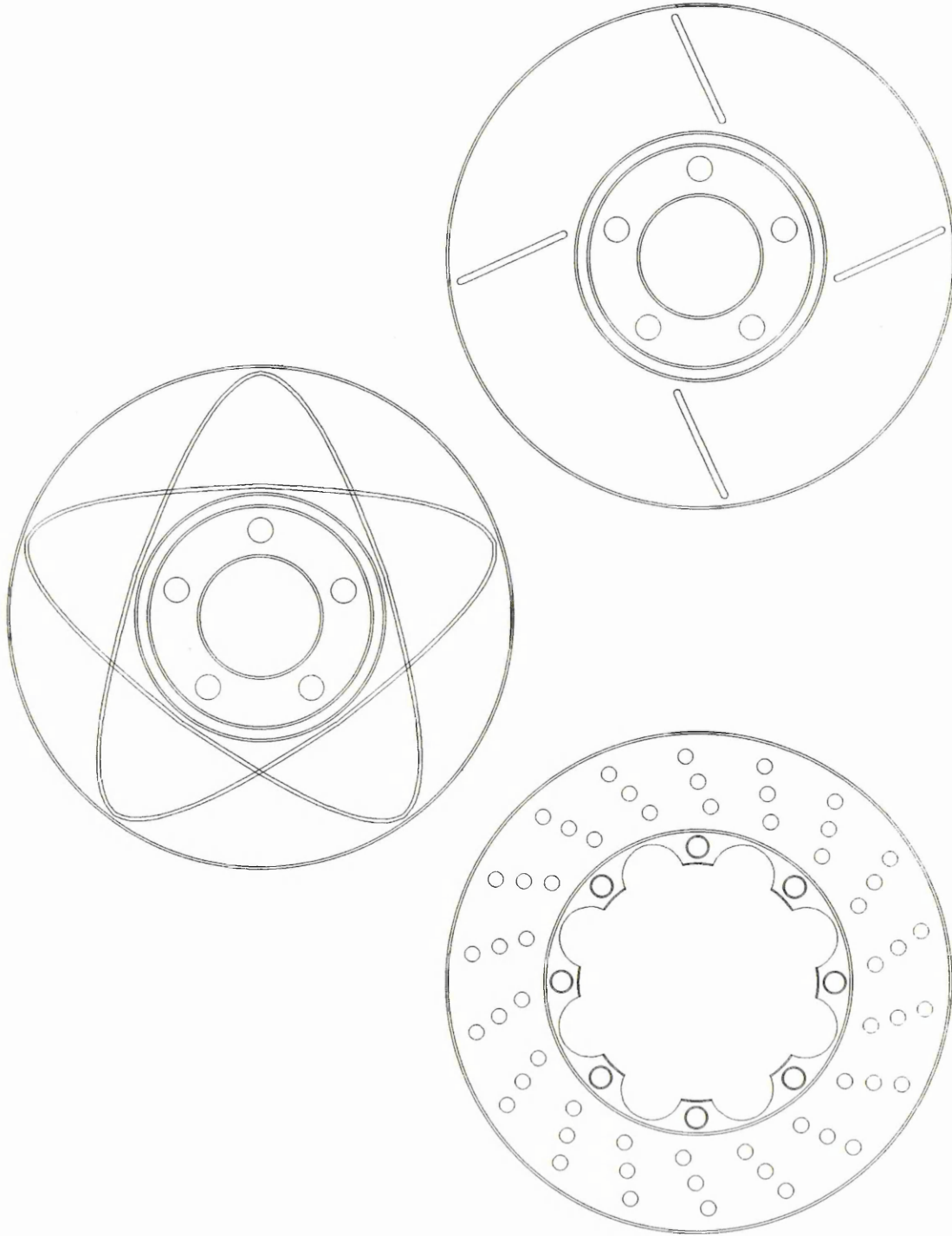


Plate 1:

Commercial, front-axle, disc brake assembly of a small Passenger / Light Goods (PLG) vehicle. The position of the caliper may vary from model to model depending upon the mounting space available. The caliper shown is mounted toward the front of the vehicle. Also visible as being attached to the stub-axle carrier are (below: from left to right); steering system tie rod and tie rod end, upper suspension arm, suspension strut assembly and the caliper brake hose.



Plate 2:

3-dimensional surface roughness profiles, generated using standard contact profilometry, of a virgin friction ring surface turned on a C.N.C. lathe (top), and of a typical, fully burnished friction ring surface (bottom).

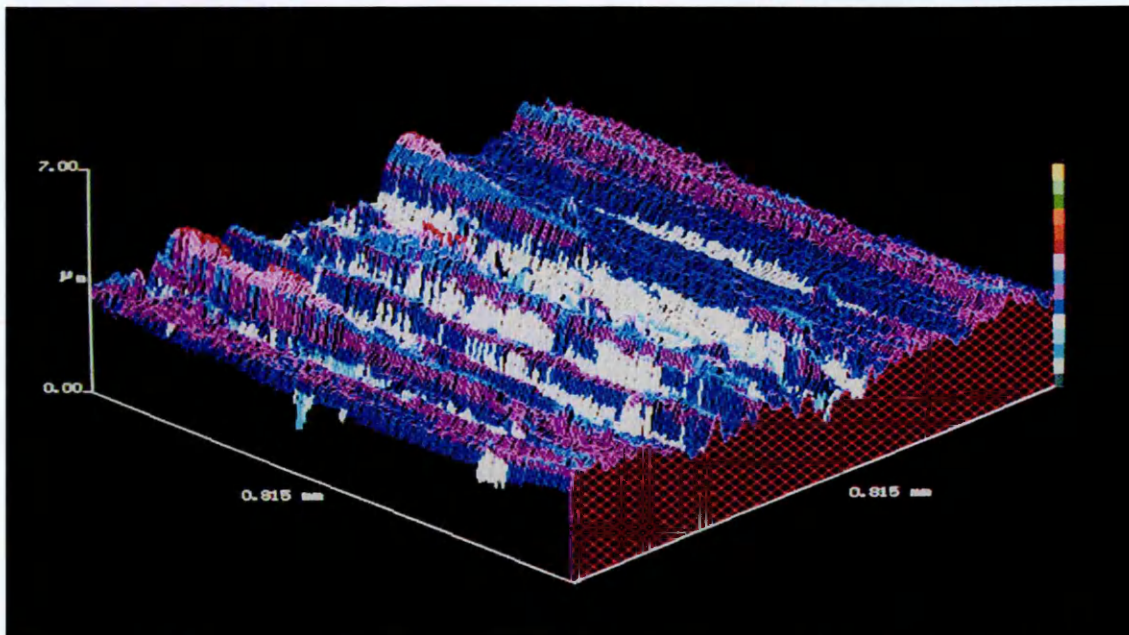
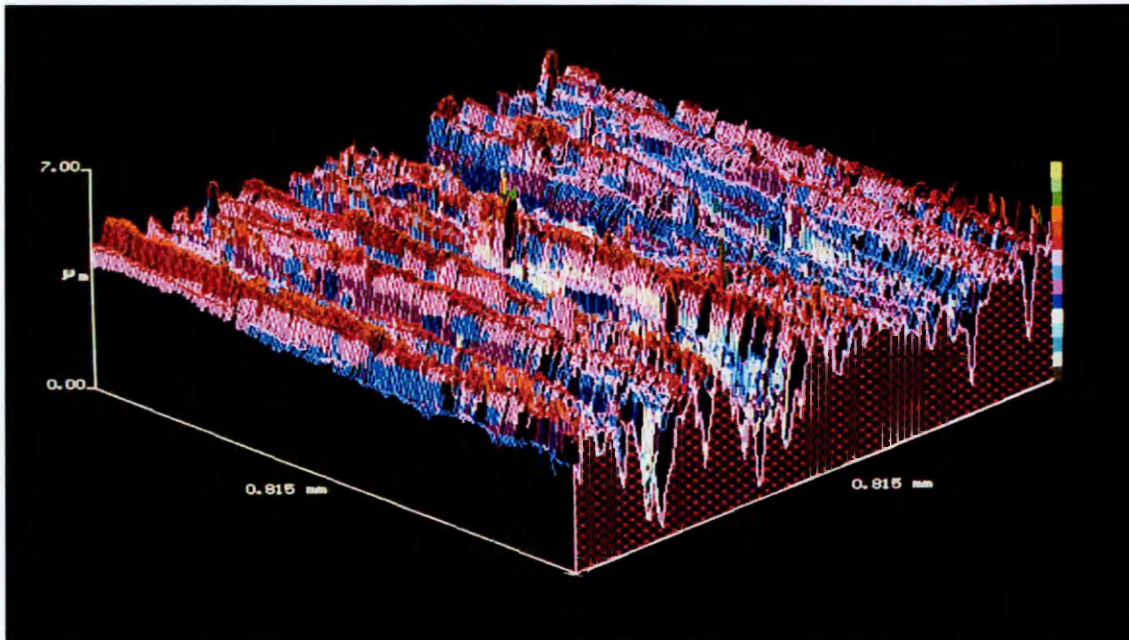


Plate 3:

An aftermarket, commercial, front-axle, disc brake pad for a small Private / Light Goods (PLG) vehicle.

*The design of pad pictured is suitable for an **Ate** fist-type floating caliper such as finds application on the **Ford Fiesta, Escort and Mondeo**, and on many **BMW** vehicles.*

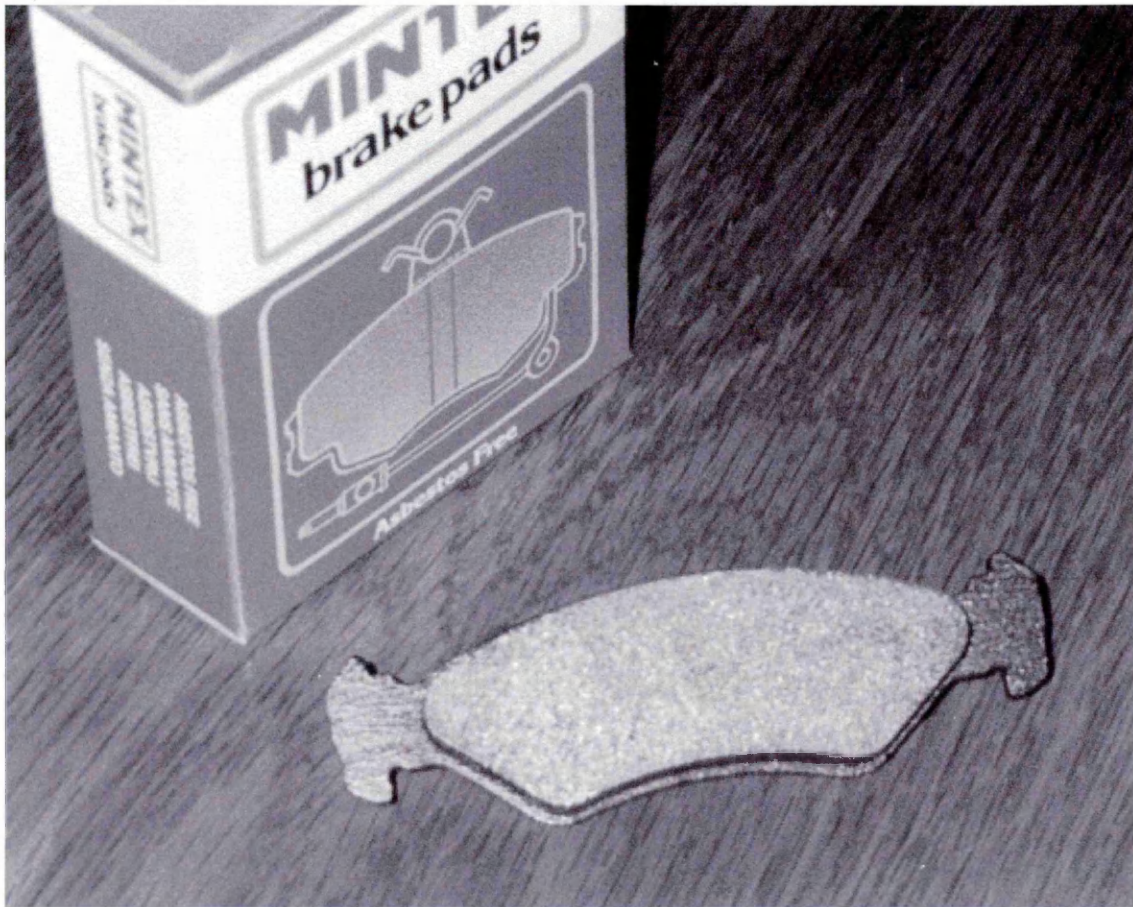


Plate 4:

Secondary electron (top left) and backscattered electron (bottom left) micrographs of a metallographically prepared surface of pad AB 7 showing microscopic particulate dispersion (mapped region) and X-ray elemental digimaps for aluminium (top right), oxygen (middle right) and calcium (bottom right).

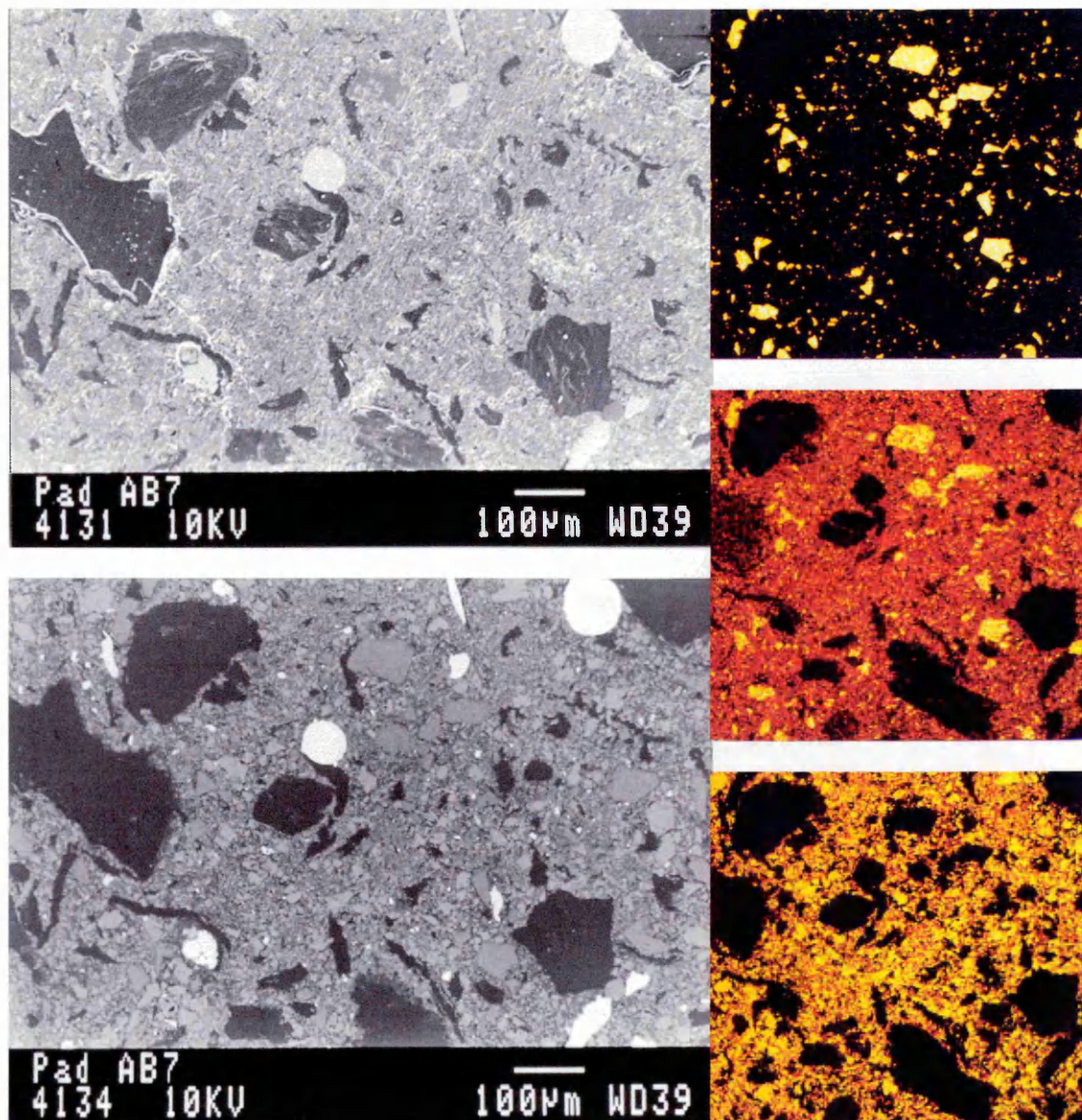


Plate 5:

Grey cast iron rotor surfaces polished using increasingly fine abrasive particulates.

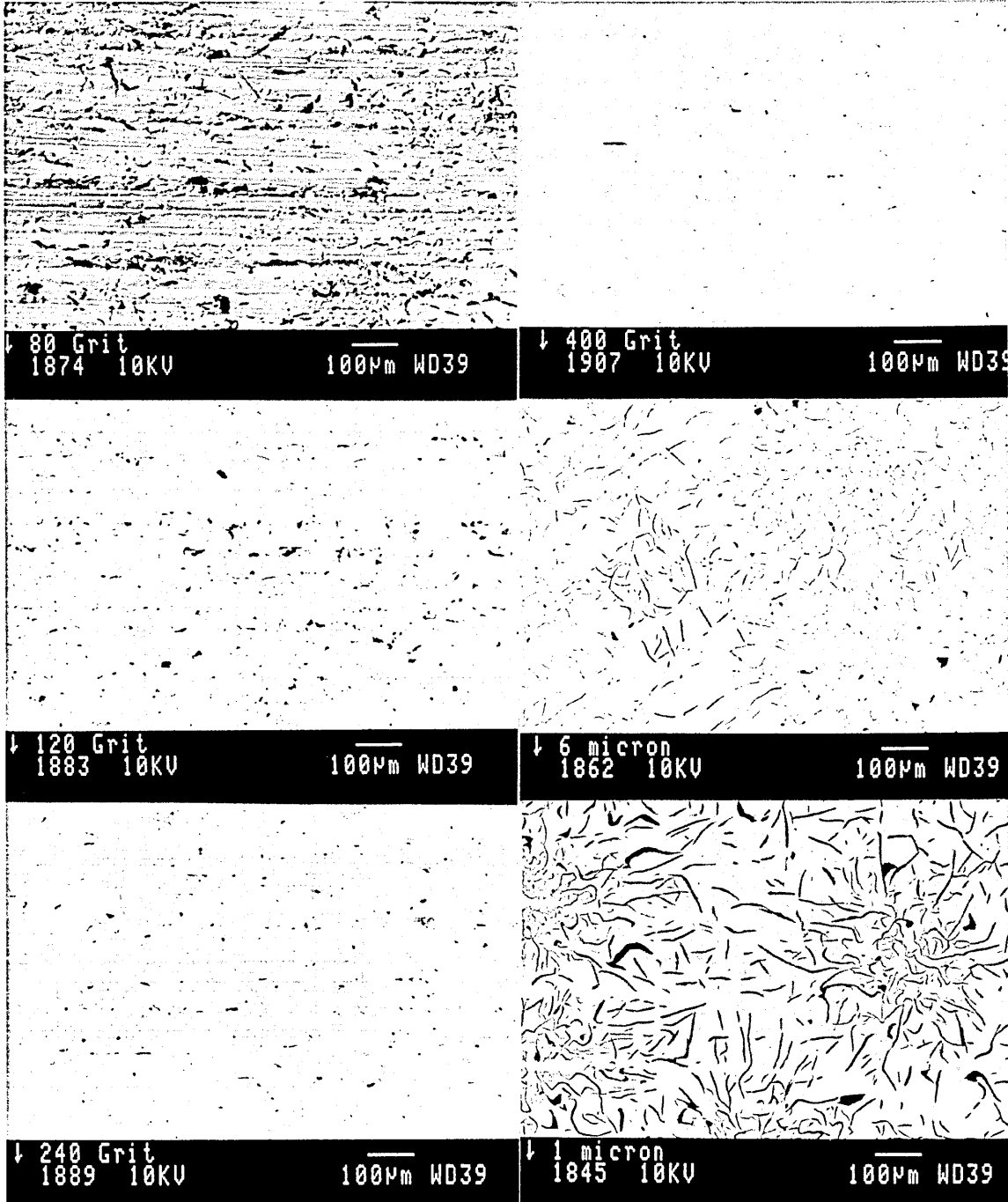


Plate 6:

Secondary electron micrographs showing the exposed, graphite lamellae structure of a formerly pearlitic, grey cast iron.



Magnification = x 280



Magnification = x 280



Magnification = x 140



Magnification = x 140



Magnification = x 70



Magnification = x 70

Plate 7:

Dark-field, backscattered electron micrographs showing regions of fine pearlite lamellae located within the matrices of 10 sample castings (mag. $\approx x 4000$).

Disc samples		7
1	4	8
2	5	9
3	6	10

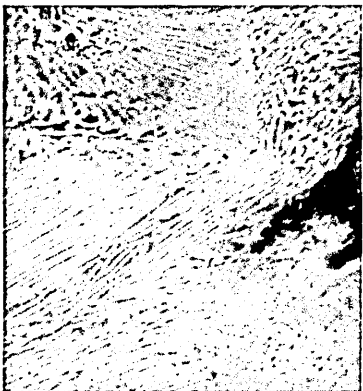
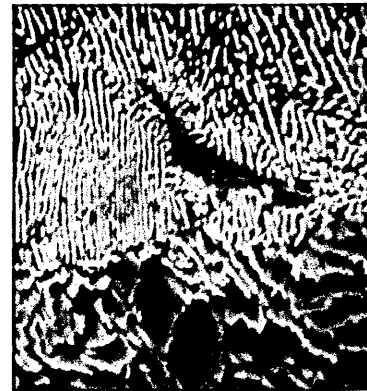
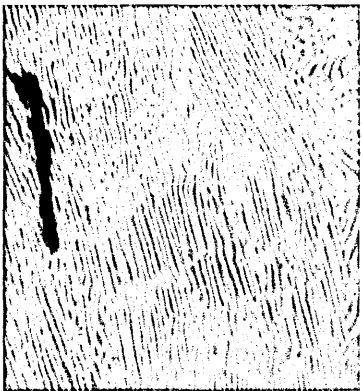


Plate 8:

Secondary electron micrographs showing gold-sputtered abrasive particulates used in commercial friction material formulations (fused alumina (angular), calcined alumina (rounded), zirconium silicate (ellipsoidal) and chromia (angular)).

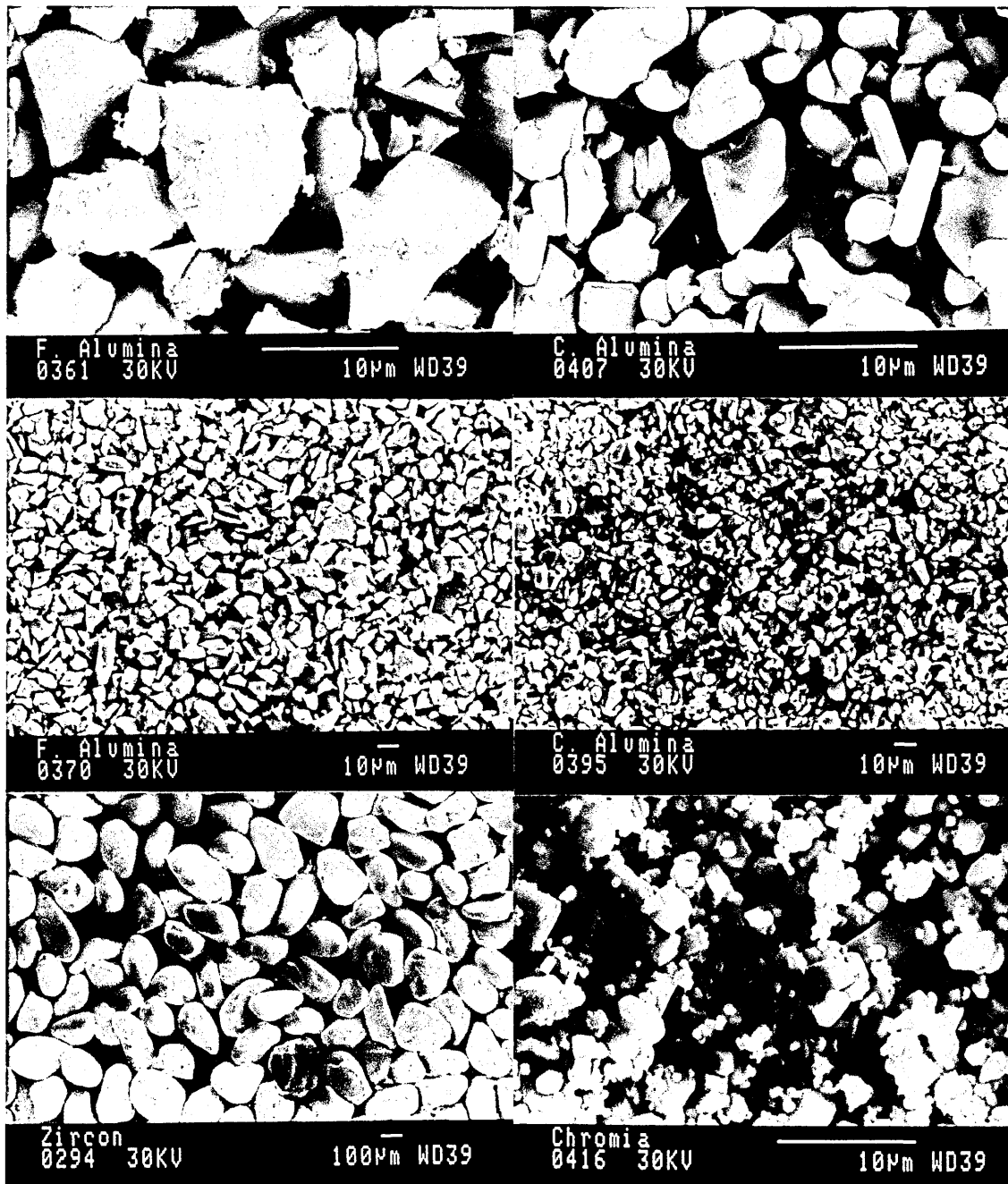


Plate 9:

Optical, bright-field micrographs showing particles of zirconium silicate (top) and a single particle of zirconium silicate embedded in the surface of a friction material host (bottom).

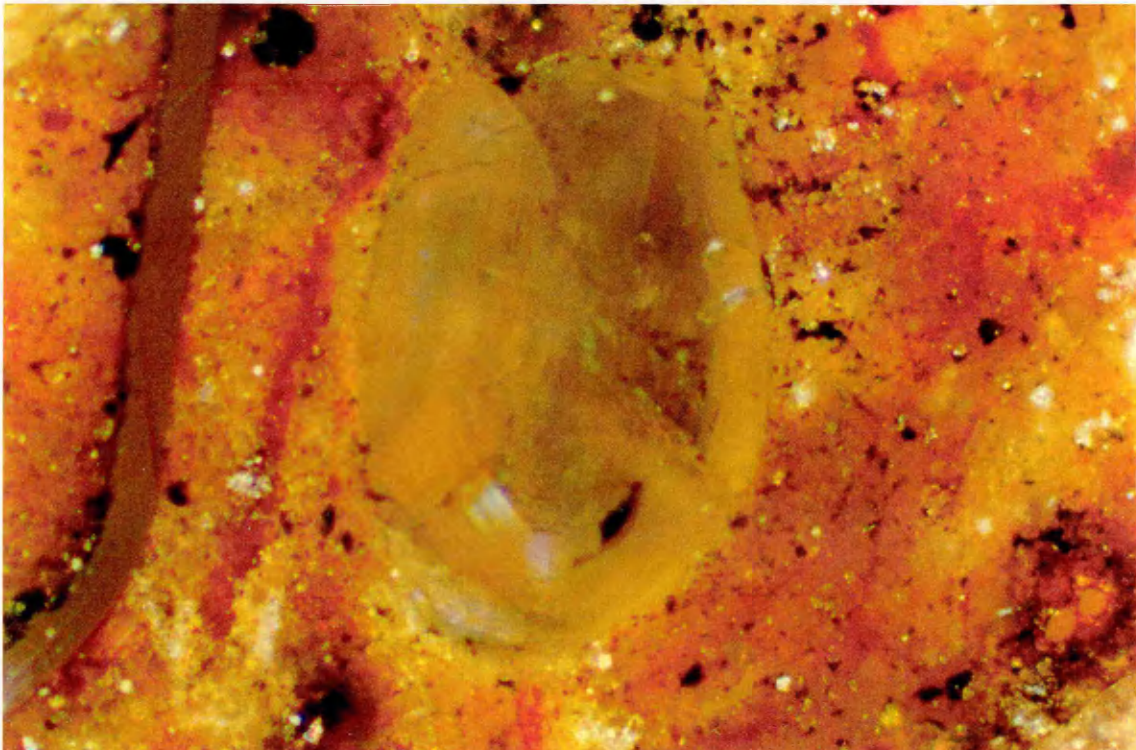


Plate 10:

X-ray elemental digimaps showing the aluminium (i.e. effectively the alumina) distribution at metallographically prepared surfaces of pads AB 1 – 3 and AB 7 – 9.

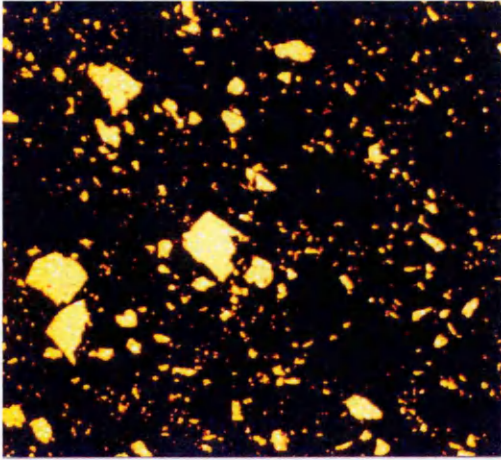
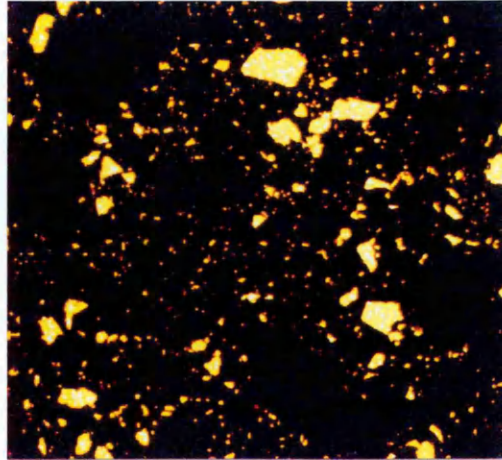
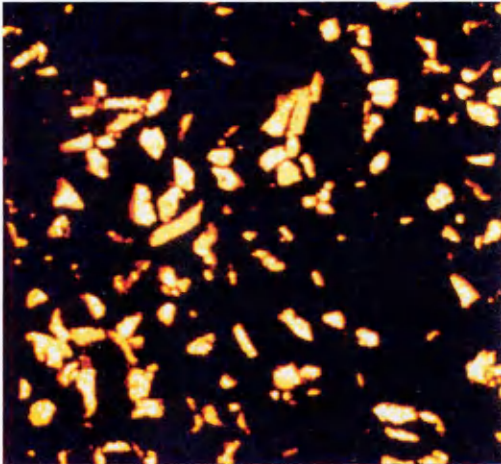
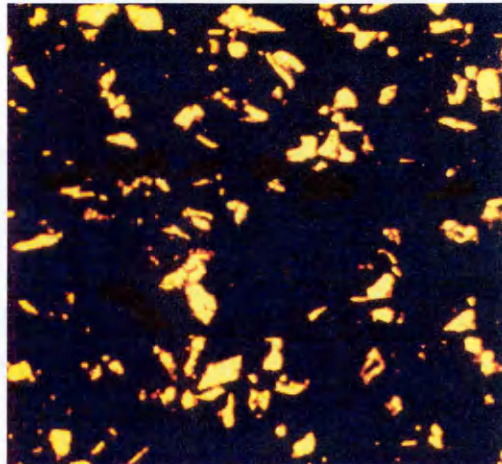
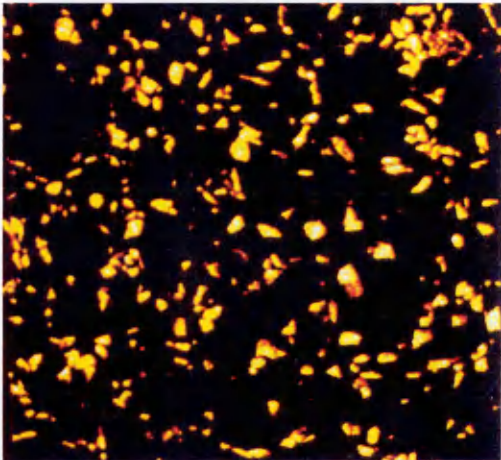
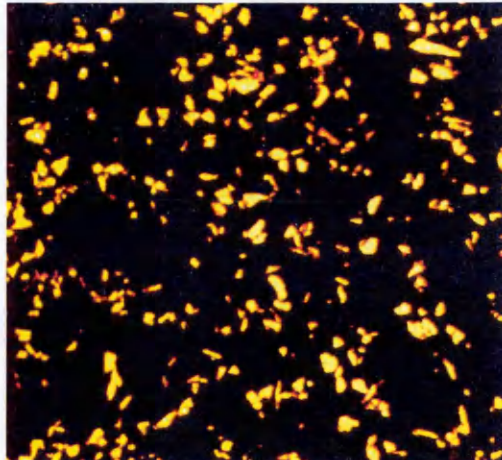
AB 1 - ALUMINA 200**AB 7 - ALUMINA 200****AB 2 - ALUMINA 500****AB 8 - ALUMINA 500****AB 3 - ALUMINA 800****AB 9 - ALUMINA 800**

Plate 11:

X-ray elemental digimaps showing the zirconium (i.e. effectively the zirconium silicate) distribution at metallographically prepared surfaces of pads AB 4 – 6 and AB 10 – 12.

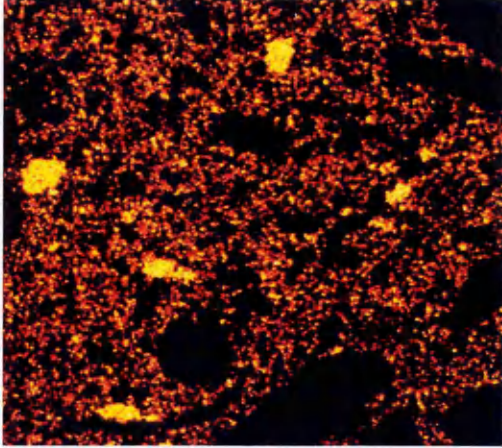
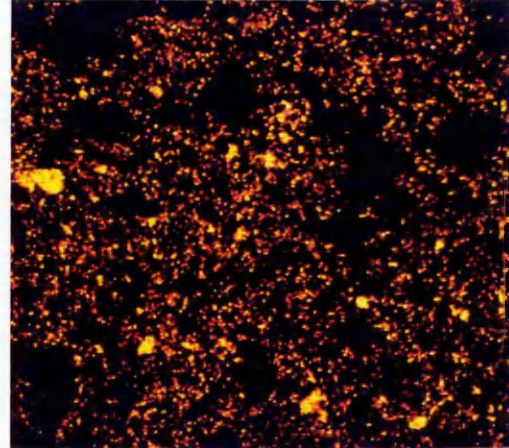
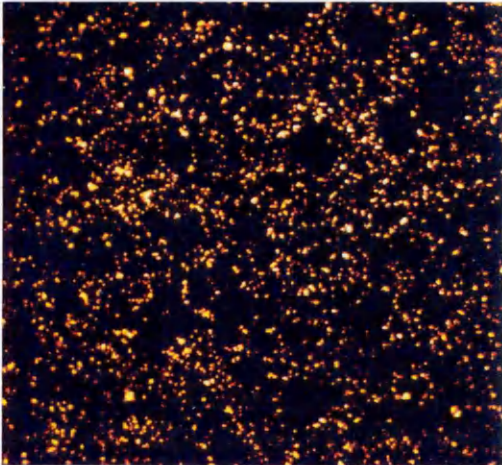
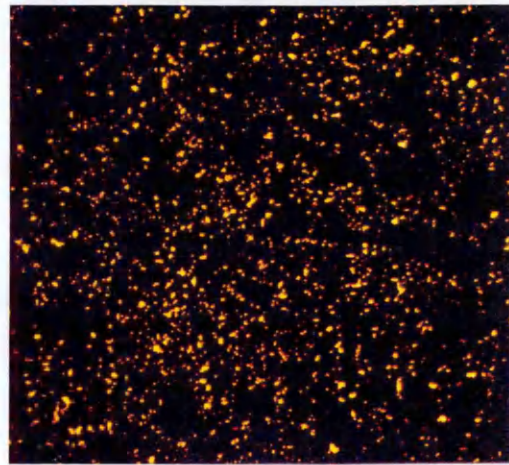
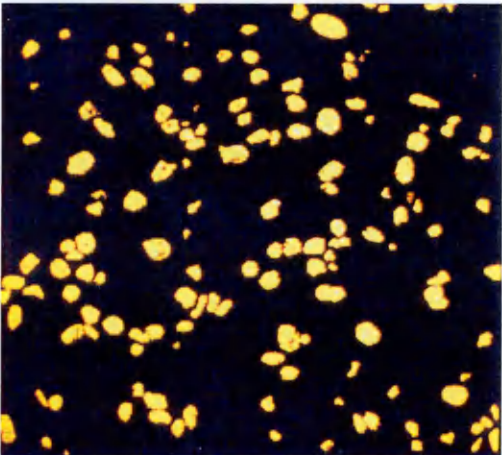
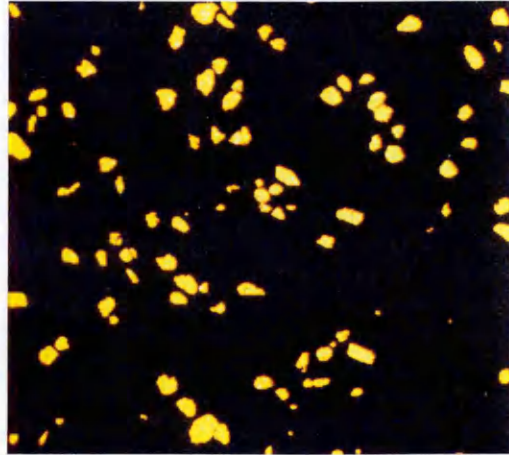
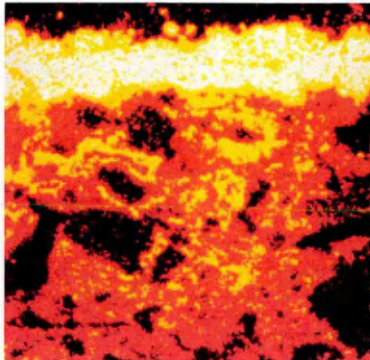
AB 4 – ZIRCONIUM SILICATE 100**AB 10 - ZIRCONIUM SILICATE 100****AB 5 - ZIRCONIUM SILICATE 200****AB 11 - ZIRCONIUM SILICATE 200****AB 6 - ZIRCON SAND****AB 12 - ZIRCON SAND**

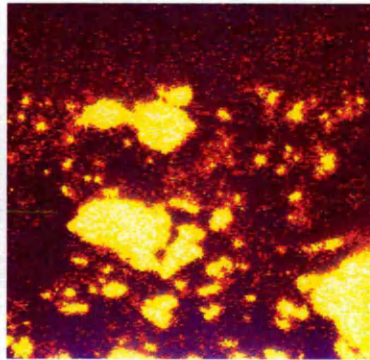
Plate 12:

Thermographic digital elemental X-ray maps (accelerating voltage = 20 kV, magnification = x 480) showing the diffusional redistribution of MFM 3 constituents during isothermal incubation at 400 °C for 24 hours.

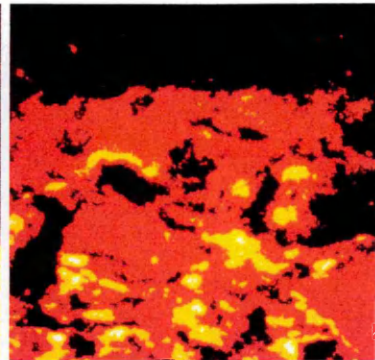
Copper (Cu)



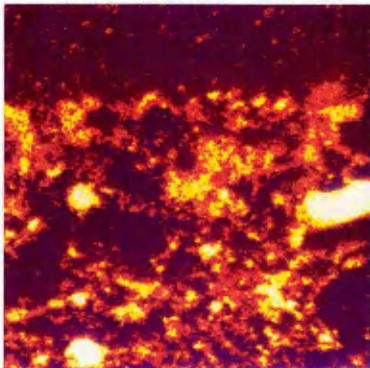
Barium (Ba)



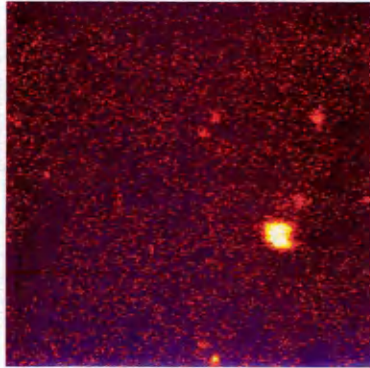
Molybdenum (Mo) / Sulphur (S)



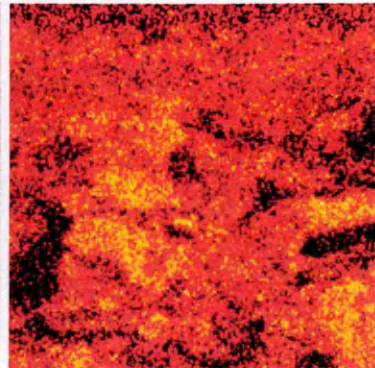
Iron (Fe)



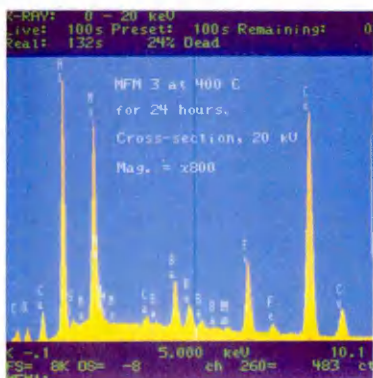
Calcium (Ca)



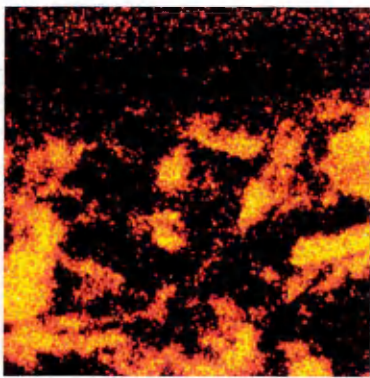
Oxygen (O)



Regional X-ray Spectrum



Carbon (C)



Aluminium (Al)



Plate 13:

Thermographic digital elemental X-ray maps (accelerating voltage = 20 kV, magnification = x 480) showing the diffusional redistribution of MFM 3 constituents during isothermal incubation at 600 °C for 24 hours.

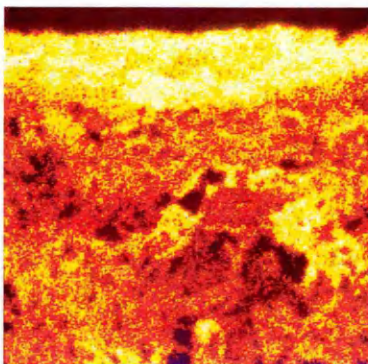
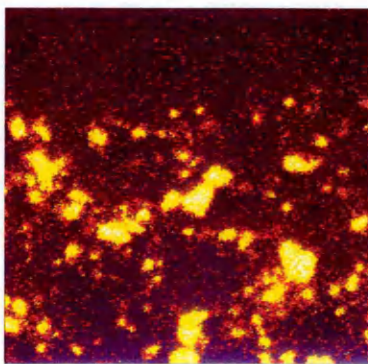
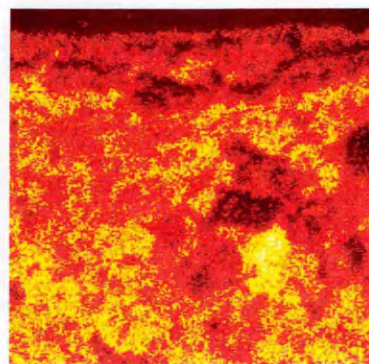
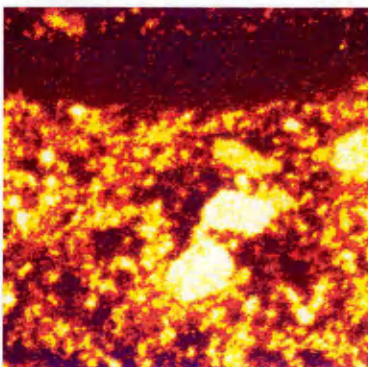
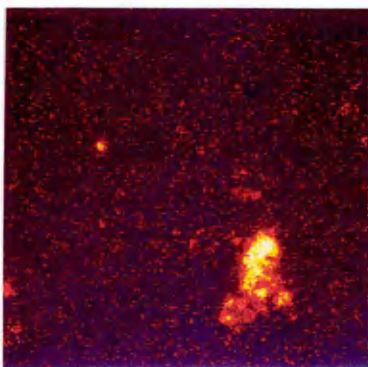
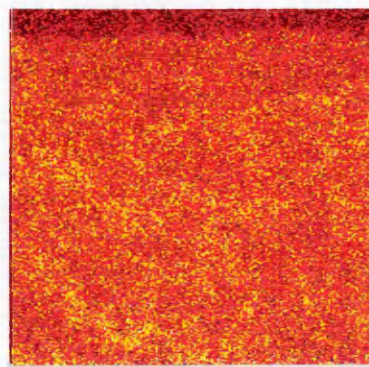
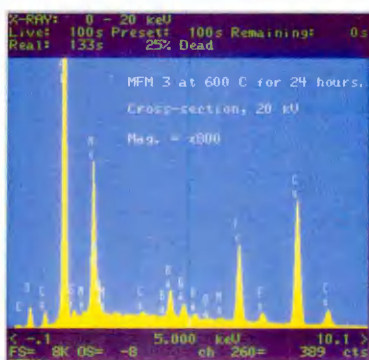
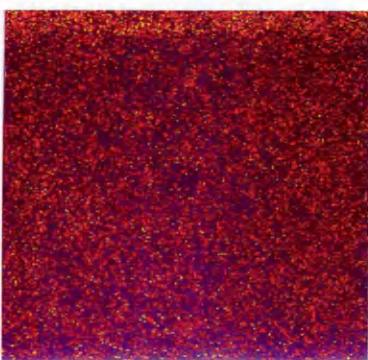
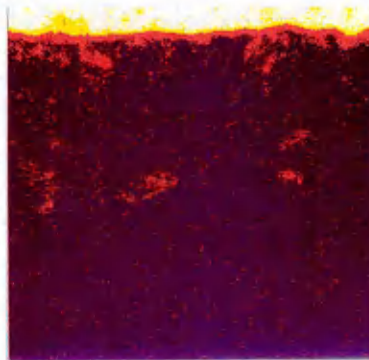
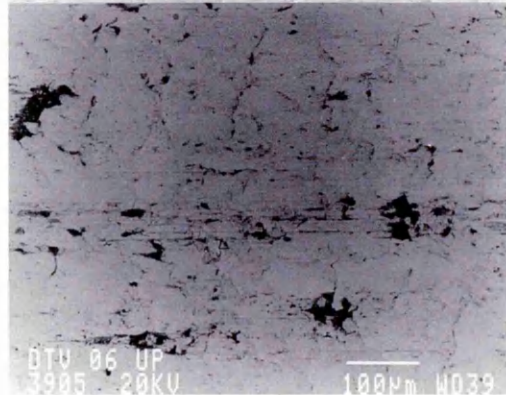
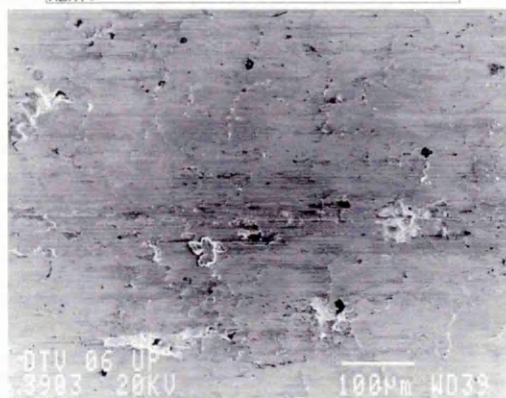
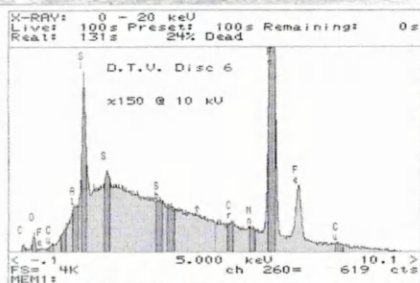
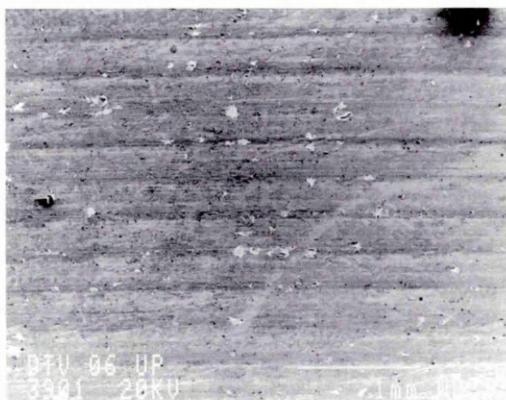
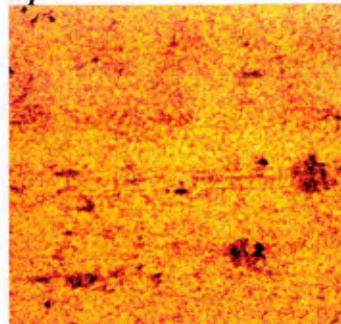
Copper (Cu)**Barium (Ba)****Molybdenum (Mo) / Sulphur (S)****Iron (Fe)****Calcium (Ca)****Oxygen (O)****Regional X-ray Spectrum****Carbon (C)****Aluminium (Al)**

Plate 14:

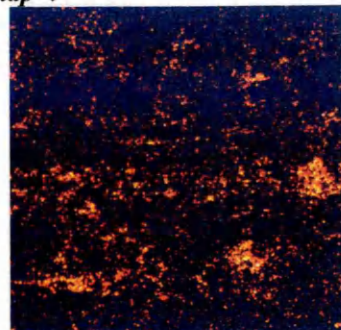
Secondary electron, backscattered electron, X-ray spectral and energy dispersive X-ray data from the surface of a grey cast iron, disc brake rotor (D.T.V. rotor no. 6) bedded against friction material; N.



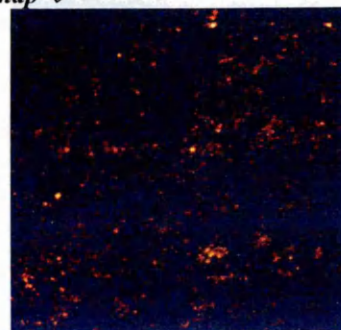
Fe X-ray digimap ↴



O X-ray digimap ↴



Si X-ray digimap ↴



S / Mo X-ray digimap ↴

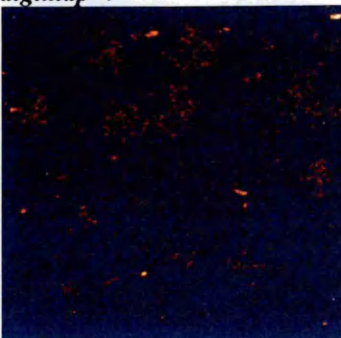
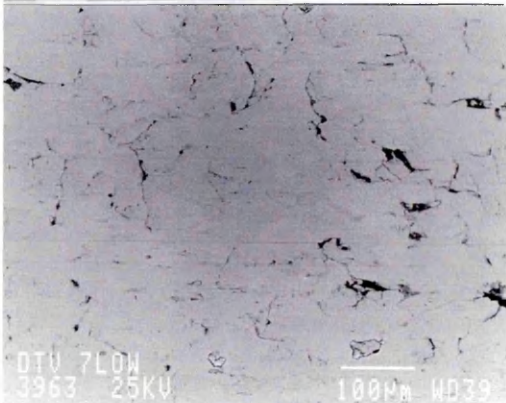
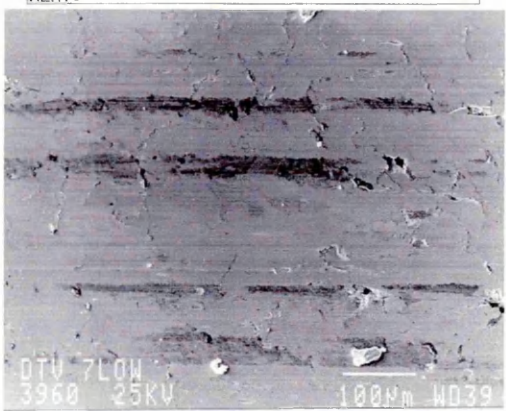
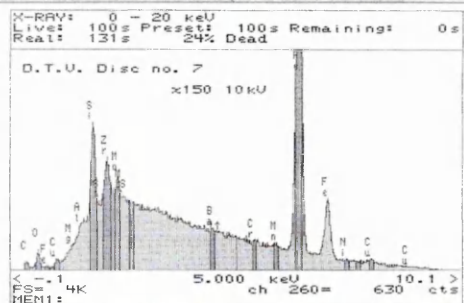
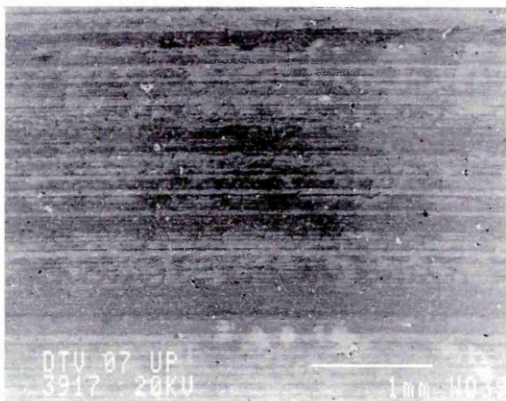
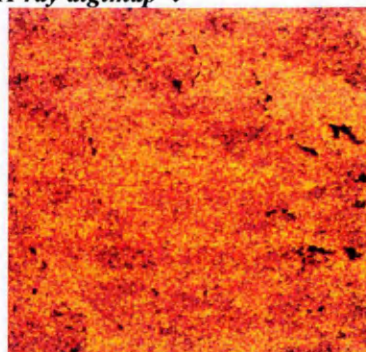


Plate 15:

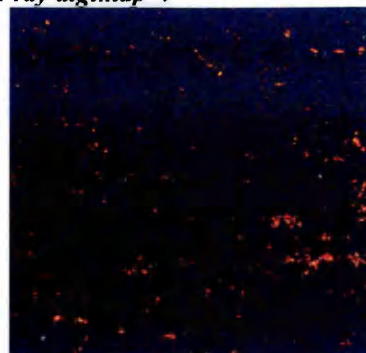
Secondary electron, backscattered electron, X-ray spectral and energy dispersive X-ray data from the surface of a grey cast iron, disc brake rotor (D.T.V. rotor no. 7) bedded against friction material; S.



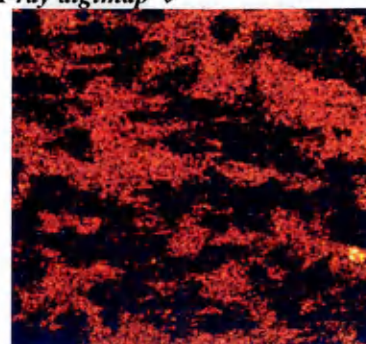
Fe X-ray digimap ↴



O X-ray digimap ↴



Si X-ray digimap ↴



Cu X-ray digimap ↴

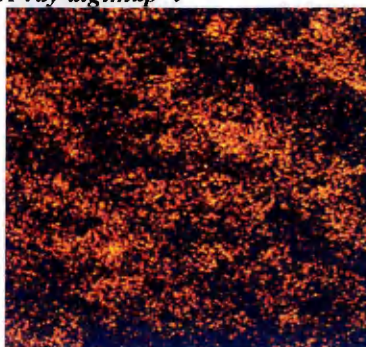
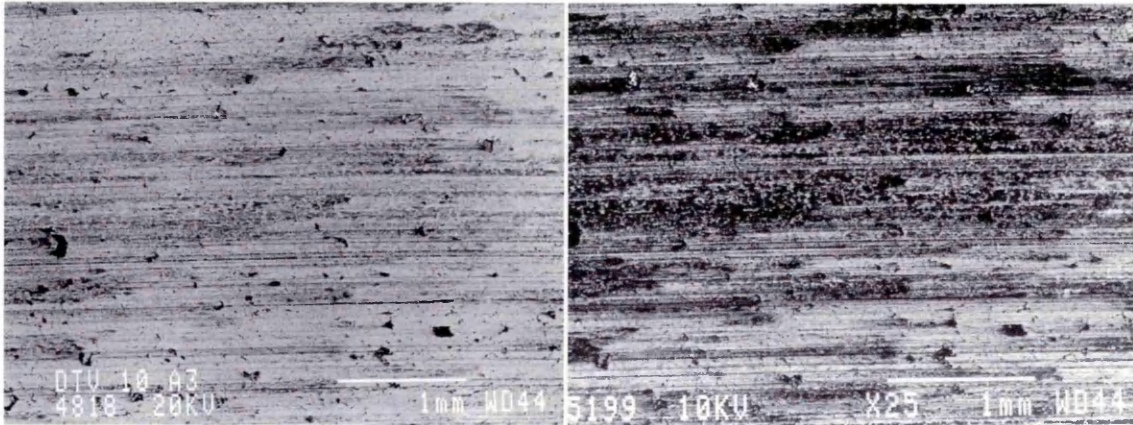


Plate 16:

Compositional, backscattered electron micrographs of the friction ring surface of D.T.V. test rotor no. 10 showing the optical effects of varying accelerating voltages.

D.T.V. Test Rotor 10 @ 20 kV

D.T.V. Test Rotor 10 @ 10 kV



D.T.V. Test Rotor 10 @ 20 kV

D.T.V. Test Rotor 10 @ 10 kV

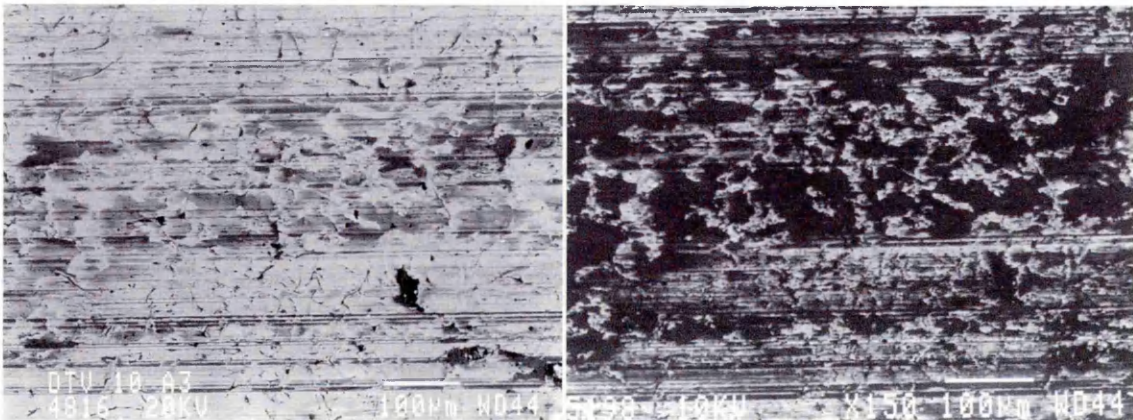
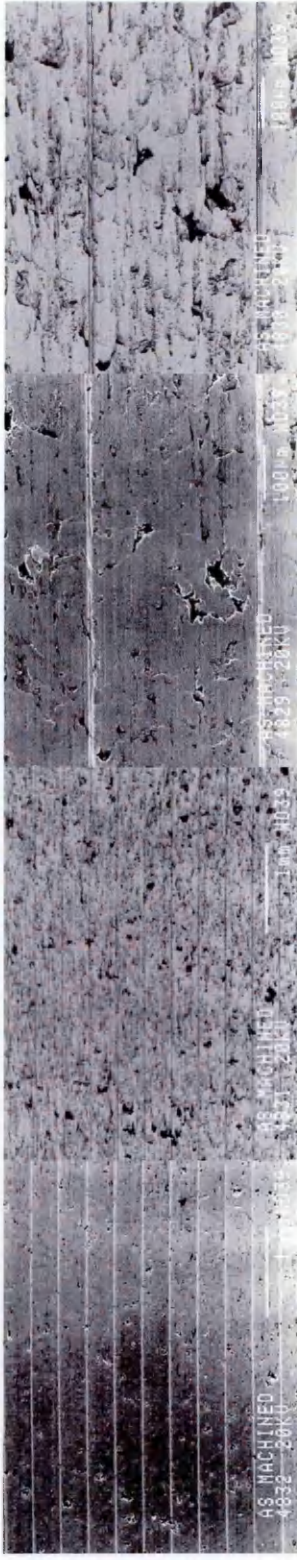
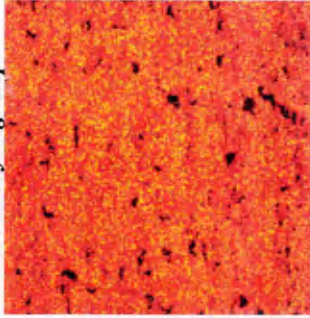


Plate 17:

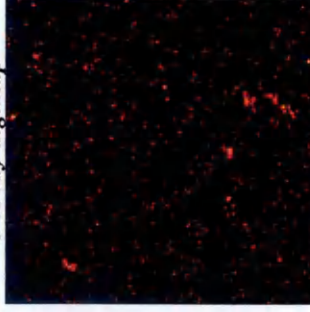
Secondary electron (top row, right, first and third) and backscattered electron (top row, right, second and forth) micrographs of the friction ring surface of a virgin, i.e. unused, grey cast iron disc brake rotor, accompanied by energy dispersive, elemental X-ray digimaps. Digimaps correspond to the area displayed in the two far right micrographs.



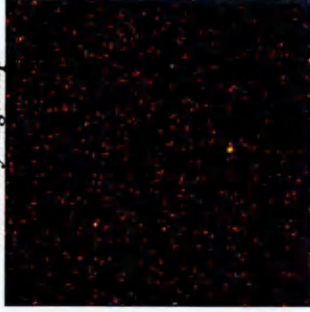
Fe X-ray digimap



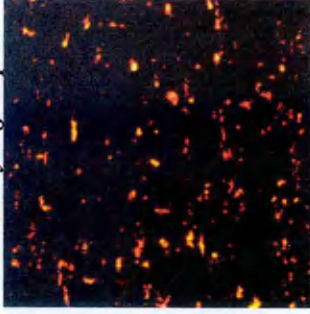
O X-ray digimap



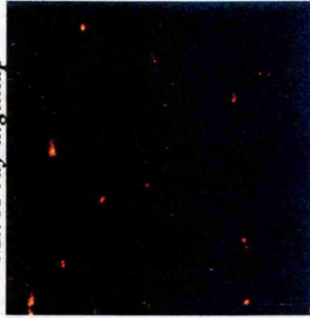
Al X-ray digimap



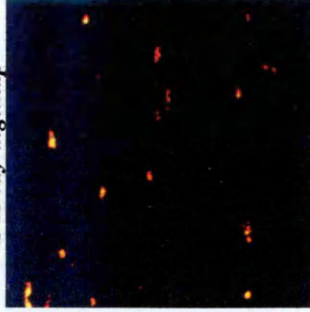
C X-ray digimap



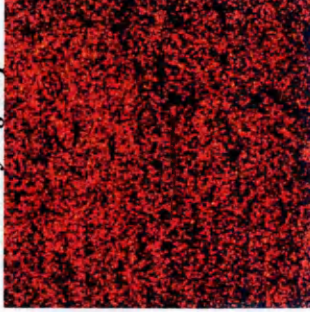
Mn X-ray digimap



S X-ray digimap



Si X-ray digimap



P X-ray digimap

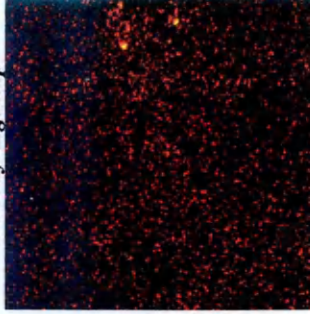


Plate 18:

The upper (or outboard) surfaces of D.T.V. test rotors nos. 10 - 13, 10 and 12 having been rubbed against friction material; N, and 11 and 13 having been rubbed against friction material; S.

D.T.V. Test Rotor 10 - N**D.T.V. Test Rotor 11 - S****D.T.V. Test Rotor 12 - N****D.T.V. Test Rotor 13 - S**

Plate 19:

Secondary electron (immediate right) and backscattered electron (middle and bottom right) micrographs of the polished outer section of D.T.V. test rotor no. 10.

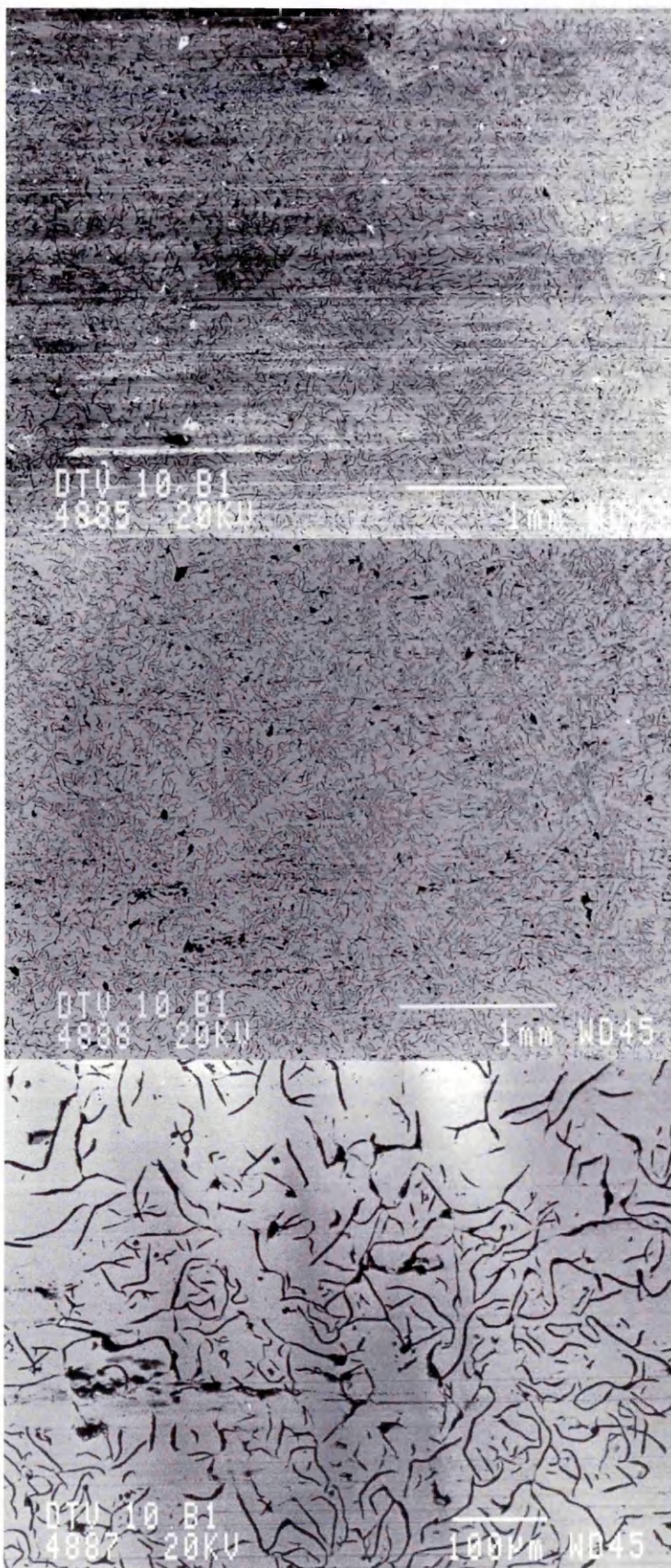
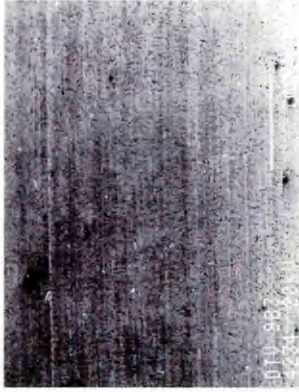
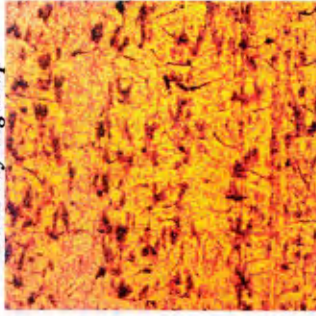


Plate 20:

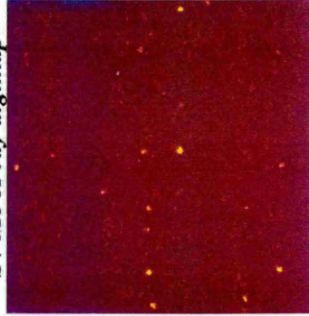
Secondary electron (top row, first and second right) and back-scattered electron (top row, far right) micrographs of the higher pressure region of the inboard surface of D.T.V. test rotor no. 9 (rubbed against friction material; N), accompanied by energy dispersive, elemental X-ray digimaps. Digimaps correspond to the area displayed in the two far right micrographs.



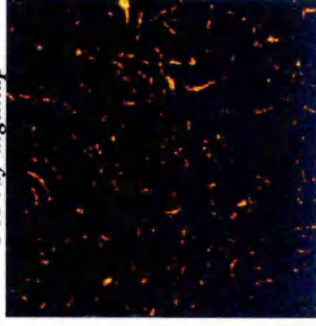
Fe X-ray digimap



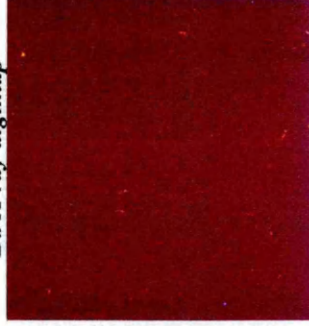
S / Mo X-ray digimap



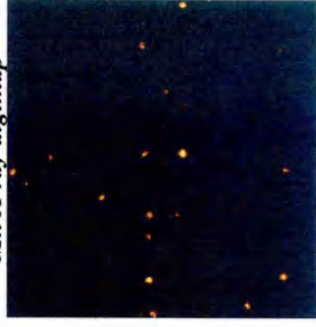
C X-ray digimap



Ba X-ray digimap



Mn X-ray digimap



Si X-ray digimap

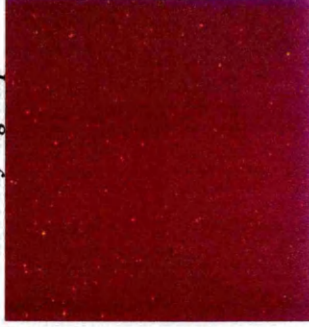
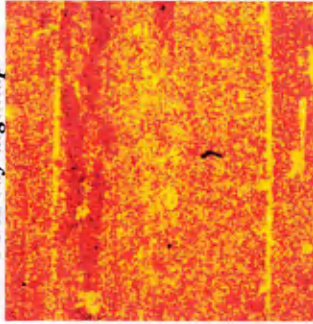


Plate 21:

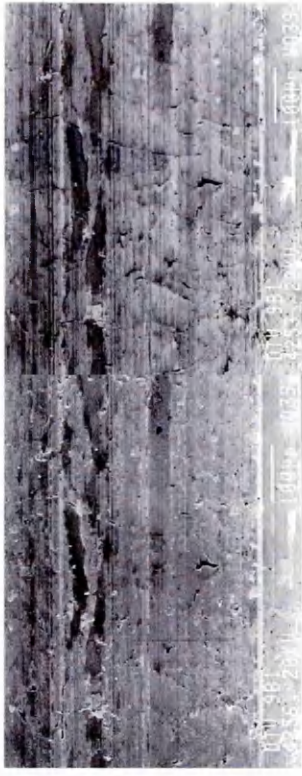
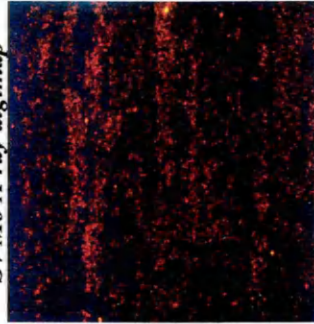
Secondary electron (top row, first and second right) and back-scattered electron (top row, far right) micrographs of the lower pressure region of the inboard surface of D.T.V. test rotor no. 9 (rubbed against friction material; N), accompanied by energy dispersive, elemental X-ray digimaps. Digimaps correspond to the area displayed in the two far right micrographs.



Fe X-ray digimap



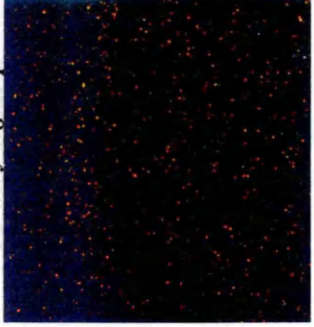
S / Mo X-ray digimap



C X-ray digimap



Cu X-ray digimap



Cr X-ray digimap



Si X-ray digimap

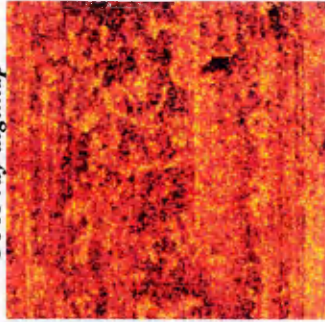


Plate 22:

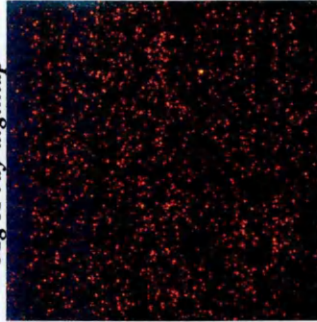
Secondary electron (top row, first and third) and backscattered electron (top row, second and fourth) micrographs of the lower pressure region of the outboard surface of D.T.V. test rotor no. 10 (rubbed against friction material; N), accompanied by energy dispersive, elemental X-ray digimaps. Digimaps correspond to the area displayed in the two far right micrographs.



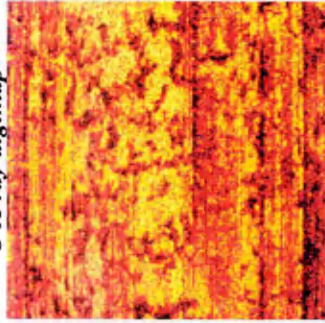
Fe X-ray digimap



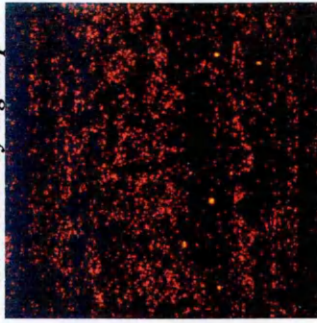
Mg X-ray digimap



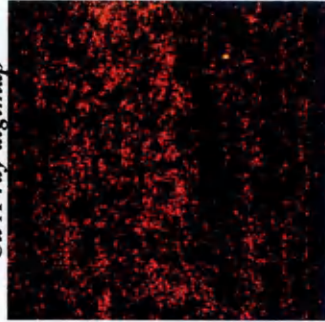
O X-ray digimap



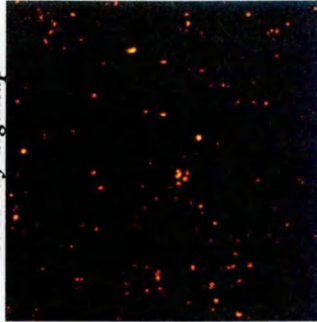
S / Mo X-ray digimap



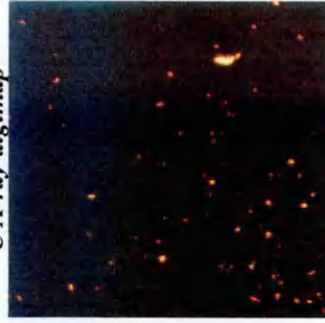
Cu X-ray digimap



Si X-ray digimap



C X-ray digimap



P X-ray digimap

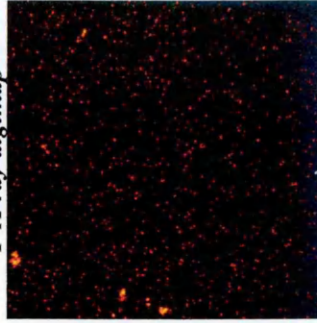


Plate 23:

Secondary electron (top row, first and third) and backscattered electron (top row, second and fourth) micrographs of the higher pressure region of the outboard surface of D.T.V. test rotor no. 10 (rubbed against friction material; N), accompanied by energy dispersive, elemental X-ray digimaps. Digimaps correspond to the area displayed in the two far right micrographs.

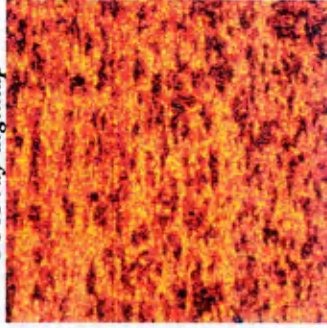
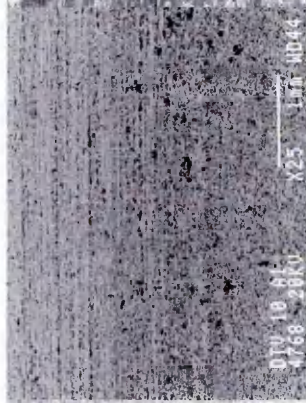
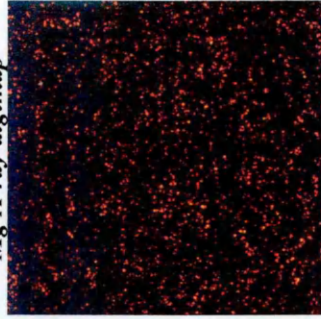
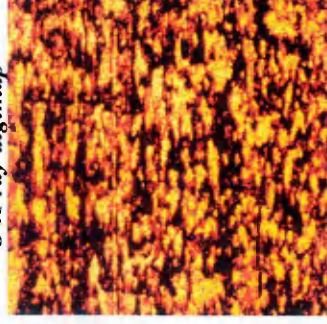
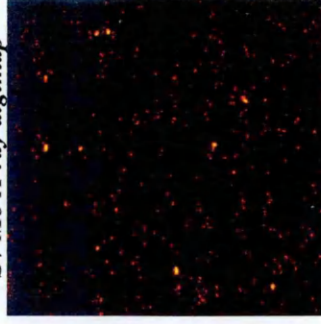
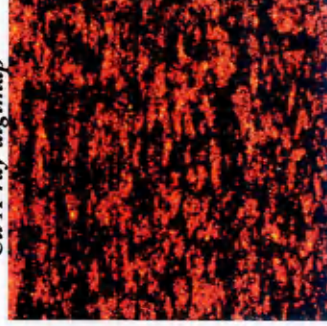
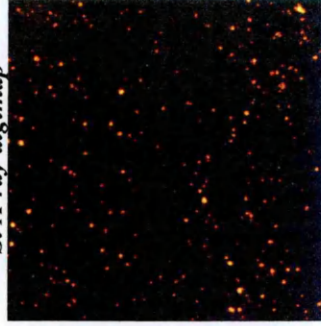
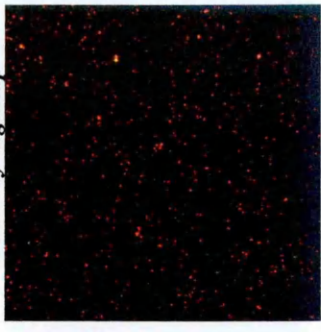
**Fe X-ray digimap****Mg X-ray digimap****O X-ray digimap****S / Mo X-ray digimap****Cu X-ray digimap****Si X-ray digimap****Sb X-ray digimap**

Plate 24:

Secondary electron (top row, right, first and third) and backscattered electron (top row, right, second and forth) micrographs of the higher pressure region of the inboard surface of D.T.V. test rotor no. 12 (rubbed against friction material; N), accompanied by energy dispersive, elemental X-ray digimaps. Digimaps correspond to the area displayed in the two far right micrographs.

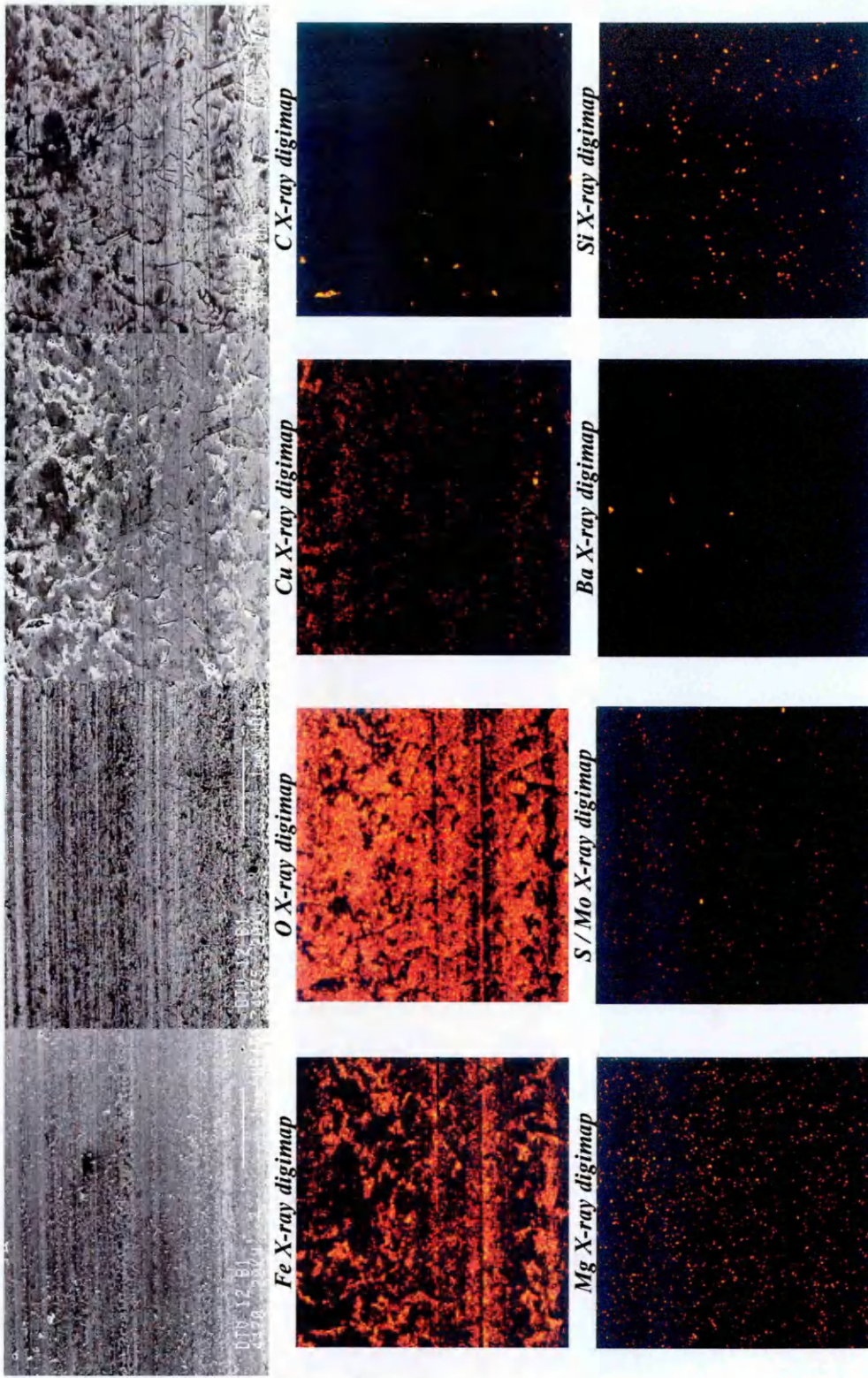
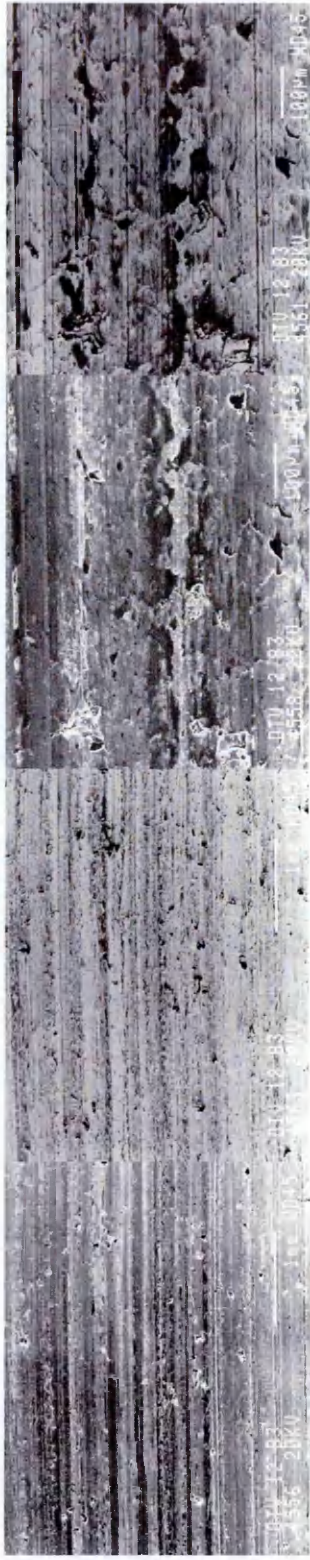
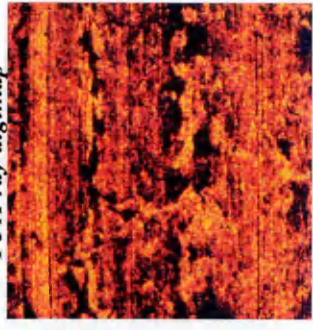


Plate 25:

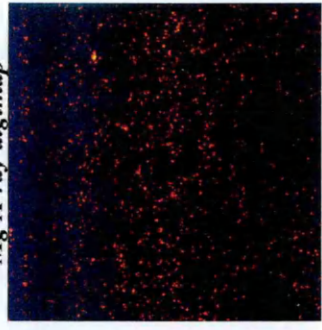
Secondary electron (top row, right, first and third) and backscattered electron (top row, right, second and forth) micrographs of the lower pressure region of the inboard surface of D.T.V. test rotor no. 12 (rubbed against friction material; N), accompanied by energy dispersive, elemental X-ray digimaps. Digimaps correspond to the area displayed in the two far right micrographs.



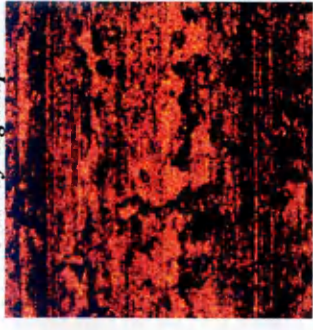
Fe X-ray digimap



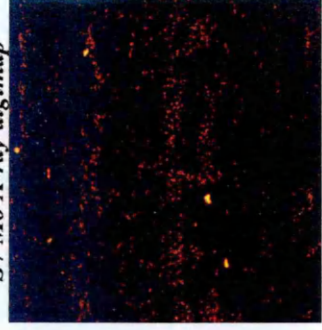
Mg X-ray digimap



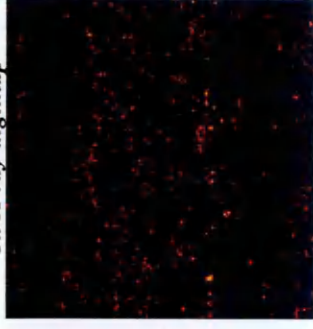
O X-ray digimap



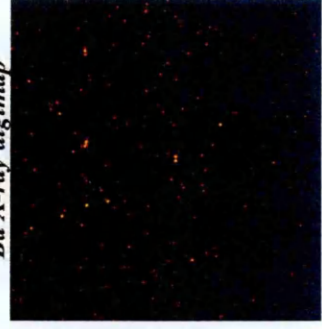
S / Mo X-ray digimap



Cu X-ray digimap



Ba X-ray digimap



C X-ray digimap



Sb X-ray digimap

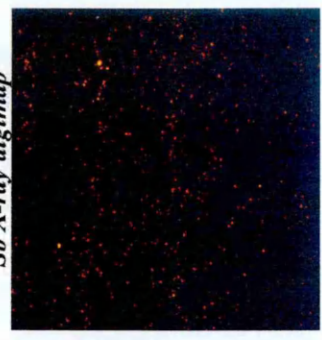
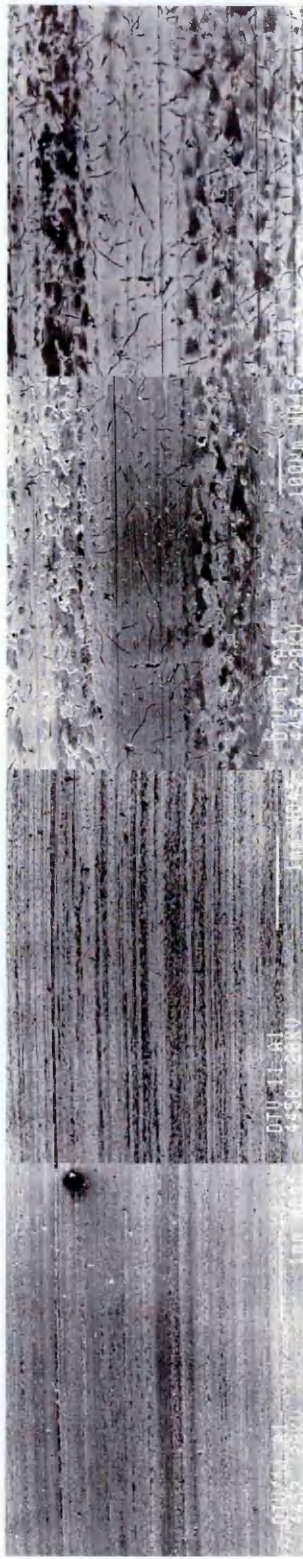
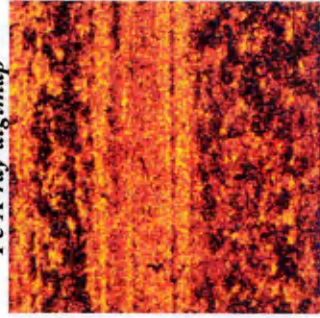


Plate 26:

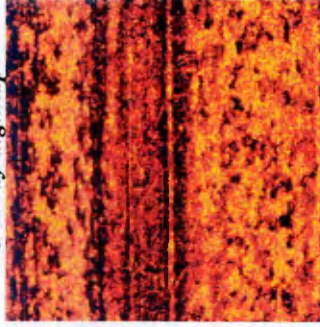
Secondary electron (top row, right, first and third) and backscattered electron (top row, right, second and forth) micrographs of the higher pressure region of the outboard surface of D.T.V. test rotor no. 11 (rubbed against friction material; S), accompanied by energy dispersive, elemental X-ray digimaps. Digimaps correspond to the area displayed in the two far right micrographs.



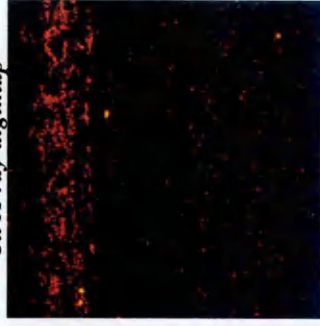
Fe X-ray digimap



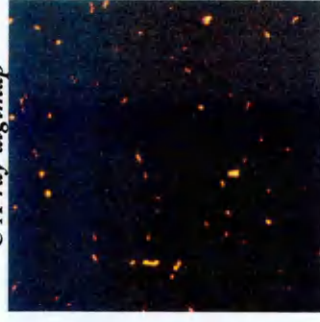
O X-ray digimap



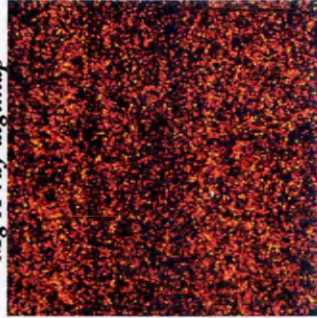
Cu X-ray digimap



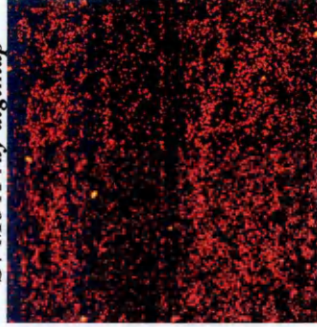
C X-ray digimap



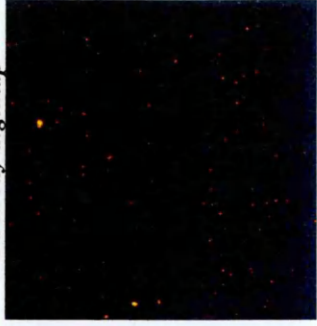
Mg X-ray digimap



S / Mo X-ray digimap



Ba X-ray digimap



P X-ray digimap

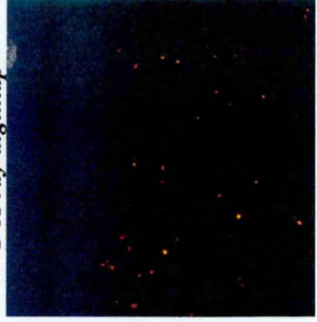
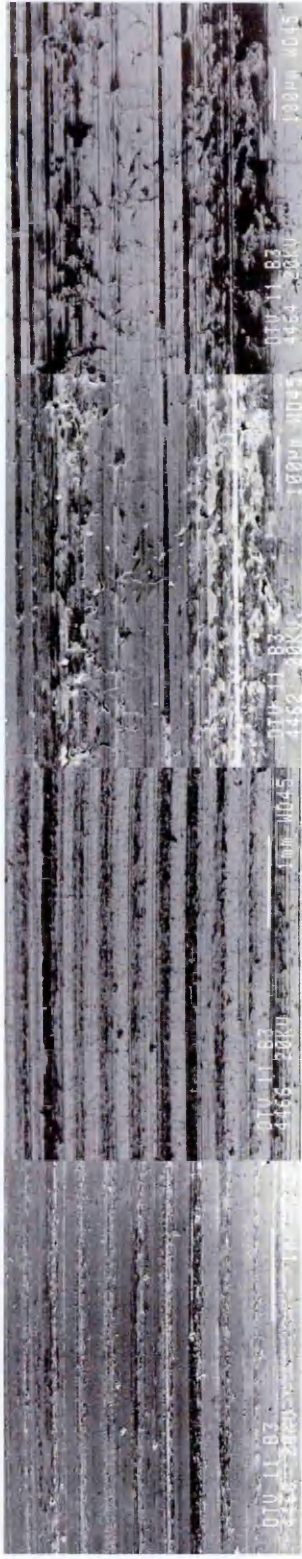


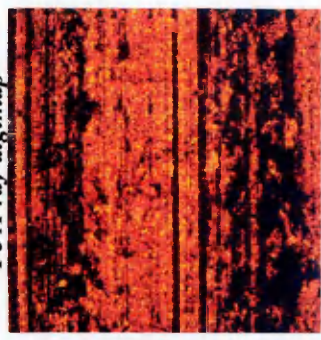
Plate 27:

Secondary electron (top row, right, first and third) and backscattered electron (top row, right, second and forth)

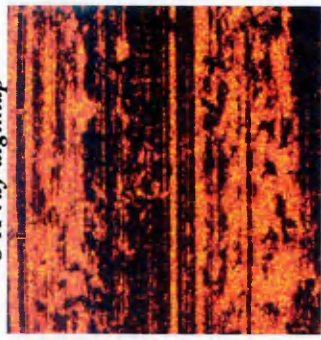


micrographs of the lower pressure region of the inboard surface of D.T.V. test rotor no. 11 (rubbed against friction material; S), accompanied by energy dispersive, elemental X-ray digimaps. Digimaps correspond to the area displayed in the two far right micrographs.

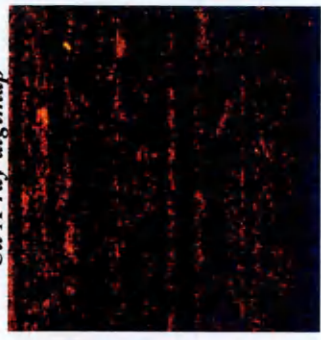
Fe X-ray digimap



O X-ray digimap



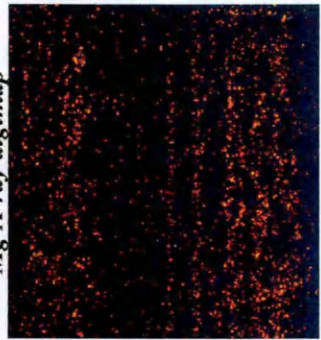
Cu X-ray digimap



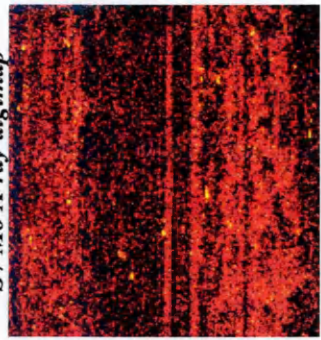
C X-ray digimap



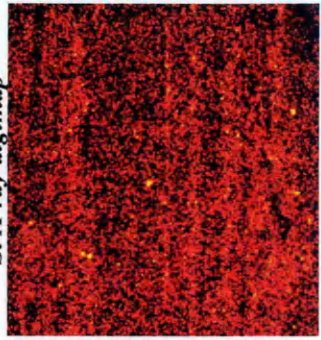
Mg X-ray digimap



S / Mo X-ray digimap



Si X-ray digimap

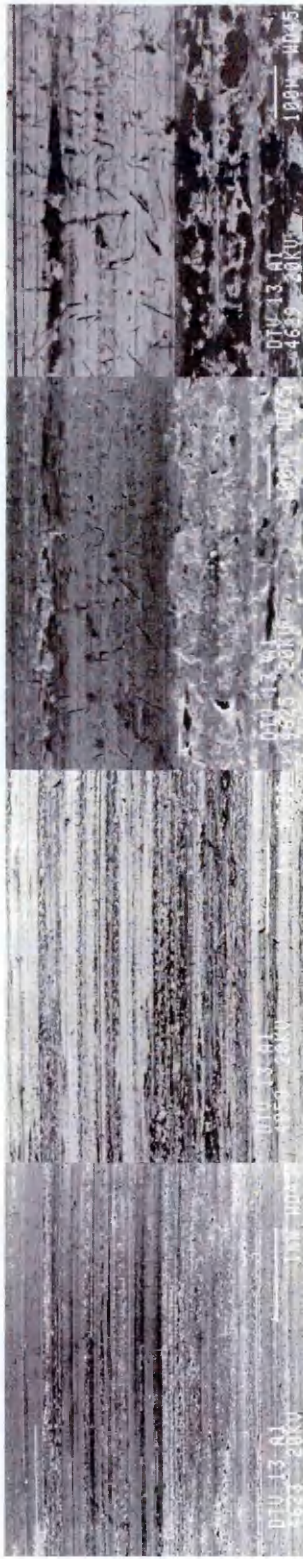


P X-ray digimap

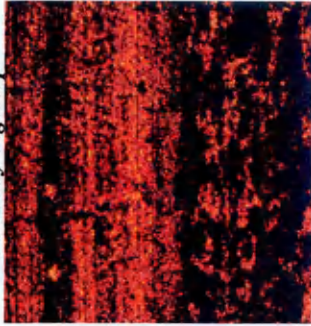


Plate 28:

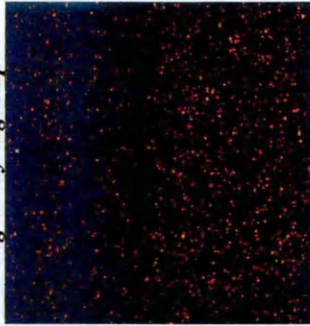
Secondary electron (top row, right, first and third) and backscattered electron (top row, right, second and forth) micrographs of the higher pressure region of the outboard surface of D.T.V. test rotor no. 13 (rubbed against friction material; S), accompanied by energy dispersive, elemental X-ray digimaps. Digimaps correspond to the area displayed in the two far right micrographs.



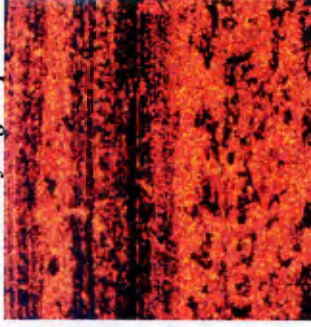
Fe X-ray digimap



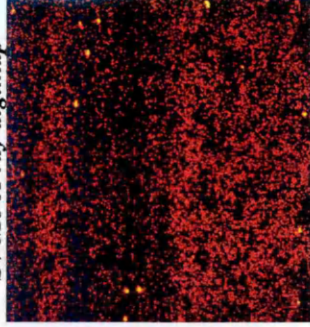
Mg X-ray digimap



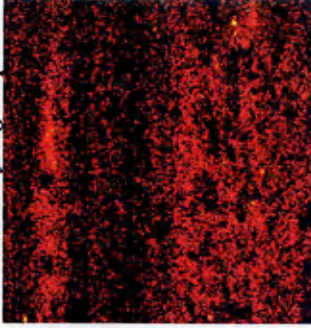
O X-ray digimap



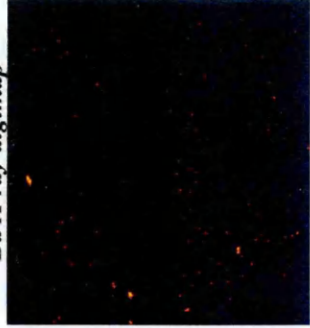
S / Mo X-ray digimap



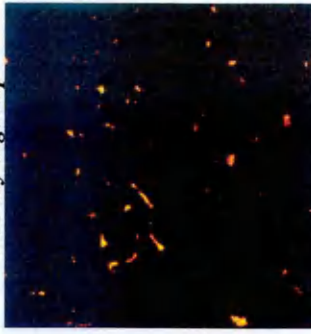
Cu X-ray digimap



Ba X-ray digimap



C X-ray digimap



Si X-ray digimap

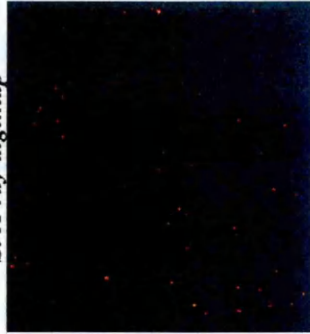


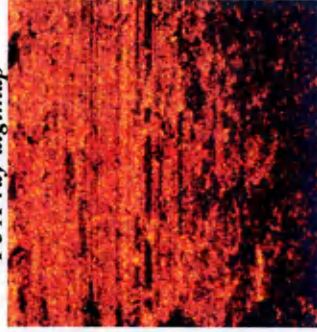
Plate 29:

Secondary electron (top row, right, first and third) and backscattered electron (top row, right, second and forth)

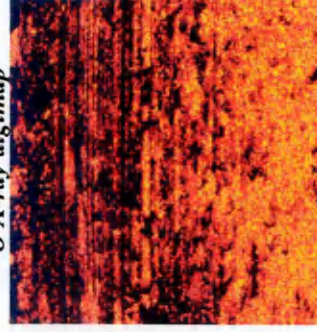


micrographs of the lower pressure region of the outboard surface of D.T.V. test rotor no. 13 (rubbed against friction material; S), accompanied by energy dispersive, elemental X-ray digimaps. Digimaps correspond to the area displayed in the two far right micrographs.

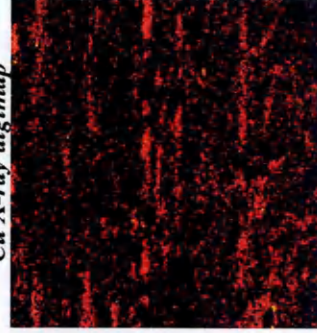
Fe X-ray digimap



O X-ray digimap



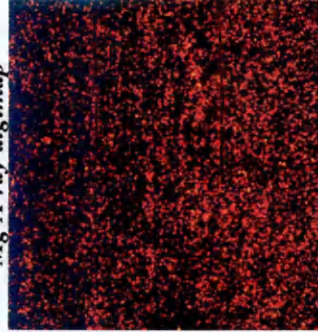
Cu X-ray digimap



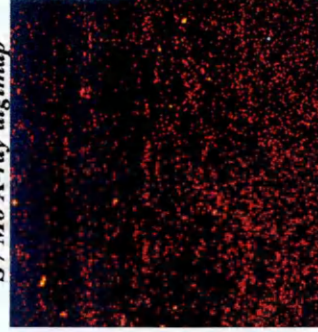
C X-ray digimap



Mg X-ray digimap



S / Mo X-ray digimap



P X-ray digimap



Si X-ray digimap

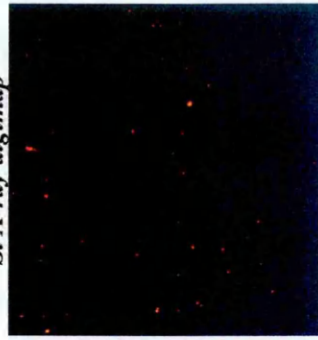
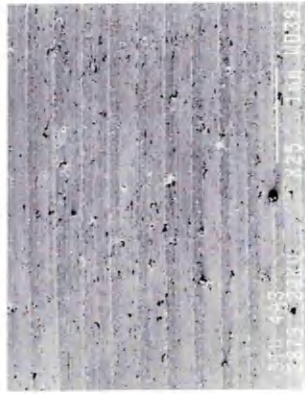
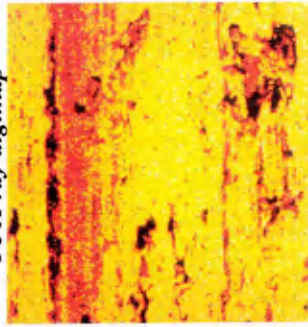


Plate 30:

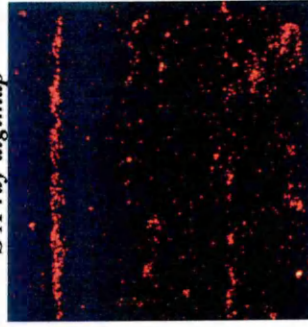
Secondary electron (top row, first and second right) and back-scattered electron (top row, far right) micrographs of the lower pressure region of the outboard surface of D.T.V. test rotor no. 4 (rubbed against friction material; Exp. A), accompanied by energy dispersive, elemental X-ray digimaps. Digimaps correspond to the area displayed in the two far right micrographs.



Fe X-ray digimap



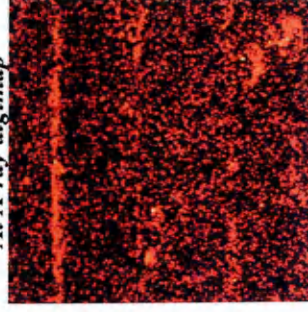
S X-ray digimap



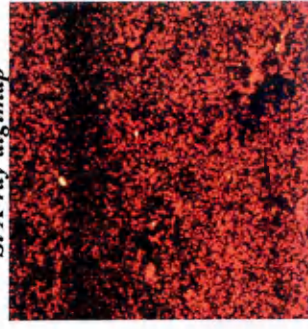
C X-ray digimap



Al X-ray digimap



Si X-ray digimap



Mg X-ray digimap

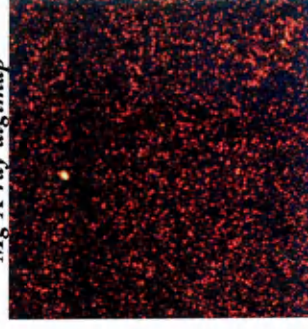
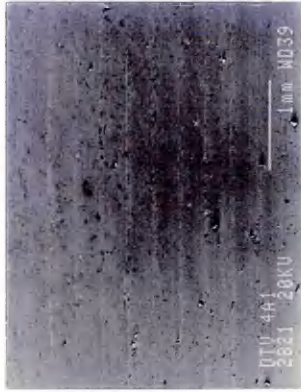
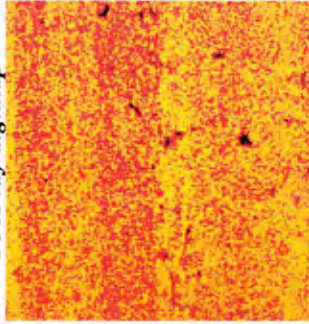


Plate 31:

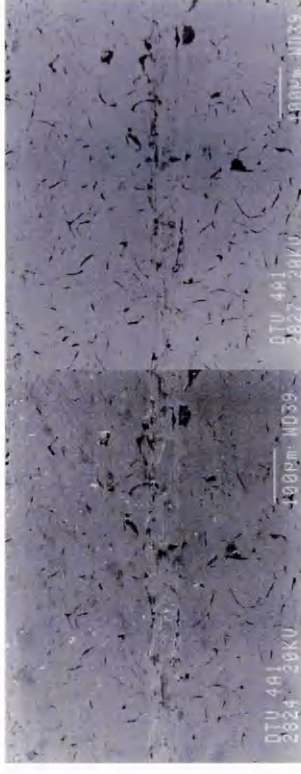
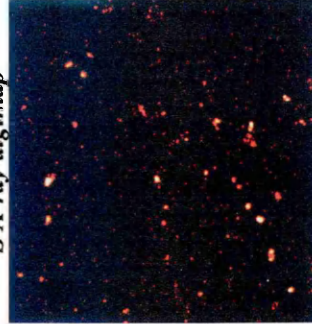
Secondary electron (top row, first and second right) and back-scattered electron (top row, far right) micrographs of the higher pressure region of the outboard surface of D.T.V. test rotor no. 4 (rubbed against friction material; Exp. A), accompanied by energy dispersive, elemental X-ray digimaps. Digimaps correspond to the area displayed in the two far right micrographs.



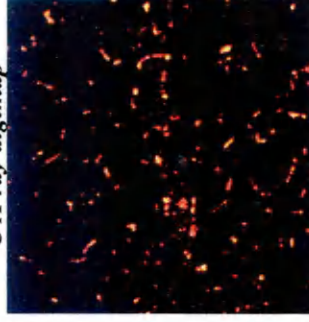
Fe X-ray digimap



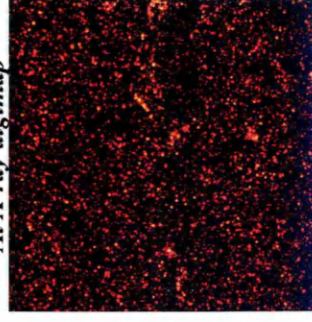
S X-ray digimap



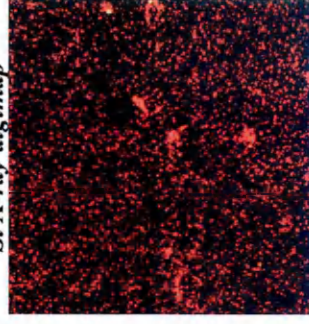
C X-ray digimap



Al X-ray digimap



Si X-ray digimap



P / Zr X-ray digimap

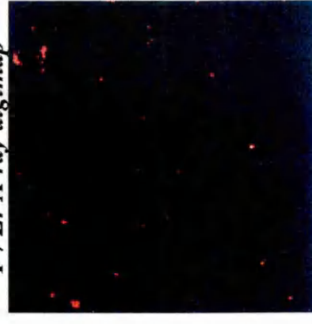
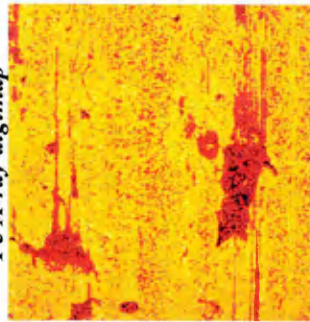


Plate 32:

Secondary electron (top row, first and second right) and back-scattered electron (top row, far right) micrographs of the higher pressure region of the inboard surface of D.T.V. test rotor no. 4 (rubbed against friction material; Exp. A), accompanied by energy dispersive, elemental X-ray digimaps. Digimaps correspond to the area displayed in the two far right micrographs.



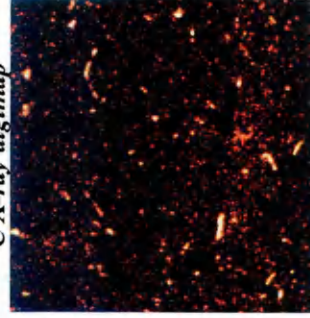
Fe X-ray digimap



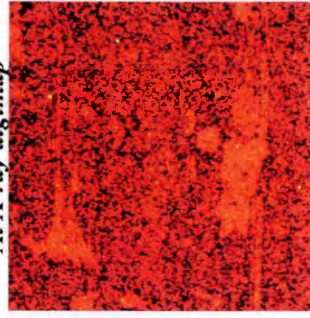
S X-ray digimap



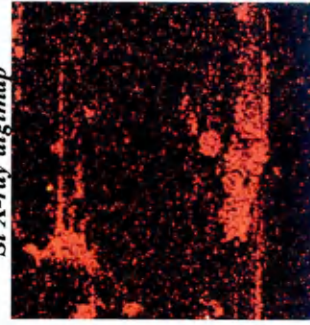
C X-ray digimap



Al X-ray digimap



Si X-ray digimap



P / Zr X-ray digimap



Appendix 11.1.:**Chemical Changes occurring at the Braking Interface:**

The essence of automotive friction braking is to convert kinetic and potential energy into heat energy, the intention being that this heat can then be dissipated harmlessly to the local environment by various conductive, convective or even radiative mechanisms. Although this is largely seen to be true, a consistently high-density flux at the braking interface ensures that chemical, physical and phase transformation transitions also occur during both the heating and cooling of a brake assembly.

As might be anticipated, it is generally only the mating elements of the assembly that are affected to a significant degree. The nature of the surfaces of these components can experience dramatic change as temperatures approach 1,000°C and these changes have been shown on numerous occasions to affect the triboproperties and performance of the brake.

11.1.1. Physico-chemical changes occurring in the Friction Material

During the 1960s and 70s, much of the work examining the chemical changes, and to a lesser extent, the physical changes taking place in friction materials during the friction process focused on the reactions of two categories of friction material constituents:

- Inorganic
- Organic

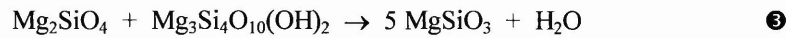
The inorganic portion of the pad was generally taken to encompass the interactions of asbestos, mineral fillers, curing agents and metallic / metallic sulphide friction modifiers, while the organic portion described resinous binders and elastomeric friction modifiers. The majority of inorganic interactions investigated during this time focused on the important thermochemical transitions affecting chrysotile asbestos fibres (118 – 124), the tribometric effects of these reactions becoming well understood.



chrysotile asbestos \rightarrow forsterite + talc + water



talc \rightarrow enstatite + quartz + water



forsterite + talc \rightarrow enstatite + water

More generic research examined the friction surface of resin-bonded disc brake pads, this being observed to develop a *Frictional Heat Affected Layer* (F.H.A.L.) as a result of tribological contact with a revolving countermember (118). The F.H.A.L. varied in its physical and chemical nature from both the original, unburnished surface, and the relatively unaffected matrix material retained beneath the layer. Increasing the duty level, and thereby the maximum operating temperature to which the pads were exposed, was seen to increase the depth of the F.H.A.L. Also notable was the fact that the depth of the F.H.A.L. was relatively unaffected by the rate at which the friction material became worn, even after ablative mechanisms had commenced. Perhaps the most important feature observed was that the sub-surface F.H.A.L. remained essentially unchanged, in all respects other than thickness, with increasing duty level whereas the immediate surface underwent constant chemical change and regeneration. Quantified features of interest of the F.H.A.L. (118) in a typical, class A friction material (1978) were as follows:

- F.H.A.L. thickness increases exponentially with increasing duty level from almost zero at 100°C to 3 mm at 500°C.
- The inorganic content of the upper 1 mm of the friction material increases by up to 25 %, this increase reacting linearly with increasing temperature. The contribution of different substances to this inorganic concentration is disparate, e.g. 25 % increase in Fe, *cf.* 75 % increase in Zn.

- The carbonaceous content increases in the upper 0.5 mm of the friction material, this being accompanied by a dramatic 50 % fall-off in the asbestos content over the same range.
- The polymeric content is reduced by 50 % in the upper 1 mm of the friction material, the depth to which this persists corresponding to F.H.A.L. depth variation with temperature.

Microscopic characterisations of the outermost surface of the F.H.A.L., with respect to the thermal response of individual friction material constituents to increasing energy absorption, are shown in table 11.1.1. (A gauge to the forensic temperatures encountered at the frictional surface interface can be gleaned from the thermophysical response of the metallic zinc constituent (3.1.3).)

Table 11.1.1.:

The sequence of visible physical changes affecting specific friction material constituents with increasing duty level, or, secondarily, with increasingly proximity to the rubbing surface as observed in reference

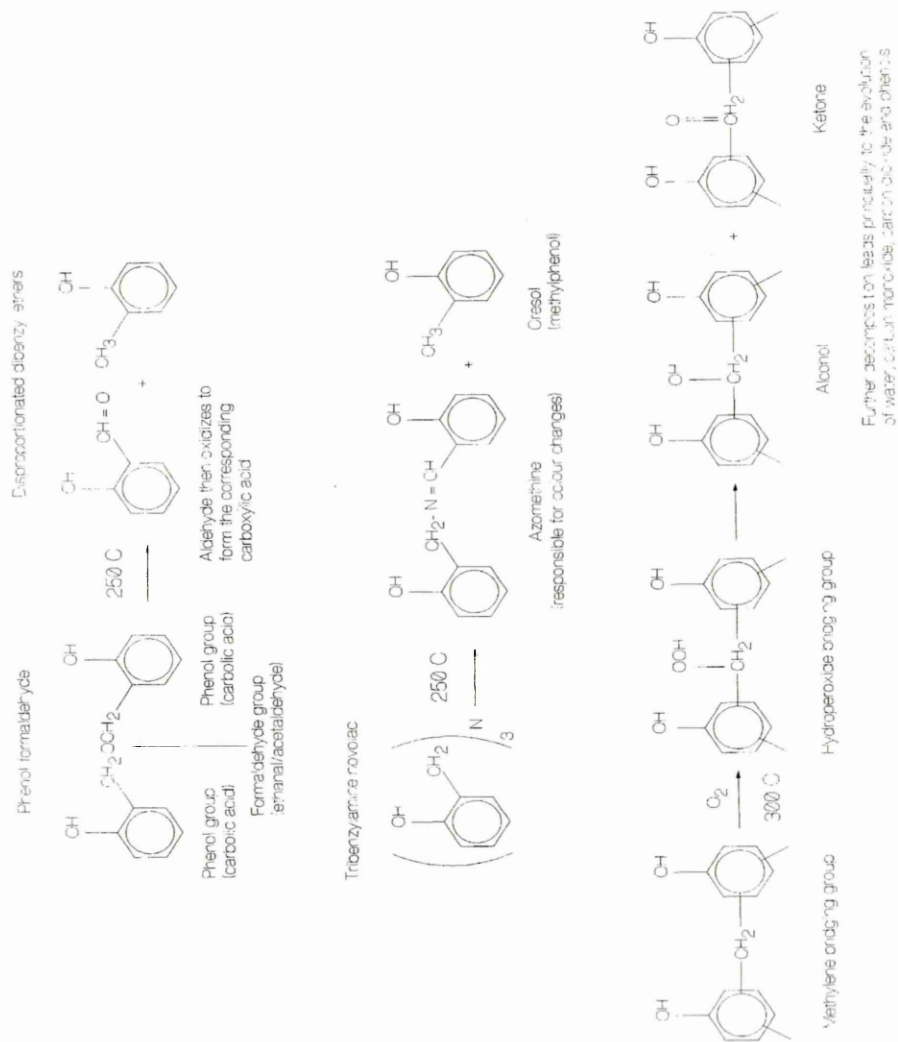
118.

Friction dust:	Rubber crumb:	Binding agent:	Asbestos fibres:	Zinc chips:
Mild softening	Mild softening and loss of resilience	Darkening and colour change	Mild colour change	Mild oxidation
Further softening and partial melting	Weakening and plasticisation	Further darkening		Continued oxidation
Hardening and darkening	Graphite-coloured, paste-like and extruded	Charring evident	Fibre bundles lose coherency	Partial incipient melting
Charring and embrittling	Embrittling and graphite / carbon-like	Further charring	Fibre dispersal and shortening	Severe oxidation and embrittling
Particles absent	Particles absent	Glazed, embrittled and carbon-like	Fibres absent	Particles absent

Much was learnt during this time about the decomposition of phenolic resins, a selection of the most common decomposition reactions being illustrated in figure 11.1.1.

Figure 11.1.1:

The decomposition of phenolic resins in air at elevated temperatures.



At the same time, suitable technologies were also enrolled to study the subtle differences in the decomposition of resinous materials. The laboratory decomposition of organic binders using *Pyrolysis*

Gas Chromatography (P.G.C.) (125 – 126) was shown capable of differentiating between variations in the organic portion of friction material formulations; Cardolites¹ differed from standard phenolics² in that their decomposition products were seen to include the following, most of which varied greatly in quantity. The volatilised materials included large quantities of light gases^{1,2}, in addition to benzene^{1,2} (C₆H₆), methylbenzene^{1,2} (toluene, C₆H₅CH₃), *m*^{1,2} + *o*¹-dimethylbenzene (xylene, C₆H₄(CH₃)₂), phenylethene¹ (styrene, C₆H₅CHCH₂), phenol^{1,2} (carbolic acid, C₆H₅OH), indene¹, *o*² + *p*^{1,2}-methylphenol (cresol, OHC₆H₄CH₃), 2, 6² and 2,4² dimethylphenol (OHC₆H₄(CH₃)₂) and several unidentified products. (It is important to note that all of these compounds are lost in their volatilised gaseous form, a situation likely repeated via their frictional surface interactions at the braking interface.)

Albeit at temperatures beyond the comfortable operating range of the materials concerned, significant attention was paid to the potential tribomechanisms acting as a result of resin breakdown. It was shown that the chemical changes occurring within the friction material as a result of frictional heating, particularly in respect of the organic portion, could produce rapid and significant differential volumetric activity. F.H.A.L. matter was identified as being more porous than the unaffected matrix (manufactured porosity ≈ 2 – 5 vol. %).

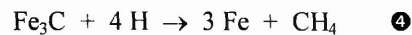
Table 11.1.2.:

Chemical changes occurring as a result of increasing frictional heating and thus, higher temperatures being encountered at the automotive friction brake interface.

<i>Temperature range (°C):</i>	<i>Chemical change:</i>	<i>Additional effects:</i>
100	Absorbed H ₂ O driven off as steam	Vapour layer, corrosive rotor attack
25 – 250	Adsorbed & polycondensed H ₂ O is evolved	H ₂ evolved via further oxidation
232 – 400	Resin decomposition to phenol, benzene, toluene, xylene and cresol	H ₂ evolved via further oxidation
500 – 700	H ₂ , CO, CO ₂ , CH ₂ and C ₂ H ₂ evolved	Carbonisation of the friction material, decarburisation of the rotor surface

Such processes were inextricably accompanied by the evolution of gaseous or liquid phases. The temperature ranges over which such reactions typically take place at the interface are illustrated in table 11.1.2.

The emission of gaseous hydrogen (H₂) resulting from the decomposition of numerous organic compounds is accompanied by additional H₂ originating from steam, a breakdown which is, ironically in this instance, catalysed by the presence of iron at elevated temperatures. Between 1975 and 1980, Scieszka *et al* worked on two publications (127 – 128) advancing the theory of hydrogen embrittlement as a rotor wear mechanism active at the friction interface. Within this work it was suggested that between 80°C and 450°C, evolved hydrogen was adsorbed by the iron countersurface, thereby increasing the hydrogen content of the *near-surface region* (0.3 – 3.0 mm) by 300 – 600 %. From a metallurgical standpoint, it is known that at around 310°C, cementite, in the presence of thermally dissociated and adsorbed hydrogen, may be decarburised to form spongy α -Fe (ferrite):



The resulting wear theory, anachronistically known as hydrogen wear, was based on the principal that hydrogen tends to segregate to intercrystalline boundaries resulting in micropore coalescence, an embrittling process during which microvolumes of iron may be detached. It is known that hydrogen penetration in steels is reduced by increased alloying with Cr, Ti and V (all standard additions to the pearlitic, grey cast irons used in automotive friction couples) but is increased in the presence of antimony compounds, e.g. Sb₂S₃ and its reaction products. Adsorption is also promoted in the presence of ferrite and cold-worked microstructure.

Appendix 11.2.:**Chemical Analysis of Cast Irons using Universal Vacuum Air Quantometry:**

The *Universal Vacuum Air Quantometer* (U.V.A.Q.), model A.R.L. 29700-B, is used to quantitatively analyse the chemical composition of steels, cast irons and non-ferrous metals such as Al- or Cu-based alloys.

The principle of the technique is that of spark emission spectroscopy. A spark discharge between the sample and a counter electrode, in an argon atmosphere, volatilises material from the sample. Atomic / ionic emissions from the discharge that are characteristic of the elements in the sample are analysed by a spectrometer system. This comprises an entrance slit, a grating to disperse the emission wavelengths, exit slits and several photomultiplier tubes to convert the emission signal into a measurable voltage. One exit slit of the photomultiplier tube combination is fitted for each element to be analysed. Two spectrometer systems are fitted to the instrument to measure the range of elements listed in table 11.2.1., one at atmospheric pressure (air spectrometer), and the other under vacuum (vacuum spectrometer). The vacuum spectrometer is evacuated to measure emission wavelengths in the ultraviolet region of the electromagnetic spectrum, i.e. 175 – 225 nm.

A PC running proprietary software controls the data acquisition process. Operating parameters such as purge time (10 seconds), pre-burn time (40 seconds) and integration time (20 seconds) are also software controlled. Samples are analysed against calibration graphs previously obtained from the analysis of certified reference standards. The output data is calculated as element mass percent.

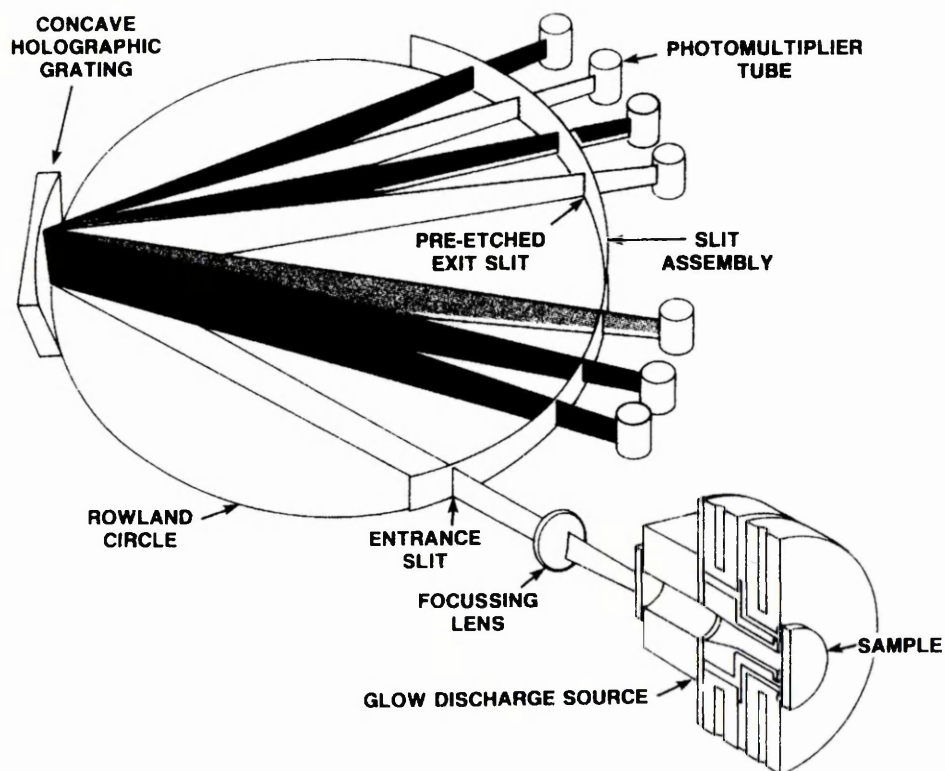
Table 11.2.1.:

<i>Element:</i>	<i>Emission wavelength (nm):</i>	<i>Element:</i>	<i>Emission wavelength (nm):</i>
C	193.09 V	Mo	202.03 V
Si	251.60	Ni	218.55 V
Mn	293.30	V	311.00
P	178.27 V	Nb	319.50
S	180.73 V	W	400.80
Cr	286.20	<i>V = Vacuum spectrometer</i>	

Appendix 11.3.:**Chemical Analysis using Glow Discharge Optical Emission Spectroscopy:**

The equipment used for the *Glow Discharge Optical Emission Spectroscopic* (G.D.O.E.S.) analysis was the *Glow Discharge Spectrometer*; G.D.S. – 750 Q.D.P., which, in addition to its capacity for the classical chemical analysis of metals, is also suitable for *Quantitative Depth Profiling*.

The analysis procedure involves a cathodic sputtering process by applying a controlled voltage to the sample (the cathode) while maintaining a controlled argon pressure across the sample surface. The surface atoms removed by the *burn*, diffuse into the argon plasma, which is where excitation and emission occurs. Separation of the atom removal and excitation provides spectral information with a linear relationship between element concentration and spectral density (signal intensity).

Figure 11.3.1.:*Simplified G.D.O.E.S. Spectrometer*

The acclaimed analytical precision of the technique for the bulk analysis of metals, especially cast irons, is due primarily to the extremely stable excitation source that creates a very flat, uniform sputter spot on the surface of the analysed sample. The technique should therefore produce highly accurate bulk content analyses. Minimal matrix interferences permit bulk calibrations over a wide concentration range to be established on one linear curve (*cf.* X.R.F. – appendix 11.4.).

Figure 11.3.1. shows the principal components of a simplified G.D.O.E.S. spectrometer. The G.D.S. – 750 Q.D.P. spectrometer section is a 0.75 m direct reader featuring a 0.55 nm.mm^{-1} first order dispersion catering for a spectral range of 150 – 456 nm. Optional wavelength extensions are available for non-metallic elements (enhancing the spectral range capability up to 110 – 900 nm). The conventional *Paschen-Runge* configured spectrometer permits up to 44 channels for analysis.

Appendix 11.4.:**Chemical Analysis of Cast Irons using X-Ray Fluorescence Spectroscopy:**

The equipment used for *X-Ray Fluorescence* (X.R.F.) spectroscopic analysis was the Philips P.W. 2,400 X-ray spectrometer, traditionally considered suitable for the non-destructive chemical analysis of materials (although destructive to glasses via discoloration and cracking mechanisms).

In order to be able to both interpret and comment on the results of X.R.F. analyses, it is first important to understand how X-ray fluorescence comes about.

11.4.1. X-Ray Fluorescence

An inevitable consequence of the photoelectric absorption of X-rays is the ejection of a bound inner-shell electron from the atom, leaving the atom in the excited state as that produced by inelastic scattering of an energetic electron that causes the inner-shell ionisation. The subsequent de-excitation, as the atom returns to the ground state by electron transitions, is the same for both cases; the excited atom follows the same routes to de-excitation, producing either characteristic X-rays or characteristic electrons (Auger electrons – appendix 11.11.), with the relative abundance given by the fluorescence yield. X-ray induced emission of X-rays is referred to as X-ray fluorescence. To distinguish the effects, primary radiation will refer to the direct production of X-rays by the ionisation of atoms by beam electrons, and secondary radiation will refer to the production of X-rays by ionisation of atoms by higher energy X-rays. Secondary radiation can be created from two different sources, characteristic and continuum X-rays. Since the X-ray photon causing fluorescence must have at least as much energy as the critical excitation energy of the atom in question, the energy of the secondary radiation will always be less than the energy that is responsible for ionising the inner shell.

11.4.2. Characteristic Fluorescence

If a mixed sample consists of atom species A and B and the energy of the characteristic radiation from element A exceeds the critical excitation for element B, then the characteristic fluorescence of B by the radiation of A will occur. The fluorescence effect depends on how closely the photon energy of A matches the critical excitation energy for B, with the maximum effect occurring when E_A just exceeds E_C ... (the specific energy value that must be exceeded by electron trajectories in order to produce characteristic X-rays) ... for B.

11.4.3. Continuum Fluorescence

Characteristic-induced fluorescence can occur only if the radiation in question is more energetic than the critical excitation energy of the element of interest and is only significant if the characteristic energy is within approximately 3 keV of the critical excitation energy. On the other hand, continuum (*Bremsstrahlung*) radiation provides a source of X-rays at all energies up to the incident beam energy. Continuum-induced fluorescence will therefore always be a component of the measured characteristic radiation from a specimen. The calculation of the intensity of continuum fluorescence involves integrating the contributions of all photon energies above the critical excitation energy for the edge of interest.

The fraction of total radiation contributed by continuum-induced fluorescence is negligible for low atomic number elements ($Z < 20$) but rises to approximately 10 % for Cu $K\alpha$ and to 30 % for Au $L\alpha$.

11.4.4. Range of Fluorescence Radiation

The range of direct, electron-induced characteristic X-ray production is constrained to lie within the interaction volume of the electrons in the target. X-rays have a much greater range in matter than do electrons, so the range of X-ray induced fluorescence is correspondingly much greater.

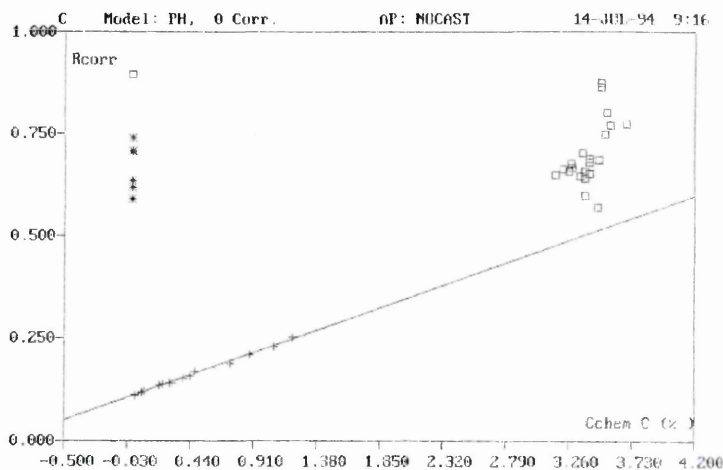
The X-ray induced fluorescence from both characteristic and continuum contributions originates in a much larger volume than the electron-induced characteristic radiation. This has the effect of degrading the spatial resolution of X-ray microanalysis. However, it is this phenomenon that enables the application of X.R.F. spectrometry as a means for bulk chemical analysis.

Separation of the atom removal and excitation provides spectral information with a linear relationship between element concentration and spectral density (signal intensity).

Comparing figures 11.4.1. and 11.4.2. illustrates some of the complexities associated with X.R.F. analysis interpretation. Furthermore, although the analysis depth for the X.R.F. technique is frequently quoted as being 10 μm , this depth varies by sample type and element, e.g. the escape depth for C is only 3 μm making analysis extremely sensitive to surface contamination, sample constitution and sample preparation.

Figure 11.4.1.:

Standard calibration plot for C in low alloy steels and cast irons (covering C contents of 0 – 4.2 %).

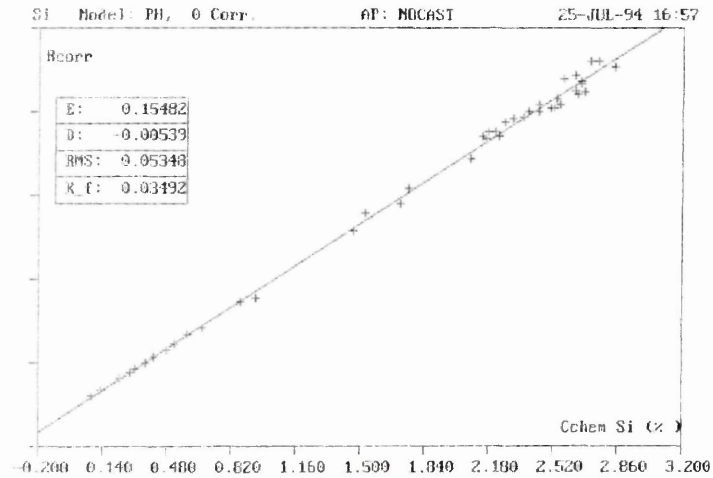


The + data points are drawn from steels containing approximately 0 – 1 mass % C. The data points represented by squares are drawn from cast iron standards. It can therefore be seen that the linear relationship between intensity versus concentration may vary significantly between different types of

samples, this being principally dependent upon the form in which the element is in within the sample (e.g. graphite or carbide or a combination of the two). Such effects are customarily known as matrix interference.

Figure 11.4.2.:

Standard calibration plot for Si in steels and cast irons (accurately covering Si contents of 0.2 – 3.2 %).



Appendix 11.5.:**Typical Carballoy Rotor Analysis:**

Manufacturers: Precision Disc Castings Ltd. / High Precision Machining Ltd.
Address: Mannings Heath Road, POOLE, Dorset, BH12 4NJ
 Washington Centre, Halesowen Road, Dudley, West Midlands, DY2 9RE
Part number: HS 4014 **Cast code:** 15 MN (i.e. 15.12.92)

The manufacturers confirm that the despatched components conform to the *Carballoy* specification (comparable with a typical BS EN 1561 : EN-GJL-200 grade iron specification).

Table 11.5.1.:*Typical compositional analysis.*

<i>Element:</i>	<i>Symbol:</i>	<i>Mass percent (%):</i>	<i>Element:</i>	<i>Symbol:</i>	<i>Mass percent (%):</i>
Carbon	C	3.49	Sulphur	S	0.08
Silicon	Si	2.14	Nickel	Ni	0.05
Manganese	Mn	0.66	Phosphorus	P	0.04
Copper	Cu	0.26	Lead	Pb	0.003
Titanium	Ti	0.025	Molybdenum	Mo	0.017
Chromium	Cr	0.16			

11.5.2. Mechanical Properties:

Tensile strength (N.mm⁻²): 212 (from a turned, as opposed to cast, test piece)

Brinell hardness (BHN): 207

Difference in hardness measured at 3 points on the braking face, 120° apart, should not exceed 20 HB.

11.5.3. Microstructural Characteristics:

Graphite structure: Predominantly of form A, flake sizes 3 – 5

Material matrix: Pearlitic and free from chill

Appendix 11.6.:**Analytical Scanning Electron Microscopy:**

Analytical Scanning Electron Microscopy (A.S.E.M.) (a.k.a. *Electron Probe MicroAnalysis (E.P.M.A.)*) broadly combines the techniques of *Scanning Electron Microscopy (S.E.M.)* and *Energy Dispersive analysis of X-rays (E.D.X. or E.D.A.X.)* and / or *Wavelength Dispersive analysis of X-rays (W.D.X.)*. A.S.E.M. represents a colossal field, a thorough appreciation of which can only be gained through study of appropriate texts (146).

Basically, electrons are generated by an electron gun and focused using either magnetic or electrostatic lenses onto a specimen surface causing the emission of several varieties of radiation. Of these, A.S.E.M. is concerned with three:

➤ ***Secondary Electrons***

An ionised product generated in the specimen.

➤ ***Backscattered Electrons***

Incident electrons that have been reflected by the specimen.

➤ ***Characteristic X-Rays***

Characteristic of the emitting element and of the particular energy level transition occurring.

For electron imaging, the required emission is selected by use of an appropriate detector and the resulting signal amplified and fed to the grids of the display tubes. With the aid of the scanning generator and beam deflectors, the incident electron beam is driven line-by-line (rasta scanning) through a square frame on the specimen surface in order to construct an image of the specimen, point-by-point.

For X-ray analyses, X-rays generated from the specimen pass through a thin beryllium window where their energy is dissipated completely by the creation of electron-hole-pairs in a cooled, reverse-biased, lithium-drifted silicon (Si(Li)) crystal. The number of electron-hole-pairs produced is directly proportional to the energy level of the detected X-ray. The Si(Li) crystal is reverse-biased so as to enable the separation and collection of the liberated charge. The field-effect transistor then converts the

collected charge into a voltage pulse of proportional amplitude. The pulse processor amplifies, shapes and integrates the voltage pulse prior to measurement by an *Analogue-to-Digital Converter* (A.D.C.). The A.D.C. measures the time it takes for each voltage pulse to decay to zero, after which a count is registered, according to this decay time, in the appropriate channel of the *Multi-Channel Analyser* (M.C.A.). Over some period of time, a large number of emitted X-rays are detected and analysed and the relationship between count frequency and channel number is displayed as the spectrum of detected X-rays. The displayed spectrum may be calibrated in terms of either X-ray energy or characteristic X-ray lines.

W.D.X. differentiates between the characteristic X-ray wavelengths of different elements. This means that it can be used to resolve overlapping equivalent peaks observed in E.D.X. and it is also superior for the detection of lighter elements.

Elemental distribution X-ray mapping is also usually possible in A.S.E.M. where E.D.S. or W.D.S. is incorporated into the S.E.M. In such cases, the energy dispersive X-ray detector is positioned close to the specimen in order to detect and analyse emitted X-rays. Determination of the energy of detected X-rays enables, by comparison with standard X-ray data, identification of the emitted elements (qualitative analysis). Quantitative analysis is also possible when the intensities of the X-ray peaks are analysed by using the Z.A.F. method to measure element concentration.

If an identifiable peak from an emitting element is *gated* (or has a window set around it) on the monitor screen, then the signal from that element becomes isolated and a voltage proportional to the detection rate is fed to the grids of the display tubes on the S.E.M. The image then displayed on the S.E.M. screen is an X-ray map of the distribution of the selected element in the specimen surface.

Appendix 11.7.:**Thermodynamics of Friction Material Constituents:**

The interpretation of the thermodynamic data generated by the controlled heating of friction material constituents was assisted by the application of fundamental thermodynamic theory. The muffle furnace heating behaviour and soak temperature stability was randomly monitored using suitably calibrated thermocouple sensors.

The potential oxidation or reduction of an element or chemical species by another element or chemical species under certain conditions of absolute temperature, pressure and the relative abundance of both interacting and non-interacting species can be predicted for a given system. Practically, this enables an assessment to be made of the likely reaction products within the system based on the interacting species' relative affinities.

In the context of the thermochemical interactions taking place at the frictional interface between an N.A.O. friction material and a grey cast iron rotor, this may well involve considering the relative affinities of those chemical species present with the available sulphur (from metallic sulphide solid lubricants) or with oxygen (from the various constituents and / or transient atmosphere encountered during O.B.W.).

Quantitative comparisons can be made by the consideration of the free energies of formation under standard conditions. In order for any chemical reaction to proceed, there must be a decrease in the Gibbs free energy, ΔG , within the system. ΔG is related to the other significant thermodynamic quantities, the change in enthalpy, ΔH , and the change in entropy, ΔS , by the simplified *Gibbs-Helmholtz* equation:

$$\Delta G = \Delta H - T.\Delta S \quad \text{①}$$

or, at S.T.P.,

$$\Delta G^\circ = \Delta H^\circ - T.\Delta S^\circ \quad \text{②}$$

The change in enthalpy with temperature can be related to the known enthalpy of a compound at any other temperature (typically 298 K) via the molar specific heat capacity of this substance at a constant pressure (C_p):

$$H_T = H_{298} + \int_{298}^T C_p \cdot dT \quad \text{③}$$

which, in this form, is a simple derivative of *Kirchhoff's equation* (1858), where,

$$C_p = A + B \cdot T + \frac{C}{T^2} + D \cdot T^2 \quad \text{④}$$

and hence,

$$\int_{298}^T C_p = \left[A \cdot T + \frac{B}{2 \cdot T^2} - \frac{C}{T} + \frac{D \cdot T^3}{3} \right]_{298}^T \quad \text{⑤}$$

Similarly, the equation describing the entropy of a substance at a temperature, T, is as follows (*Boltzmann* (1866)):

$$S_T = S_{298} + \int_{298}^T \frac{C_p}{T} dT \quad \text{⑥}$$

where,

$$\frac{C_p}{T} = \frac{A}{T} + B + \frac{C}{T^3} + D \cdot T \quad \text{⑦}$$

and hence,

$$\int_{298}^T \frac{C_p}{T} = \left[A \cdot \ln(T) + B \cdot T - \frac{C}{2 \cdot T^2} + \frac{D \cdot T^2}{2} \right]_{298}^T \quad \text{⑧}$$

$$\Delta G_T = \left(\Delta H^\circ + \int_{298}^T C_p dT \right) - \left(T \cdot \left(\Delta S^\circ + \int_{298}^T \frac{C_p}{T} dT \right) \right) \quad \text{⑨}$$

$$\Delta G_T = \Delta H_{298} + \left[A.T + \left(\frac{B}{2.T^2} - \frac{C}{T} + \frac{D.T^3}{3} \right) \right]_{298}^T$$

$$+ T \cdot \left[\Delta S_{298} + \left(A.\ln(T) + B.T - \frac{C}{2.T^2} + \frac{D.T^2}{2} \right) \right]_{298}^T \quad \bullet \bullet$$

$$\Delta G_T = \Delta H_{298} + \left\{ \left[A.T + \left(\frac{B}{2.T^2} - \frac{C}{T} + \frac{D.T^3}{3} \right) \right] - \left[298.A + \frac{B}{2 \times 298^2} - \frac{C}{298} + \frac{298^3 \times D}{3} \right] \right\}$$

$$+ T \cdot \left\{ \Delta S_{298} + \left\{ \left(A.\ln(T) + B.T - \frac{C}{2.T^2} + \frac{D.T^2}{2} \right) - \left(A.\ln(298) + 298.B - \frac{C}{2 \times 298^2} + \frac{D \times 298^2}{2} \right) \right\} \right\}$$

• •

$$\Delta G_T = \Delta H^\circ + (T - 298).A + (T^2 - 298^2) \cdot \frac{B}{2} + \left(\frac{1}{298} - \frac{1}{T} \right) \cdot C + \left(\frac{T^3}{3} - \frac{298^3}{3} \right) \cdot D$$

$$- T \cdot \left\{ \Delta S^\circ + (\ln(T) - \ln(298)).A + (T - 298).B + \left(\frac{1}{2 \times 298^2} - \frac{1}{2.T^2} \right) \cdot C + \left(\frac{T^2}{2} - \frac{298^2}{2} \right) \cdot D \right\}$$

• •

The conversion factor of (moles of product / moles of oxidant) enables ΔH manipulation to present comparable free energy data. It is, however, important to note that the application of C_p in this way precludes the application of these expressions below 298 K, i.e. these equations are only valid above 25°C.

Having established a basic plot of Gibbs energy of formation (or reaction) for a range of, for example, oxides or sulphides, a great many modifications are possible to improve its accuracy. The basic reactions are assumed to be between pure substances and one atmosphere of the appropriate gaseous reactant. The compounds involved are also assumed stoichiometric, which is rarely the case. The level of purity (which may simply denote the presence of additional compounds not involved in the reaction being considered)

is expressed in terms of either an activity, a , for solids, or a partial pressure, P , for gases. These are interrelated using the *Vant Hoff Isotherm*:

$$\Delta G = \Delta G^\circ + R.T. \ln \left\{ \frac{a_{\text{PRODUCT}} \cdot a_{\text{PRODUCT}}}{a_{\text{REACTANT}} \cdot a_{\text{REACTANT}}} \right\} \quad \bullet \bullet \bullet$$

Although such activities have not been rigidly applied to the data accumulated during this study, the activity, or partial pressure of oxygen in air (as opposed to an atmosphere of pure oxygen) has been taken account of for all oxidation reactions (including the sulphidation of oxygen). By taking into account the partial pressure of oxygen in air ($O_2 = 0.2095 \%$), and assuming the system behaviour to be non-Raoultain, the theoretical propensity for reactions to take place or for existing compounds to remain stable is slightly less favourable although only to the extent shown:

$$R.T. \ln \left\{ \frac{1}{P_{O_2}} \right\} = 8.31441 (J.mol^{-1}.K^{-1}).T(K). \ln \left\{ \frac{1}{0.2095} \right\} = 0.01300T (kJ.mol^{-1}) \quad \bullet \bullet \bullet$$

However, further difficulties may arise upon evolution of various gaseous decomposition products such as H_2O , H_2 , CO and CO_2 , which may affect the overall partial pressure of oxygen. Such complications are, however, neglected since in broad terms the total interfacial system will be exposed to the same changes in atmospheric composition and secondly, the cross-flow dynamics of the stator / rotor system usually ensure that gaseous build-up is limited.

A great many problems present themselves in attempting to establish an accurate thermodynamic representation of the interactions occurring in complex systems. Firstly, the theoretical approach taken to predicting thermochemistry does not enable the direct assessment of the interactions between an uncombined metallic element, M , and two non-metallic components (usually in the gaseous form), e.g. O_2 and S , without the application of Predominance diagrams (*cf.* phase diagrams and Pourbaix diagrams) which are inappropriate in complex systems. Secondly, the activities of both reactants and products cannot be accurately predicted at the interface since it is difficult to quantify the contribution

made by ferrous components acting at the interfacial regions to thermochemical interactions. It is therefore clear that any surmised conclusions deriving from this treatment of the problem should be considered qualitatively.

With reference to the Ellingham-type diagrams shown in figures 22 and 23, if ΔG° for compound formation becomes positive, the compound is no longer stable and will spontaneously decompose. Reduction reactions may be readily identified, compounds for curves lower on the diagram (i.e. possessing a greater $-\Delta G^\circ$ at a specific temperature) will displace compounds with curves higher on the diagram, e.g. reduce the oxide.

In considering the tribological interactions taking place between automotive braking friction couples, many of the important reactions plotted in figures 22 and 23 are outlined in tables 11.7.1. and 11.7.2., respectively. (These data are only comparable when considered in combination with a single mole of the common reactant (i.e. gaseous O_2). The form of those compounds considered does not take into account subsequent transformations such as instantaneous sublimation.)

Superficial observations might include an affirmation of the high relative stability of MnS alluded to in **5.1.1.1.** Not comprehensively noted on the diagram are the points at which phase transformations take place, although the gradients do change at these points, not least due to the changes in entropy. Sb_2S_3 , for example, liquefies at $550^\circ C$, but its low relative stability suggests that it will have been considerably oxidised before this temperature is attained.

Table 11.7.1.:*Binary constituent oxides potentially active at the frictional surface interface.*

Oxide:	Theoretical oxidation reaction:	Moles of reactant / s : O₂ : product / s
CO	$2 \langle C \rangle + (O_2) \rightarrow 2 \langle CO \rangle$	2 : 1 : 2
CO ₂	$\langle C \rangle + (O_2) \rightarrow \langle CO_2 \rangle$	1 : 1 : 1
CuO	$2 \langle Cu \rangle + (O_2) \rightarrow 2 \langle CuO \rangle$	2 : 1 : 2
Cu ₂ O	$4 \langle Cu \rangle + (O_2) \rightarrow 2 \langle Cu_2O \rangle$	4 : 1 : 2
Fe _{0.945} O	$2 \langle Fe \rangle + (O_2) \rightarrow 2 \langle Fe_{\approx 1}O \rangle$	2 : 1 : 2
Fe ₃ O ₄	$\frac{3}{2} \langle Fe \rangle + (O_2) \rightarrow \frac{1}{2} \langle Fe_3O_4 \rangle$	$\frac{3}{2} : 1 : \frac{1}{2}$
Fe ₂ O ₃	$\frac{4}{3} \langle Fe \rangle + (O_2) \rightarrow \frac{2}{3} \langle Fe_2O_3 \rangle$	$\frac{4}{3} : 1 : \frac{2}{3}$
H ₂ O	$2 \langle H_2 \rangle + (O_2) \rightarrow 2 \langle H_2O \rangle$	2 : 1 : 2
MoO ₃	$\frac{2}{3} \langle Mo \rangle + (O_2) \rightarrow \frac{2}{3} \langle MoO_3 \rangle$	$\frac{2}{3} : 1 : \frac{2}{3}$
MoO ₃	$\frac{2}{7} \langle MoS_2 \rangle + (O_2) \rightarrow \frac{2}{7} \langle MoO_3 \rangle + \frac{4}{7} \langle SO_2 \rangle$	$\frac{2}{7} : 1 : \frac{2}{7} : \frac{4}{7}$
SO ₂	$\langle S \rangle + (O_2) \rightarrow \langle SO_2 \rangle$	1 : 1 : 1
Sb ₂ O ₃	$\frac{4}{3} \langle Sb \rangle + (O_2) \rightarrow \frac{2}{3} \langle Sb_2O_3 \rangle$	$\frac{4}{3} : 1 : \frac{2}{3}$

Table 11.7.2.:*Binary constituent sulphides potentially active at the frictional surface interface.*

Sulphide:	Theoretical sulphidation reaction:	Moles of product / s : S₂ : reactant / s
CuS	$2 \langle Cu \rangle + (S_2) \rightarrow 2 \langle CuS \rangle$	2 : 1 : 2
Cu ₂ S	$4 \langle Cu \rangle + (S_2) \rightarrow 2 \langle Cu_2S \rangle$	4 : 1 : 2
FeS	$2 \langle Fe \rangle + (S_2) \rightarrow 2 \langle FeS \rangle$	2 : 1 : 2
FeS ₂	$\langle Fe \rangle + (S_2) \rightarrow \langle FeS_2 \rangle$	1 : 1 : 1
H ₂ S	$2 \langle H_2 \rangle + (S_2) \rightarrow 2 \langle H_2S \rangle$	2 : 1 : 2
MoS ₂	$\langle Mo \rangle + (S_2) \rightarrow \langle MoS_2 \rangle$	1 : 1 : 1
MnS	$2 \langle Mn \rangle + (S_2) \rightarrow 2 \langle MnS \rangle$	2 : 1 : 2
PbS	$2 \langle Pb \rangle + (S_2) \rightarrow 2 \langle PbS \rangle$	2 : 1 : 2
SO ₂	$2 \langle O_2 \rangle + (S_2) \rightarrow 2 \langle SO_2 \rangle$	2 : 1 : 2
Sb ₂ S ₃	$\frac{4}{3} \langle Sb \rangle + (S_2) \rightarrow \frac{2}{3} \langle Sb_2S_3 \rangle$	$\frac{4}{3} : 1 : \frac{2}{3}$

Appendix 11.8.:**X-Ray Diffraction:**

X-Ray Diffraction (X.R.D.) (147) is a widely used technique that enables the identification of compounds via their unique atomic lattice arrangements.

To describe the principle, an X-ray source provides polychromatic radiation, typically from a Cu target. The monochromator positioned in front of the detector is ‘tuned’ to select only the strong $K\alpha$ emission lines of the source (e.g. Cu $K\alpha_1$), the system then being considered as operating with monochromatic X-radiation. The sample is rotated about its central axis. Initially, the source, the surface of the sample and the detector are in line across the diameter of the diffractometer circle. As a scan proceeds, the detector is rotated through an angle of $2\theta^\circ$ per standard rate unit while the sample is rotated about its plane by θ° per standard rate unit. This geometry is strictly maintained throughout and usually a scan commences at a 2θ angle of 20 or 30° in order to avoid the direct beam.

The X-rays deflected from the specimen surface are reflected according to Bragg's Law, by families of crystal planes such that whenever a reflection is obtained, the following condition applies:

$$n \cdot \lambda = 2 \cdot d_{\{hkl\}} \cdot \sin \theta \quad \bullet$$

where n = order of diffraction represented by an integer, typically 1 (dimensionless).

λ = wavelength of the incident beam (m).

$d_{\{hkl\}}$ = interlamellar spacing of adjacent diffracting crystal planes, {h, k & l} (m).

θ = angle of the specimen to the detector ($^\circ$).

As the scan proceeds, X-rays are detected only when the angular relationship between the source, sample and detector matches the condition for a Bragg reflection for a family of planes within the sample. Therefore, the various Bragg reflections manifested by the specimen are detected at appropriate angles

(2 θ -values) throughout the scan. The signal monitored is proportional to the detected count rate and may be outputted in any preferred form.

Values of θ , $d_{\{hkl\}}$ and relative peak intensity can then be compared with values from the powder file of the A.S.T.M. (*American Society for the Testing of Materials*) using a 'finger print' method in order to identify the sample constituents.

Each of the basic and heat-treated samples outlined in the text that were still capable of handling subsequent to their respective treatments were subjected to X.R.D. scans using monochromatic Cu $K\alpha_1$ radiation, generally between 15° and 70°. The equipment used was a Philips PW 1820 and associated proprietary analysis software.

Appendix 11.9.:**Full-scale Inertial Dynamometer Testing:**

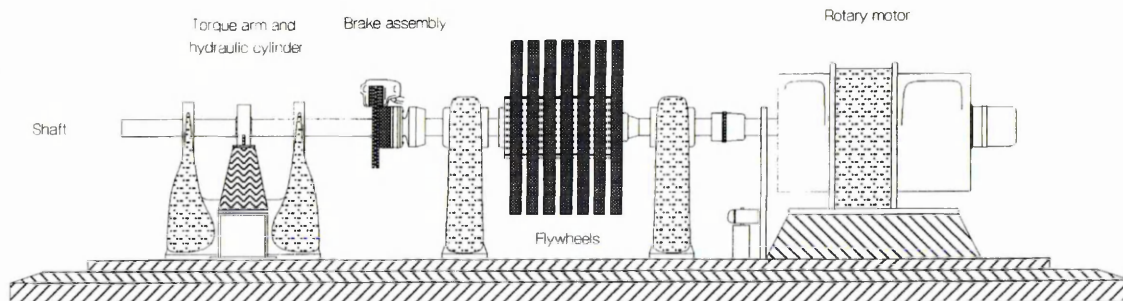
The basic concept and subsequent popularity of the inertial dynamometer as a tool to simulate vehicle braking has been borne out by constant improvements and adaptation since their establishment as a laboratory test machine early in the history of friction material development. The factor that has dictated this proliferation is the equipment's utilisation of commercial brake assemblies.

A typical fixed, single-end, full-scale inertial dynamometer (figure 11.9.1.) incorporates two heavy shafts; a primary shaft driven by an electric motor and carrying a bank of differential flywheels, and, a secondary shaft in line with the first for applied torque load measurement. A commercial brake rotor (disc or drum) is bolted to the end of the primary shaft, which is analogous to the stub-axle in a vehicle-based disc brake system. The retarding mechanism (caliper or backplate and shoe assembly) is anchored to the immediately adjacent end of the secondary shaft, analogous to the hub or stub-axle carrier in a vehicle-based disc brake system. During operation, this secondary shaft is prevented from rotating with the first by a torque reaction member that allows measurement of the applied torque load.

The range of flywheels on the primary shaft are intended to simulate that fraction of the vehicle weight or inertia (J_v) for which the brake under test would be responsible during automotive braking. Those flywheels not required for a specific test need not be removed from the rig but remain stationary since they are bearing mounted.

Figure 11.9.1.:

Schema of a fixed, single end, full-scale, inertial dynamometer for laboratory brake testing.



During an automotive brake application, the tribosystem converts and absorbs the vehicle's kinetic energy according to the following equation (140):

$$\text{Kinetic energy of a braking vehicle} = \int_{t_1}^{t_2} T_B \cdot \omega \, dt \quad \text{①}$$

where T_B = braking torque or braking moment during vehicle deceleration (N.m).

ω = angular velocity at the vehicle axle (radians.s⁻¹).

t_1 = commencement of braking (s).

t_2 = completion of braking (s).

As a derivative form, the instantaneous braking torque or moment developed during that same braking operation may be given by:

$$T_B = J_v \frac{d\omega}{dt} \quad \text{②}$$

where J_v is the vehicular equivalent moment of inertia. This in turn enables us to confirm the known relation for the energy content of a rotating body:

$$\text{Kinetic Energy} = \frac{1}{2} J_v (\omega_2^2 - \omega_1^2) \quad \text{③}$$

where ω_1 = original angular velocity at t_1 (radians.s⁻¹).

ω_2 = final angular velocity at t_2 (radians.s⁻¹).

Additionally, the combined weight of the flywheels selected is usually adjusted in order to take account of parasitic drag coefficients and drive-line deceleration (138). Early inertial dynamometer testing

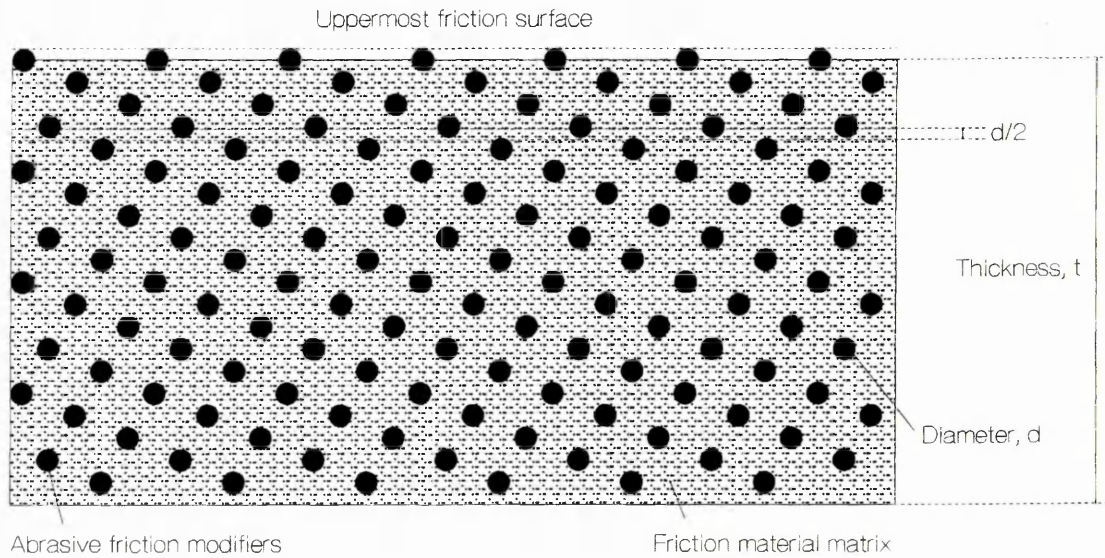
involved disarming the electric motor for the duration of the brake application although later developments enabled partial inertia contributions of quantified magnitude to be simulated by continuing to drive the shaft during braking. Further basic improvements incorporated the simulation of air-flow over the brake taking into account decreasing road speed during brake application and vehicle-specific air-flow and aerodynamics.

One of the greatest drawbacks associated with single-end dynamometers is that the estimated brake input is invariable. It is far more accurate to use a dual-end, full-scale inertial dynamometer (139 – 140) consisting a fore and rear brake assembly on each end of the primary shaft, thus significantly simplifying flywheel selection (bisected vehicle characteristics) and enabling the transfer of work from fore to rear and vice-versa according to in-service performance variations.

Dynamometer test results, like those obtained through vehicle testing, are not as consistent or as reproducible as their smaller, more specialised tribotesting counterparts. In subsequent tests where all the apparently appreciable variables are duplicated, variability in the friction coefficient to within +/- 5 % is not uncommon (135). However, inertial dynamometers do show the closest correlation with vehicle-based field trials and lend themselves to a great many specialist test applications and configurations such as those required for noise or vibration studies.

Appendix 11.10.:**Calculation of Abrasive Particulate Loading:****Figure 11.10.1.:**

Cross-sectional schematic representation of an abrasive-bearing friction material.



Nominal apparent swept area of pad, A_a	=	5,724 mm ²	(= 5.724 x 10 ⁻³ m ²)
Nominal original pad thickness, t	=	12.3 mm	(= 1.23 x 10 ⁻² m)
Nominal original pad volume, V	=	70,405.2 mm ³	(= 7.041 x 10 ⁻⁵ m ³)
Mean particle diameter, d	≈	135 μm	(≈ 120 - 150 x 10 ⁻⁶ m) [Ⓡ]
Volume fraction of abrasive, f	=	unknown	(volume %)

[Ⓡ] = Applies to an example particulate, zircon sand, as used in pads AB 6 and 12.

Let us consider a regular section of friction material with a constant cross-section and finite length. The volume of the pad is given by V , the thickness by t , and the nominal swept surface area of the top face by A_a . Each pad contains a number of abrasive particles, the quantity given by the volume fraction, f . Assuming these particles to be uniformly dispersed throughout the material and, for the sake of simplification during the first iteration, of spherical morphology of mean diameter, d (derived from the

results of external particle size analyses), and hence each approximating to having a volume,

$$V_{abrasive} = \frac{4}{3} \cdot \pi \cdot \left(\frac{d}{2}\right)^3.$$

We will assume that surface-impinging particles may protrude by up to $d/2$ from the uppermost surface of the pad. It will be assumed that abrasives protruding beyond their mid-point are lost during machining / sample preparation / friction due to limited adherence with the friction material matrix. It is obvious from the X-ray elemental digimaps that abrasive particles break the surface since particle diameters much greater than the crown of an average-sized particle can be observed, thus partially satisfying our assumptions.

Thus, we shall consider the particles to be capable of protruding to their centres (maximum protrusion = $d/2$, figure 11.10.1.).

For friction material pad AB 6,

No. of particles observed in a given area	=	150 particles
Size of given area	=	11 x 11 mm
Therefore, no. of particles per unit area	=	1.24 particles.mm ⁻²
Therefore, no. of particles at the swept surface	=	7,096 particles
Therefore, no. of particles per pad volume	=	7,096 particles x 12.3 mm / (0.135 mm / 2)
	=	1.29 x 10 ⁶ particles per pad
Equivalent volume of this quantity of abrasive	=	1.29 x 10 ⁶ x 4/3 x π x (0.135 mm / 2) ³
	=	1666 mm ³
Therefore, volume fraction, f	=	2.37 %

However, given the disproportionate volume influence of larger particles, this range should be quoted at both extremes of the nominal particle size range, i.e. if all zircon sand particles were of 120 μm , the same calculation would yield a volume fraction of 1.87 % but at 150 μm diameter, the same quantity of particles would represent 2.92 % of the total pad volume. Similarly, if we were to determine that such

particulates become plucked from the matrix prior to reaching a half-diameter of exposure, say by only protruding to a distance equating to one third of a diameter before extraction, then the same 135 μm particles would show a calculated volume fraction 50 % higher at 3.55 %. In general however, all of these values will be above the real volume constitution of abrasives due to the earlier assumptions relating to particle morphology.

For smaller particle sizes, e.g. $\varnothing < 50 \mu\text{m}$ ($\varnothing / 2 < 25 \mu\text{m}$), it becomes necessary to include the effect of the electron beam's interaction volume since sub-surface particles are actually being detected to the X-ray penetration depth (the estimated depth of the interaction volume of escaping X-rays produced from an electron probe of primary accelerating voltage 10 kV is of the order of 1 μm).

Appendix 11.11.:**X-ray Photoelectron Spectroscopy:**

X-ray Photoelectron Spectroscopy (X.P.S., formerly bracketed under a group of surface analytical techniques collectively known as *Electron Spectroscopy for Chemical Analysis* (E.S.C.A.)) enables the constitutional analysis of the outermost layers of a material. Although becoming popular for the chemical and elemental analysis of surfaces from ca. 1967, it is only over the past decade or so that X.P.S. has received significant attention in the investigation of separated tribosurfaces to elucidate the thermochemical interactions taking place during friction.

All elements other than hydrogen and helium may be detected and the lower limit of detection of any particular element is about 1 %, although this may be prejudiced by interferences from other elements present within the specimen.

The basic analysis of a specimen surface represents an average over several mm² and the technique can be applied to solids, liquids or gases. The instrument used for such chemical analyses is an electron spectrometer.

X.P.S. utilises the properties of X-radiation (or similar, *cf.* synchrotron radiation, or ultraviolet light and its application in *Ultraviolet Photoelectron Spectroscopy* (U.P.S.)) in order to cause the emission of photoelectrons when they fall on matter. The basis of the elemental analysis is that the kinetic energy of the photoelectron is characteristic of the elements present in the specimen. The photoelectrons (β -rays) emitted from the specimen possess a specific kinetic energy, E_K , which is proportional to the difference between the characteristic energy of the incident exciting X-radiation, $h\nu$, and the former binding energy of the simultaneously expelled electron, E_B , i.e.:

$$E_K = h\nu - E_B \quad \bullet$$

Thus, a spectrum of binding energy for the energy values of a specimen can be obtained. Each element has its own characteristic binding energy spectrum and the elemental composition of a specimen can be determined by the inspection of an X.P.S. trace.

The X.P.S. equipment, described simply, consists of a monochromatic X-radiation source, an electron energy analysing spectrometer and a specimen holder, all of which are enclosed under ultra-high vacuum.

The nomenclature that is used to categorise peaks in an X.P.S. spectrum is based upon the total angular momentum, characterised by the quantum number j , of affected electrons. The total angular momentum of an electron is a vectorial summing of its orbital angular momentum, the electron orbit being described by l , and the electronic spin, designated s , which takes values of $\pm 1/2$. These two components contribute to the binding energy of an electron by reflecting the inherent magnetic field of an electron orbiting an atomic nucleus. X.P.S. therefore applies spectroscopic nomenclature, as shown in table 11.11.1.

Table 11.11.1.:

X-ray and spectroscopic notation showing the nomenclature commonly used in both X.P.S. and A.E.S.

Duplicated from reference 171.

Quantum numbers:			X-ray	X-ray	Spectroscopic
n ($n=1,2,3,4,\dots$)	l ($l=0,1,2,3,\dots$)	j ($j=l+s$ ($s=\pm 1/2$))	Suffix:	Level:	level:
1	0	1 / 2	1	K	1 s $\frac{1}{2}$
2	0	1 / 2	1	L_1	2 s $\frac{1}{2}$
2	1	1 / 2	2	L_2	2 p $\frac{1}{2}$
2	1	3 / 2	3	L_3	2 p $\frac{3}{2}$
3	0	1 / 2	1	M_1	3 s $\frac{1}{2}$
3	1	1 / 2	2	M_2	3 p $\frac{1}{2}$
3	1	3 / 2	3	M_3	3 p $\frac{3}{2}$
3	2	3 / 2	4	M_4	3 d $\frac{3}{2}$
3	2	5 / 2	5	M_5	3 d $\frac{5}{2}$
etc.	etc.	etc.	Etc.	etc.	etc.

The interpretation of X.P.S. data must usually be assisted by the parallel interpretation of several concomitant phenomena. One example is the exploitation of surface analytical data resulting from the emission of Auger electrons using *Auger Electron Spectroscopy* (A.E.S.) or *Scanning Auger Microscopy*

(S.A.M.). In essence, A.E.S. provides both chemical and elemental information about a surface (although at higher spatial resolution the chemical data is lost due to electron-stimulated desorption effects).

Auger electron emission occurs when atoms are bombarded by electrons of sufficient kinetic energy (1 – 10 keV). Upon being struck by this electron beam, a core electron is ejected from an energy level of E_x within the atom. The resultant interstice is filled by another electron within the atom. The balance between the original energy level of this second electron, E_y , and its new level, E_x , is inflicted on a third electron, the Auger electron. The Auger electron, which before receiving its energy supplement, occupied an energy level, E_z , is then ejected exhibiting energy characteristics that are unique to the atom from which it was thrown. The kinetic energy of the Auger electron, E_a , is sometimes described by the following approximation:

$$E_a = E_z + E_y - E_x \quad \text{②}$$

From table 11.11.1., Auger transitions are described in terms these three electrons, the traditional nomenclature used being that of X-ray levels, e.g. *KLL* transitions (which include KL_1L_1 , KL_1L_2 , KL_1L_3 , KL_2L_2 , KL_2L_3 and KL_3L_3) where a *K* core electron is knocked out, an *L* electron replaces it and another *L* electron is ejected as an Auger electron.

The phenomenon of Auger electron emission actually occurs within an interaction volume approximately 1 μm deep. However, the detectable energy range of these electrons falls between 0 and 2,000 eV, a range where severe inelastic scattering on the electrons after their ejection means that only those from the outermost monolayers are detectable.

The process of X-ray photoelectronic excitation also induces complementary atomic phenomena that may provide diagnostic assistance in the interpretation of data. Since the mechanics of photoelectron emission inherently involves the ejection of a core electron, valence electrons react vigorously to the perceived increase in nuclear charge, spontaneously rearranging themselves by a process known as relaxation. This phenomenon may enable electrons to become excited to higher level interstices, a process known as shake-up. This transition is detected as smaller photoelectron peaks (typically 10 %),

or satellites, of slightly lower kinetic energy than those of the causal phenomenon. These shake-up satellites are more pronounced in the case of certain transition metals, such as copper, where the effect enables the differentiation between Cu^+ (copper I) and Cu^{2+} (copper II) compounds. An example of the latter is shown in figure 43 where large and discrete shake-up satellites indicate the presence of copper II compounds.

Although generally considered a non-destructive procedure, evidence is accumulating to suggest that, under conditions of ultra-high vacuum and exposure to various forms of both primary and secondary radiation, the surface of a specimen may experience numerous thermo-ionic responses that may physically and chemically alter the surface under investigation. One example relating directly to the investigation of automotive braking transfer films was detailed by Wirth *et al* (97), whereby changes in the oxidation state of copper compounds were observed. The copper compounds encountered were generally seen to be reduced by continued exposure to the exciting X-radiation. Such observations are critical to the verifiable correlation of triboperformance to frictional surface interactions and tribochemistry (discussed after the presentation of reference 172).